

III-Nitride Based Visible Single-Photon Sources

by

Saniya V. Deshpande

A dissertation submitted in partial fulfillment
of the requirements for the degree of
Doctor of Philosophy
(Electrical Engineering)
in The University of Michigan
2015

Doctoral Committee:

Professor Pallab K. Bhattacharya, Chair
Professor Joanna Mirecki-Millunchick
Professor Theodore B. Norris
Associate Professor Zhaohui Zhong

© Saniya V. Deshpande 2015

All Rights Reserved

ACKNOWLEDGEMENTS

First and foremost, I would like to thank my doctoral advisor Prof.Pallab Bhattacharya for giving me the opportunity to work on interesting and challenging projects, and providing me with resources to execute them; most valuable of which has been his undivided attention and time. Despite his busy schedule, he was always available for discussions and guidance. I especially appreciate his help and patience during the publication process. His excitement for new ideas and determination to see them through are contagious. It has been a truly enriching experience to work with and learn from an educator with such unrelenting dedication towards his work and students.

I would like to thank my doctoral committee- Prof. Joanna Mirecki-Millunchik, Prof. Theodore Norris, and Prof. Zhaohui Zhong for their suggestions and critiques throughout the development of this thesis. Prof. Millunchick provided valuable feedback and understanding of the material through TEM characterization. Prof. Norris always asked insightful questions that led us to study the material and devices in greater depth. I thank Prof. Zhong for his time and effort in reading my thesis and his valuable comments. He was also one of the best teachers in graduate school. I would like to thank Prof. Duncan Steel for conceiving novel experiments to study the properties of the material I have grown.

I am thankful to former and present members of the Bhattacharya group, especially Dr. Meng Zhang and Dr. Animesh Banerjee who showed me the ropes of MBE. I owe a great deal to fellow MBE growers Shafat Jahangir, Thomas Frost,

Dr. Wei Guo and Dr. Sishir Bhowmick for their help during many daunting MBE repairs that had to be performed over the last few years. Thomas Frost and Arnab Hazari provided excellent quantum dot samples for this study. Special thanks to Thomas Frost for being a great collaborator on many projects and for his unfailing helpfulness with everything. Dr. Junseok Heo introduced and taught me various optical measurements. I would like to thank Cameron Nelson from the Steel group for investigating optical properties of material grown by me. Lifan Yan from Prof. Millunchick's group, did a great job with structural characterization of nanowires and was the first one to observe many interesting properties during TEM, that eventually led to a more detailed study.

I appreciate the support and efforts of the Lurie Nanofabrication Laboratory staff in keeping the operation running smoothly. Dennis Schweiger was always available to troubleshoot and fix problems in the MBE lab. Dr. Vishva Ray has kept the E-beam lithography and SEM systems working efficiently with minimal down-time, which made it possible to implement ideas expeditiously. Thanks to Dr. Siddharth Gaba for teaching me many useful tricks on the Raith E-beam, which were instrumental in improving my process yields. I owe a great deal to Greg Allion, Matthew Oonk, and Anthony Sebastian for their help with tools and processes, often on weekends and holidays. Dr. Nadine Wang and the LNF User Committee continually strive to make the cleanroom more user-friendly and they are doing a great job. I am indebted to fellow cleanroom users for their generous advice related to tools and processes. I thank Dr. Kai Sun and Dr. Haiping Sun from EMAL for their help with STEM imaging and EDX analysis.

I acknowledge the administrative support provided by Lisa Vogel, Melanie Caughey, Beth Stalnaker, and Steven Pejuan. I appreciate the efforts of Laura Jarels in purchasing for managing all our purchases very efficiently, especially those last minute helium orders. I am grateful to the Rackham Dissertation Writing Committee for

proof-reading many chapters of this thesis. I would like to acknowledge the National Science Foundation (MRSEC program) for their financial support for majority of this work. I would also extend my thanks to the EECS Department for funding opportunities to present my work at various conferences.

I was lucky to have many friends in the EECS department and Ann Arbor who were an important part of my graduate school experience. Sid and Madhura have been my family away from home. Finally, this thesis is dedicated to my parents-Medha and Vilas Deshpande, and my late grandparents, who taught me to dream big and supported me in all my endeavors.

TABLE OF CONTENTS

ACKNOWLEDGEMENTS	ii
LIST OF FIGURES	ix
LIST OF TABLES	xviii
LIST OF APPENDICES	xix
LIST OF ABBREVIATIONS	xx
ABSTRACT	xxii
CHAPTER	
I. Introduction	1
1.1 Introduction	1
1.2 Physics Of Single Photons	2
1.3 Why Produce Single Photons?	6
1.3.1 Quantum Cryptography	7
1.3.2 Quantum Information Processing	9
1.3.3 Quantum Metrology	9
1.4 Sources Of Single Photons	10
1.4.1 Single Atoms And Ions	10
1.4.2 Single Molecule	11
1.4.3 Nitrogen Vacancy (NV)	12
1.4.4 Quantum Dots	12
1.5 Important Attributes Of A Single-Photon Source	13
1.5.1 Operating temperature	14
1.5.2 Wavelength	14
1.5.3 Efficiency	15
1.5.4 Polarization	15
1.5.5 Speed	15
1.6 Nitride-based Quantum Dots As Single-Photon Sources . . .	16
1.6.1 Etched Quantum Dots	17

1.6.2	Stranski-Krastanov Grown Dots	18
1.6.3	Nanowire Quantum Dots	19
1.7	Thesis Overview	20
II. MBE Growth Of Nanowire Heterostructures		24
2.1	Introduction	24
2.2	MBE Growth of GaN Nanowires	25
2.2.1	Nucleation Mechanism For Self-Induced GaN Nanowire Growth	26
2.2.2	Axial Growth And Nanowire Elongation	31
2.2.3	Growth Conditions For GaN Nanowires	31
2.2.4	Defects In GaN Nanowires	34
2.2.5	Varying Nanowire Density And Diameter	36
2.3	Growth Of InGaN/GaN Disk-In-Nanowire Heterostructures .	38
2.4	Growth Of Nanowire Diodes	41
2.5	Summary	45
III. Optical Characterization Of Nanowire Heterostructures		46
3.1	Introduction	46
3.2	Photoluminescence From GaN Nanowires	47
3.2.1	Photoluminescence At Room And Low Temperature .	47
3.2.2	Temporal Behavior Of Luminescence From GaN Nanowires	48
3.3	Emission From InGaN/GaN Disk-In-Nanowires	49
3.3.1	Temperature Dependent Photoluminescence	49
3.3.2	Time Resolved Photoluminescence From InGaN/GaN Disks-In-Nanowires	53
3.3.3	Micro-Photoluminescence	54
3.4	Heterostructure Design	57
3.5	Optical Characteristics Of Single InGaN Disk-In-Nanowire .	58
3.5.1	Exciton And Biexciton Complexes In Nitrides	60
3.5.2	Luminescence From Single Disk-In-Nanowire	64
3.5.3	Second-Order Correlation	65
3.6	Summary	67
IV. Electrically Driven Single-Photon Emission InGaN Disk-In-Nanowire		69
4.1	Introduction	69
4.2	Growth And Structural Characterization	71
4.3	Photoluminescence	71
4.4	Fabrication Of Single Nanowire Diodes	72

4.4.1	Fabrication Of Single Nanowire Diodes On Other Substrates	73
4.4.2	Electrical Characteristics Of Single Nanowire Diodes	74
4.4.3	Improving Diode Performance	75
4.5	Electroluminescence From Single Dot-In-Nanowire	80
4.5.1	Spectra From Blue Emitting Single Nanowire LEDs	80
4.5.2	Spectra From Green Emitting Single Nanowire LEDs	81
4.6	Second-Order Correlation Measurement	83
4.6.1	Blue Single-Photon Emission	85
4.6.2	Green Single-Photon Emission	87
4.6.3	Analysis	88
4.7	Output Polarization	90
4.8	Junction Temperature	90
4.9	Summary	95
V.	Electrically Driven Single-Photon Emission At Room Temperature	97
5.1	Introduction	97
5.2	Growth And Characterization	100
5.2.1	MBE Growth Of Quantum Dot Diode	100
5.2.2	AFM Characterization Of QD Layer	102
5.2.3	XRD Characterization Of Heterostructure	105
5.2.4	Analysis Of In Composition Using STEM-EDX	105
5.2.5	Photoluminescence From Ensemble Of QDs	108
5.3	Single Quantum Dot LEDs	109
5.3.1	Electroluminescence From A Single Aperture At Low Temperature	110
5.3.2	Electroluminescence From A Single Aperture At Room Temperature	112
5.4	Single-Photon Emission From A Single Quantum Dot	113
5.4.1	Single Photons On Demand	116
5.5	Summary	120
VI.	On The Formation And Nature Of InGaN Quantum Dots In GaN Nanowires	121
6.1	Introduction	121
6.2	Growth And Characterization	123
6.2.1	MBE Growth Of InGaN/GaN and GaN/AlGaN Disk-In-Nanowires	123
6.2.2	Photoluminescence from InGaN/GaN and GaN/AlGaN Disk-In-Nanowires	125
6.3	Carrier Lifetime Measurements	125

6.3.1	Carrier Lifetime Measurement In InGaN/GaN Disk-In-Nanowires	125
6.3.2	Carrier lifetime measurement in InGaN/GaN quantum dots	131
6.4	Electron-hole scattering	132
6.5	TEM characterization	134
6.6	Single-Photon Emission	139
6.7	DINW Edge Emitting Laser	141
6.7.1	Linewidth Enhancement Factor	144
6.8	Simulation Of Quantum Dot Size	144
6.9	Summary	146
VII.	Conclusions And Future Directions	148
7.1	Summary	148
7.1.1	Quantum Disk-In-Nanowire Based Single-Photon Source Operating At 200 K	148
7.1.2	Single Disk-In-Nanowire Based Electrically Injected Single-Photon Source	149
7.1.3	Quantum Dot Based Single Photon Diode Operating At Room Temperature	149
7.1.4	Understanding The Nature Of Quantum Confinement In Disk-In-Nanowires	150
7.2	Future Directions	150
7.2.1	Site-Controlled Nanowire Growth	150
7.2.2	Improving single-photon source Efficiency Using A Microcavity	151
7.2.3	Strong Coupling And Lasing	154
7.2.4	Generation Of Entangled Photon-Pairs	155
7.2.5	Electron Energy Loss and Gain Spectroscopy In Bi-based InGaN/GaN Disk-In-Nanowires	156
APPENDICES	158
BIBLIOGRAPHY	170

LIST OF FIGURES

Figure

1.1	Single-photon emitting system, emits a single photon upon optical or electrical excitation followed by subsequent relaxation	2
1.2	Schematic of the Hanbury Brown-Twiss (HBT) measurement system	3
1.3	Classification of light as (a) coherent, (b) bunched and (c) anti-bunched based on nature on the photon stream	4
1.4	$g^{(2)}(\tau)$ for different forms of light	5
1.5	Number of publications on related research areas each year [7] . . .	6
1.6	Schematic of BB84 implementation of QKD between Alice and Bob. PC1 and PC2 represent two pockel cells that provide polarization control as a function of applied voltage. PBS stands for a polarized beam splitter and D1, D2 are identical single-photon detectors. [6] .	8
1.7	Quantum dots formed by etching of a single quantum well heterostructure (a) schematic of device and (b) scanning electron microscopy (SEM) of fabricated site-controlled quantum dot nanopillars [42] .	18
1.8	MBE grown self-organized quantum dots: (a) cross-sectional transmission electron microscopy (XTEM) image of GaN/AlN self-organized quantum dots [43] (b) atomic force microscopy (AFM) image of uncapped InGaN/GaN quantum dots (courtesy Thomas Frost)	20
1.9	TEM of (a) GaN/AlGaN nanowire quantum dot single-photon emitter, operating at room temperature [45] and (b) InGaN/GaN nanowire quantum dot single-photon emitter, operating at 200 K [46].	21
2.1	Gen-II plasma-assisted molecular beam epitaxy (PAMBE) system. .	25

2.2	(a) (1x1) to (b) (7x7) transition of the Si(111) surface reconstruction observed by reflection high energy electron diffraction(RHEED). 6 additional spots have appeared between the main (1x1) spots.[63]	26
2.3	HRTEM of thin amorphous Si_xN_y layer at the interface of Si and GaN nanowires	28
2.4	Schematic diagram representing the different physical processes involved in the incubation period during the nucleation phase. The subcritical-sized nuclei vanish owing to Ga adatom surface diffusion towards critical-sized clusters. [67]	29
2.5	HRTEM images of samples grown for (a) 7 and (b) 16 minutes, reveal the transitions of GaN island shapes during the nucleation process: from spherical cap-shaped islands to the nanowires. The shape of spherical caps is outlined for the sake of clarity. [68]	30
2.6	Schematic showing various processes (adatom adsorption, desorption and diffusion) in action during the growth of GaN nanowires [70]	32
2.7	Phase diagram of growth of GaN under a fixed nitrogen flux, showing various regimes of growth [71]	33
2.8	Cross-sectional TEM micrograph showing a threading dislocation originating at the nanowire/Si interface and terminating at the sidewall [55]	34
2.9	TEM images of a zipper defect array between two relatively misoriented and coalescing nanowires on their Si substrate: (a) low resolution and (b) high resolution TEM images of nanowires growing with different c-axes orientations. (c) and (d) shows TEM images of the zipper defects formed at the site of coalescence. [66].	36
2.10	Effect of substrate temperature and Ga flux on nanowire density and diameter shown in top-view SEM images	37
2.11	Emission from InGaN/GaN disk-in-nanowires (a) TEM image of a GaN nanowire with multiple InGaN disks and (b) emission from InGaN disks over the visible spectral range [57]	39
2.12	Elemental composition measured from an energy dispersive spectroscopy line scan along the nanowire c-axis across InGaN disk, for (a) blue and (b) green emitting disk in GaN nanowires	40

2.13	(a) SEM image taken at 45° tilt of an ensemble of nanowire p-n junctions and (b) TEM image of a single dot-in-nanowire p-n junction	42
2.14	(a) Schematic of nanowire p-n junction light emitting diode fabricated from a nanowire forest and (b) its measured electrical characterisitics at room temperature	44
3.1	Photoluminescence spectrum from an ensemble of GaN nanowires measured at 300 K	48
3.2	Photoluminescence spectrum from an ensemble of GaN nanowires measured at 10 K	49
3.3	PL decay transient measured from undoped GaN nanowires at room temperature, solid curve denotes monoexponential fit to measured data.	50
3.4	Temperature dependent photoluminescence from $In_{0.25}Ga_{0.75}N$ disk in GaN nanowires; inset shows the Varshni fit to peak emission values as a function of temperature.	51
3.5	Temperature dependent photoluminescence from $In_{0.37}Ga_{0.63}N$ disk in GaN nanowires. No S-shaped behavior is observed in the peak energy as a function of temperature, as shown in the inset	52
3.6	Transient PL decay shows a lifetime of (a) 1.1 ns at low temperature and (b) 410 ps at room temperature from green emitting InGaN disk-in-nanowires	53
3.7	Schematic of the micro-photoluminescence (μ -PL) setup [77]	55
3.8	μ -PL measurement from a sample containing dispersed nanowires. Figure (a) shows a CCD image of a spatially isolated single disk. Figure (b) shows the difference in the spectrum with and without a pinhole. The size of the pin hole is adjusted to capture the photoluminescence from a single disk. (Courtesy: Lei Zhang)	56
3.9	Temperature dependent photoluminescence from a single $In_{0.1}Ga_{0.9}N$ disk	56
3.10	Effective barrier heights in an InGaN/GaN quantum well structure (a) without and (b) with band-bending cause by polarization fields. [78]	58
3.11	Schematic and SEM of the heterostructure	59

3.12	TEM of an InGaN disk in AlGaN nanowire heterostructure	59
3.13	Photoluminescence from a forest of $In_{0.2}Ga_{0.8}N/Al_{0.1}Ga_{0.9}N$ disk-in-nanowires at room temperature. The inset shows SEM-EDX spectrum from $Al_{0.1}Ga_{0.9}N$ nanowires	60
3.14	(a) Schematic of the exciton and biexciton energy levels in a quantum dot and (b) modelling of biexciton binding energy based on quantum dot aspect ratio in GaN/AlN dots [43]	63
3.15	μ -PL from a single InGaN disk at (a) 10 K and (b) 200 K. (c) Pump-power dependence of the integrated intensity of biexciton peak at 200 K.	65
3.16	Second-order correlation measured at biexciton line under 80 MHz pulsed optical excitation at (a) 10 K and (b) 200 K	66
3.17	Analysis of pulsed second-order correlation data to extract quantum disk lifetime	68
4.1	Schematic of a single disk-in-nanowire diode	72
4.2	Measurement of IQE of as-grown nanowires through excitation dependent PL at low temperature and room temperature	73
4.3	Identification of single nanowire position with respect to alignment mark under SEM	74
4.4	An (a) SEM and (b) AFM image of single nanowire diode with Ti/Au contacts	75
4.5	Single nanowire diode fabricated on a Si_3N_4 TEM membrane	76
4.6	Current voltage characteristics of blue emitting single nanowire diode, the inset show I-V curve on a logarithmic scale.	77
4.7	Calculation of series resistance of GaN dot-in-nanowire p-n junction	78
4.8	Current voltage characteristics of green emitting single nanowire diode after improvements in growth and metallization scheme. Inset shows I-V curve on a logarithmic scale. Red dotted ellipse denotes voltage range where resistance was measured	79

4.9	Exciton and biexciton electroluminescence from a single dot-in-nanowire in blue spectral range	80
4.10	Variation of integrated intensity of peaks with injection current	81
4.11	Temperature dependent electroluminescence from a single dot-in-nanowire in green spectral range	82
4.12	Arrhenius plot of exciton and biexciton electroluminescence from a single dot emitting in the green spectral range	83
4.13	Energy position of the exciton transition from QD electroluminescence and Varshni fit to measured data	84
4.14	Linewidth of the exciton transition as a function of temperature	84
4.15	Second order correlation from (a) exciton and (b) biexciton electroluminescence from single dot-in-nanowire in the blue spectral range at 10 K	86
4.16	Time resolved PL from the biexciton transition	87
4.17	Second order correlation from exciton electroluminescence of single dot-in-nanowire emitting in green spectral range at 10 K and 125 K. Inset of figure (a) shows the transient decay of exciton PL. Inset of figure (b) shows a periodic stream of single photons recorded by a single photon detector	89
4.18	Polarization of electroluminescence from single dot-in-nanowire	91
4.19	Steady state temperature profile of nanowire p-n junction	92
4.20	Estimated device temperature as a function of injection current density. Inset shows temporal variation of device temperature.	93
4.21	Calculated and measured emission energy shift as a function of the injected current density (calculated: red dots, measured: black squares)	94
5.1	Electrical characteristics of a single GaN/AlGaN disk-in-nanowire diode at room temperature.	99
5.2	Electroluminescence from a single GaN/AlGaN disk-in-nanowire diode at 10 K.	100
5.3	Schematic of the quantum dot diode heterostructure.	101

5.4	AFM of n-doped layers shows smooth surface morphology.	102
5.5	Quantum dot heights follow scaling distribution. Plot of scaling function versus normalized dot height.	103
5.6	Atomic force micrograph of a single InGaN dot	104
5.7	XRD spectrum of the complete heterostructure.	105
5.8	Transmission electron micrograph of a cross-section of single InGaN dot	106
5.9	Elemental composition across the cross-section of single InGaN dot measured in an EDX spectrum.	107
5.10	Photoluminescence measured under non-resonant saturation excitation, from an ensemble of quantum dots at low temperature and room temperature.	108
5.11	Current voltage characterisitics of a single quantum dot diode at room temperature. Inset shows an optical micrograph of a fabricated device with a GSG probing geometry.	109
5.12	Electroluminescence from a single aperture at 20 K and variation of integrated intensities of peaks with injection.	111
5.13	Electrominescence from a single aperture at room temperature. . . .	112
5.14	Integrated intensity of exciton transition increases linearly with injected current density.	113
5.15	Blue-shift of emission peak measured from a control ensemble LED, as a function of injection current.	114
5.16	Second-order correlation from an exciton line at room temperature and 15 K.	115
5.17	$g^{(2)}(0)$ and lifetime as a function of injected current density. . . .	116
5.18	Calculated exciton occupation probability of a quantum dot. . . .	116
5.19	On demand single photons using a pulsed electrical trigger at 200 MHz.	117

5.20	Biassing scheme for time resolved electroluminescence (TREL)s measurement.	118
5.21	TREL from a single exciton line at room temperature at varying injections.	118
5.22	Polarization of InGaN quantum dot emission.	119
6.1	SEM images showing 45° oblique view of InGaN/GaN dot-in-nanowire ensembles with different average diameters. The scale bar for all figures is $1\mu\text{m}$	124
6.2	Room temperature PL from InGaN/GaN and GaN/ $\text{Al}_{0.2}\text{Ga}_{0.8}N$ DINW nanowire samples of different diameters measured under non-resonant saturation excitation. The In composition in InGaN/GaN DINWs is $\sim 40 - 55\%$ and varies with the nanowire diameter.	126
6.3	Transient decay typically observed from ensemble of InGaN/GaN DINWs with an average diameter of 50 nm. The measured data are analyzed using a stretched exponential model with β parameter 0.8.	127
6.4	Total lifetime and its radiative and non-radiative components derived from temperature dependent PL and TRPL measurements, for InGaN/GaN dot-in-nanowires with two different diameters 50 nm and 25 nm. Both InGaN/GaN DINW samples show an increase in radiative lifetime with temperature.	128
6.5	Transient decay typically observed from GaN/ $\text{Al}_{0.2}\text{Ga}_{0.8}N$ DINW. The measured data are analyzed using a mono-exponential model.	129
6.6	Radiative lifetime of GaN/ $\text{Al}_{0.2}\text{Ga}_{0.8}N$ dot-in-nanowires with two different diameters 60 nm and 25 nm shows a nearly constant trend with temperature.	130
6.7	Atomic force micrograph of InGaN/GaN quantum dot layer grown by molecular beam epitaxy. The In composition is estimated to be $\sim 40\%$ and quantum dot density is $\sim 5 \times 10^{10}\text{cm}^{-2}$	131
6.8	Total carrier lifetime and its radiative and non-radiative components for InGaN/GaN QDs. The sample shows an increase in radiative lifetime with temperature.	132
6.9	The electron-hole scattering process in a quantum dot at low temperatures	133

6.10	HRTEM image of 25 nm GaN nanowire with a single InGaN disk showing InGaN quantum dot formation. Inset shows a low magnification image of a single InGaN/GaN DINW (Courtesy: Lifan Yan)	135
6.11	HAADF image of 80 nm GaN nanowire with multiple InGaN islands (Courtesy: Lifan Yan).	136
6.12	HRTEM shows similar InGaN QD-like islands in a 100 nm diameter GaN nanowire grown under entirely different growth conditions. The InGaN QD-island size increases with growth time, as seen in subsequent QD-islands (Courtesy: Prof. Zetian Mi).	137
6.13	TEM image of GaN/ $Al_{0.2}Ga_{0.8}N$ DINW shows sharp quantum well like interfaces with no island formation (Courtesy: Lifan Yan). . . .	138
6.14	Second-order correlation under pulsed optical excitation (at 80 MHz) in a Hanbury-Brown and Twiss (HBT) measurement from a single 25 nm InGaN/GaN DINW showing anti-bunching with $g^2(0)$ is 0.27	140
6.15	Second-order correlation under pulsed optical excitation (at 80 MHz) in a Hanbury-Brown and Twiss (HBT) measurement from a single 25 nm GaN/ $Al_{0.2}Ga_{0.8}N$ DINW which does not show anti-bunching	140
6.16	Schematic of the edge emitting disk-in-nanowire laser ($\lambda=533$ nm) and its calculated mode profile [59]	141
6.17	Electroluminescence spectrum of the laser below and above threshold, under cw excitation (Courtesy: Shafat Jahangir).	143
6.18	Light-output measured as a function of injected current density for the InGaN/GaN DINW laser (Courtesy: Shafat Jahangir).	143
6.19	Linewidth enhancement factor α as function of the emission derived from Haki-Paoli measurements below lasing threshold (Courtesy: Shafat Jahangir).	145
6.20	Calculated energetically stable diameter for a Volmer-Weber InGaN QD formed in GaN nanowires of different dimensions (Courtesy: Prof. Zetian Mi)	146
7.1	SEM micrograph of selective area GaN nanowire growth within holes in oxide mask [124].	151

7.2	Schematic of an electrically driven nanowire LED in a microcavity [125].	153
7.3	Schematic of photonic crystal GaN nanowire laser [126]	154
7.4	AFM topography of a photonic crystal nanocavity aligned to a hill of material on the surface arising from a InAs QD buried below [127]	155
7.5	Single nanowire diodes fabricated on TEM membranes shown schematically in (a). (b) depicts a low-magnification SEM image of fabricated device and (c) shows the I-V characteristics of the device measured at room-temperature.	157
A.1	Top view SEM image: Input to MATLAB	159
A.2	Distribution of nanowire diameters: Output from MATLAB	160
C.1	SEM micrograph of fabricated device, shown in increasing levels of magnification	167
D.1	Raw output file showing nanowire temperature	169

LIST OF TABLES

Table

1.1	Summary of performance of various types of single-photon sources	16
1.2	Band-offsets in InGaN/GaN heterostructures emitting in different wavelength ranges.	17
2.1	Standard growth conditions for GaN nanowires with an average diameter of 25 nm	37
2.2	Growth conditions for InGaN disks emitting over the visible range	38
4.1	Specific contact resistance measured for various metallization scheme using transmission line measurements (TLM)	76
6.1	MBE growth conditions of disk-in-nanowire samples	124

LIST OF APPENDICES

Appendix

A.	Determining average nanowire diameter	159
B.	Fabrication of single nanowire LED	161
C.	Fabrication of single QD LED	165
D.	COMSOL simulation of nanowire temperature	168

LIST OF ABBREVIATIONS

SPS single photon source

HBT Hanbury-Brown Twiss

LED light emitting diode

qubits quantum bits

QKD quantum key distribution

BB84 Bennett-Brassard 84

NV nitrogen vacacy

QD quantum dot

MBE molecular beam epitaxy

MOCVD metal organic chemical vapor deposition

RHEED reflection high energy electron diffraction

WZ wurtzite

ZB zinc blende

SEM scanning electron microscopy

XTEM cross-sectional transmission electron microscopy

TEM transmission electron microscopy

AFM atomic force microscopy

IPA isopropyl alcohol

BHF buffered hydrofluoric acid

EDX energy dispersive x-ray spectroscopy

PL photoluminescence

TREL time resolved electroluminescence

TLM transmission line measurements

DBR distributed Bragg reflector

CB Coulomb blockade

XRD X-ray diffraction

IQE internal quantum efficiency

ABSTRACT

III-Nitride Based Visible Single-Photon Sources

by

Saniya Deshpande

Chair: Prof. Pallab K. Bhattacharya

A quantum dot (QD) is a nanometer-scale inclusion of a smaller bandgap semiconductor material inside a larger bandgap one. Electrons and holes in the QD can occupy only a given set of states with discrete energy levels, such as in an atom. Thus, a QD can act like an atomic two-level system, where the relaxation from an excited state to ground state releases a single photon.

Nitride semiconductors, with their wide bandgap and large exciton binding energy (> 28 meV), have been used as single-photon sources up to room temperature but only through optical excitation. In this work, two different approaches have been investigated for single photon emission: the InGaN/GaN dot-in-nanowire and InGaN/GaN self-organized quantum dot.

InGaN/GaN dot-in-nanowire heterostructures were grown on silicon by molecular beam epitaxy (MBE). Emission from InGaN/GaN dot-in-nanowires can be tuned over the visible spectral range by changing the indium composition. Structural characterization through TEM imaging reveals the nanowires and InGaN quantum dot are free of defects. We estimate an In composition of 25% and 37% in blue ($\lambda=430$ nm) and green ($\lambda=520$ nm) emitting dot-in-nanowires, respectively, by energy dispersive

x-ray spectroscopy (EDX). Optical characterization through temperature dependent photoluminescence (PL) measurements shows high radiative efficiencies of 52% in the blue and 35% in the green emitting dot-in-nanowires. Nanowire p-n junctions containing a single InGaN quantum dot were dispersed on silicon substrates with thermal oxide and used to fabricate single nanowire light emitting diodes (LEDs). The single nanowire LED exhibits sharp excitonic transitions, with linewidths \sim 2-3 meV at 10 K. Single-photon emission under both optical and electrical excitation excitation was observed from single dot-in-nanowire LEDs. The blue-emitting sample shows single-photon emission with $g^{(2)}(0) = 0.16$ and 0.25 at the exciton and biexciton energy, respectively, at 10 K. The temperature characteristics of the emitter were improved by engineering the confinement in the quantum dot and reducing the diode resistance (to $\sim 26 M\Omega$). We demonstrate electrically driven single photon emission, with a $g^{(2)}(0) = 0.35$, from a single InGaN quantum dot emitting in the green spectral range up to 125 K. The quantum dot electroluminescence is polarized along the nanowire c-axis. A detailed study of optical and structural properties of InGaN/GaN dot-in-nanowires shows the formation of self-organized Volmer-Weber dots, with diameters smaller than the nanowire size, in the active region.

A planar GaN diode with a single layer of self-organized InGaN/GaN quantum dots was grown on GaN-on-sapphire. The quantum dot density was controlled through growth parameters and is $2 \times 10^9/cm^2$. These quantum dots, which are ~ 15 nm \times 3nm, luminesce in the red spectral range. Single quantum dot light emitting diodes were fabricated and electroluminescence from these was observed up to room temperature. The exciton emission shows single-photon emission with $g^{(2)}(0) = 0.29$ at room temperature. This $g^{(2)}(0)$ value indicates a three-fold decrease in probability of multi-photon emission events. On-demand single-photon emission at an excitation repetition rate of 200 MHz was achieved, by electrical pumping of the quantum dot.

Nitride-based high temperature single photon sources have potential applications

in quantum cryptography, quantum computation, metrology and other areas. Visible single-photons are particularly attractive because Si based single-photon detectors are most efficient in this wavelength range.

CHAPTER I

Introduction

1.1 Introduction

Since the conception of the idea of a photon by Einstein [1], more than a century ago, tremendous progress has been made in the field of photonics, but devices capable of producing single photons on demand, or “single-photon turnstile devices” have been realized only recently [2]. The demonstration of single-photon sources has only recently become possible due to the availability of high quantum-efficiency single-photon detectors [3]. Single-photon emission is a quantum phenomenon, entirely different from other light emission processes in classical devices like the light emitting diode (LED) or laser.

Just like the way the discovery of stimulated emission led to the development of the laser and inspired numerous applications, it is speculated that the development of a high efficiency, stable single-photon source could enable a whole new range of scientific and engineering endeavors. Quantum information processing, quantum key distribution, and quantum metrology are examples of applications that require single photons. Different applications, however, have different requirements of performance metrics. A source that is an on-demand, high-speed, high efficiency, inexpensive emitter of single photons at room temperature, has been a long-standing goal and has been the main driving force of the work in this thesis.

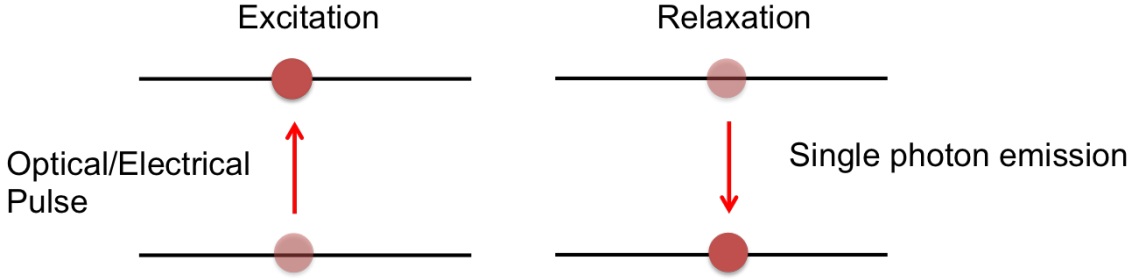


Figure 1.1: Single-photon emitting system, emits a single photon upon optical or electrical excitation followed by subsequent relaxation

1.2 Physics Of Single Photons

A single photon source (SPS), as the name suggests, releases exactly one photon at a time, which can be emitted through a variety of mechanisms in different systems (Fig.1.1). The principle of a single-photon source can be best understood by comparing statistical properties of photons in different types of light. The nature of light can be determined and understood through the study of the second-order correlation function of its intensity. The second-order correlation is given as [4]:

$$g^{(2)}(\tau) = \frac{\langle I(t)I(t+\tau) \rangle}{\langle I(t) \rangle \langle I(t+\tau) \rangle} = \frac{\langle E(t)E(t)^*E(t+\tau)E(t+\tau)^* \rangle}{\langle E(t)E(t)^* \rangle \langle E(t+\tau)E(t+\tau)^* \rangle} \quad (1.1)$$

where $I(t)$ and $E(t)$ are the intensity and electric field of the light beam at time t , respectively, and the symbol $\langle \dots \rangle$ indicates the time averaged value. While classically the correlation function is given as a function of intensity, it can also be written in terms of the number of photon counts because the number of photon counts recorded at the detector is proportional to the measured intensity.

$$g^{(2)}(\tau) = \frac{\langle n_1(t)n_2(t+\tau) \rangle}{\langle n_1(t) \rangle \langle n_2(t+\tau) \rangle} \quad (1.2)$$

where $n_i(t)$ represents the number of counts detected by detector i at time t .

The second-order correlation function is measured in a Hanbury-Brown Twiss

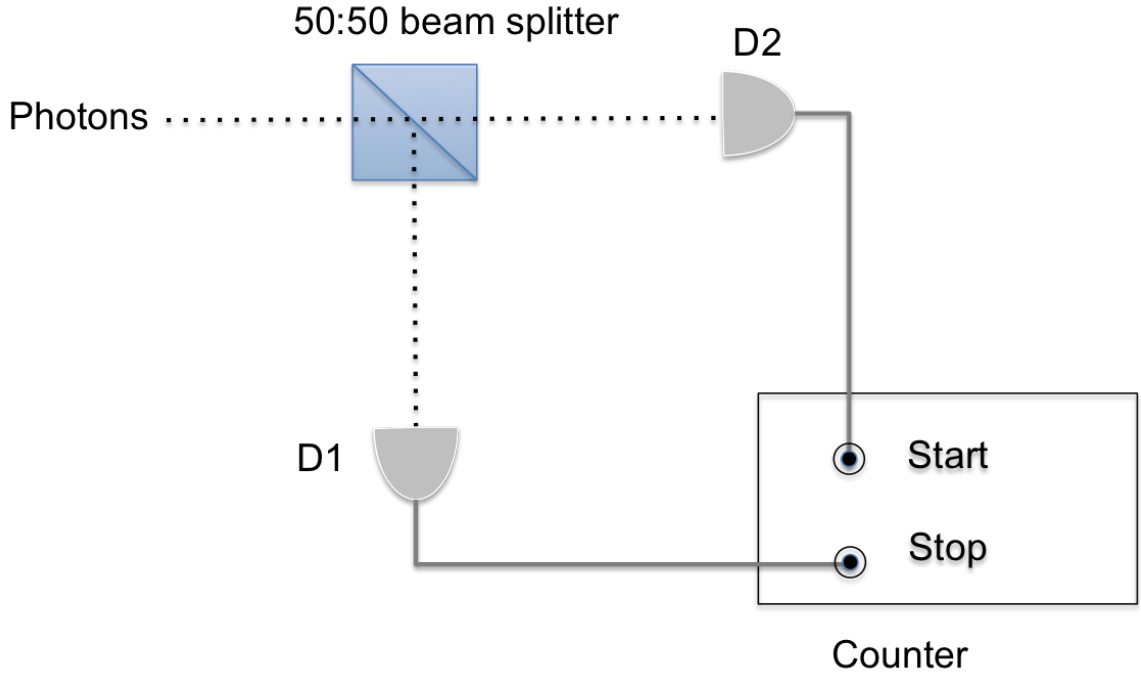


Figure 1.2: Schematic of the Hanbury Brown-Twiss (HBT) measurement system

(HBT) experiment in which a stream of photons is divided into two equal parts by a 50:50 beam splitter and transmitted to two output ports (shown in Fig.1.2) [5]. The photon streams impinge on two identical single-photon detectors, which trigger the start and stop pulses of an electronic counter. The counter keeps a log of the number of pulses at each detector and the time elapsed between the start and stop pulses. Equation 1.2 implies that second-order correlation at zero delay, $g^{(2)}(0)$, is related to the joint probability of detecting a second photon at time $t = \tau$, given that the first photon was detected at time $t = 0$. The nature of light can be classified to three types based on the value of the second-order correlation at zero delay, $g^{(2)}(0)$ (Fig.1.3) [6] :

- (a) *Coherent light*. In the classical picture, emission from a laser is a wave with constant amplitude and phase. Coherent light is characterized by its lack of fluctuations or a completely random photon distribution. The second-order correlation function of such a wave is always equal to unity ($g^{(2)}(\tau) = 1$, for all values of τ) which makes it a convenient reference to compare with other forms of light.

(b) *Bunched light.* In a macroscopic light source such as a black-body radiation lamp, many independent emitters contribute to the total emission. Therefore, the field is a superposition of many incoherent waves. This type of light is referred to as thermal light. Additionally, every spectral line of light originating from a classical source has intensity fluctuations on the time-scale of its coherence time and is, hence, chaotic. In the photon picture, both of these can be thought of as streams of photons with photons lumped together in bunches. As a result, the probability of detecting a second photon, after detecting the first photon at $t=0$, decreases with time, which results in $g^{(2)}(\tau) > 1$.

(c) *Antibunched light.* In an antibunched source of light, photons have regular gaps between them, rather than a random spacing as in the case of coherent light. As a result of the regular interval between photons, the probability of registering a photon event increases with time. Antibunched light has $g^{(2)}(0) < g^{(2)}(\tau)$ or $g^{(2)}(0) < 1$. Thus it is quieter than a coherent light source and is a purely quantum effect with no classical analogue. The nature of $g^{(2)}(\tau)$ for different flavors of light is schematically

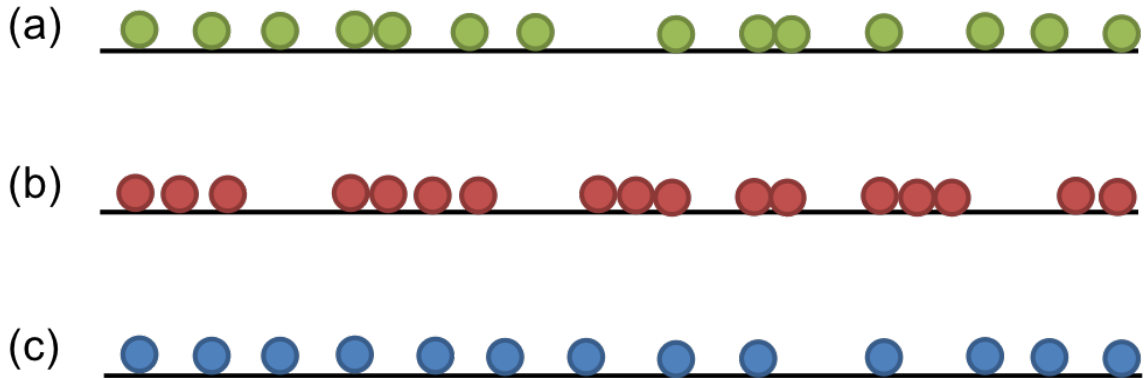


Figure 1.3: Classification of light as (a) coherent, (b) bunched and (c) antibunched based on nature on the photon stream

represented in Fig.1.4.

In a true single-photon emitter, there is zero probability of detecting two photons at detectors D_1 and D_2 at the same time, hence the counter records no events when

the time delay is zero $\tau = 0$, which results in $g^{(2)}(0) = 0$. In practice, the finite time resolution of the detectors will lead to a finite non-zero value of $g^{(2)}(0)$, even with an ideal source. For some applications, a low multi-photon emission probability is desired and thus a heavily attenuated laser is employed. However, for many applications as will be discussed in the following section, a true single-photon source would be much superior to an attenuated laser.

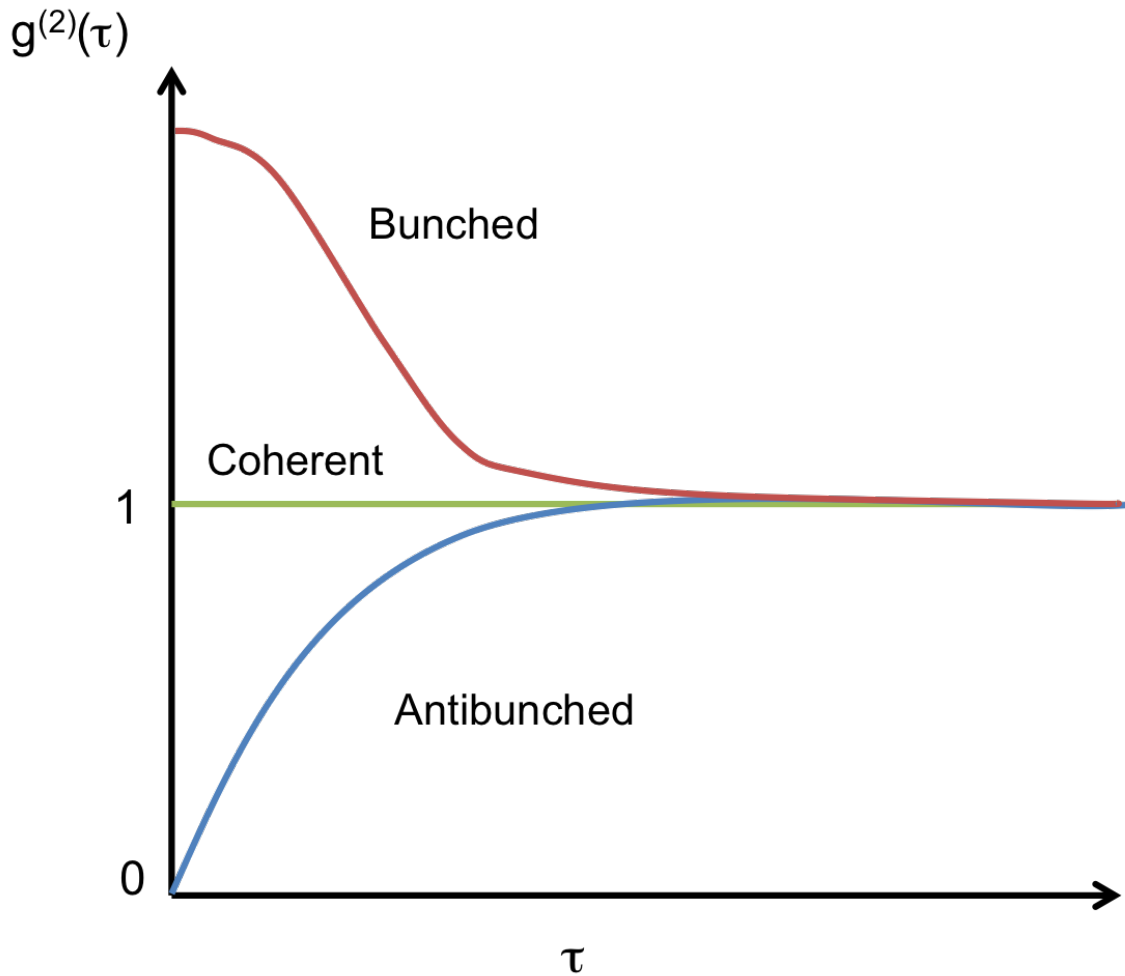


Figure 1.4: $g^{(2)}(\tau)$ for different forms of light

1.3 Why Produce Single Photons?

There has been an exponential rise in the research on development of single-photon sources over the years, as shown in Fig.1.5. The major driving force for research on single-photon sources has been the rise of quantum information processing, which involves encryption, communication, and measurement of data using quantum states or objects. Single photons have several advantages in quantum information processing:

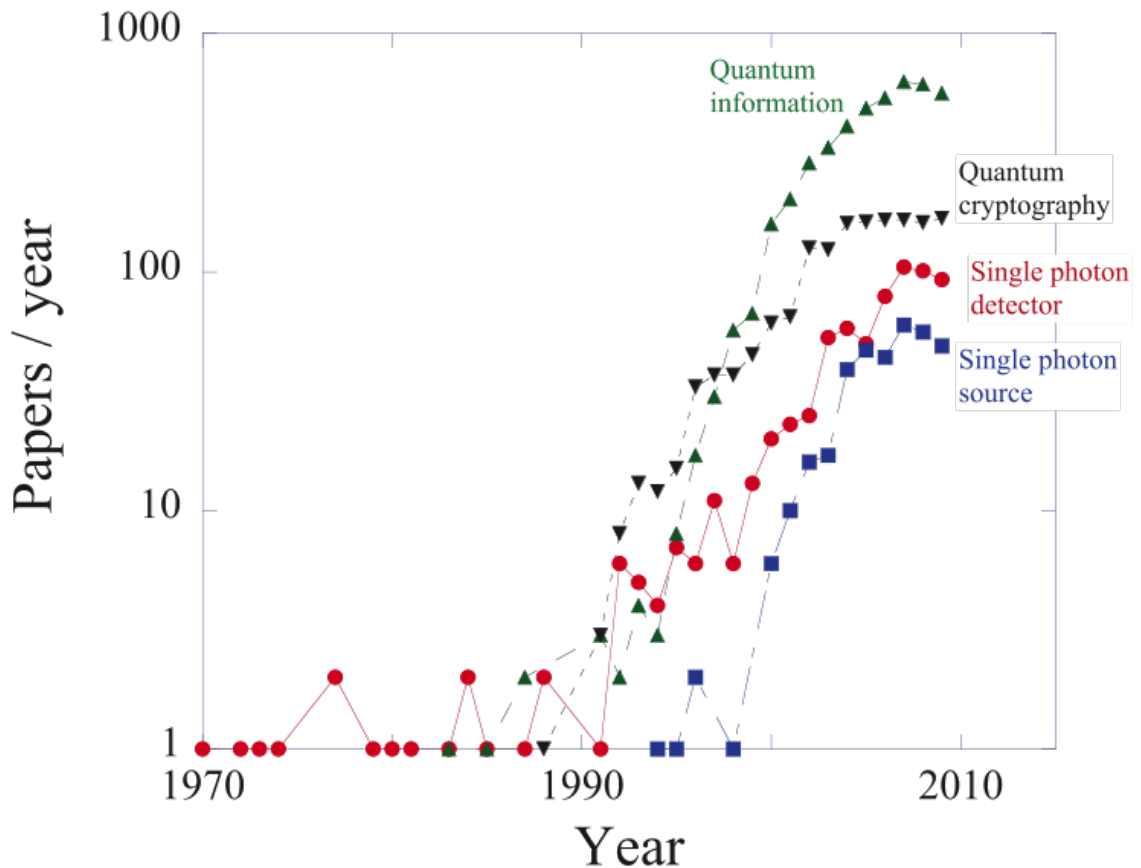


Figure 1.5: Number of publications on related research areas each year [7]

- (i) Single photons can serve as identical and indistinguishable quantum bits (qubits).
- (ii) They travel at the speed of light and only weakly interact with their environment over long distance, which results in lower loss and noise.
- (iii) Photons can be manipulated with linear optics.

(iv) Photons can transport information through free-space or fiber coupling.

Some of the important motivations for developing reliable single-photon sources are discussed in detail below.

1.3.1 Quantum Cryptography

Quantum cryptography or quantum key distribution (QKD) provides an unconditionally secure method of exchanging a private key between two parties: Alice and Bob [8–10]. Even if an eavesdropper, Eve, intercepts the data being exchanged between Alice and Bob, she cannot extract information from the quantum state without modifying it. According to the quantum no-cloning theorem, Eve cannot produce an identical quantum copy of the quantum data bit. Thus, eavesdropping by Eve inevitably introduces detectable errors in the communication between Alice and Bob, who will know that the safety of the communication channel has been compromised.

In the simplest version of the Bennett-Brassard 84 (BB84) protocol [8], information is encoded as the polarization state of a single photon with binary 1 and 0 represented by orthogonal polarization states. Two sets of conjugate bases for the polarization of single photons are used. The \oplus basis has binary 1 and 0 corresponding to photons with polarization angles of 0° and 90° , and the \otimes basis to photons with polarization angles of 45° and 135° , respectively. Alice can send a string of binary data, which is encoded in either of the two polarization bases at random. Bob measures the incoming polarization states using one of the two detection basis, also at random. Since both encoding and detection are performed by choosing a random basis, Bob and Alice's bases will match 50% of the time. Bob then exchanges information about the detection basis with Alice over a public communication channel, without revealing his results. Alice can now identify the subset of bits where they both chose the same basis and the data is perfectly correlated. They discard all the uncorrelated bits and the remainder of the bits gives them a sifted data key. Such a

sift-key is completely random and neither Alice nor Bob can influence the result. A schematic view of the BB84 protocol can be seen below in Fig.1.6. In the final step,

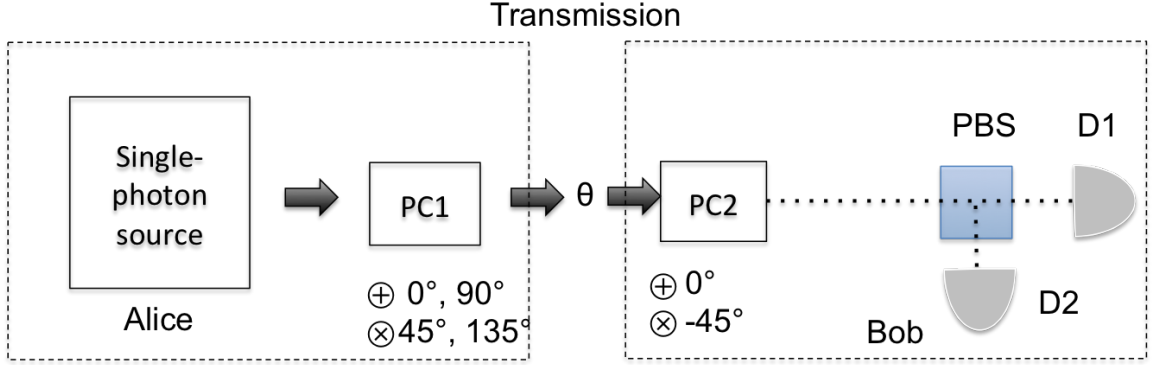


Figure 1.6: Schematic of BB84 implementation of QKD between Alice and Bob. PC1 and PC2 represent two pockel cells that provide polarization control as a function of applied voltage. PBS stands for a polarized beam splitter and D1, D2 are identical single-photon detectors. [6]

Bob transmits a subset of the sifted bits, on which Alice performs an error analysis. If the error rate is less than 25% she deduces there was no eavesdropping during the communication. If an eavesdropper, who is equipped with identical single-photon sources, detectors and other apparatus as Alice and Bob, intercepts the data, she still has to choose the detection basis randomly. After she sends an ersatz bits to Bob with a 50% matching probability with Alices bits, there is an additional 50% error rate when Bob and Alice exchange the sift key because of Bobs random choice of the detection basis. The total error rate is high (25%) and with this error analysis, Alice can detect the presence of Eve in the communication channel and perturbation of the single photons.

The first experimental demonstration of QKD was performed with attenuated laser pulses, with Alice and Bob at a free-space separation of 30cm [11]. Since then, tremendous progress has been made in the field [12, 13] and QKD over distances as large as 200 km and at GHz repetition rates has been demonstrated [14]. Free-space QKD using an electrically injected quantum dot has recently been shown up to 1 km

as well [15].

1.3.2 Quantum Information Processing

The basic unit of quantum information is the qubit, which is a coherent superposition or Hilbert space of two-level eigenstates. If the two levels are $|0\rangle$ and $|1\rangle$, the qubit is their complex linear combination with $|\psi\rangle = \alpha|0\rangle + \beta|1\rangle$, where α and β are complex amplitudes such that $|\alpha|^2 + |\beta|^2 = 1$. The continuous complex amplitudes α and β convey information and can be used to generate infinite qubit-states that do not correspond to the classical values 0 or 1 and therein lies the power of quantum information processing.

Among the many proposed means of attaining qubits is the use of single photons. For instance, a qubit can be a photon with two eigenstates represented by horizontal or vertical polarizations in a given basis. Logical states can also be coded as physical qubits using one photon in one of two output modes of a beam splitter. In a classical computer, logic gates are the building blocks of memory and the processor. Similarly, in a quantum computer, data is stored in a quantum register (collection of N-qubits) and processed using quantum logic gates. However, the important point of difference between the two is that in quantum computing, with N qubits we input $2N$ data points in the quantum computer, which gives it a significantly larger state-space. Manipulation of $2N$ coefficients derived from N qubits within the quantum logic gates improves the efficiency of quantum computation, which makes it capable of handling the NP class of problems better than a classical computer [16, 17].

1.3.3 Quantum Metrology

The Heisenberg uncertainty relation puts a fundamental limit on the precision of a measurement, which most standard measurement methods do not reach. Fock states, such as the $n = 1$ single-photon state, are squeezed states of light, with a fixed number

of photons but indeterminate phase, due to quantum-mechanical uncertainty. Shot noise for coherent light with a mean photon number N is N , while for a Fock state, such as a single-photon state, shot noise is completely eliminated. This elimination of shot noise will allow better measurements of weak absorptions [18]. A perfect single-photon source associated with perfect detection would give access to arbitrarily small absorptions, impossible to measure with a laser source because of photon noise.

1.4 Sources Of Single Photons

There are a variety of systems such as single atoms [19–21], ions [22–24], molecules [25–27], nitrogen vacancies [28–30] and quantum dots that have been studied as single-photon emitters. These different systems rely on a similar principle of single-photon generation- excitation of a two-level system through an optical or electrical pulse and emission of a single photon as the carrier relax to a lower energy state. Often the single-photon emitter is embedded in an optical cavity to engineer the emission characteristics.

1.4.1 Single Atoms And Ions

Single-atom emitters [19–24] work in the strong-coupling regime of cavity quantum electrodynamics. Single atoms are first captured and cooled inside a magneto-optical trap (MOT). After the MOT is turned off, the atoms fall freely under the gravitational force, where they pass through a high-finesse optical cavity. A single-atom emitter should have only one atom trapped inside the cavity. The single trapped atom has two metastable ground states $|g\rangle$ and $|u\rangle$ and one excited state $|e\rangle$. The resonance of the optical cavity is made close to the transition of $|g\rangle \rightarrow |e\rangle$ and the transition of $|u\rangle \rightarrow |e\rangle$ is on-resonance with the pump laser pulse. With appropriate control of the pump laser pulse and atom-cavity coupling, single-photon emission from the $|e\rangle \rightarrow |g\rangle$ transition is achieved.

A major advantage of atoms is that their states are perfectly reproducible and documented, including the hyperfine structure of the levels. With the right atom or ion, transitions can be found throughout the visible and near-IR parts of the spectrum (Cs at 852 nm, Rb at 780 nm, etc.) [19–21]. In the absence of a Doppler effect and of collisions with residual gas, which are unavoidable in real experiments, the transitions are narrow and lifetime-limited.

The main challenge for the attainment of a single-photon source is in the isolation, manipulation and trapping of single atoms, which requires sophisticated and expensive setups, including high-resolution stabilized lasers at several frequencies, ultra-high vacuum, and nearly absolute zero temperatures.

1.4.2 Single Molecule

Another SPS implementation is to excite single molecules at cryogenic temperatures [25–27]. The molecular electron transition involved can be approximated by a 3-level system, which consists of a singlet ground state $|S0\rangle$, a singlet excited state $|S1\rangle$, and a triplet intermediate state $|T1\rangle$ where each state represents a set of molecular vibrational energy levels. An electron in a vibrational level of the ground state is optically transferred to a vibrational level in the excited state, and then radiatively relaxes back to the ground-state vibrational manifold. Thus the single-photon emission spans a broad spectrum. The single-photon emission occurs repetitively while the cycling of $|S0\rangle \rightarrow |S1\rangle \rightarrow |S0\rangle$ continues, until the electron transitions to the dark state $|T1\rangle$, which normally occurs with a small probability. To emit a single photon on-demand, a pulsed pump laser can be used with its pulse duration shorter than the lifetime of $|S1\rangle$.

At low temperatures, the phonon broadening of the optical transitions is reduced and the quantum efficiency is close to unity. Molecular photostability is often severely limited at room temperature because of the many photochemical processes that can

be activated from the excited state by thermal fluctuations. Molecular systems are also prone to detrimental photo-blinking and photo-bleaching effects [31].

1.4.3 Nitrogen Vacancy (NV)

Color centers in diamond are substituted defects, formed by a substitutional nitrogen atom and a vacancy site which forms a three level systems with an optical dipole transition. The optical transition of nitrogen vacacy (NV) centers can be modeled by a three-level energy system with ground state $|g\rangle$ and excited state $|e\rangle$, where $|e\rangle$ is also thermally coupled to a metastable state $|s\rangle$. The excited state can decay to the ground state $|g\rangle$ and emit a single photon [28–30]. The long lifetime of this shelving state $|s\rangle$ results in a decrease in the single-photon emission rate and also causes photon bunching when looking at longer time scales than the color centers main transition lifetime. One important advantage of this implementation is that NV centers are photostable and do not exhibit bleaching or photo blinking. Due to the near unity radiative efficiency of an NV-center single-photon source, emission has been seen up to room temperature both optically and electrically [32]. Realizing electrical pumped devices, is however, challenging due to the difficulty and the cost of the growth of doped diamond layers necessary to fabricate p-n junctions.

1.4.4 Quantum Dots

Quantum dots consist of nanometer scale islands of smaller-band-gap semiconductor embedded in a larger-band-gap material. The small size of a quantum dot (QD) results in quantized atom-like discrete energy states. Semiconductor quantum dots of various material systems have been extensively investigated as single-photon sources. They can be created by several bottom-up techniques such as MBE, acMOCVD, droplet epitaxy, colloidal synthesis or top down techniques like etching 2D layers.

In the weak-excitation regime, a bound state of an electron-hole pair in such a

quantum dot forms an exciton. Radiative relaxation of the exciton transition results in single-photon emission. The radiative lifetime in QDs is of the order of a nanosecond, which can produce high-speed single photons on demand.

Quantum dots can be excited either optically or electrically [32–39]. By embedding quantum dots in the active region of a p-i-n diode, electron-hole pair carriers can be generated incoherently in the barrier by applying a voltage bias. If the QD radiative recombination time is longer than the recombination time of the free electron hole pairs in the semiconductor, each excitation pulse will lead to at most one photon emission event at the corresponding excitonic transition.

Two electron-hole pairs can also be excited to form a biexciton or multi-exciton states. These multi-excitonic and exciton transitions differ in energy due to the local Coulomb interaction. The biexciton line could also be selected as a source of single photons as it too shows antibunching but it requires a higher exciting intensity than the single exciton. The bi-exciton and exciton lines can also be used to generate entangled pairs of single photons [40]. Quantum dots can also be integrated into micro-cavities such as distributed Bragg reflector (DBR) mirrors, micropillar, disk, sphere, or photonic-crystal cavities to increase the speed and brightness of the source, or to control the emission into a specific directional mode [35, 36].

1.5 Important Attributes Of A Single-Photon Source

An ideal single-photon source would be one for which: a single photon can be emitted at any arbitrary time defined by the user (i.e., the source is deterministic, or on-demand), the probability of emitting a single photon is 100%, subsequent emitted photons are indistinguishable, and the repetition rate is arbitrarily fast (limited only by the temporal duration of the single-photon pulses). Some of the important figures of merit are described below and summarized in Table 1.1.

1.5.1 Operating temperature

Solid state atom-like emitters in general exhibit phonon-induced linewidth broadening, and at high temperatures, excited state transitions will often overlap, leading to loss of single-photon character. In addition, for many epitaxial QD systems, the thermal energy exceeds the confinement potential at higher temperatures, and the QDs will stop luminescing as the temperature is raised. For practical applications, it is desirable to have a single-photon source that works at room temperature. Liquid nitrogen cooling (available above 77 K) or thermoelectric cooling (above 200 K) is also significantly more practical than liquid helium cooling (4 K).

1.5.2 Wavelength

Ideally, a single-photon source would have a narrow linewidth emitter and would be tunable over a very broad frequency range. This would allow selection of the optimal wavelength for a particular application. For quantum cryptography, for example, it is desirable to transmit single photons over long distances with minimal losses. Silica telecommunications wavelength fibers have two main transmission windows at 1550 and 1320 nm, with the lowest loss and dispersion, respectively. However, photon detectors in these wavelength ranges are typically made of InGaAs and currently have significantly worse performance than the Si photodetectors, which have peak detection efficiency in the visible range. For applications where high detection efficiency is important, emitters in this wavelength range are more desirable. Furthermore, plastic fibers have transmission windows in the visible range. Emitters in the blue and UV part of the spectrum are also potentially interesting for QKD as the emitters and receivers telescopes shrink with wavelength.

1.5.3 Efficiency

The efficiency of a single-photon source is the fraction of triggers leading to the generation of a single photon. For QKD, the higher this efficiency and the lower the error rate, the greater the security of the communication. Very low error rates are necessary for quantum information processing which demands near unity efficiencies of single-photon sources for both applications.

1.5.4 Polarization

A single-photon source that emits in a specific polarization is important for most applications. The polarization is usually determined by the microscopic nature of the emitter (the orientation of its dipole moment) and by the way it is coupled to the emission mode.

1.5.5 Speed

The speed of a single-photon source is determined by its emission lifetime. In an ideal system, the linewidth of the emitter will be lifetime limited. Practically however, solid-state systems are often excited through incoherent pumping and thus the speed of relaxation from higher energy levels to the excited level state must also be taken into account. This can lead to both longer effective lifetimes and jitter in the emission time of a single-photon pulse. The spontaneous emission lifetime of a single quantum dot can be modified by embedding it in a photonic microcavity. High speeds (1-10 Gb/s) are desirable in order to achieve the high data rates desired for quantum information processing, and QKD [41].

Source	Prob. or Det.	Temperature	Wavelength	Bandwidth
Attenuated laser	P	300 K	Vis-IR	GHz
Single molecule	D	300 K	500-700 nm	30 MHz
Color center (NV)	D	300 K	640-800 nm	1 GHz
Single ion in cavity	D	0	Atomic line	5 MHz
Single atom in cavity	D	0	Atomic line	10 MHz
InAs QD	D	5 K	Near IR	1 GHz
II-VI (CdSe) QD	D	300 K	500-900 nm	3 GHz
III-nitride QD	D	300 K	UV-visible	1.5 GHz

Table 1.1: Summary of performance of various types of single-photon sources

1.6 Nitride-based Quantum Dots As Single-Photon Sources

There have been many reports of single-photon emission from III-V quantum dots. However all of these—whether optically or electrically driven have been at cryogenic temperatures. In recent years, there has been intense interest in developing wide-band-gap nitride materials.

III-nitride materials, i.e. GaN, InN and AlN and their ternary alloys, e.g. InGaN and AlGaN, can crystallize in either the wurtzite (WZ) or zinc blende (ZB) form. The wurtzite form is thermodynamically preferred and is widely studied for its optoelectronic applications. Nitride quantum dots can be achieved by sandwiching a narrow bandgap material InGaN (or GaN) in a wider bandgap matrix GaN(or AlGaN). In a quantum dot the energy is quantized in all three dimensions, and the density of states of the material becomes a delta function. In gallium nitride GaN, the exciton binding energy is very large, $\sim 30\text{meV}$ at room temperature . This value increases with confinement and as a consequence of this large binding energy, the oscillator strength of the radiative transition is also large. The band offsets in InGaN/GaN and GaN/AlGaN heterostructures are also significantly larger than the room temperature thermal energy ($k_B T$). Band offsets in meV for InGaN/GaN quantum wells, assuming 60:40 rule are shown in Table 1.2 below.

As a result, the excitonic emission from nitrides is stable up to room temper-

Wavelength	Conduction band offset	Valence band offset
Blue	270 meV	180 meV
Green	610 meV	406 meV
Red	840 meV	560 meV

Table 1.2: Band-offsets in InGaN/GaN heterostructures emitting in different wavelength ranges.

ature and single-photon emission has been observed at high temperatures, all the way up to room temperature. It has been suggested that short wavelength visible single-photons emitted by nitride single-photon sources would be useful for free-space quantum cryptography, as they allow for the reduction in transmitter and receiver telescope sizes. The visible wavelength range is important because commercial silicon based single-photon detectors are most efficient and sensitive in this spectral range. Also, plastic and polymer fibers, which are becoming increasingly prevalent, have transmission windows in the green-red wavelength range .

There are several approaches by which nitride quantum dots for single-photon emission have been demonstrated.

1.6.1 Etched Quantum Dots

In this top-down approach, a quantum well sample, grown either by MBE or MOCVD is etched down to few nanometers by dry or wet etching techniques, to achieve a quantum dot (Fig.1.7) [42]. This is commonly done by a combination of electron beam lithography and reactive ion etching. The grown quantum well sample is coated with PMMA polymer and circular areas are exposed via e-beam lithography. After developing the PMMA, the exposed areas are covered with a metal layer which acts as a metallic protective mask (or “hard mask”) for subsequent etching. The etched nanopillars often undergo a wet-etching treatment to clean the surface roughness caused by dry etching. Single-photon emission has been observed from InGaN/GaN etched quantum dots up to 100 K in the blue spectral range. This

method is promising because it allows site-control of the quantum dot position.

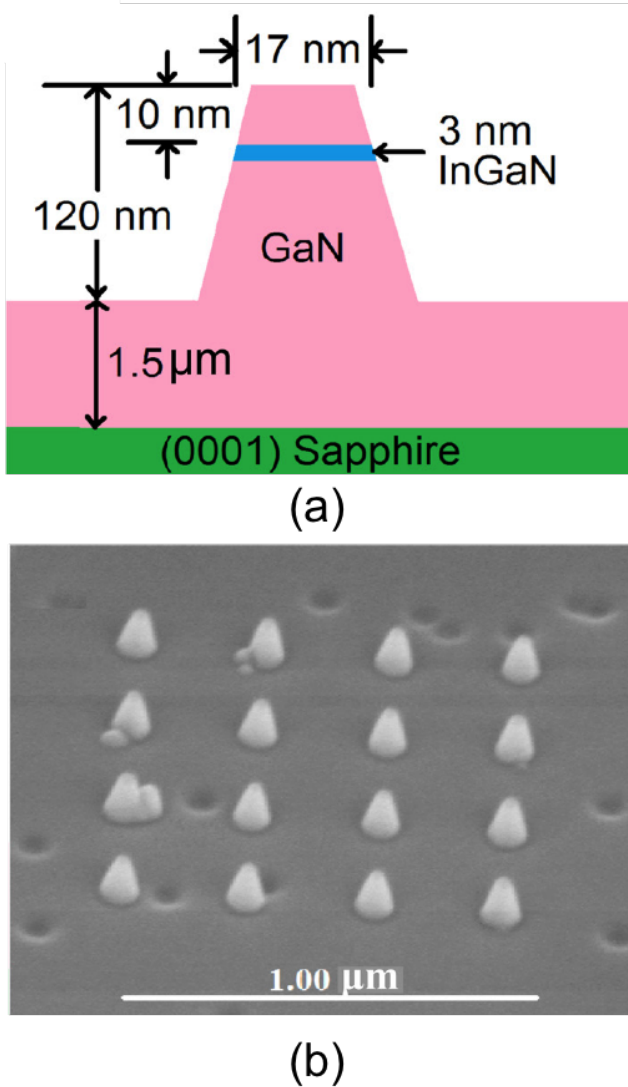


Figure 1.7: Quantum dots formed by etching of a single quantum well heterostructure
(a) schematic of device and (b) SEM of fabricated site-controlled quantum dot nanopillars [42]

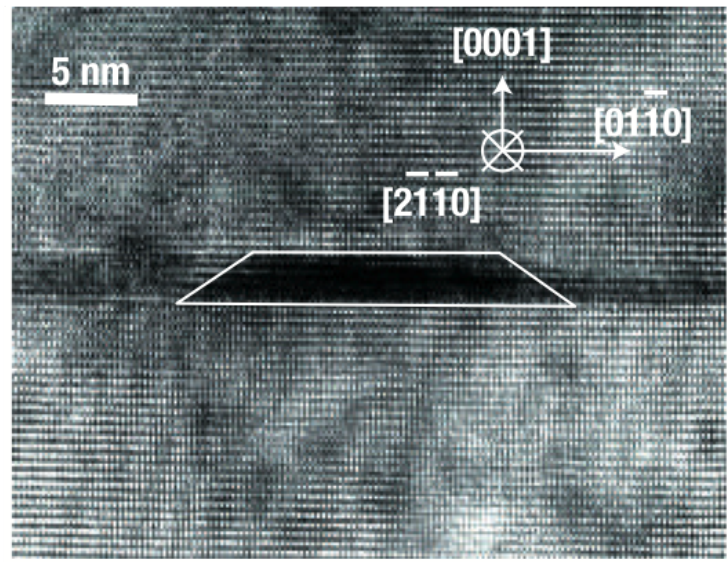
1.6.2 Stranski-Krastanov Grown Dots

The Stranski-Krastanov growth mode is one of the growth modes of MBE, driven by the strain from the lattice mismatch between the QD material and the underlying barrier material. The initial growth of the two dimensional layer- by-layer of GaN is called the wetting layer. The strain energy is reduced through the formation of

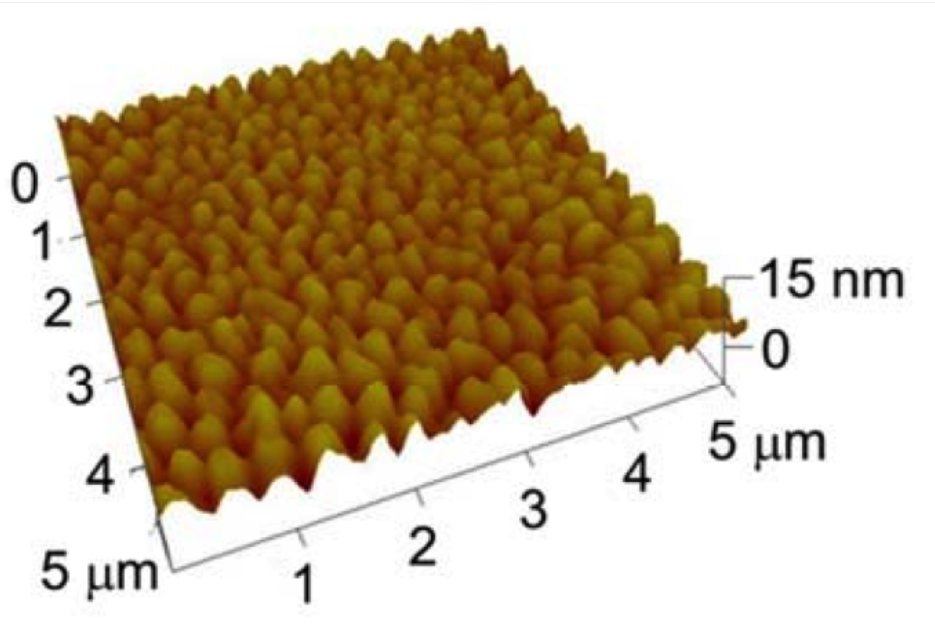
nanometer sized islands on the wetting layer (as seen in the transmission electron microscopy (TEM) image in Fig.1.8 (a)). The formation of islands occurs when the growth reaches a critical thickness. In order to function in an optoelectronic device, a capping layer is often grown on top of the QDs. For the case of GaN grown on AlN, there is a lattice mismatch of 2.4% with small interface energy between the GaN and AlN. Single-photon emission from such a self-organized GaN/AlN quantum dot was observed up to 200 K by Kako et al [43]. The shape, average size and density of islands also depend on other factors, such as the lattice mismatch, the growth temperature, the growth rate, growth interruptions, and the number of grown monolayers of QD material. An atomic force microscopy (AFM) image from an uncapped InGaN QD sample is shown in Fig.1.8 (b). It has been recently shown that InGaN/GaN quantum dots emit single photons up to room temperature [44].

1.6.3 Nanowire Quantum Dots

GaN nanowires have appeared as promising building blocks for nanoscale devices owing to their high crystalline quality and their integration possibilities. With nanowires, a QD structure can be constructed by inserting a slice of a lower gap InGaN (GaN) within the GaN (AlGaN) nanowires (Fig. 1.9). The most important advantage of the nanowire quantum dots is that they can be grown on cheap silicon substrates. Additionally, the strain relaxation on the sidewalls is very efficient in nanowires which leads to superior optical properties. The nanowires also offer a convenient geometry to fabricate devices and for the study of isolated emitters-either by controlling the density through growth or detaching them from the growth substrate. Single-photon emission from GaN nanowire-quantum dots has been observed up to room temperature [45]. Encouraging results have also been obtained from InGaN/GaN nanowire-quantum dots along both c-plane and m-plane. Single-photon emission up to 200 K has been demonstrated from both [46, 47].



(a)



(b)

Figure 1.8: MBE grown self-organized quantum dots: (a) XTEM image of GaN/AlN self-organized quantum dots [43] (b) AFM image of uncapped InGaN/GaN quantum dots (courtesy Thomas Frost)

1.7 Thesis Overview

This dissertation focuses on the development of nitride quantum dot based single-photon emitters. Single quantum dots and disks-in-nanowires have been investigated

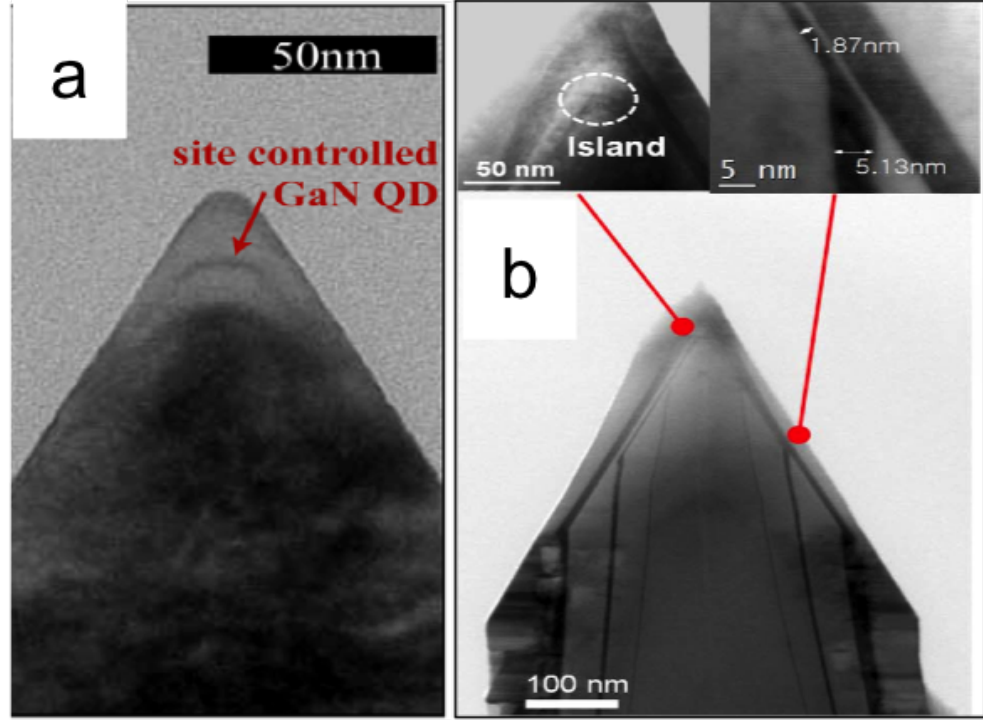


Figure 1.9: TEM of (a) GaN/AlGaN nanowire quantum dot single-photon emitter, operating at room temperature [45] and (b) InGaN/GaN nanowire quantum dot single-photon emitter, operating at 200 K [46].

for this application. Optimized MBE growth conditions for growth of nanowires with a small average diameter were developed. Similarly, growth conditions of low-density small quantum dots, emitting at long wavelengths were determined. Through rigorous structural characterization and tuning of growth conditions, a high radiative (greater than 40%) was achieved in all samples grown. The optimized disk-in-nanowires and quantum dots were then used as the active region for realizing optically and electrical pumped single-photon sources.

Chapter II discusses the growth conditions for GaN nanowires and InGaN/GaN disk-in-nanowire heterostructures in a Veeco Gen II plasma assisted MBE system. The grown material is structurally characterized using scanning electron microscopy (SEM), transmission electron microscopy (TEM), and energy dispersive x-ray spectroscopy (EDX).

Chapter III elaborates on the optical properties of the nanowire heterostruc-

tures. Temperature dependent photoluminescence and time-resolved photoluminescence (TRPL) measurements have been performed on ensembles of nanowires. The optical properties of single emitters have been investigated through single dot spectroscopy. Micro-photoluminescence (μ -PL) from single disk-in-nanowires is detected up to 200 K and anti-bunching is confirmed through second-order correlation measurements.

Chapter IV describes the growth, characterization and fabrication of single dot-in-nanowire light emitting diodes (LED). The electroluminescence from these diodes shows exciton and biexciton transitions, which have been confirmed to be sources of single photons. The heterostructure design and fabrication process were optimized to reduce the series resistance of the device and generate electroluminescence up to 125 K. The lifetime and polarization of the emitted single photons have also been investigated.

Chapter V discusses growth and characterization of a single layer of InGaN/GaN quantum dots. Growth conditions are adjusted to obtain a low quantum dot density, to allow probing of single dots for their luminescence. The quantum dots emit in the red spectral range and are embedded in a p-i-n diode. The single quantum dot LED emits single photons up to room temperature. Triggered generation of single photons up to 200 MHz was demonstrated using electrical excitation.

In Chapter VI, we delve into an in-depth study of the nature of quantum confinement in InGaN/GaN disk-in-nanowires. From the unique nature of the temperature dependence of the radiative lifetime and direct transmission electron microscopy, it is evident that self-organized InGaN islands are formed in the disk regions and these islands behave as quantum dots. This observation is confirmed by single-photon emission from a single disk-in-nanowire. Edge emitting lasers, with InGaN disks as the gain media were fabricated and their emission is studied. A sharp minimum in the linewidth enhancement factor—which is a signature of quantum dots in the gain

medium of lasers, was observed.

Chapter VII summarizes the work done in this dissertation and suggests some exciting future work to improve the performance of nitride-based single-photon sources.

CHAPTER II

MBE Growth Of Nanowire Heterostructures

2.1 Introduction

The lack of high-quality, inexpensive substrates for growth of GaN has motivated the study of GaN nanowires. These can easily nucleate and grow on silicon despite the large lattice mismatches of 18%. GaN nanowires have been successfully grown by MBE and metal organic chemical vapor deposition (MOCVD). They grow vertically on (001) and (111) Si along the wurtzite c-axis [48–52]. Structural and optical characterization by several groups has shown that the resulting nanowires have a substantially lower defect density than bulk GaN grown on lattice mismatched sapphire or SiC substrates because of their large surface-to-volume ratio [53–55]. The strain relaxation during epitaxy also leads to a weaker piezoelectric polarization field. For these reasons, nanowires show excellent optical and electrical properties. They have been used to make visible light emitting diodes with high efficiency and reduced droop [56, 57]. Single nanowires and their ensembles have been used to develop optically and electrically pumped lasers with very low lasing thresholds [58, 59]. Similarly they have been used as single photon sources where they are uniquely advantageous because of their favorable optical properties [47, 60, 61].

This chapter discusses the MBE growth of GaN nanowires and their characterization through structural measurements. The nanowire growth mechanism is discussed

and strategies to vary the density and diameters are elucidated. InGaN disks in GaN nanowires can be used to emit across the whole visible spectrum. The growth of blue, green and red emitting disks-in-nanowires is discussed. Finally, the growth of state-of-the-art nanowire p-n junctions is presented.

2.2 MBE Growth of GaN Nanowires

All the nanowires in this study were grown in a Veeco Gen-II plasma-assisted molecular beam epitaxy (PAMBE) system as shown in Fig. 2.1. The MBE system is equipped with standard effusion cells Ga, Al, In, dopant cells for Mg and Si and a nitrogen RF source. The nanowires were grown on either (111) or (001) “epi-

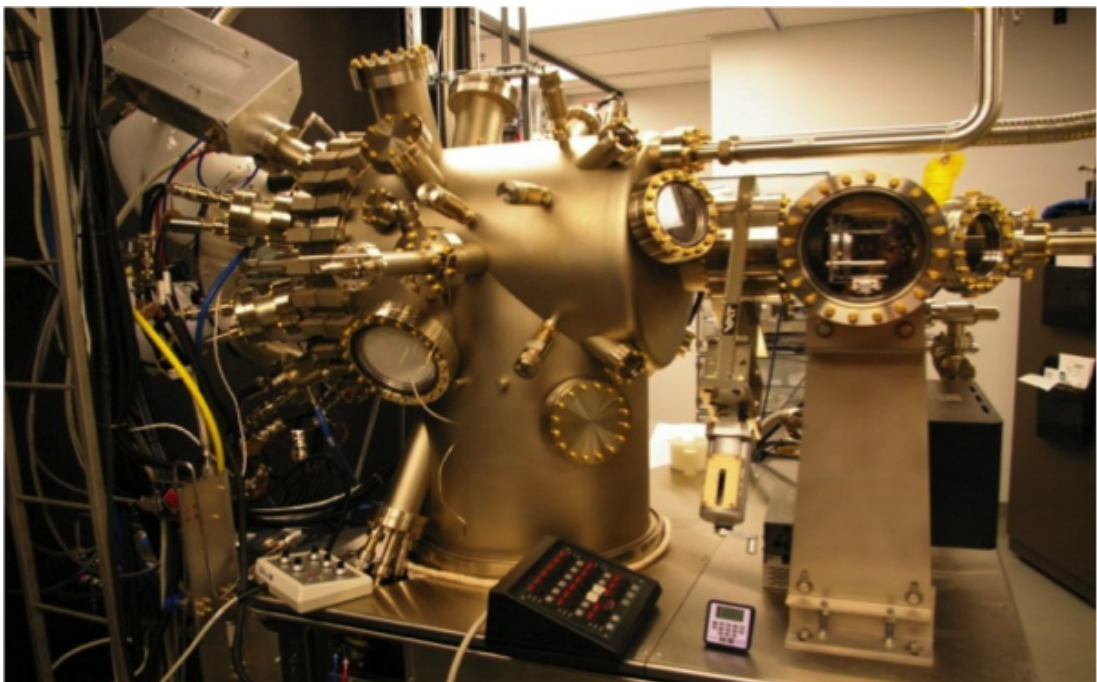


Figure 2.1: Gen-II plasma-assisted molecular beam epitaxy (PAMBE) system.

ready” n-doped Si substrate with resistivity $< 0.001 \Omega \text{ cm}$. The substrates were first cleaned using standard solvents- acetone, isopropyl alcohol (IPA) and water. Following this clean, the silicon wafers were treated with buffered hydrofluoric acid (BHF) for 1 minute to remove native oxide prior to loading them into the MBE

chamber. However Si is extremely sensitive to oxygen and the oxidation of Si is unavoidable even during the brief exposure to atmosphere while loading the substrate into the MBE chamber. The Si wafer is degassed in two steps in the MBE system—first in the introduction chamber for 1 hour at 200°C and then in the growth chamber at 980°C, for 1 hour, to remove any residual oxide. Following the in-situ annealing, the (1x1) silicon reflection high energy electron diffraction (RHEED) reconstruction becomes observable in (111) silicon. The substrate temperature is lowered until the RHEED reconstruction transitions from (1x1) to (7x7), which is known to occur at 830°C (Fig.2.2) [62]. The thermocouple and pyrometer temperatures are calibrated using the RHEED transition before each growth run.

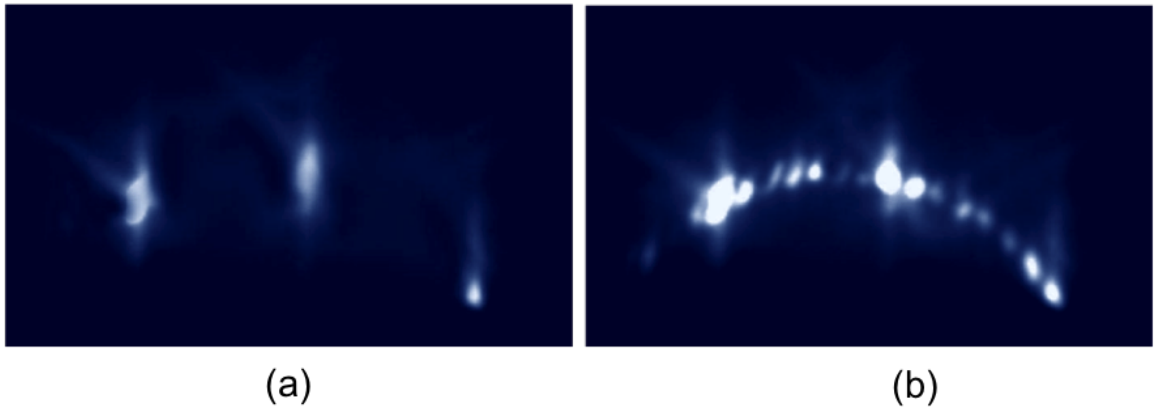


Figure 2.2: (a) (1x1) to (b) (7x7) transition of the Si(111) surface reconstruction observed by reflection high energy electron diffraction(RHEED). 6 additional spots have appeared between the main (1x1) spots.[63]

2.2.1 Nucleation Mechanism For Self-Induced GaN Nanowire Growth

GaN nanowire growth can be initiated by depositing few monolayers of Ga before growth. The nanowires grow with or without the Ga droplet deposition step. It was previously hypothesized that Ga droplets serve as catalysts in a VLS-type growth mechanism. However, none of the reports in literature with ex-situ TEM investigations show the presence of Ga droplets, on the surface or on the tip of the nanowires

[64, 65]. Thus, it is believed that the Ga droplets are not critical for the nucleation of GaN nanowires. All nanowires studied in this work were grown without this Ga droplet deposition step.

The initial nucleation phase of nanowires is marked by the self-induced formation of GaN nuclei of critical size, which eventually govern the structural morphology of nanowires. Nanowire nucleation is believed to be composed of a series of steps: an initial incubation period followed by the nucleation of stable GaN clusters, and then a transition period leading to the formation of nanowire nuclei through shape transitions [51].

If the growth of nanowires is directly performed on Si substrate, without any AlN buffer layer, the formation of an amorphous Si_xN_y layer is inevitable due to the reactivity of the Si substrate to active nitrogen species from the plasma, at high temperature.



During this period, two competing reactions can lead to the formation of GaN or Si_xN_y . The high substrate temperature and nitrogen rich environment, causes strong Ga adatom desorption and thus to a low probability of GaN nucleation. On the contrary, the reaction between Si and nitrogen, has a higher velocity and a continuous Si_xN_y layer is formed. Due to the low diffusion of nitrogen atoms through the Si_xN_y layer, the nitridation process is self-limiting to a nominal layer thickness of about 3-5 nm. A high resolution TEM (HRTEM) image of the Si_xN_y inter-layer from Prof. Millunchick's group is shown in Fig. 2.3.

The incubation period is a metastable phase, during which Ga atoms can adsorb onto, desorb from, diffuse on the surface, or form meta-stable nuclei, as presented in Fig. 2.4 [67]. The incubation period typically results in a delay in the nucleation

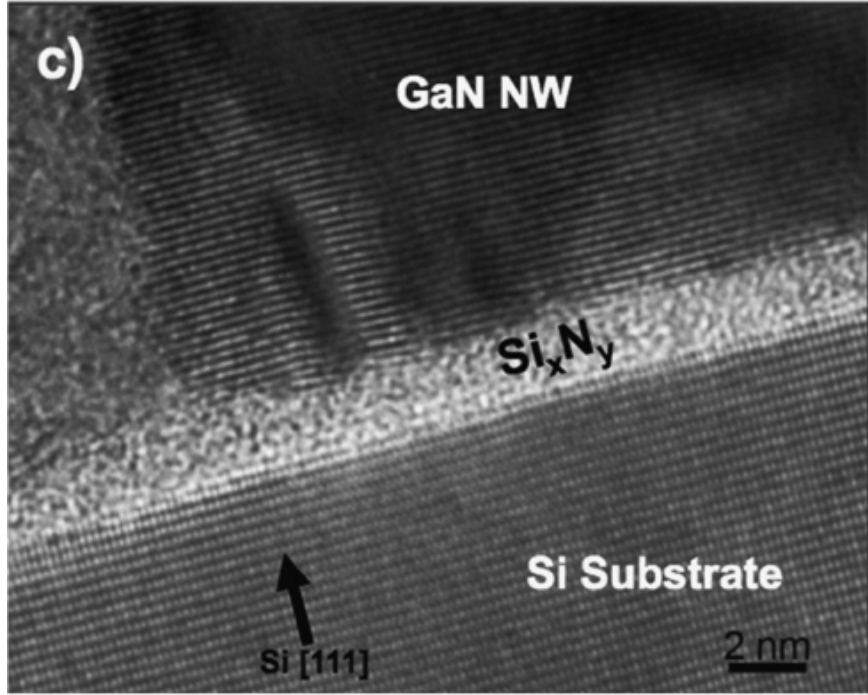


Figure 2.3: HRTEM of thin amorphous Si_xN_y layer at the interface of Si and GaN nanowires [66]

phase and eventually ends when stable nuclei are formed. The incubation time is a function of growth conditions and can last from several tens of seconds to several tens of minutes depending on growth temperature and Ga flux.

The end of the incubation period is marked by the occurrence of the first GaN spots along rings on the RHEED patterns. This nucleation stage is associated with the formation of the first stable 3D GaN islands. A typical HRTEM image of a GaN nucleus shown in Fig. 2.5 (a) depicts the spherical cap-shaped islands nucleated on a continuous amorphous Si_xN_y interlayer with a thickness of 2 nm. In the next phase, GaN islands thus undergo a shape transition from spherical caps to nanowires (Fig. 2.5 (b)). For the growth on the amorphous Si_xN_y interlayer, the epitaxial constraint is relaxed and the epitaxial strain is very low.

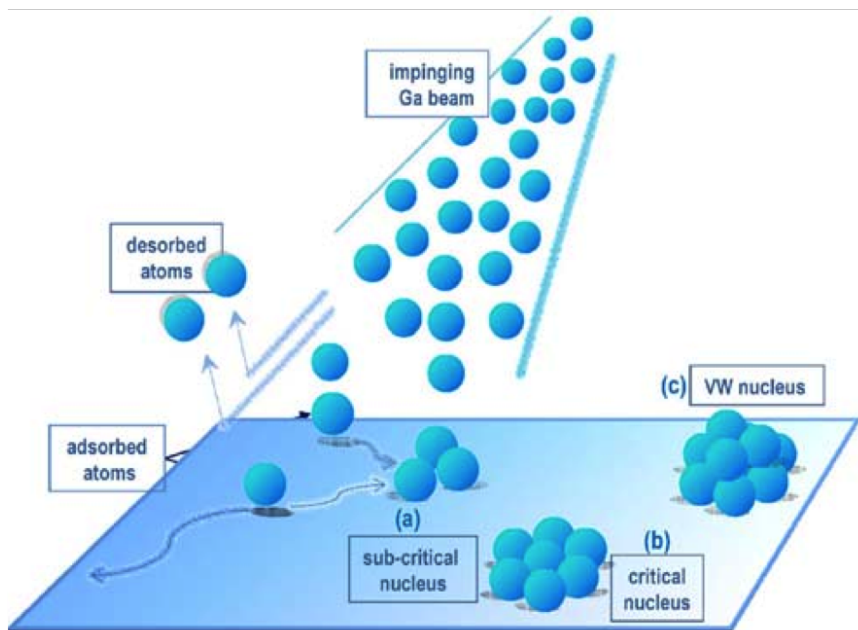


Figure 2.4: Schematic diagram representing the different physical processes involved in the incubation period during the nucleation phase. The subcritical-sized nuclei vanish owing to Ga adatom surface diffusion towards critical-sized clusters. [67]

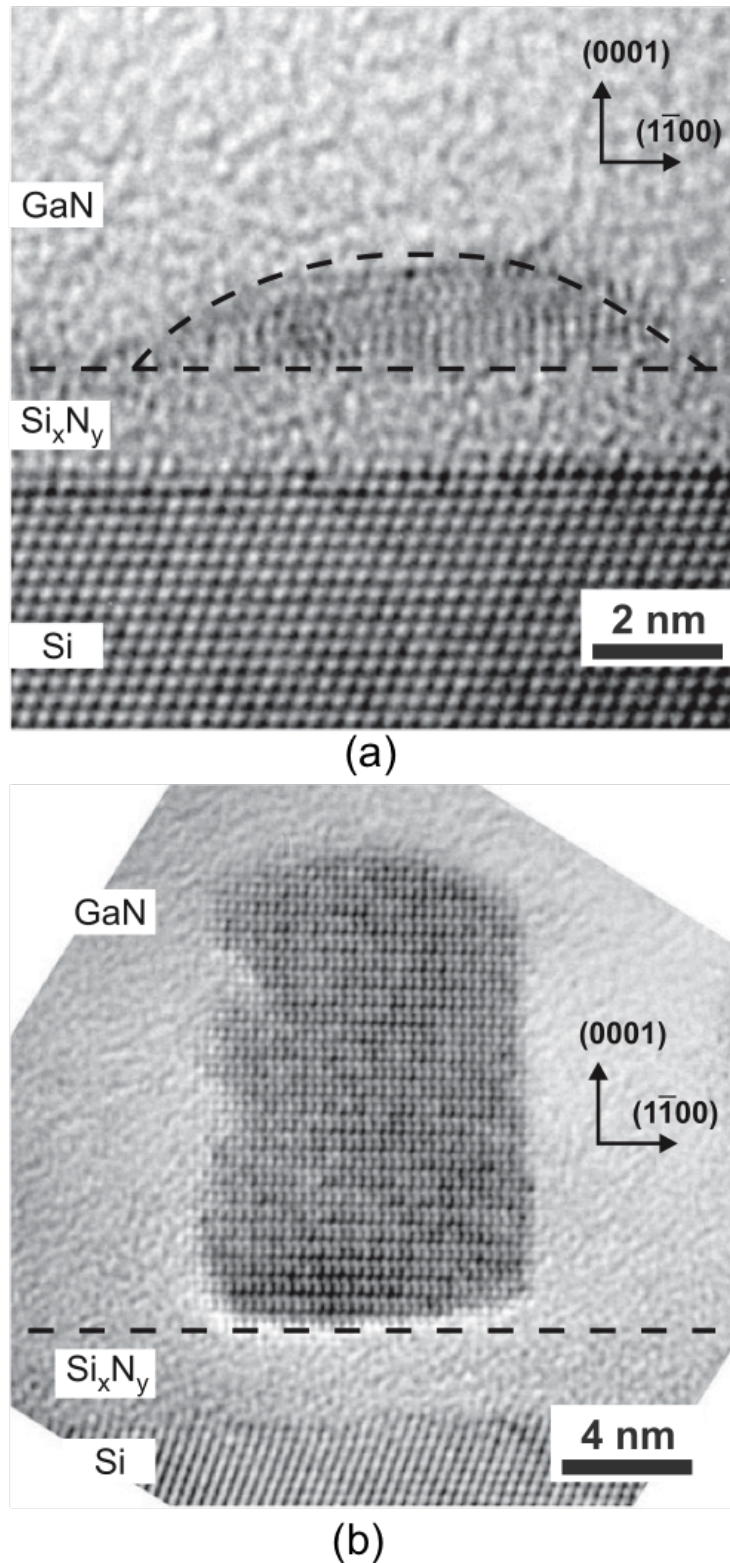


Figure 2.5: HRTEM images of samples grown for (a) 7 and (b) 16 minutes, reveal the transitions of GaN island shapes during the nucleation process: from spherical cap-shaped islands to the nanowires. The shape of spherical caps is outlined for the sake of clarity. [68]

2.2.2 Axial Growth And Nanowire Elongation

As the nanowires grow, the top surface of nucleated wires (c-axis) acts like an efficient collector of adatoms (shown in Fig. 2.6). The adatoms diffuse to the wire apex from its lateral sides driven by a lower chemical potential at the top surface. In addition to the direct impingement of atoms at the tip of the nanowire, there is an important contribution to the total nanowire growth due to the diffusion of adatoms towards the tip on side faces. Lymerakis et al. have revealed from density-functional theory (DFT) calculations that the diffusion barriers for Ga adatoms on non-polar m-planes (sidewalls) are strongly anisotropic in the plane: a smaller diffusion barrier of 0.21 eV has been found normal to the c-axis while the non-polar m-planes are unstable against atomic N [69]. Therefore, it is expected that the incorporation of Ga adatoms is more likely on the polar c-planes than on the non-polar m-planes which accounts for the higher nucleation rate on the polar c-planes [69] and the preferential axial growth of GaN NWs. For low and intermediate NW densities, there is a continuous nucleation of wires, whereas the wires already nucleated continue to grow in length and diameter. Towards higher densities, the space for nucleation of other wires is not available and the nucleation rate approaches zero [64]. After a certain growth time, if the nanowire density is large enough, the nucleation ceases and a few wires coalesce into thicker ones, which will be discussed in detail in the following section. Many other nanowires continue to grow separately [51].

2.2.3 Growth Conditions For GaN Nanowires

The self-induced growth of GaN nanowires by PA-MBE takes place within a fairly broad window of growth parameters. Generally, the nanowires are grown under nitrogen rich growth conditions and at a high substrate temperature between 720°C-850°C. It has been established by various groups that GaN nanowires generally grow under N-rich conditions N/Ga ratio $>>1$. The exact nitrogen to Ga flux ratio is difficult to

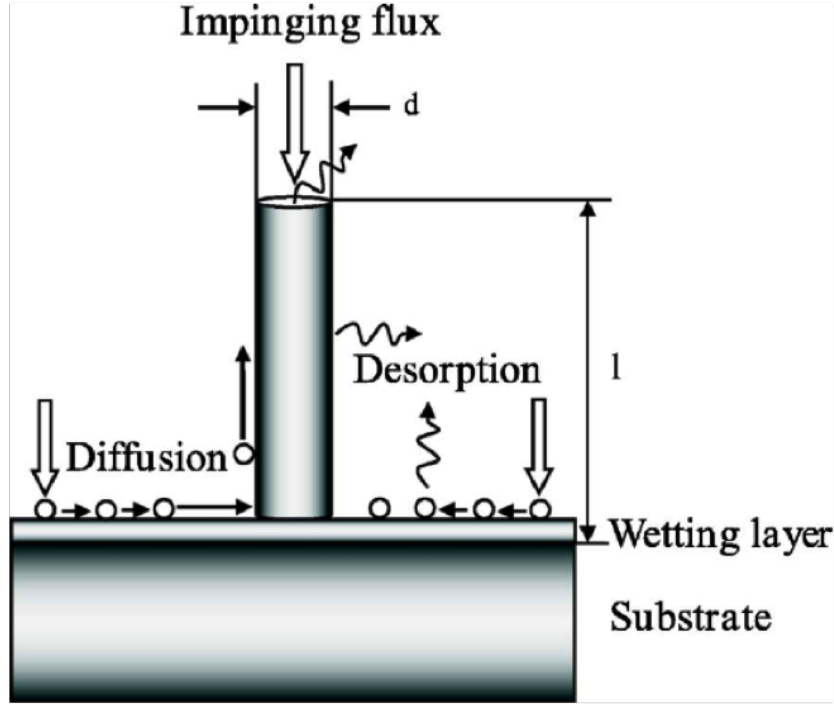


Figure 2.6: Schematic showing various processes (adatom adsorption, desorption and diffusion) in action during the growth of GaN nanowires [70]

calculate because of the rate of desorption of Ga, which cannot be easily measured. Also the fraction of activated atomic nitrogen, intricately depends on the exact conditions and efficiency of the plasma source. Nanowires in this work were grown under a constant nitrogen flow rate of 1 sccm at a RF plasma power of 400 W. Under these conditions, the ratio of the nitrogen and Ga overpressure exceeds 80.

Depending on the specific values of the Ga flux and substrate temperature, the resulting growth could fall under three distinct regimes of growth: compact films, nanowires or no growth. The growth diagram in Fig. 2.7 presents these different regimes of growth as a function of Ga flux and substrate temperature as studied by Calleja et al. [71]. We obtained qualitatively similar results, with differences in the specific temperature and flux based on conditions of the MBE chamber. As seen in the diagram, at low temperatures around 750°C, the preferred growth mode is two dimensional, which leads to formation of GaN films. Even at low Ga fluxes at these

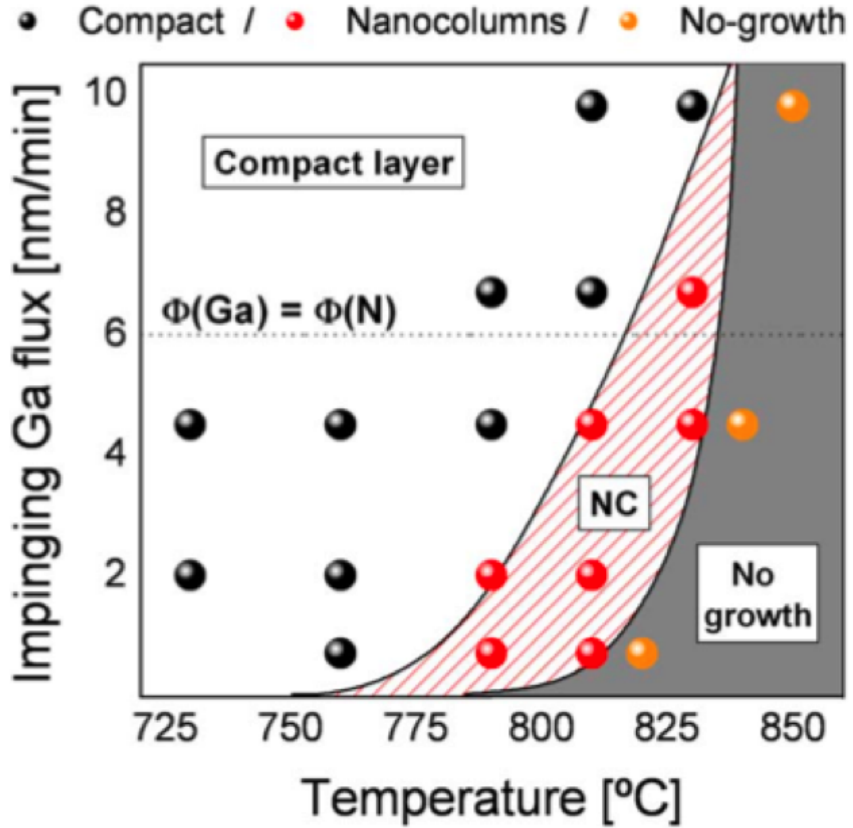


Figure 2.7: Phase diagram of growth of GaN under a fixed nitrogen flux, showing various regimes of growth [71]

low temperatures, it is difficult to obtain nanowire growth. The compact layer-to-nanowire regime boundary shifts toward higher temperatures with increasing Ga flux. This suggests a mechanism driven by Ga adatom diffusion, which leads to localized nucleation of GaN islands. In the absence of such a mechanism Ga adatoms would cover the substrate surface homogeneously, giving rise to a 2D layer. The no-growth region indicates the growth conditions for which it is not possible to grow GaN due to the exponential increase of desorption of Ga adatoms and decomposition of GaN with temperature. Increasing the Ga flux to compensate for the Ga desorption can shift this boundary to the right.

2.2.4 Defects In GaN Nanowires

GaN nanowires grown by MBE are typically free of strain because strain mismatch between the substrate and the growing GaN can readily be relieved by dislocation formation perpendicular to the (0 0 0 1) planes. The small diameter of the wire and ease of dislocation glide within the c-plane allow annihilation of the dislocations at the nanowire surface, leaving the active area of the crystal to grow defect-free after a few nanometers of axial growth (Fig. 2.8). [55]

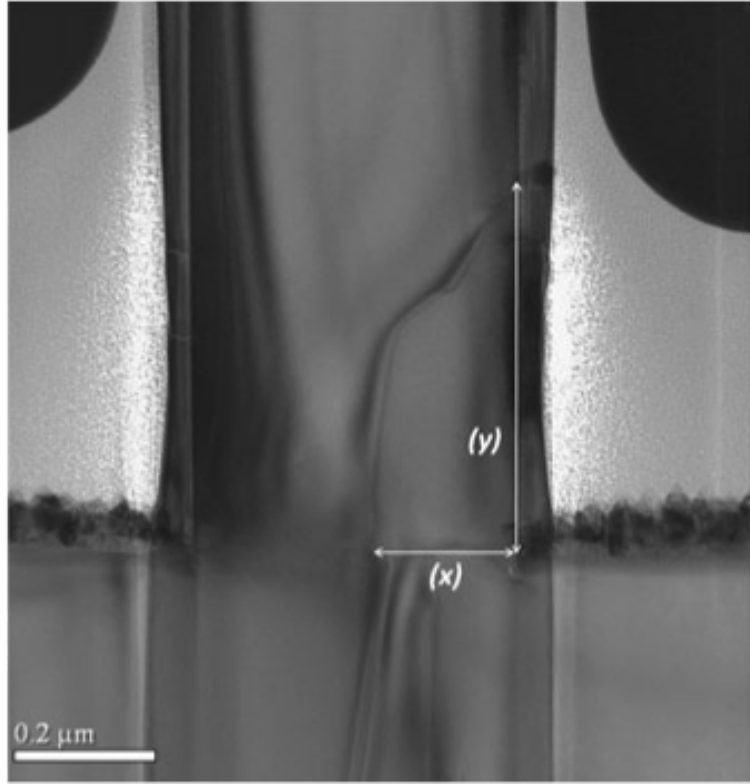


Figure 2.8: Cross-sectional TEM micrograph showing a threading dislocation originating at the nanowire/Si interface and terminating at the sidewall [55]

For light emitting applications a high density of nanowires is needed to achieve high light output. For high densities at which adjacent nanowires are close to each other or in contact at the start of growth, nanowires may coalescence to form bundles. As GaN nanowires coalesce, the density of distinct nanowire columns decreases, increasing the effective size of the final nanowire columns and this generates defects

in the nanowires.

TEM imaging of the nanowire samples was used to examine the crystalline quality of the nanowires and to determine the structure of the nanowires along coalescence boundaries. TEM imaging of nanowires can be performed in two ways:

1) Cross-sectional TEM (XTEM) imaging.

A piece of as-grown GaN nanowire on Si sample is bonded to another using M-bond. The specimen is mechanically polished using diamond paper, followed by focused ion milling (using Ar atoms) until it is thin enough to be transparent to the electron beam, at the interface of the two GaN nanowire samples.

2) Direct TEM imaging

Nanowires are removed from the grown substrate, into isopropyl alcohol. The solution is ultra-sonicated and drop cast on a holey carbon TEM grid for imaging.

TEM images of nanowires on Si confirm that the nanowires grow along the c-axis. Cross-section TEM imaging, (Fig. 2.9 (a) and(b)) shows that nanowires grow with a range of c-axis misorientations relative to the Si substrate normal. The variety of different in-plane orientations, results in rotational misalignments relative to one another. Variation in nanowire crystallographic orientation relative to the Si substrate has been previously attributed to thickness variation or roughness in the Si_xN_y amorphous layer. Nanowire misorientation is accommodated by the formation of chains of defects, such as dislocations, along the boundary between the coalescing nanowires. The crystallographic misorientation between coalescing nanowires is accommodated by the formation of zipper-like arrays of both dislocations and basal plane stacking faults. The locations of accommodating defects alternate across the interface, giving the array a zipper-like appearance, as seen in TEM images from [66]. Figures 2.9 (c) and (d) from [66] show high resolution TEM images of the defect interface, and Fourier filtering of that image for clear identification of the coalesced interface and resulting basal plane stacking faults. Instead of propagating out from the interface

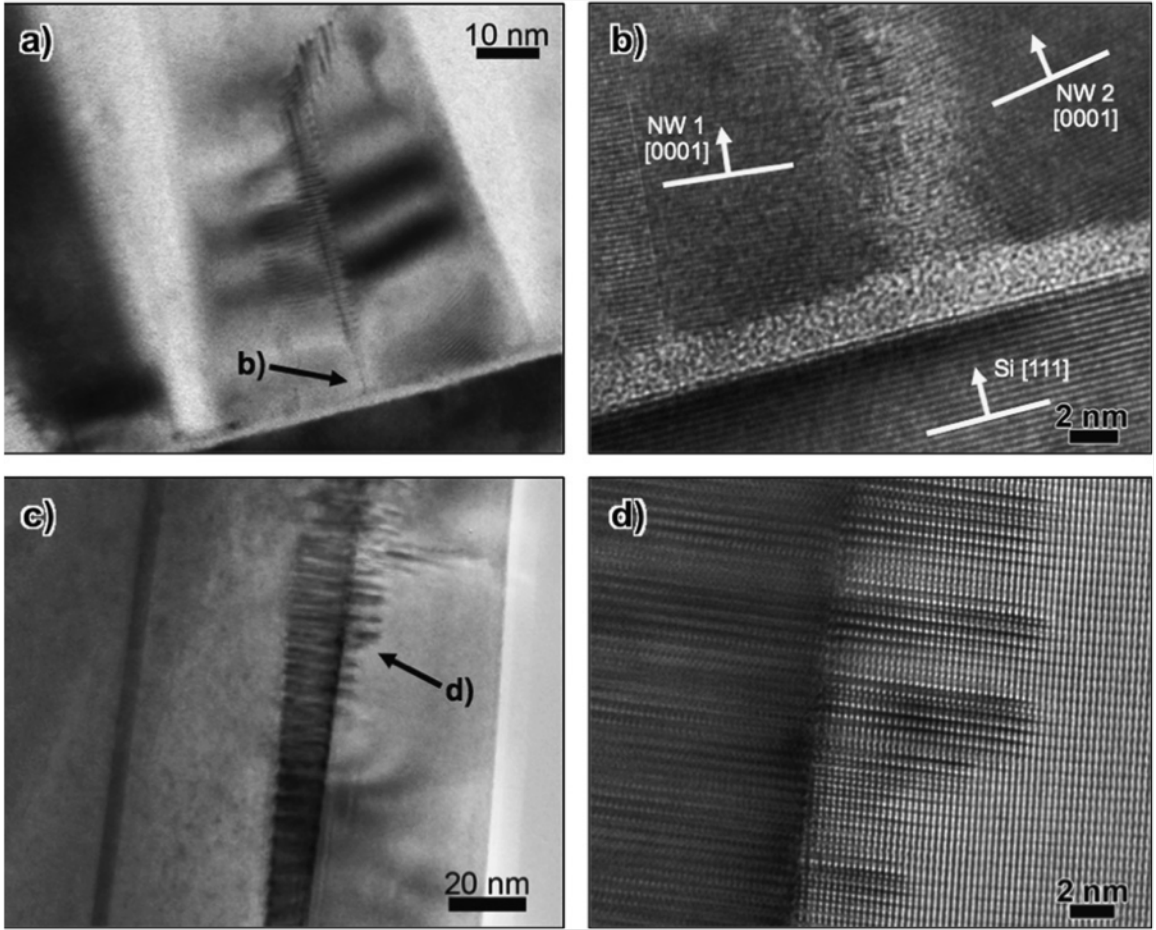


Figure 2.9: TEM images of a zipper defect array between two relatively misoriented and coalescing nanowires on their Si substrate: (a) low resolution and (b) high resolution TEM images of nanowires growing with different c-axes orientations. (c) and (d) shows TEM images of the zipper defects formed at the site of coalescence. [66].

to bridge the thickness of the coalescing nanowires, the stacking faults terminate in the body of the wire a short distance from the coalescing interface.

2.2.5 Varying Nanowire Density And Diameter

The aerial density and diameter of nanowires can be varied in the range of 10^8 - 10^{11} cm^2 and 20-80 nm respectively by varying the growth temperature, Ga flux and growth time. The GaN growth temperature was varied between 780°C-830°C and the

Ga flux was varied between 8×10^{-8} to 1.2×10^{-7} Torr, to obtain different nanowire diameters. The growth rate is 275-300 nm/hr, depending on the Ga flux. Growth conditions for growth of nanowires with an average diameter of 25 nm are given in Table 2.1. The effect of growth temperature and Ga flux is depicted in Fig. 2.10.

Substrate temperature	830°C
Nitrogen flux	1 sccm (400 W)
Gallium flux	10^{-7} Torr
Growth rate	275 nm/hr

Table 2.1: Standard growth conditions for GaN nanowires with an average diameter of 25 nm

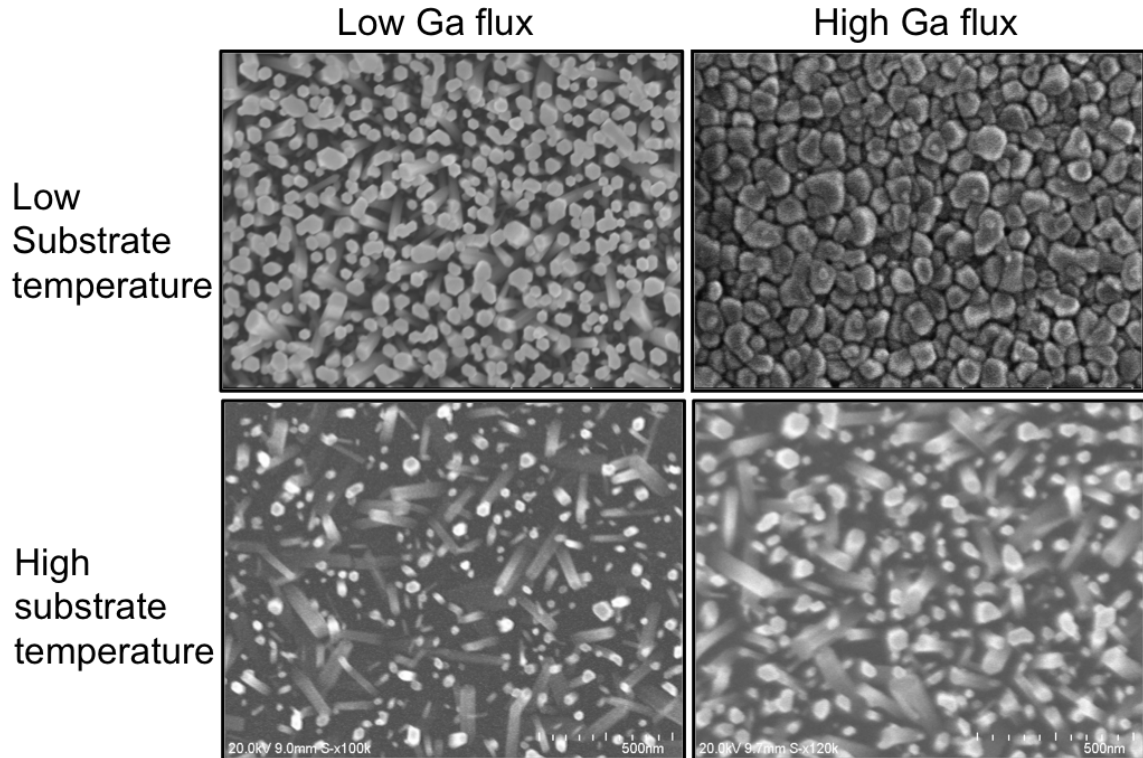


Figure 2.10: Effect of substrate temperature and Ga flux on nanowire density and diameter shown in top-view SEM images

2.3 Growth Of InGaN/GaN Disk-In-Nanowire Heterostructures

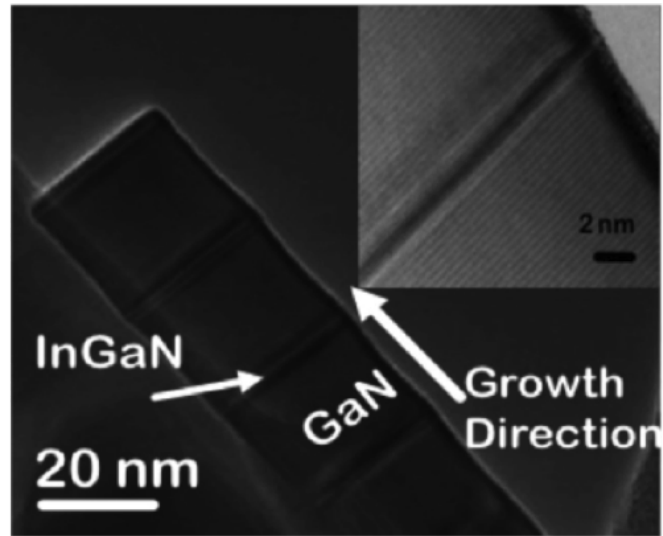
By inserting a single or multiple InGaN disk in the GaN nanowires, the emission can be varied over the entire visible spectral range [50, 56, 57]. A TEM and photoluminescence (PL) spectrum from a GaN nanowire containing multiple InGaN disks is shown in Fig. 2.11 (a) and (b), respectively. The underlying GaN is grown using the same growth conditions as described in Sec 2.2. During the growth of InGaN disks, the substrate temperature is lowered to $\sim 530^{\circ}\text{C}$ - 580°C to compensate for the low sticking coefficient of In adatoms. Both substrate temperature and In-to-total group III flux ratio are varied to optimize the radiative efficiency of the InGaN disks. If the substrate temperature is too low, the photoluminescence (PL) intensity at room temperature becomes very weak, possibly due to the presence of growth defects which result from limited adatom diffusion. If a high substrate is employed during the growth of InGaN, a broad PL emission with low intensity is observed, possibly due to In phase segregation. After growth of the disk, 12 nm of GaN is grown as a capping layer, at the same temperature.

The emission wavelength can be tuned by increased the In content in the well, which depends on the In flux and substrate temperature. The following table presents growth conditions for optimized growth of disk-in-nanowires.

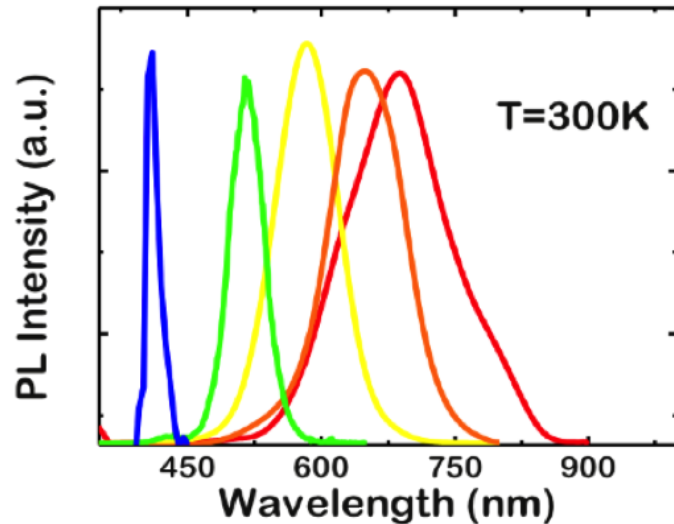
Emission color	Substrate temperature	Indium flux
Blue	535°C	6×10^{-8} Torr
Green	525°C	8×10^{-8} Torr
Red	510°C	10^{-7} Torr

Table 2.2: Growth conditions for InGaN disks emitting over the visible range

The In content in the QD samples was studied using scanning TEM microscopy (in a JEOL 2100F) equipped with in-situ EDX. EDX line-scans performed along the c-axis of the nanowire, through the quantum dot as shown in Fig 2.12. The scans,



(a)



(b)

Figure 2.11: Emission from InGaN/GaN disk-in-nanowires (a) TEM image of a GaN nanowire with multiple InGaN disks and (b) emission from InGaN disks over the visible spectral range [57]

with a spatial resolution of 0.2 nm, show the quantum dot width and In composition in blue and green emitting QD samples. The blue emitting quantum dot has a dot height of about 2 nm (measured from the full-width half maximum of the peak) and In composition of 25%, while the green emitting quantum dot has a dot height of

nearly 3 nm and In composition of 37%.

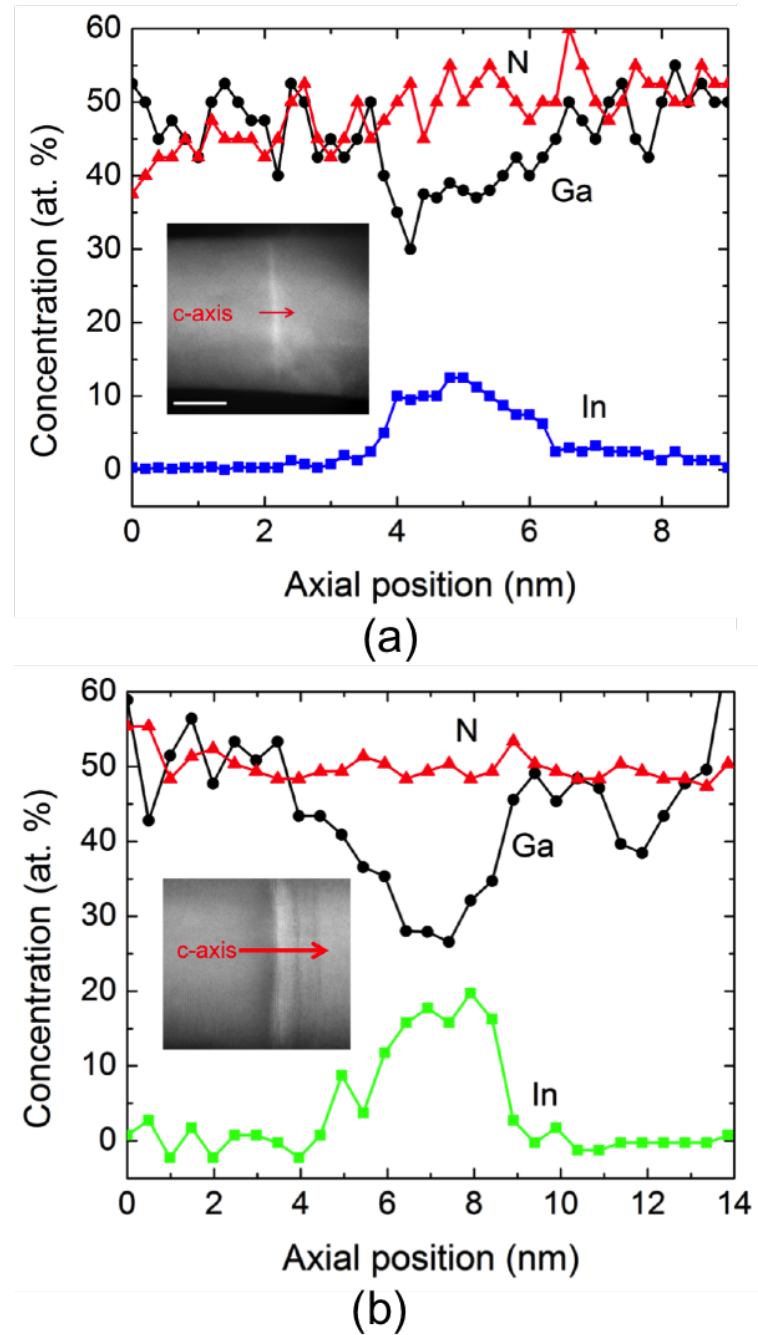
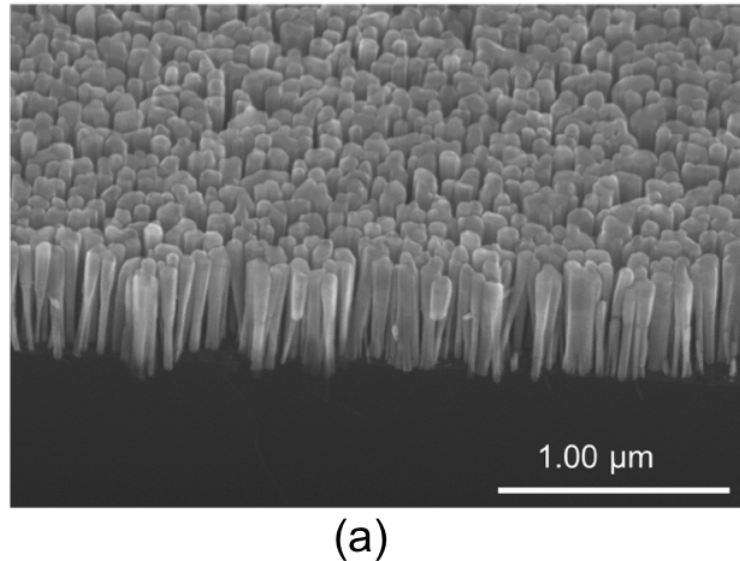


Figure 2.12: Elemental composition measured from an energy dispersive spectroscopy line scan along the nanowire c-axis across InGaN disk, for (a) blue and (b) green emitting disk in GaN nanowires

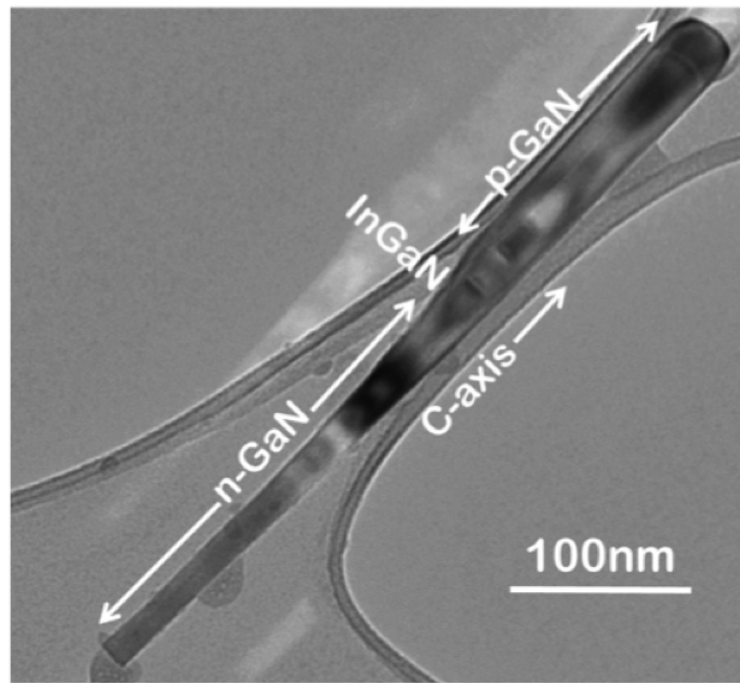
2.4 Growth Of Nanowire Diodes

Multiple or single InGaN disks can be embedded in the active region of a p-n junction. For the growth of the nanowire p-n junction, the dopants used for n-GaN and p-GaN are silicon and magnesium, respectively. For the growth of n-doped GaN, the Si shutter is opened during GaN growth, at the same substrate temperature as GaN growth. The Si flux used is $\sim 8 \times 10^{-10}$. GaN is unintentionally n-doped up to levels as high as $3 \times 10^{18} \text{ cm}^{-3}$. With the addition of Si, the n doping levels achieved are $5 \times 10^{18} \text{ cm}^{-3}$.

P-doping of GaN has been a serious challenge. This is mainly because of high n-type background doping of GaN arising from oxygen impurity incorporation and N-vacancies. Additionally, the high activation energy of Mg results in poor hole doping. Molecular beam epitaxy (MBE) growth of highly p-doped GaN films (3×10^{18}) at a low substrate temperature under N_2 -rich conditions, was first demonstrated by Bhattacharya et. al. [72]. These conditions prevent the formation of nitrogen vacancies, yielding very high p-doping levels in GaN. The growth of p-doped GaN nanowires is also performed under nitrogen rich conditions, at a reduced substrate temperature of 680°C to promote Mg incorporation. A high Mg flux 1×10^{-8} Torr is used. An SEM image of an ensemble of nanowire p-n junctions and TEM of a single nanowire are shown in Fig. 2.13 (a) and (b), respectively. The p-end of the nanowire has a larger diameter due to the lower substrate temperature during growth, which increases the lateral growth rate.



(a)

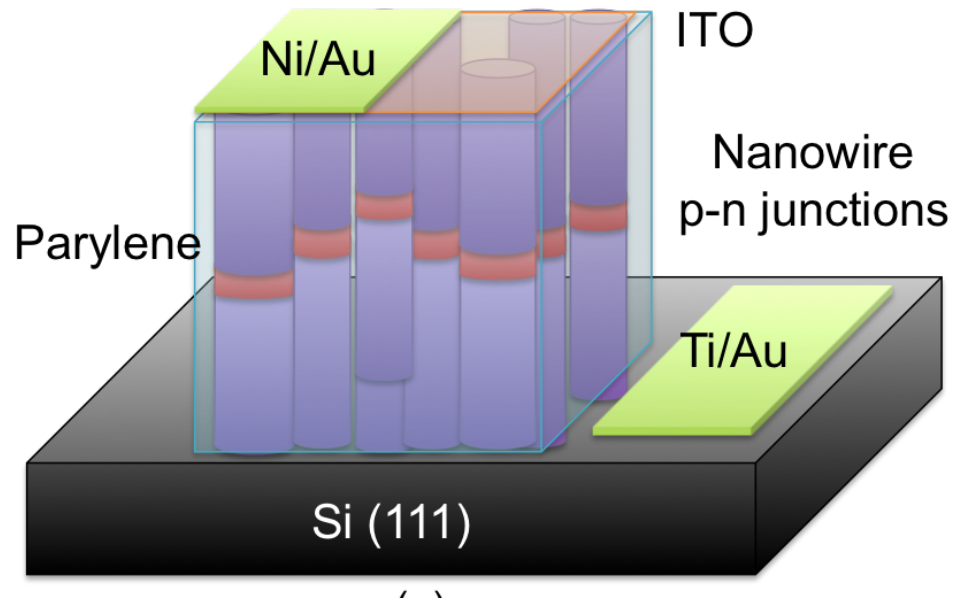


(b)

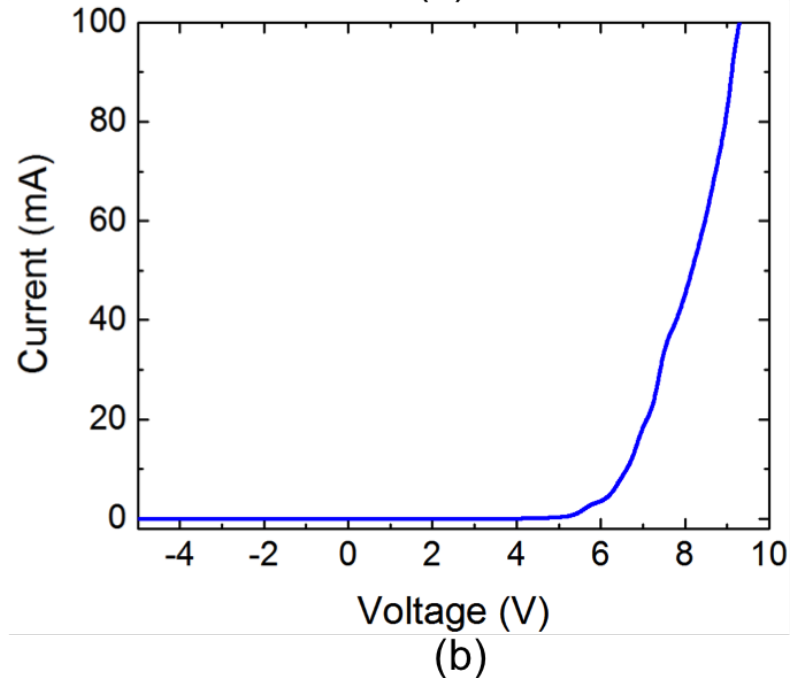
Figure 2.13: (a) SEM image taken at 45° tilt of an ensemble of nanowire p-n junctions and (b) TEM image of a single dot-in-nanowire p-n junction

Doping levels were measured through Hall measurements performed on similarly doped planar films. The n-doping is estimated to be $5 \times 10^{18} \text{ cm}^{-3}$ while p-doping is $5 \times 10^{17} \text{ cm}^{-3}$. Efficient doping and injection of electrons-holes into the nanowire active region can be confirmed from electrical characteristics of nanowire diodes.

To test this, 300 nm of Si-doped n-type GaN nanowire is first grown, followed by the active region consisting of an InGaN (2 nm)/GaN (12 nm) disk and, 250 nm Mg-doped p-type GaN. Devices were fabricated from ensembles of nanowires by first passivating them with parylene, which also served to planarize the structure for subsequent p-contact deposition. Before depositing the p-contact, the parylene is etched just enough to expose the tops of nanowires and Ni/Au (5 nm/5 nm) and 200 nm indium tin oxide (ITO) are deposited as transparent electrodes. Aluminum is deposited on the n-type Si substrate to form the bottom electrode. The room temperature current-voltage characteristics of the device exhibits a series resistance of 24Ω and a turn-on voltage of $\sim 5 \text{ V}$ which confirms the doping levels estimated from Hall measurements on equivalently doped samples. A schematic of the ensemble LED and its electrical characteristics are shown in Fig. 2.14 (a) and (b), respectively.



(a)



(b)

Figure 2.14: (a) Schematic of nanowire p-n junction light emitting diode fabricated from a nanowire forest and (b) its measured electrical characteristics at room temperature

2.5 Summary

In summary, we have investigated the plasma assisted molecular beam epitaxy growth of GaN nanowires on silicon. Since different applications require different nanowire densities and diameters, growth parameters to controllably vary both average size (20 nm to 100 nm) and density ($1 \times 10^8 - 2 \times 10^{12}/cm^{-2}$) have been determined. InGaN/GaN disks-in-nanowires emitting in the blue ($\lambda = 420$ nm), green ($\lambda = 530$ nm) and red ($\lambda = 620$ nm) spectral range were grown. Detailed structural characterization using SEM, HRTEM, and EDX was performed to investigate the crystal quality of the material and to estimate the elemental compositions of the disks. Single and multiple InGaN disks were embedded in a p-n doped regions to form a nanowire light emitting diodes.

The next chapter will discuss the optical characteristics on visible disk-in-nanowires.

CHAPTER III

Optical Characterization Of Nanowire Heterostructures

3.1 Introduction

The InGaN disk-in-nanowire heterostructure, grown on silicon, has several advantages over previously studied self-assembled quantum dots grown on sapphire and GaN pseudo-substrates. GaN and AlGaN nanowires grown epitaxially on (001) and (111) silicon substrates are relatively free of extended defects as described in Chapter 2. The surface recombination velocity in GaN nanowires is 10^3 cm/s, which is two orders of magnitude smaller than that on a planar surface of GaAs [52]. The strain of the quantum dot heterostructure embedded in a nanowire can efficiently relax on the nanowire sidewalls during growth. A nanowire- quantum dot does not have a two-dimensional wetting layer underneath it as in InGaN/GaN self-organized quantum dots. This prevents the leakage of carriers from the quantum dot into the wetting layer at higher temperatures.

The InGaN quantum disks grown by MBE have been investigated through various optical characterization techniques. The radiative efficiency of grown heterostructures is studied through temperature dependent photoluminescence measurements. The lifetime of the disks is derived through time resolved measurements. Photolumines-

cence (PL) from a single disk is measured through micro-photoluminescence (μ -PL) spectroscopy. Second-order correlation from a single quantum disk shows single-photon emission. The single InGaN disk-in-nanowire emits single photons in the blue spectral range which could have potential applications in free-space quantum cryptography due to the availability of high speed single photon detectors in this range [43]. While photon anti-bunching has been reported from a variety of emitters, practical applications require efficient, high-speed, and high temperature operation. This is the first demonstration of triggered single-photon emission from InGaN/GaN disks up to 200 K, a temperature that can be easily achieved by Peltier cooling.

3.2 Photoluminescence From GaN Nanowires

3.2.1 Photoluminescence At Room And Low Temperature

The optical properties of the nanowires were examined by PL measurements by exciting the samples with the frequency tripled output of a mode-locked Spectra Physics Tsunami Ti:Sapphire laser emitting at 267 nm and focusing the sample emission to a monochromator (with a spectral resolution of 0.03 nm) equipped with a photomultiplier tube (PMT). Luminescence from GaN nanowires at room temperature was found to be free of any deep level yellow bands, indicating absence of any defect states related to Ga vacancies during crystal growth [73]. Figure 3.1 shows a typical room temperature PL from a GaN nanowire grown on (111) Si.

Clear excitonic peaks were observed from GaN nanowires at low temperatures (Fig. 3.2). The wurtzite crystalline structure gives rise to three free exciton transitions, $X_{A,B,C}$. Interband momentum-matrix calculations show the X_A and X_B excitons are purely polarized perpendicular to the c-axis whereas the X_C exciton is strongly polarized parallel to the c-axis. The absence of dislocations leads to drastically reduced nonradiative exciton recombination rates and hence reduced exciton

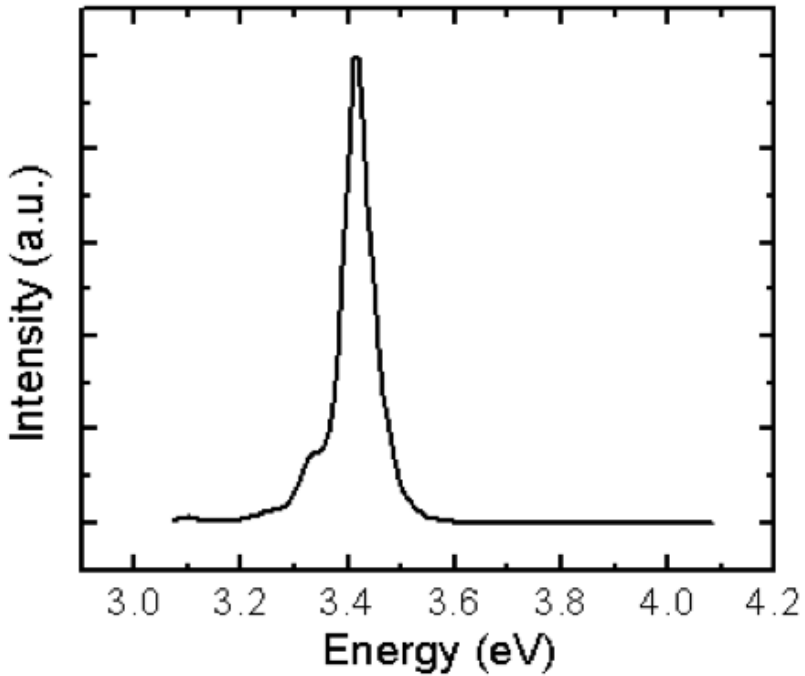


Figure 3.1: Photoluminescence spectrum from an ensemble of GaN nanowires measured at 300 K

linewidth. The peaks labelled DBX_A is the bound exciton transitions. The broad and weak shoulder at 3.4 - 3.45 eV is related to the surface. The X_A line at 3.472 eV has a narrow linewidth of ~ 5 meV and has a shoulder which may be ascribed to DBX_B . The lineshape of the exciton transitions resembles a Lorentzian function instead of a Gaussian function, suggesting negligible inhomogeneous broadening of the exciton resonances in the nanowires.

3.2.2 Temporal Behavior Of Luminescence From GaN Nanowires

The temporal behavior of the PL from the GaN nanowires is measured in a time resolved photoluminescence (TRPL) measurement (Fig 3.3). The GaN nanowire sample is excited by a pulsed laser at 80 MHz (12.5 ns, with pulse width 130 fs). The PL emission is filtered using the monochromator and detected by a single-photon

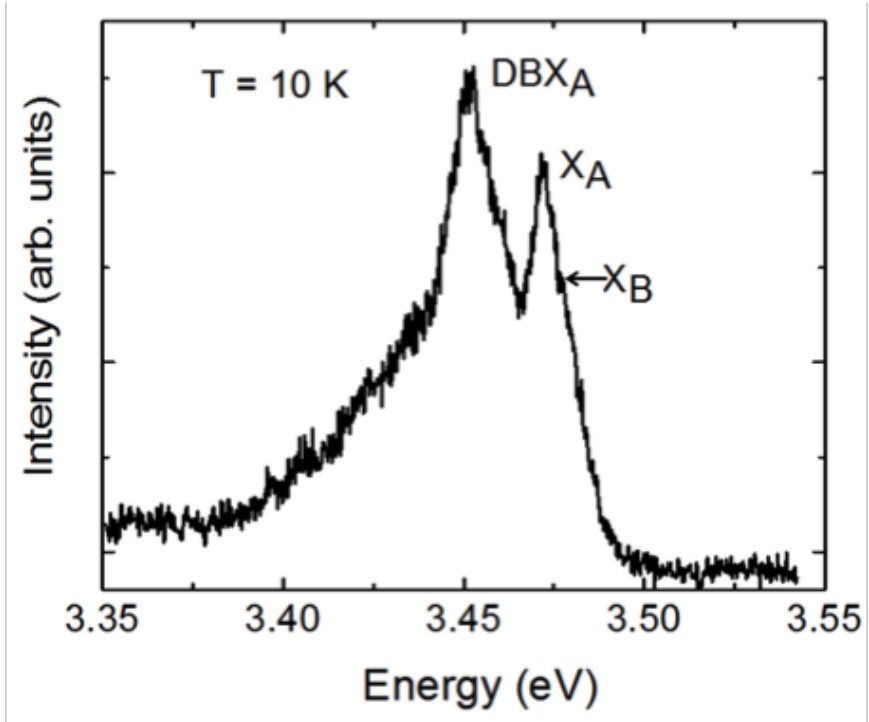


Figure 3.2: Photoluminescence spectrum from an ensemble of GaN nanowires measured at 10 K

avalanche photodiode. The PL decay can be analyzed using a monoexponential model to obtain a lifetime of ~ 575 ps at room temperature.

3.3 Emission From InGaN/GaN Disk-In-Nanowires

3.3.1 Temperature Dependent Photoluminescence

Temperature-dependent PL spectra from disk-in-nanowire ensembles containing a single disk emitting in the blue and green spectral range are shown in Figs. 3.4 and 3.5. For the blue emitting sample, strong InGaN emission was observed at a wavelength of 450 nm, with a linewidth of 14 nm, which is similar to that reported for planar InGaN/GaN single quantum wells [74]. As nanowires are non-resonantly excited, weak emission from GaN is also seen at 358 nm. The blue shift of the GaN emission compared with the 365 nm emission of bulk GaN is a signature of quantum

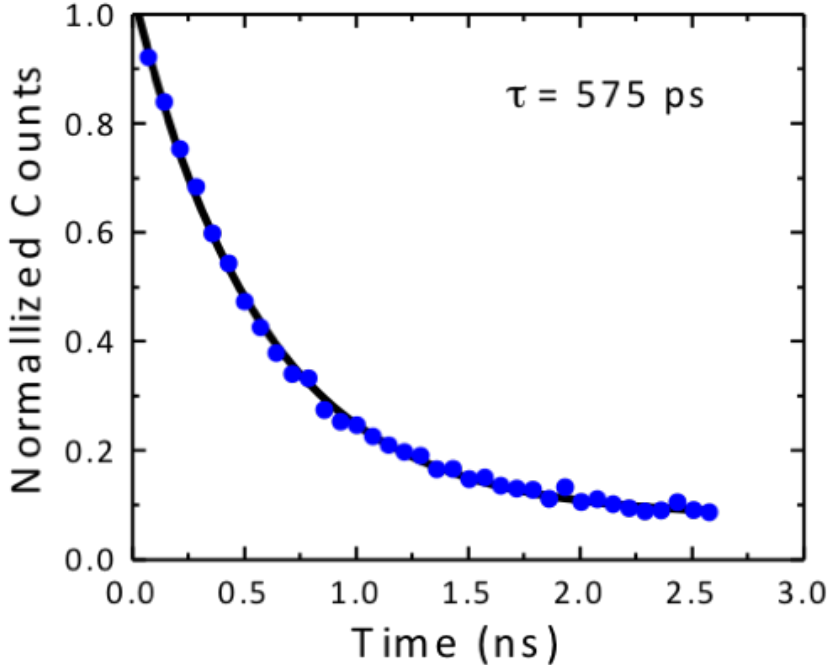


Figure 3.3: PL decay transient measured from undoped GaN nanowires at room temperature, solid curve denotes monoexponential fit to measured data.

confinement in the nanowires. The temperature dependent variation of the InGaN luminescence peak is plotted in the inset of the figure and the trend is analyzed with the Varshni equation [75].

$$E = E_0 - \frac{\alpha T^2}{\beta + T} \quad (3.1)$$

The data is in excellent agreement with the Varshni equation, yields α and β values of 8.3×10^{-4} eV/K and 825 K. The S-type behavior is not seen, indicating the absence of any significant compositional inhomogeneity or clustering in the InGaN region.

Similarly green emitting samples have a photoluminescence peak at 520 nm (shown in Fig. 3.5) and relatively narrow emission linewidth of 40 nm at room temperature. No defect-related yellow band was observed in the PL spectra. The temperature dependent PL peak energy follows the Varshni equation, with α and β values of 1.2×10^{-4} eV/K and 625 K. The absence of S-shaped behavior despite the relatively

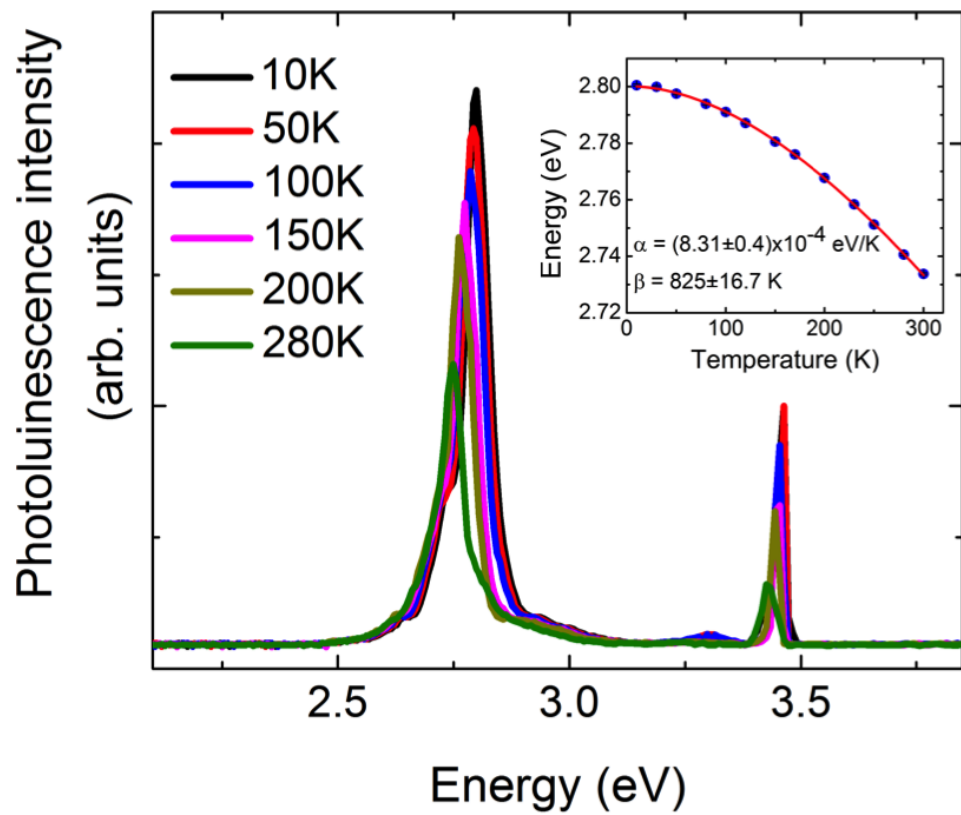


Figure 3.4: Temperature dependent photoluminescence from $In_{0.25}Ga_{0.75}N$ disk in GaN nanowires; inset shows the Varshni fit to peak emission values as a function of temperature.

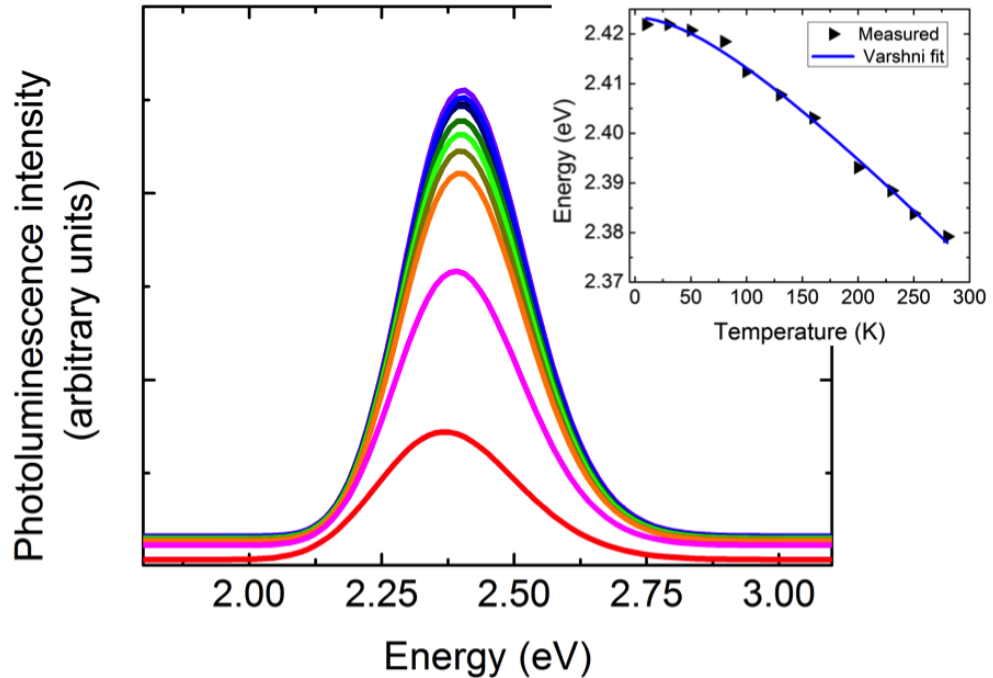


Figure 3.5: Temperature dependent photoluminescence from $In_{0.37}Ga_{0.63}N$ disk in GaN nanowires. No S-shaped behavior is observed in the peak energy as a function of temperature, as shown in the inset

large 37% Indium composition in the InGaN disk, proved the InGaN region is free of compositional non-uniformities. The internal quantum efficiency (IQE) of emission is measured as a ratio of the integrated photoluminescence intensity at room temperature and low temperature. It is assumed that at a low temperature of ~ 10 K, all non-radiative recombination centers are frozen and the IQE is 100%. A radiative efficiency τ_r of 52% is estimated in the blue emitting, and 36% in the green emitting InGaN QD sample.

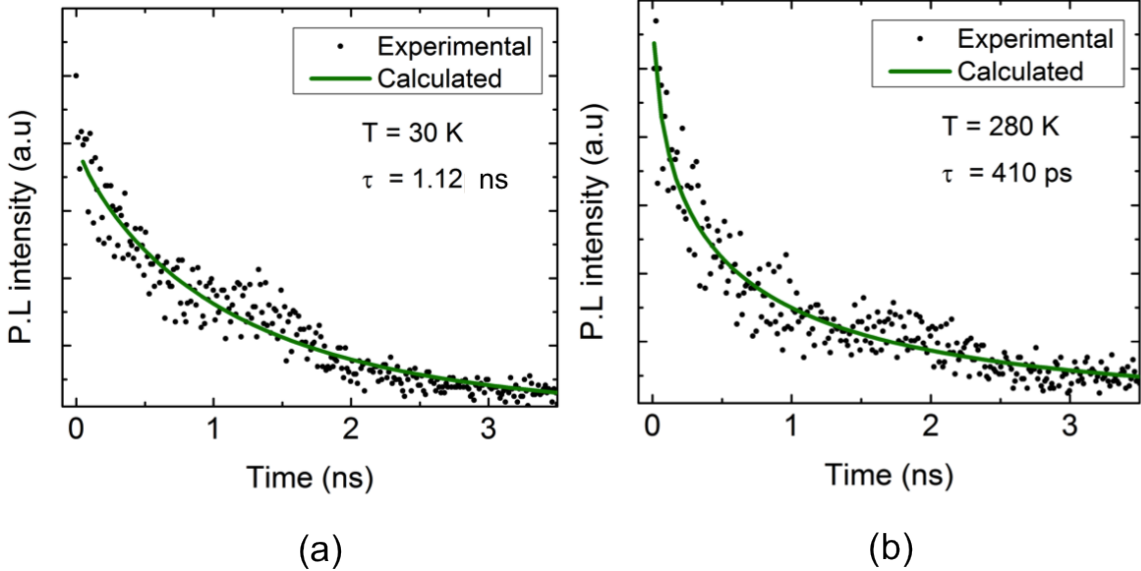


Figure 3.6: Transient PL decay shows a lifetime of (a) 1.1 ns at low temperature and (b) 410 ps at room temperature from green emitting InGaN disk-in-nanowires

3.3.2 Time Resolved Photoluminescence From InGaN/GaN Disks-In-Nanowires

The decay transients for InGaN quantum disks are analyzed using a stretched exponential form and can be fit using equation:

$$I = I_0 \exp\left(\frac{-t}{\tau}\right)^\beta \quad (3.2)$$

where I_0 is the maximum intensity, τ the lifetime and β the stretching coefficient related to the In segregation and clustering in the InGaN disk. The total lifetime strongly depends on the temperature, as seen in Fig. 3.6, because of the decrease in non-radiative lifetime with temperature. The β coefficient for the green emitting QDs is 0.85 and this deviation from a $\beta = 1$ arises from the compositional inhomogeneities in the quantum dot alloy. The lifetime decreases from 1.1 ns to 410 ps from low temperature (30 K) to room temperature (280 K) and both values are significantly lower

than lifetimes measured in InGaN quantum wells [76]. This data can be analyzed in combination with the temperature dependent photoluminescence data, using the following equations:

$$\frac{1}{\tau} = \frac{1}{\tau_r} + \frac{1}{\tau_{nr}} \quad (3.3)$$

and

$$\eta_i = \frac{\tau_{nr}}{\tau_r + \tau_{nr}} \quad (3.4)$$

where

$$\eta_i = \frac{I(T)}{I(10K)} \quad (3.5)$$

Using these equations and a η_i value of 35%, we obtain $\tau_r = 1.12$ ns and $\tau_{nr} = 603$ ps at room temperature.

3.3.3 Micro-Photoluminescence

Single-QD spectroscopy is performed by micro-photoluminescence (μ -PL) measurements in the far field in a confocal geometry. The same microscope objective is used to focus the excitation beam on the sample and to collect the PL signal. The experimental set-up is schematized in Fig. 3.7. The sample is mounted on the cold finger of a continuous flow helium cryostat. The excitation beam, provided by a tunable pulsed Ti:sapphire laser, is focused on the sample with a spot size of approximately $1\mu\text{m}$. The sample is accurately positioned using XY piezoelectric stages with a precision of $\sim 0.05 \mu\text{m}$. Moreover, a pinhole located in an image plane allows for spatial resolution and increases the signal-to-noise ratio. The size of the pinhole is determined by the magnification of the collection optics (microscope + lens). For

the measurement of exciton/bi-exciton luminescence from a single QD our setup the magnification is about 100 so that a $100\mu\text{m}$ pinhole selects a $1\mu\text{m}$ area on the sample surface (Fig.3.8).

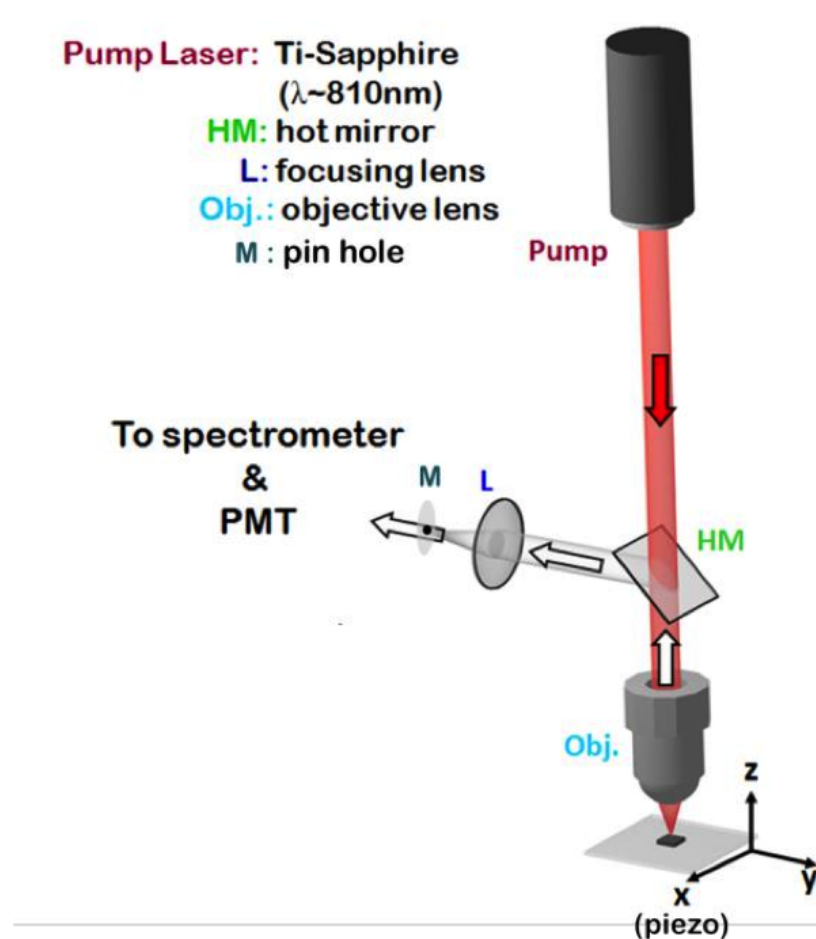


Figure 3.7: Schematic of the micro-photoluminescence ($\mu\text{-PL}$) setup [77]

A low density ($1 \times 10^8/\text{cm}^2$) $\text{In}_{0.1}\text{Ga}_{0.9}\text{N}/\text{GaN}$ disk-in-nanowire sample was studied. The $\mu\text{-PL}$ spectra showed sharp emission peaks with linewidth around 4 meV, at 10 K. Upon increasing the sample temperature, the emission peak shows significant broadening and rapid quenching in emission intensity.

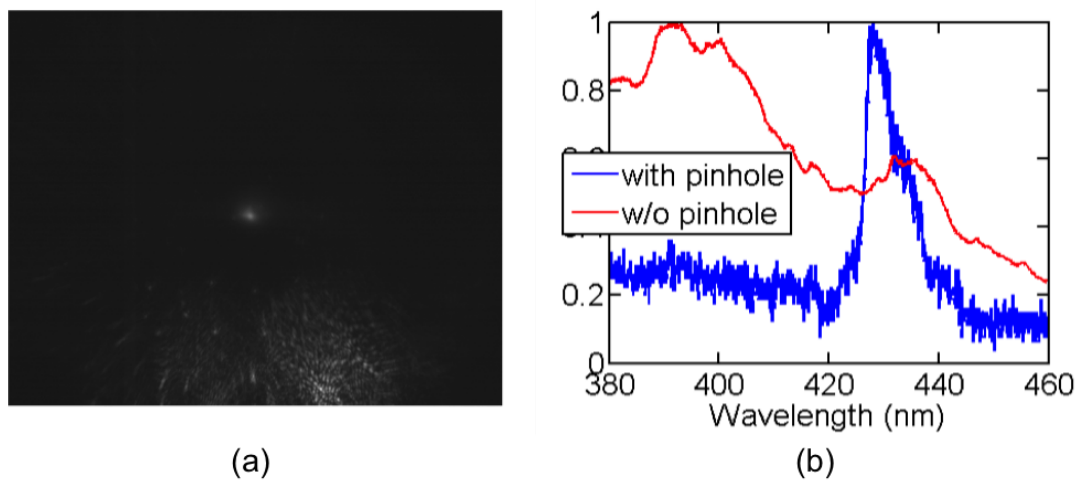


Figure 3.8: μ -PL measurement from a sample containing dispersed nanowires. Figure (a) shows a CCD image of a spatially isolated single disk. Figure (b) shows the difference in the spectrum with and without a pinhole. The size of the pin hole is adjusted to capture the photoluminescence from a single disk. (Courtesy: Lei Zhang)

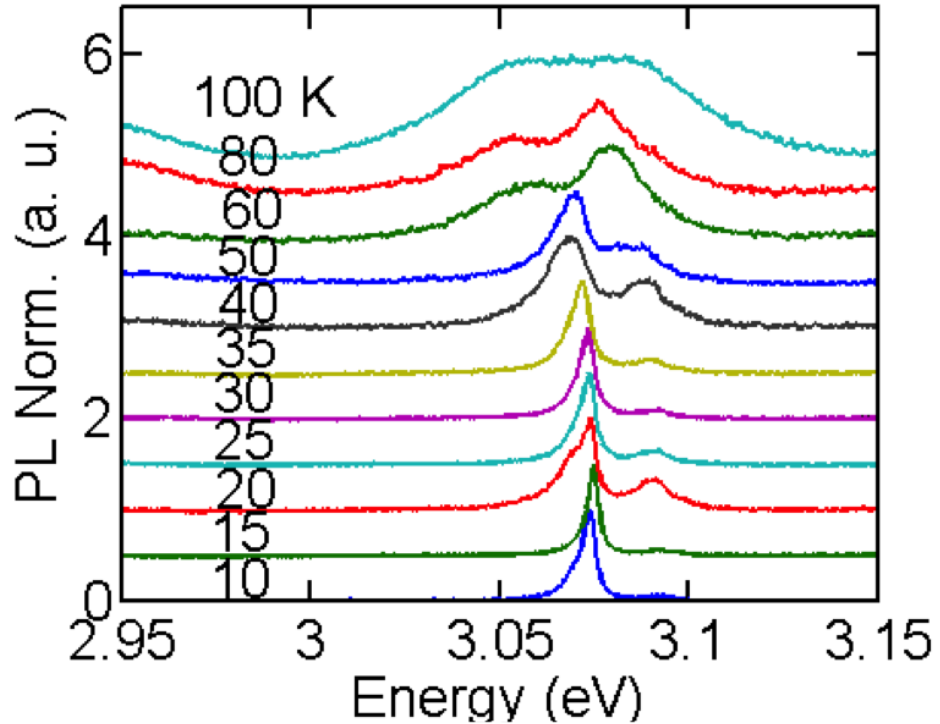


Figure 3.9: Temperature dependent photoluminescence from a single $In_{0.1}Ga_{0.9}N$ disk. (Courtesy: Lei Zhang)

3.4 Heterostructure Design

Built-in polarization is a major debilitating issue in nitride heterostructures, which leads to poor temperature stability in InGaN/GaN heterostructures. Fig. 3.10 (a) shows the schematic of the band lineups for a conventional InGaN/GaN quantum well structure without the polarization fields and (b) with polarization fields. In Fig. 3.10 (a), the band offsets are symmetric at the bottom and top GaN barrier sides and the band lineup is flat. However, for c-plane (polar) InGaN quantum well, the existence of the spontaneous and piezo-electric polarization fields results in bending of the energy bands. The electrostatic field leads to an asymmetric distribution of the electrons and holes in the QW and the tilting of the band lineups results in the thermionic leakage of electrons to the top GaN barrier and the leakage of holes to the bottom GaN barrier. This greatly reduces the effective band-offset seen by carriers and leads to significant leakage in nitride-based quantum-wells.

To achieve higher operating temperatures, an $In_{0.2}Ga_{0.8}N/Al_{0.1}Ga_{0.9}N$ disk-in-nanowire heterostructure was adopted to provide larger band-offsets and hence ensure higher operating temperatures. The $In_{0.2}Ga_{0.8}N/Al_{0.1}Ga_{0.9}N$ disk-in-nanowire is shown schematically for a single nanowire in the inset of Fig 3.11. The nanowires were grown on silicon substrate by plasma-assisted molecular beam epitaxy (PA-MBE), using MBE growth techniques described in Chapter 2. The grown sample was characterized by scanning electron microscope (SEM) imaging, shown in Fig. 3.11, which reveals a nanowire density of $2 \times 10^{11} cm^2$. A transmission electron microscopy (TEM) image is shown in Fig. 3.12. The high-resolution image in the inset shows a defect-free interface between the InGaN and AlGaN layers. The diameter of the nanowire is 25 nm. A room temperature photoluminescence (PL) spectrum from the nanowire ensemble is shown in Fig. 3.13. The emission peaks corresponding to AlGaN (at 335 nm) and InGaN quantum disk (at 450 nm) suggest that the Al mole fraction in the AlGaN is $\sim 10\%$ and In mole fraction in the quantum disk is $\sim 20\%$.

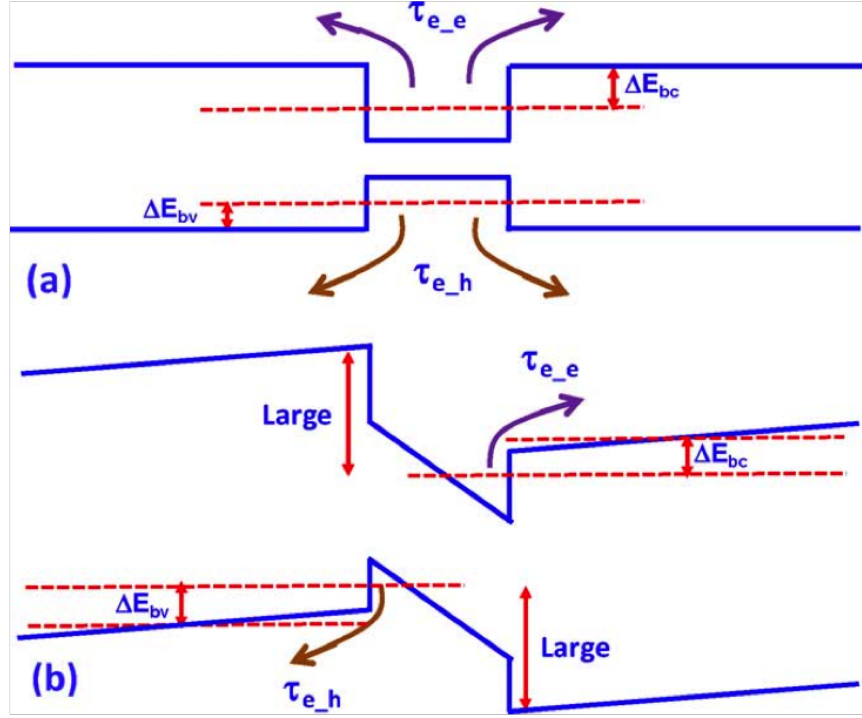


Figure 3.10: Effective barrier heights in an InGaN/GaN quantum well structure (a) without and (b) with band-bending cause by polarization fields. [78]

. These values are close to estimates from growth conditions and are supported by SEM-Energy Dispersive X-ray Spectroscopy (EDS) data shown in the inset.

3.5 Optical Characteristics Of Single InGaN Disk-In-Nanowire

The optical properties of the dispersed QD-nanowires were studied in more detail by μ -PL measurements. Nanowires from the as-grown sample are mechanically removed from the substrate using a razor and transferred to a 10 mL solution of IPA. The nanowire-IPA solution is ultra-sonicated for 20 minutes to separate the nanowires from each other and then dispersed on silicon wafer to artificially create a density of 10^8 cm^{-2} . The silicon wafer is patterned using alignment marks to identify nanowire positions. The silicon wafer is coated with Al mirror to prevent the leakage

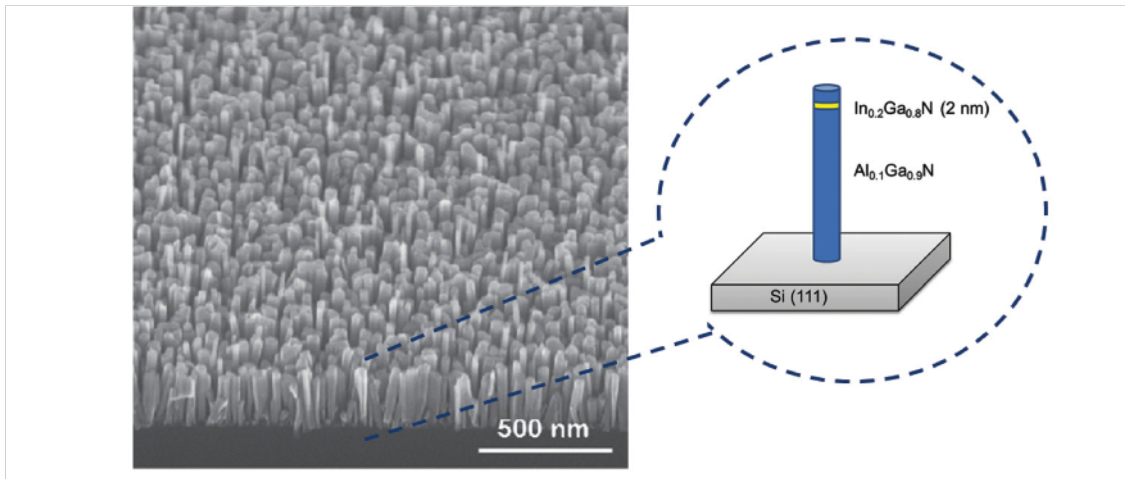


Figure 3.11: Schematic and SEM of the heterostructure

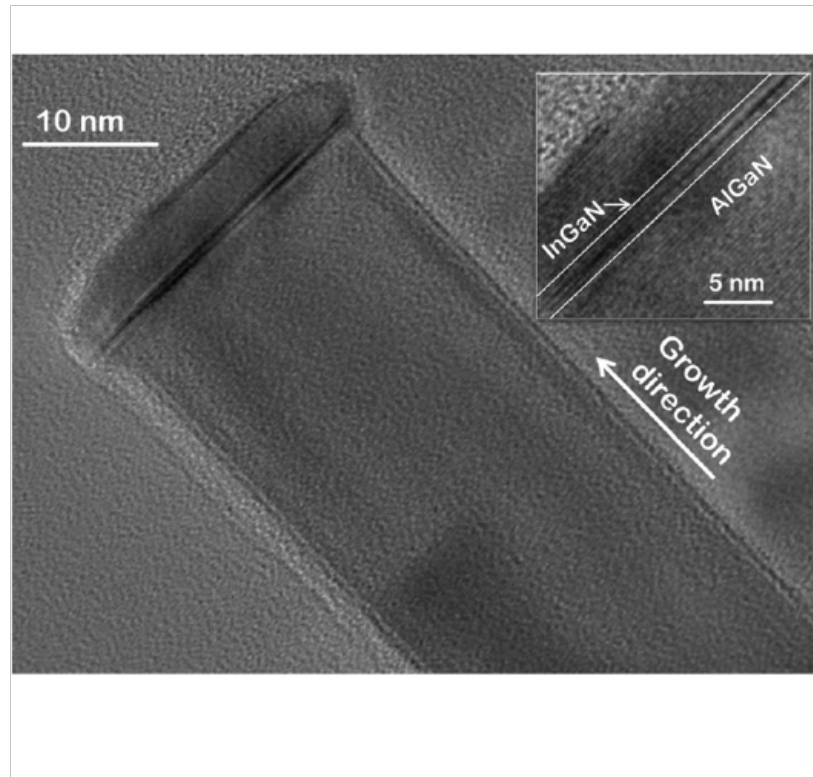


Figure 3.12: TEM of an InGaN disk in AlGaN nanowire heterostructure

of light into the substrate and obtain higher brightness from a single quantum disk.

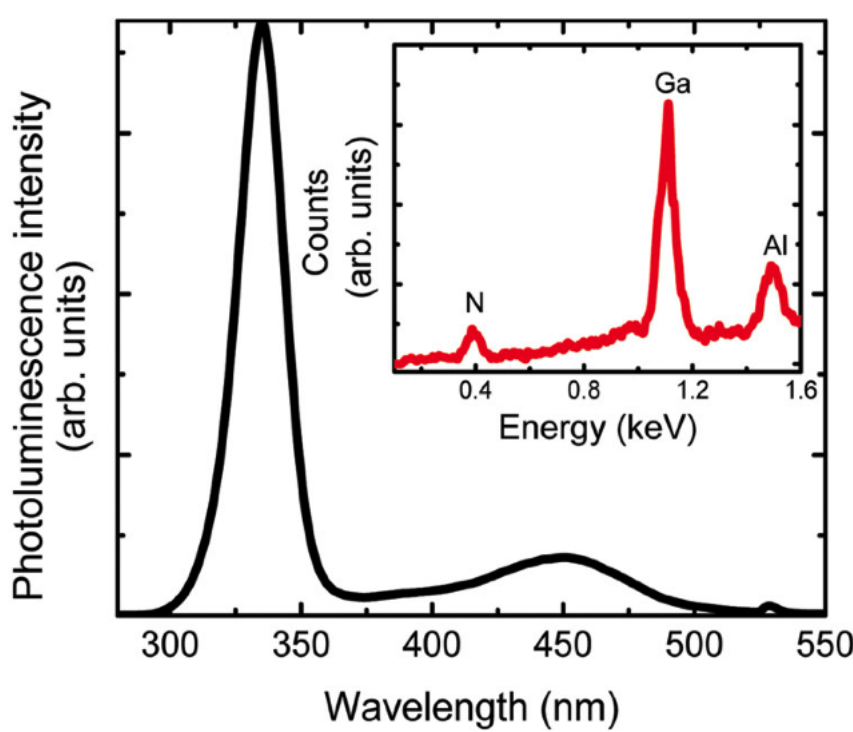


Figure 3.13: Photoluminescence from a forest of $In_{0.2}Ga_{0.8}N/Al_{0.1}Ga_{0.9}N$ disk-in-nanowires at room temperature. The inset shows SEM-EDX spectrum from $Al_{0.1}Ga_{0.9}N$ nanowires

3.5.1 Exciton And Biexciton Complexes In Nitrides

In direct gap semiconductors, the promotion of an electron to the conduction band leaves a hole in the valence band. The Coulombic interaction between the oppositely charged electron and hole leads to the formation of a bound state called an exciton which appears as a new line in the absorption spectrum, separated from the band gap E_g by the exciton binding energy E_b . The exciton can be seen as a hydrogenic quasi-particle, whose binding energy is analogous to the hydrogen Rydberg energy. Semiconductor excitons are generally of the Wannier type, meaning that the electron-hole relative wavefunction is delocalized over many lattice sites.

If a bulk semiconductor material containing QDs is optically pumped non-resonantly (using photons with an energy greater than the bulk band gap), then electrons in the bulk will be excited from the valence band to the conduction band. Each such exci-

tation will generate one free electron in the conduction band and one free hole in the valence band. In general, if the temperature is low, it is possible for both electrons and holes to diffuse through the bulk semiconductor matrix and become trapped in a QD. In the case of cuboid-shaped QDs surrounded by infinite potential barriers, these captured carriers will then be held in the quantized energy levels. If exactly one electron and one hole become trapped in a single QD, there will be Coulombic attraction between the electron-hole pair. This will result in the formation of a quasiparticle known as an exciton, or X. The binding energy of the exciton will determine by the separation of the confined carriers, and hence by the size of the QD. Over time, it will be possible for the electron and hole comprising the exciton to radiatively recombine, resulting in the emission of a photon with a characteristic exciton energy. In addition to the single exciton state, higher-order processes are also possible. If two electrons and one hole become trapped in a single QD, for example, then a charged exciton known as an X will result. A charged exciton of the opposite sign known as an X^+ will result from the trapping of one electron and two holes. The trapping of two electrons and two holes will give rise to a biexciton, or XX. The biexciton binding energy (B_{XX}) is the difference in recombination energy between the exciton and biexciton is given by:

$$E_X - E_{XX} = -(2J_{eh} + J_{ee} + J_{hh}) \quad (3.6)$$

In GaAs-based QDs, the magnitude of J_{eh} is comparable to but slightly larger than J_{ee} and J_{hh} so the XX energy is red-shifted with respect to the X energy. In contrast, the wurtzite structure of InGaN is known to result in a large built-in piezoelectric field of the order of MV/cm, which produces a spatial separation of the electrons and holes in the QD. This strong localization, together with the smaller dielectric constant, results in much larger Coulomb interactions in InGaN QDs than in GaAs-

based QDs. The interaction energy between an electron and a hole (J_{eh}) is negative and hence tends to reduce the recombination energy, while the interaction energies between two electrons (J_{ee}) and between two holes (J_{hh}) are positive and tend to increase the recombination energy.

In nitride quantum dots, the exciton biexciton splitting was found to take both positive and negative values depending on the particular QD examined [79] and its size, shape and indium composition. However generally, the electron-hole separation leads to a reduction in J_{eh} and for most quantum dots $|J_{eh}| < J_{ee} < J_{hh}$ holds true. Consequently, it is expected that the XX recombination energy will be blue-shifted with respect to the X energy, which leads to negative biexciton binding energy in III-nitride QDs.

Kako et al. have studied the biexciton binding energy by solving the one-band Schrödinger equations for electrons and holes within the Hartree approximation. In this model of a GaN/AlN quantum-dot structure, it is approximated as a truncated hexagonal pyramid. Figure 3.14 shows calculation results of biexciton binding energies with different height/diameter aspect ratios, as functions of single-exciton energy. From this figure, it is seen that a large height/diameter aspect ratio results in a large energy separation between the exciton and biexciton. The biexciton binding energies for the height/diameter aspect ratio of 0.2 are almost twice those for 0.1.

A second important aspect is the response of exciton and biexciton peaks to excitation power density, which constitutes an important way to identify these transitions. The intensity of an X recombination line should show a linear dependence on the excitation power density (before saturation), whereas an XX recombination line should show a quadratic dependence. The exciton occupation probability can be calculated for various injection current densities P , using the Poisson formula: $I_1/I_0 = \alpha \times \exp(-\alpha)$ where $\alpha = P/P_0$ and P_0 is the saturation excitation density. In this simple model, the parameter α corresponds to the mean exciton population in a quantum dot obtained

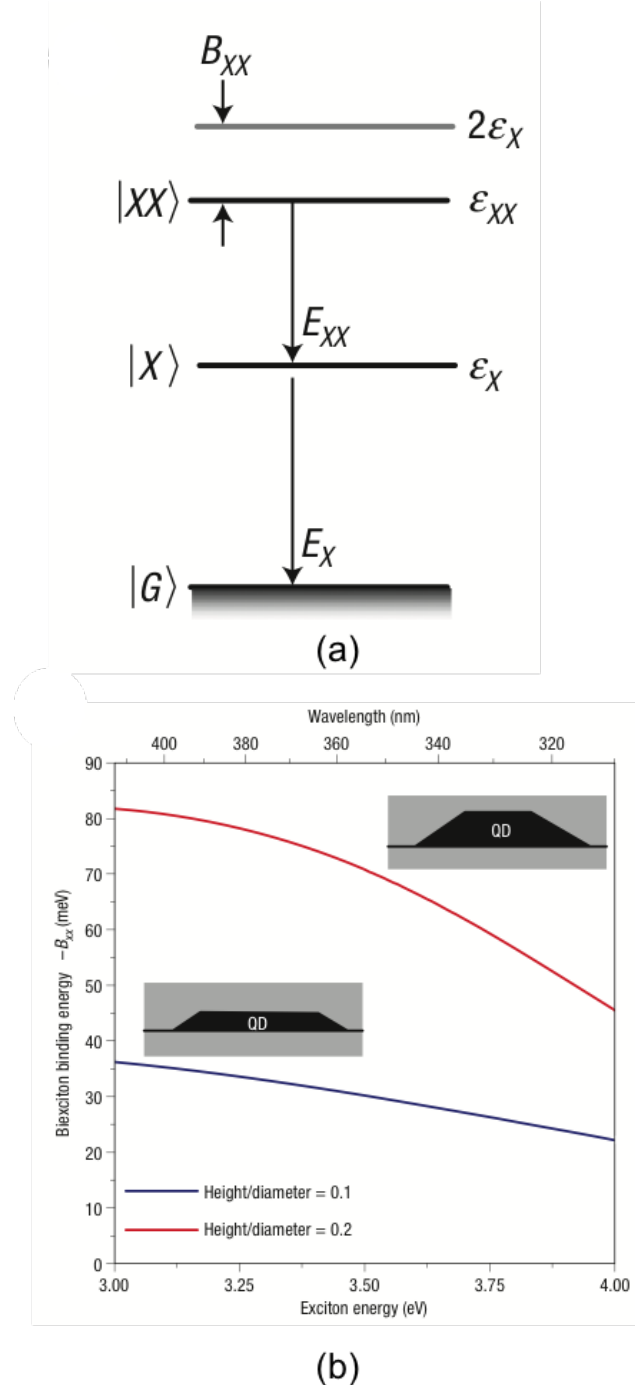


Figure 3.14: (a) Schematic of the exciton and biexciton energy levels in a quantum dot and (b) modelling of biexciton binding energy based on quantum dot aspect ratio in GaN/AlN dots [43]

by fitting the intensity of the emission peak with fitting parameters I_0 and P_0 . At small excitation powers, linear increase of integrated intensity of the peak with pump

power, suggests that it corresponds to a single-exciton transition. On the other hand, the biexciton peak follows the Poisson-distribution model with $I_1/I_0=\alpha^2 \times \exp(-\alpha)$ where the integrated intensity increases quadratically with pump power.

3.5.2 Luminescence From Single Disk-In-Nanowire

The sample is mounted on the cold finger of a continuous flow helium cryostat. A single $In_{0.2}Ga_{0.8}N$ quantum disk in a nanowire was resonantly excited by a frequency- doubled mode-locked Ti:sapphire laser. The same microscope objective was used to focus the incident excitation to a spot size of $5 \mu m^2$ and to collect the luminescence from the dispersed nanowire sample. Figure 3.16 shows the micro-photoluminescence spectrum from a single nanowire-QD at 10 K. Sharp excitonic transitions with linewidths of ~ 1 to 2 meV are observed (Fig. 3.15 (a)). These are believed to be exciton and biexciton transitions, which can be observed in the μ -PL spectra up to 200 K (Fig. 3.15 (b)).

At 200 K, the linewidths of excitonic transitions are 15-20 meV due to thermal broadening. The linear and quadratic dependence of the integrated intensity of the exciton and biexciton transitions on excitation power, measured at 200 K, are shown in Fig. 3.15 (c). At high excitation values, the strength of the exciton intensity drops whereas that of the biexciton intensity saturates at a higher value of intensity. These trends are expected since at lower values of excitation there is a competition in occupancy of exciton and biexciton states and at high excitation, the biexciton state occupancy can approach unity. Also, the lifetime of biexciton states is shorter than that of exciton states. There is negligible blue shift of the peak emission energy of the exciton transitions with increasing excitation, which suggests a very small polarization field in the quantum disk, in agreement with the previous observations. Similar data from a single GaN/AlN dot in a GaN nanowire have been reported by Renard et al. [80]

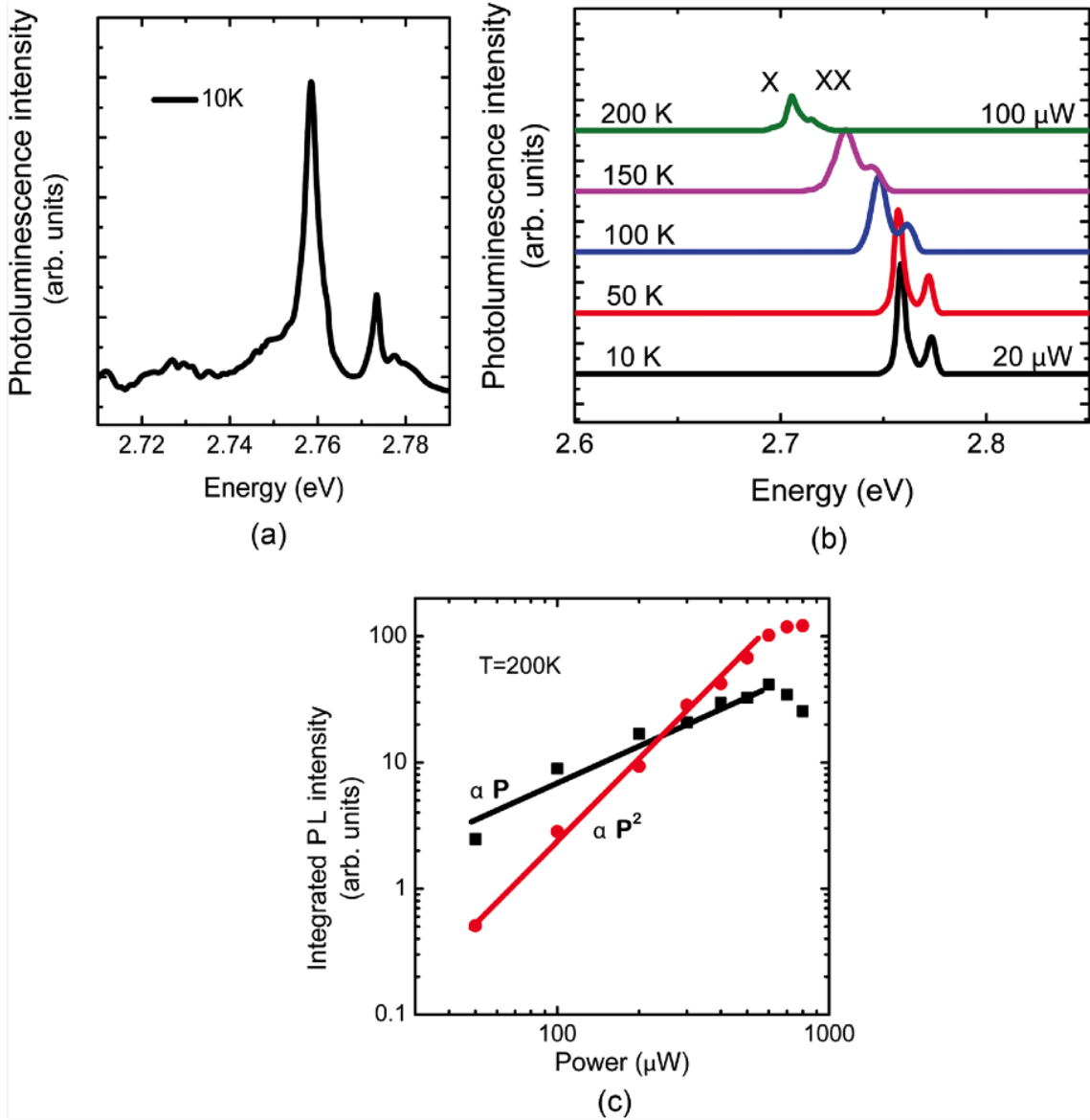


Figure 3.15: μ -PL from a single InGaN disk at (a) 10 K and (b) 200 K. (c) Pump-power dependence of the integrated intensity of biexciton peak at 200 K.

3.5.3 Second-Order Correlation

Second-order correlation measurements were performed with a Hanbury, Brown, and Twiss system. The start and stop pulses are provided by ID Quantique single-photon avalanche diodes which receive the biexciton signal split by a non-polarizing

50:50 beam splitter. For an ideal single-photon source, the second-order correlation function (described in Chapter 1) should be equal to zero at zero time delay. Figure 3.16 shows the second-order correlation of the biexciton resonance at 10 K and 200 K, respectively. The decrease in the correlation function at zero time delay indicates anti-bunching at the biexciton energy in both cases. The value of $g^{(2)}(0)$ is 0.28 at 10K, which corresponds to a 3-fold decrease in unwanted multi-photon emission events compared to a Poissonian source of the same intensity. At 200 K, the $g^{(2)}(0)$ value at the biexciton energy is 0.54. The degradation of the value of $g^{(2)}(0)$ could be due to contamination from thermally broadened biexciton and exciton lines and phonon sidebands.

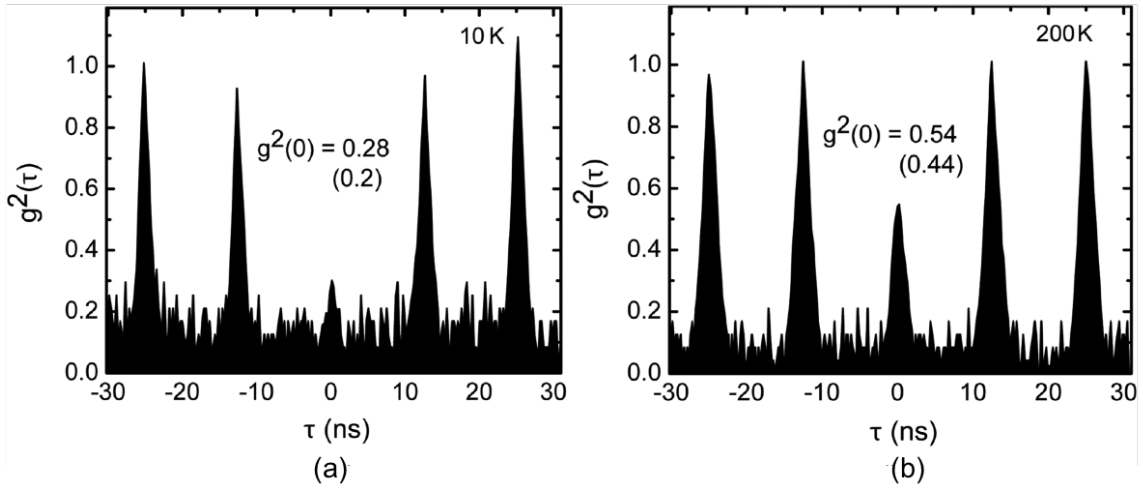


Figure 3.16: Second-order correlation measured at biexciton line under 80 MHz pulsed optical excitation at (a) 10 K and (b) 200 K

The finite value of the second-order correlation at zero time delay could also have a contribution from unwanted background counts originating from uncorrelated stray light or dark counts. In order to eliminate the effect of background counts, we apply a correction using [28]:

$$g^{(2)}(0) = 1 + \frac{g^{(2)}(0)_{meas} - 1}{\rho^2} \quad (3.7)$$

where ρ is the ratio of signal-to-total counts, including dark counts. The $g^{(2)}(0)$ values derived after background correction at 10 K and 200 K are 0.2 and 0.44, respectively.

In Fig 3.17, we have analyzed the second-order correlation data obtained at 10 K with the function [81]:

$$g^{(2)}(\tau) = \sum_{i=-2}^2 A_i \exp\left(\frac{-|t - i \times t_1|}{\tau}\right) \quad (3.8)$$

where the A_i s are the peak amplitudes, τ is the emission lifetime, and t_1 is a fitting parameter that corresponds to the separation between pulses. We derive a biexciton lifetimes of 702 ps from the analysis of data at 10 K. The PL decay data has been separately analyzed using a stretched exponential model (β value of 0.85) to yield a lifetime of 697 ps at 10 K. The two values are in good agreement. At the measurement temperature of 10 K, the lifetime represents the radiative lifetime. The small lifetime is attributed to a relatively strong 3D confinement and reduced polarization field in the nanowire heterostructure.

3.6 Summary

Optical properties of GaN nanowires and InGaN/GaN disk-in-nanowires were investigated through temperature dependent PL and TRPL measurements. Blue and green emitting InGaN/GaN disk-in-nanowires with high internal quantum efficiencies of 42% and 35%, respectively, were grown. The InGaN disk emission does not show any characteristics of In segregation. A short recombination lifetime ~ 400 ps is measured from $In_{0.37}Ga_{0.63}N/GaN$ disks at room temperature and a radiative lifetime of 1.1 ns is derived. Single nanowire PL was investigated through μ -PL measurements. PL from a single InGaN/AlGaN disk shows sharp exciton and biexciton peaks up to 200 K. Second-order correlation confirms single-photon emission with a $g^{(2)}(0)$ of 0.2 at 10 K and 0.44 at 200 K.

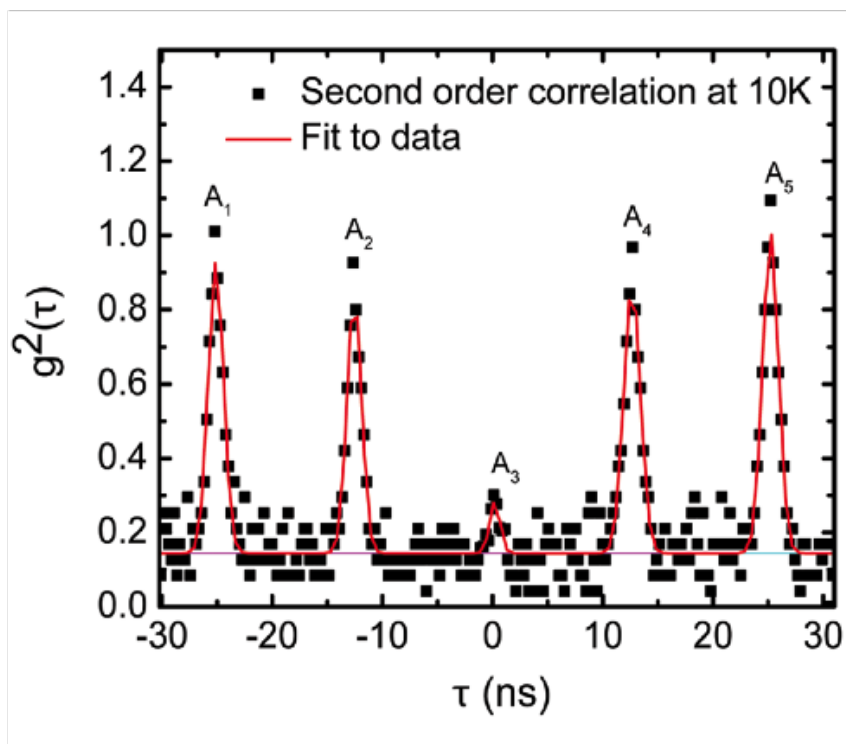


Figure 3.17: Analysis of pulsed second-order correlation data to extract quantum disk lifetime

The electrical properties and electroluminescence from single InGaN/GaN disk-in-nanowire p-n junctions will be discussed in the following chapter.

CHAPTER IV

Electrically Driven Single-Photon Emission InGaN Disk-In-Nanowire

4.1 Introduction

An early approach to electrical pumping of a single-photon source involved the controlled injection of carriers into a mesoscopic quantum well. This technique is an extension of a single-electron tunnel junction involving controlled injection of a single electron and hole. In the first such single-photon turnstile device [82], the quantum well was alternately populated with electrons and holes through resonant tunnelling by applying an alternating bias. The quantum well was sandwiched between tunnel junctions with p-n doped regions on either side. The sample had to be held at low temperature, to ensure that the charging energy of the quantum well was larger than the thermal energy of the carriers in the tunnel reservoirs. The Coulomb blockade (CB) effect prevents injection of more than one carrier at a time. The current regulation leads to regulated photon emission. However, the required operation temperature in this device was less than 1 K, making the device impractical for practical systems.

Unlike mesoscopic quantum wells, quantum dots allow the number of confined carriers to be controlled instead of requiring control of injection of single electrons

and holes, without resorting to the Coulomb blockade effect, thus allowing for higher-temperature operation. Since the early demonstration of a quantum dot (QD) single-photon source, there have been numerous reports on single-photon emission in a wide range of temperatures, with or without the use of a microcavity and with optical or electrical excitation [33–37, 43, 46, 83–86]. Generally, the electrically driven quantum-dot single-photon emitters are all-epitaxial heterostructures. However, polarization control is not easily achieved. For quantum cryptography protocols based on polarization encoding, it is desirable to have a single-photon source whose output is not randomly polarized, but has a fixed polarization depending on the size and shape of the emitter [87].

As discussed in Chapter 2, GaN and In(Ga)N nanowires can be epitaxially grown catalyst free on silicon substrates in the wurtzite crystalline form, with relatively few extended defects. They can be doped p-and n-type with suitable dopant species up to levels similar to those achieved in planar structures. This has resulted in development of state-of-the-art emitters such as LEDs and lasers using ensembles of nanowires.

In this work we have fabricated single dot-in-nanowire diodes and measured electroluminescence from them for the first time. The single dot/nanowire junction diode is fabricated on (001) silicon and the experiments have been performed at an ambient temperature of 10 K. The junction temperature is estimated to be higher due to Joule heating of the highly resistive diode. Sharp exciton and biexciton transitions are observed at 436.56 nm and 435.03 nm, respectively, in the electroluminescence spectra. Single-photon emission is observed at the biexciton emission wavelength with a value of the second-order correlation function $g^{(2)}(0)$ equal to 0.25. The emitted photons are linearly polarized along the c-axis of the nanowire. The radiative lifetime of biexciton emission obtained from time-resolved photoluminescence (TRPL) measurements is 711 ps, and this value is in excellent agreement with the value of the lifetime obtained from analysis of second-order correlation data. Single-photon emis-

sion with a larger recombination lifetime of 1.1 ns was also observed at the exciton energy. The value of $g^{(2)}(0)$ for the exciton transition is 0.16. With modifications to the heterostructure and improvement of diode characteristics, single-photon emission from a nanowire diode was observed up to 125 K.

4.2 Growth And Structural Characterization

The device used to demonstrate single-photon emission in this work is a GaN nanowire pn junction with an InGaN dot in the active region. The InGaN/GaN dot-in-nanowire heterostructure, shown schematically in Fig. 4.1 for a single nanowire, was grown on (111) Si substrate by PA-MBE. The heterostructure consists of n (Si) and p (Mg) doped GaN regions, sandwiching an intrinsic GaN region. The GaN region contains a 2 nm InGaN disk. Growth conditions for growth of nanowire p-n junctions and blue emitting InGaN disks have been described in detail in Chapter 2. Energy-dispersive X-ray (EDX) spectroscopy was performed to confirm the location, composition and thickness of the QD region. An average alloy composition of 25% is derived in the 2 nm.

4.3 Photoluminescence

Temperature- dependent PL spectra from an QD-nanowire ensemble sample, without the p-GaN grown on top, are measured and presented in Fig. 3.4. Strong InGaN QD emission was observed at a wavelength of \sim 450 nm, with a linewidth of 14 nm. The S-type behaviour is not seen, indicating the absence of any significant compositional inhomogeneity or clustering in the InGaN region. To determine the radiative efficiency of emission from the InGaN (QD) region we have performed an excitation dependent photoluminescence measurement at 10 K and 280 K (Fig. 4.2). A radiative efficiency η_r equal to 52% is estimated from the integrated photoluminescence

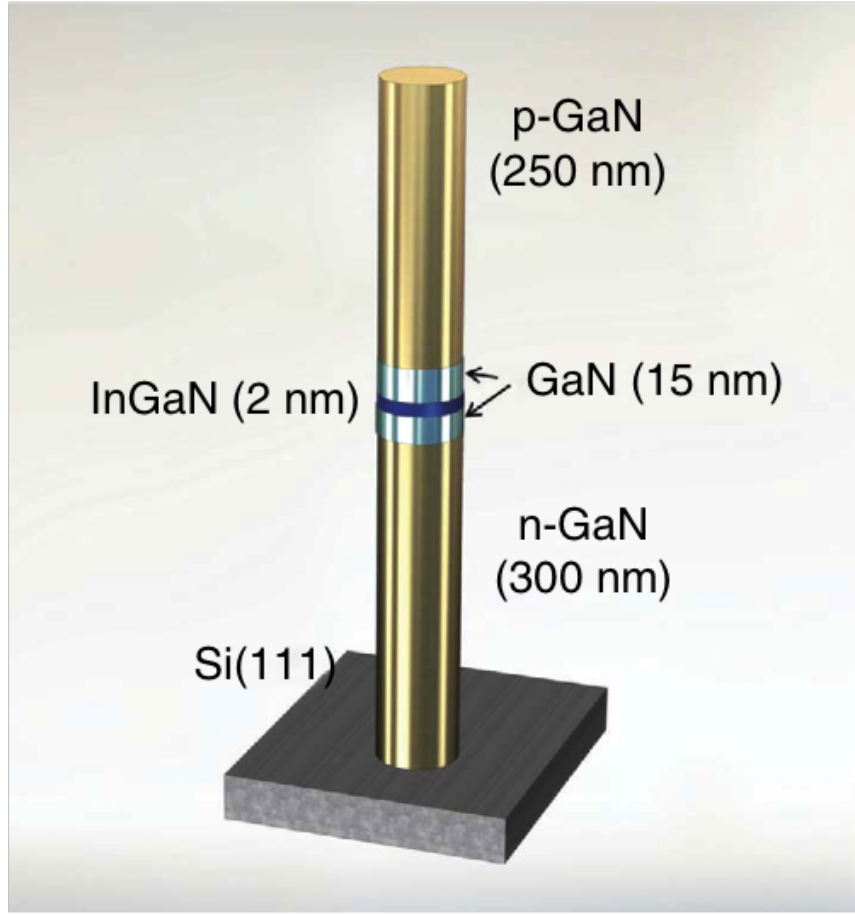


Figure 4.1: Schematic of a single disk-in-nanowire diode

intensity at these temperatures at an excitation of $80\text{KW}/\text{cm}^2$, at which a saturation of peak intensities is observed. It is assumed that non-radiative recombination centers are frozen at 10 K.

4.4 Fabrication Of Single Nanowire Diodes

The nanowires from the as-grown nanowire forest were mechanically removed from the substrate. They were transferred into a solution of isopropyl alcohol and the solution was ultrasonicated in a bath for 20 to 30 minutes. A small volume of the solution was dropped on a (001) silicon wafer covered with 100 nm of thermal oxide (SiO_2) using a pipette. The silicon wafer was pre-patterned with alignment markers. Single

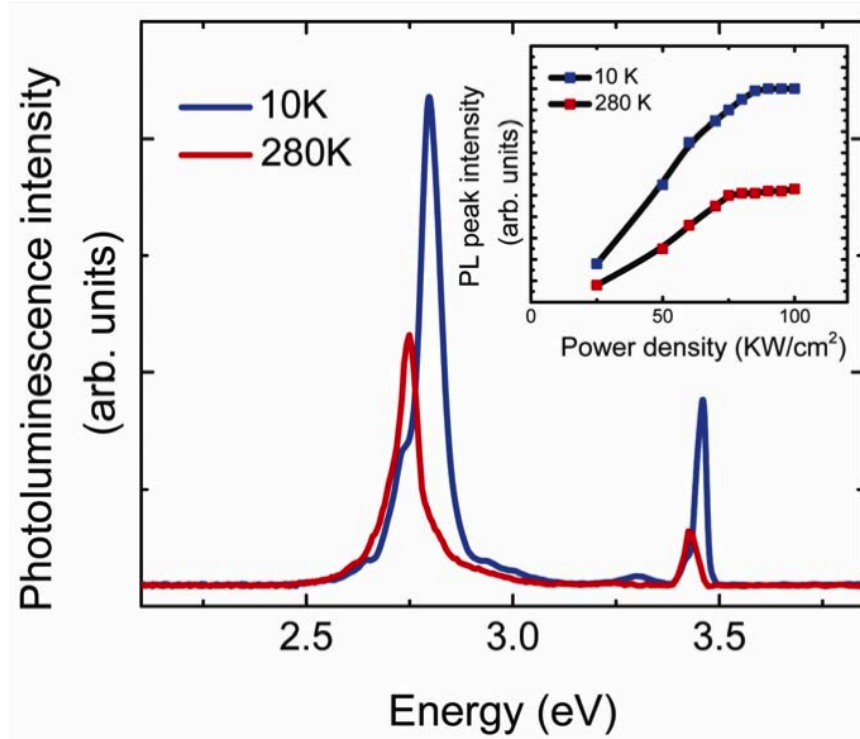


Figure 4.2: Measurement of IQE of as-grown nanowires through excitation dependent PL at low temperature and room temperature

nanowires were identified using SEM imaging and their co-ordinates were recorded with respect to the alignment marks (Fig. 4.3) Contact electrodes were exposed on PMMA A4 e-beam resist using electron beam lithography (Raith 150). Ti/Au (5 nm/45 nm) contacts were deposited using electron beam evaporation under a vacuum of 2×10^{-6} Torr. After liftoff, large contact pads ($100 \mu\text{m} \times 100 \mu\text{m}$) were defined to allow easy probing. The contacts were annealed through rapid thermal annealing in a N_2 ambient at 450°C for 30 min and the devices were wire bonded onto chip carriers for measurements. An SEM and atomic force microscope (AFM) image of one such finished nanowire diode is presented in Fig.4.4.

4.4.1 Fabrication Of Single Nanowire Diodes On Other Substrates

The single nanowire diode fabrication technology can be extended to fabricate single nanowires LEDs on a variety of substrates. Single nanowire diodes were suc-

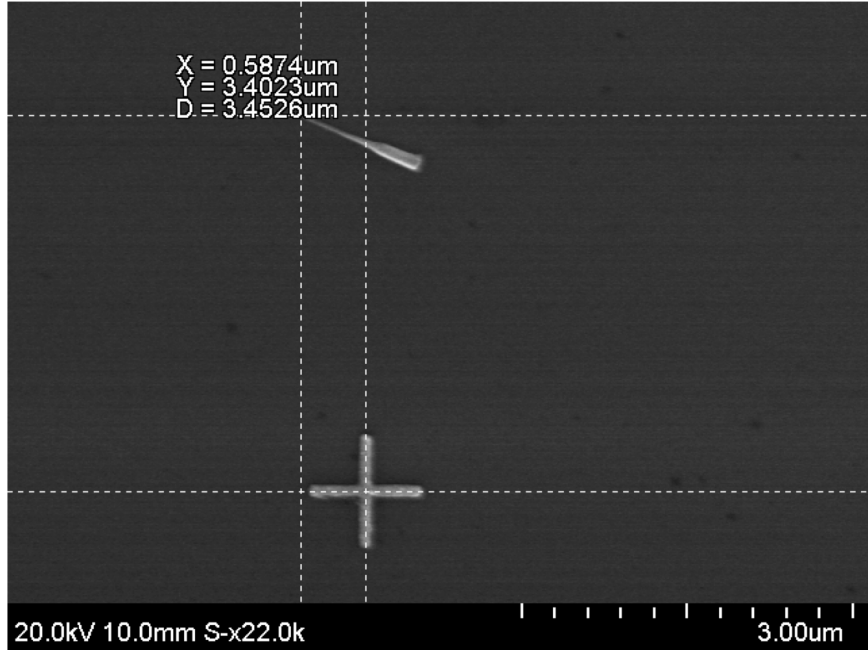


Figure 4.3: Identification of single nanowire position with respect to alignment mark under SEM

cessfully fabricated on transparent fused silicon substrates for transmission studies. During SEM imaging and e-beam writing on a transparent substrate such as fused silica, charging is a major issue due to the non-conducting nature of the substrate. To overcome this, typically a layer of conducting polymer (AquaSAVE) is spun over the resist, before e-beam exposure. After completion of the e-beam write, the polymer is removed in deionized water first followed by developing the e-beam resist and rinsing.

Nanowire diodes have also been successfully fabricated on TEM membranes. The TEM grid is mounted on a carrier silicon wafer using PMMA for ease of handling the sample and to prevent rupture of the 30 nm Si_3N_4 membrane. An SEM image of one such fabricated diode is shown below in Fig. 4.5.

4.4.2 Electrical Characteristics Of Single Nanowire Diodes

The current voltage characteristics of the single QD-nanowire pn junction measured at room temperature are presented in Fig. 4.6. The diode has a very small

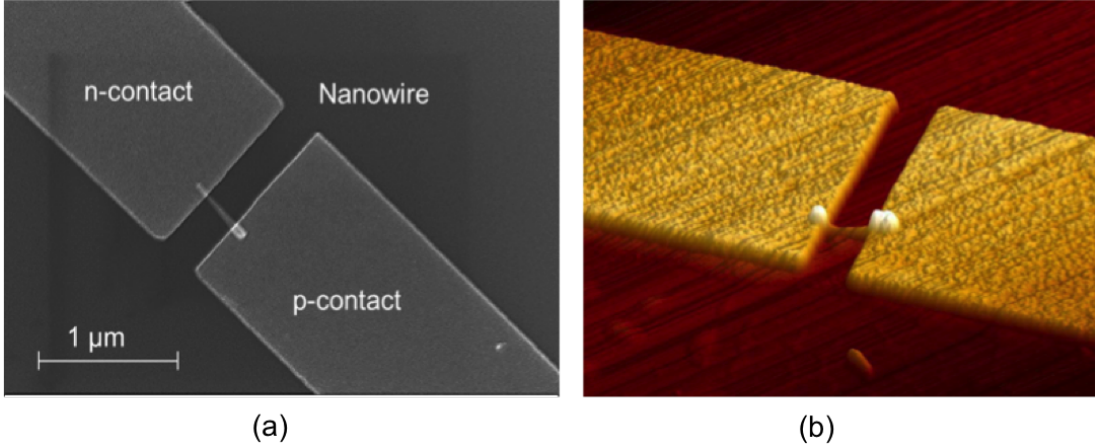


Figure 4.4: An (a) SEM and (b) AFM image of single nanowire diode with Ti/Au contacts

reverse current (range of pA) and exhibits no breakdown up to a reverse bias of 20 V. The resistance of the diode is calculated carefully by taking into account that at low current levels, the junction voltage (V_J) makes up most of the voltage drop across the device (V). At higher current levels, the voltage drop across the series resistance (IR_S) becomes significant and voltage drop across the depletion region is reduced to $V_J = V - IR_S$. To determine the series resistance R_S , starting with a forward bias semilog plot, we extend the ideal-diode part of the plot to the slope-over region and calculate the ΔV voltage displacement between the two curves as a function of I (Fig. 4.7). Since, $\Delta V = V - V_J = IR_S$, the slope of the line through a plot of ΔV versus I yields the series resistance. Using this method, the measured series resistance is calculated as 2.38 GΩ at room temperature, derived in the bias range of 2 - 20 V, in which single-photon measurements have been made.

4.4.3 Improving Diode Performance

After the first batch of fabrication, improvements were made to the fabrication process to reduce the series resistance. Instead of employing Ti/Au as the contact on p-GaN, other metallization schemes were explored to create an optimized p-contact. Transmission line measurements (TLM) were performed on p-GaN films doped with

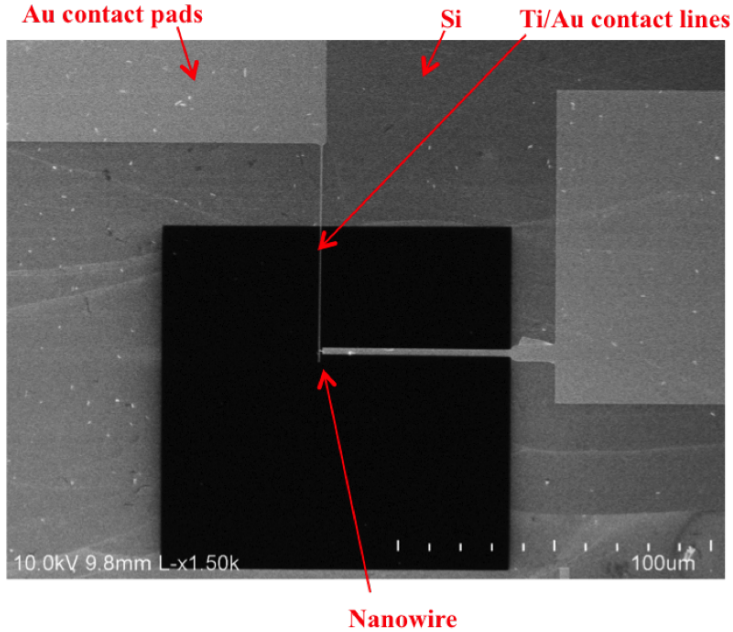


Figure 4.5: Single nanowire diode fabricated on a Si_3N_4 TEM membrane

Mg up to similar levels. All samples were treated with $(NH_4)_2S_X$ at $60^\circ C$. This step has been known to passivate the surface in III-V semiconductors [88]. Additionally, the excess sulfur reacts with nitrogen vacancies in the exposed layer of p-GaN, which increases the effective p-doping. Several metallization schemes were studied and the resulting specific resistance has been tabulated below in Table 4.1. Pd/Au (5 nm/

Metallization	Specific contact resistance ($ohm - cm^2$)
Ti/Au	9.58e-04
Ni/Au	8.74e-05
Pt/Au	3.68e-06
Pd/Au	1.92e-06

Table 4.1: Specific contact resistance measured for various metallization scheme using TLM

50 nm) which creates the best ohmic contact was used to make the p-GaN contact [89]. The nanowire surface was treated with dilute buffered hydrofluoric acid prior to p-contact metal deposition to ensure perfect contact metallurgy. The contacts showed excellent ohmic behavior after annealing at $450^\circ C$ in nitrogen and oxygen

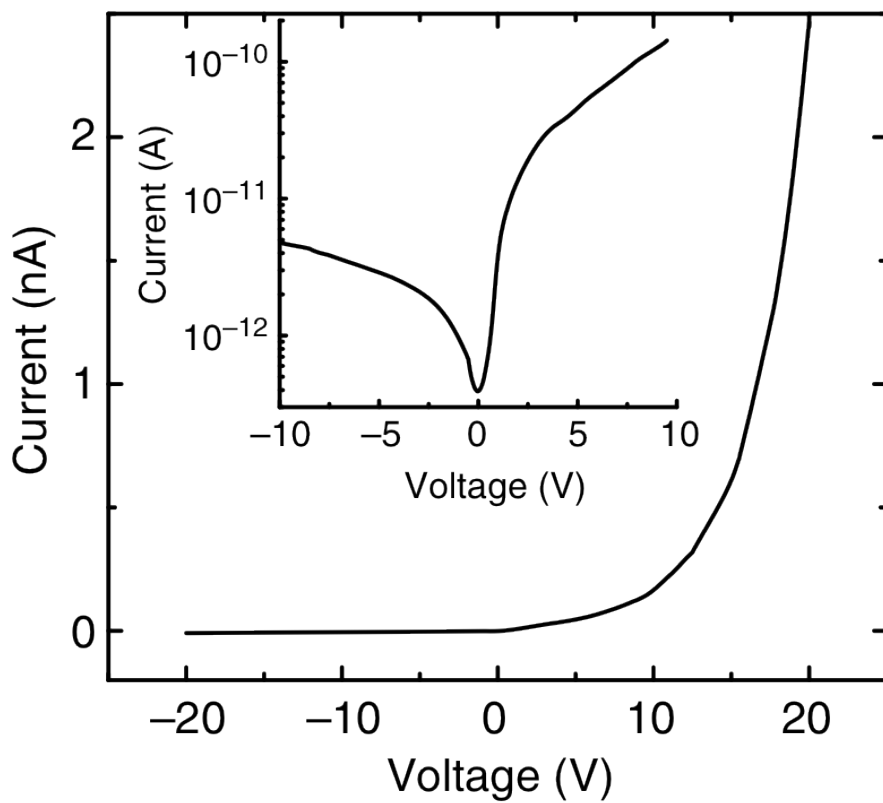


Figure 4.6: Current voltage characteristics of blue emitting single nanowire diode, the inset show I-V curve on a logarithmic scale.

ambient. The current-voltage characteristics of the single nanowire p-n junction at room temperature are significantly improved and are presented in Fig. 4.8. The series resistance at a bias of 17 V is $25 \text{ M}\Omega$.

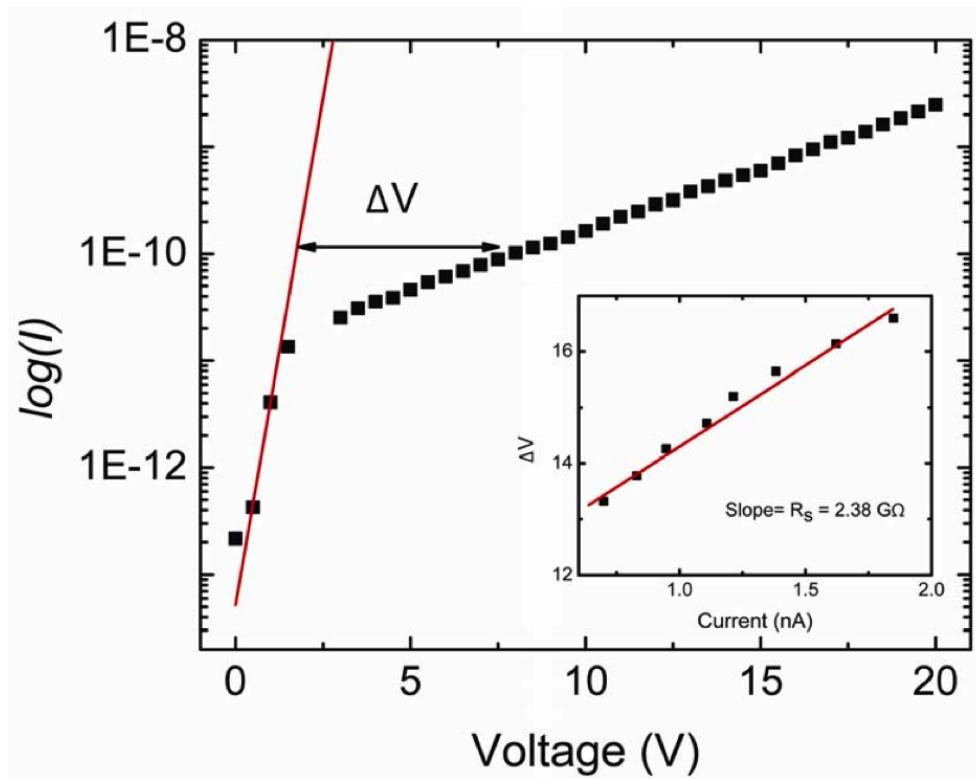


Figure 4.7: Calculation of series resistance of GaN dot-in-nanowire p-n junction

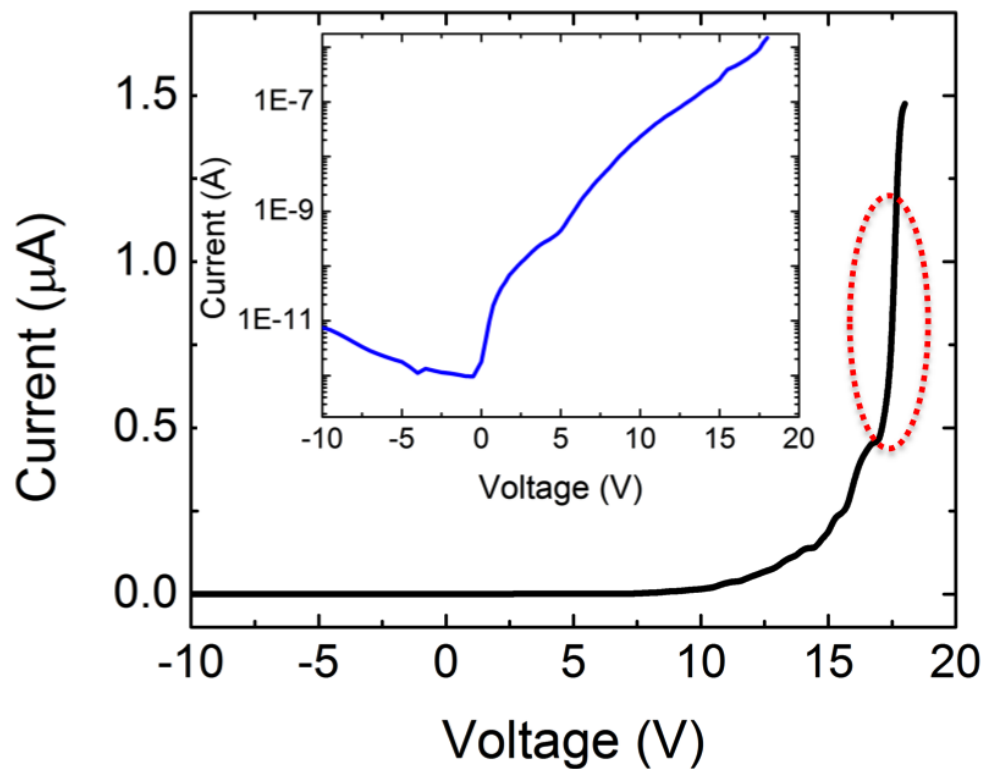


Figure 4.8: Current voltage characteristics of green emitting single nanowire diode after improvements in growth and metallization scheme. Inset shows I-V curve on a logarithmic scale. Red dotted ellipse denotes voltage range where resistance was measured

4.5 Electroluminescence From Single Dot-In-Nanowire

4.5.1 Spectra From Blue Emitting Single Nanowire LEDs

Typical micro-electroluminescence (μ -EL) spectra from the nanowire-QD device under forward bias at different injection currents are shown in Fig. 4.9. Sharp reso-

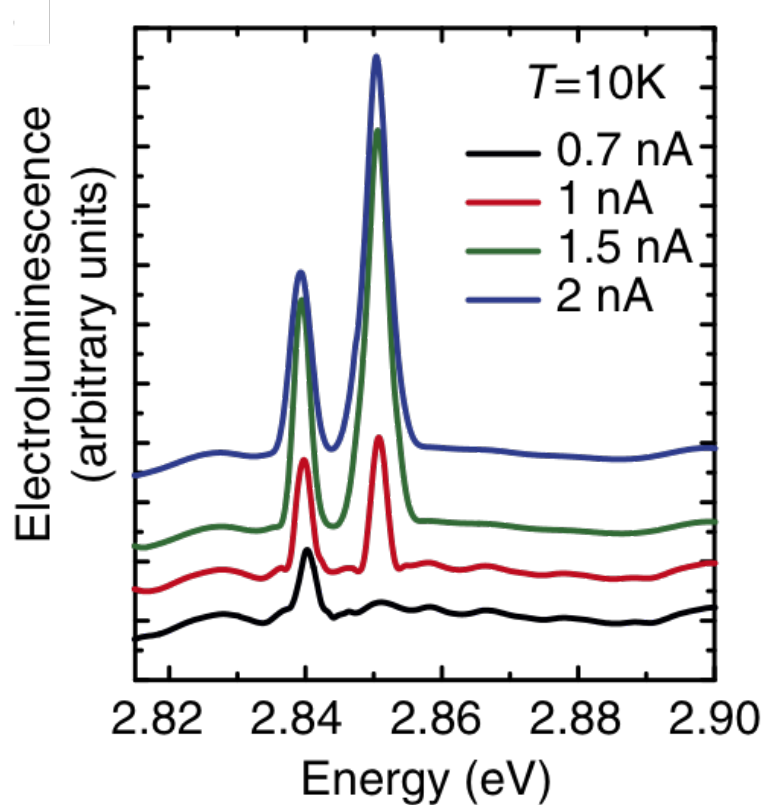


Figure 4.9: Exciton and biexciton electroluminescence from a single dot-in-nanowire in blue spectral range

nances with linewidths ranging from 2 to 3 meV are observed in the spectra. At low injection currents, a sharp peak at 2.84 eV is observed. The integrated intensity of the peak increases linearly with the injection current ($\propto 1.04 \pm 0.02$). With increase in injection current, a second peak is observed at 2.85 eV, which increases quadratically with injection current ($\propto 1.93 \pm 0.09$). The linear and quadratic dependence of intensity on injected current and their subsequent saturation, as shown in Fig. 4.10, confirm that the resonances are from single exciton and biexciton transitions, respec-

tively. The measured negative biexciton binding energy of 10 meV is in the range of previously reported values for single InGaN QDs.

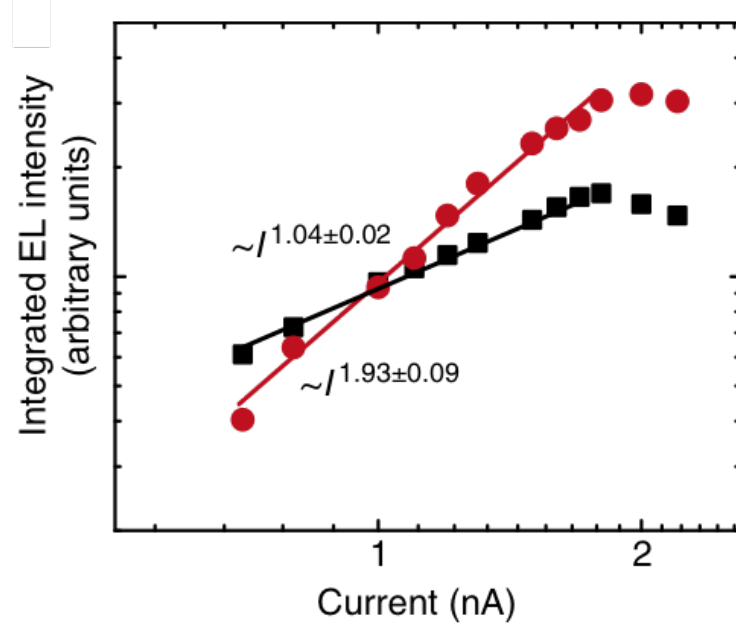


Figure 4.10: Variation of integrated intensity of peaks with injection current

4.5.2 Spectra From Green Emitting Single Nanowire LEDs

Electroluminescence measurements were performed under cw electrical excitation in the temperature range of 10 – 150 K in a continuous flow Helium cryostat. The μ -EL spectrum at 10 K shows two predominant sharp resonances around 2.39 eV. The integrated intensity of these transitions has a nearly linear and quadratic dependence on injection current, hence these resonances can be ascribed to the exciton and biexciton transitions, respectively. The strength of the exciton transition drops for injection currents beyond 10 nA due to competition from the biexciton state. The biexciton luminescence also saturates at the high injection currents, which suggests triexcitons and higher order excitons cannot be excited in these dots. μ -EL spectra for progressively higher device temperatures are shown in Fig. 4.11. The normalized integrated intensities of exciton and biexciton luminescence are plotted as Arrhenius

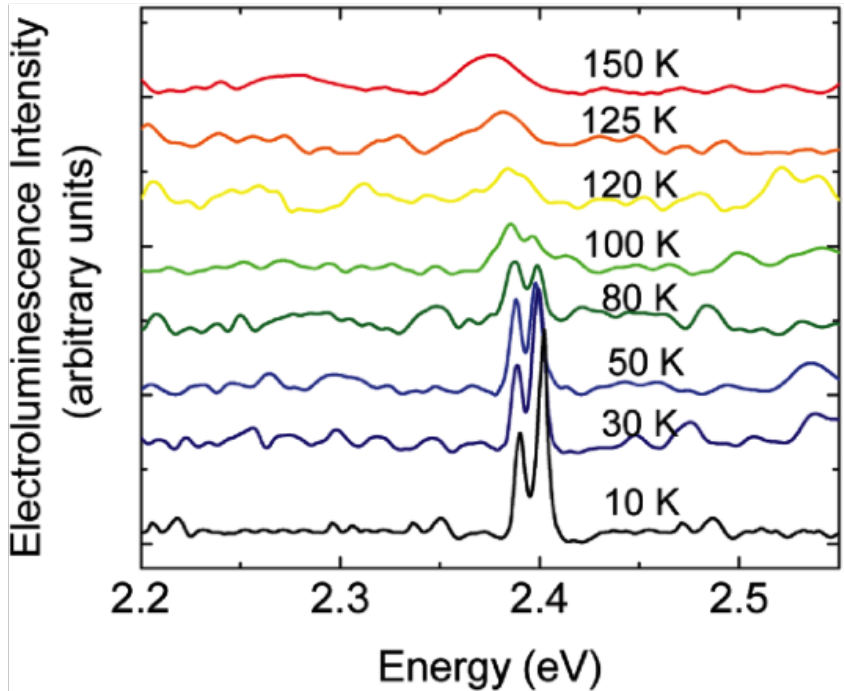


Figure 4.11: Temperature dependent electroluminescence from a single dot-in-nanowire in green spectral range

plots in Fig. 4.12. The plot show that the radiative efficiency of the exciton luminescence is almost 75% at 150 K which indicates that the dominant mode of carrier recombination up to this temperature is still through radiative channels. This has been confirmed through independent temperature dependent time resolved photoluminescence (TRPL) measurements where a reduction in the recombination lifetime due to dominant non-radiative recombinations is observed at high temperature. The biexciton EL quenches rapidly with temperature and shows a radiative efficiency of about 25% at 100 K, which is the highest temperature at which the biexciton luminescence can be distinguished. Since the exciton transition exhibits better temperature stability, we investigated it as a high temperature single photon emitter and studied its temperature dependent EL characteristics.

The variation of the exciton emission energy as a function of temperature is shown in Fig. 4.13. The emission energy follows the variation predicted by the Varshni

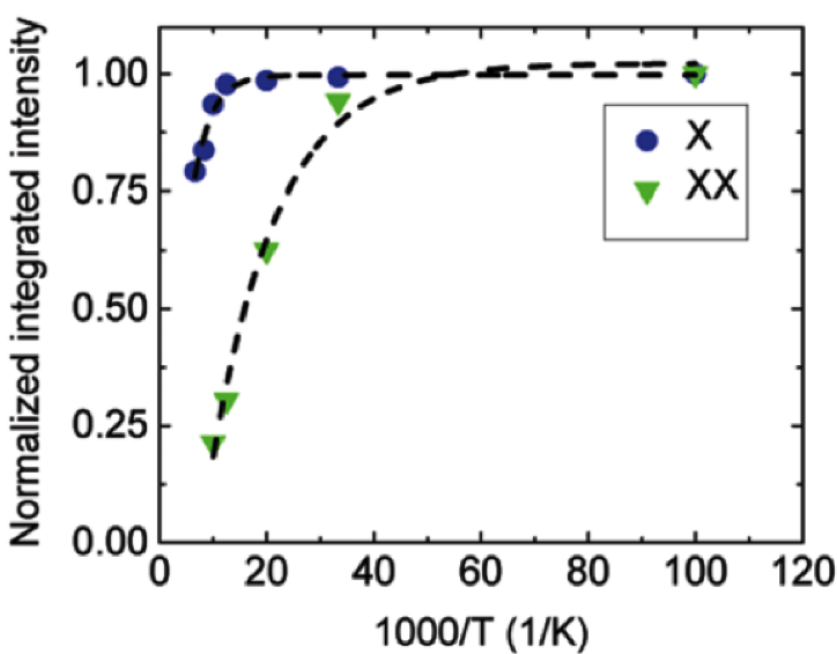


Figure 4.12: Arrhenius plot of exciton and biexciton electroluminescence from a single dot emitting in the green spectral range

equation with α and β values of 4.5×10^{-4} eV/K and 629 K, respectively. The absence of a S-shaped dependence, which is commonly observed in InGaN quantum wells, can be attributed to a reduced polarization field and the absence of local In clusters in the quantum dot.

The low temperature exciton emission linewidth is 2 meV. The variation of linewidth of the exciton with temperature is shown in Fig. 4.14. The linewidth increases due to phonon-broadening and is \sim 15 meV at 150 K. Beyond this temperature, quantum dot luminescence was not detectable.

4.6 Second-Order Correlation Measurement

The second-order correlation of the exciton and biexciton was measured under continuous electrical excitation using a Hanbury Brown and Twiss measurement system, as explained in Chapter 3. A continuous current is injected into the single nanowire device using a Keithley 6200 precision current source. For an ideal single-photon

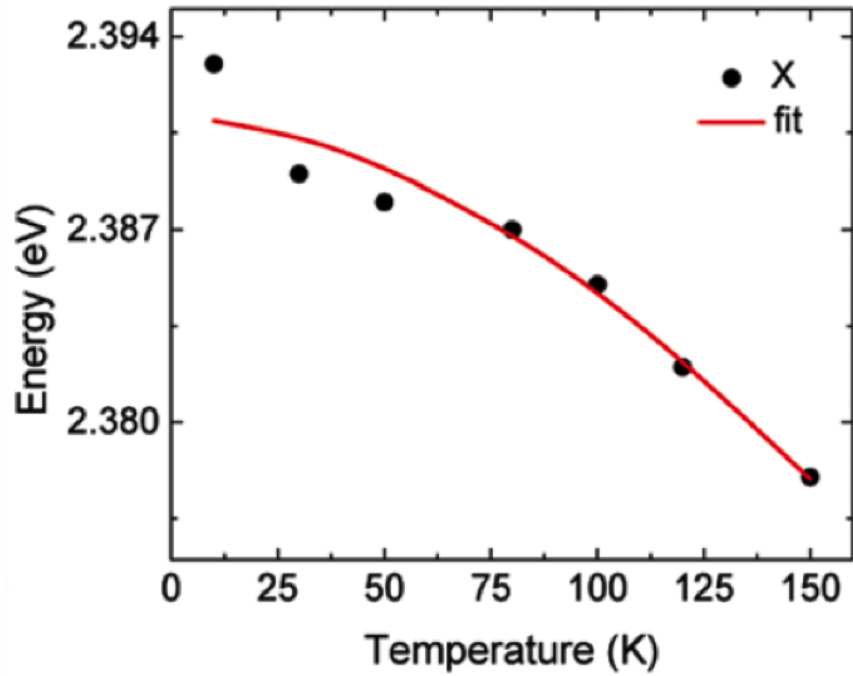


Figure 4.13: Energy position of the exciton transition from QD electroluminescence and Varshni fit to measured data

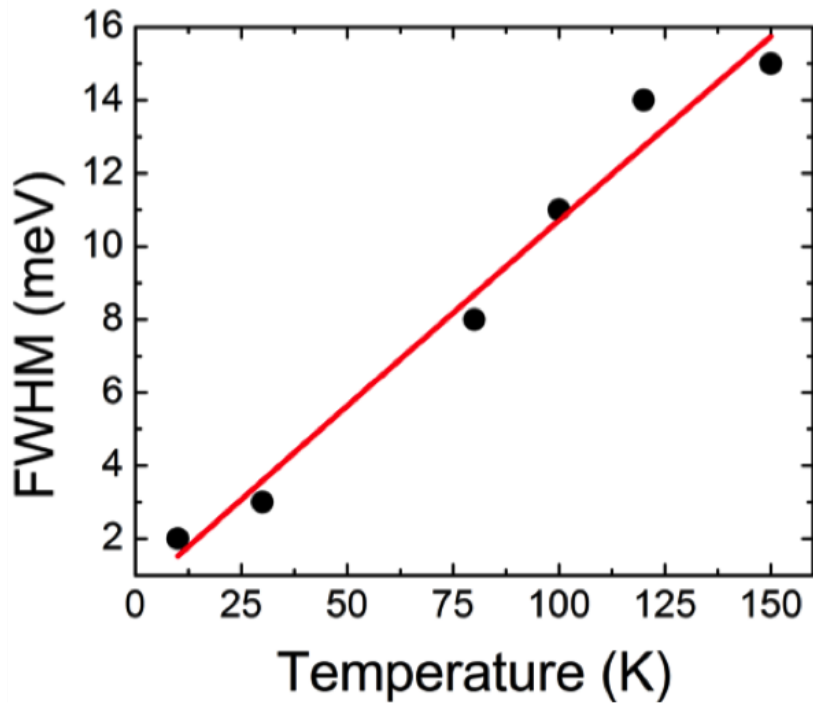


Figure 4.14: Linewidth of the exciton transition as a function of temperature

source, the second-order correlation function:

$$g^{(2)}(\tau) = \frac{\langle I(t)I(t+\tau) \rangle}{\langle I(t) \rangle \langle I(t+\tau) \rangle} \quad (4.1)$$

where τ is the time delay and $I(t)$ is the electroluminescence intensity at time t , should be equal to zero at zero time delay.

4.6.1 Blue Single-Photon Emission

Figures 4.15 (a) and (b) exhibit the second-order correlation measured for the exciton and biexciton resonances, respectively. The second-order correlation was measured under continuous excitation below saturation, at an injection current density of $142A/cm^2$ (1 nA). The comparatively large separation between exciton and biexciton lines and narrow emission linewidths at 10 K allow us to spectrally filter and study each transition as a single-photon emitter. The dip in the correlation spectrum at zero time delay indicates anti-bunching in both exciton and biexciton complexes. The correlation data was analyzed with the function:

$$g^{(2)}(\tau) = 1 - a \times \exp\left(\frac{-\tau}{b}\right) \quad (4.2)$$

where a and b are the $g^{(2)}(0)$ and recombination lifetime respectively. The solid lines represent the calculated values of $g^{(2)}(\tau)$. The value of $g^{(2)}(0)$ for the exciton transition is 0.3, which corresponds to a 3-fold decrease in unwanted multi-photon emission events compared to attenuated coherent light sources. The anti-bunching dip is shallower in case of the biexciton emission, where $g^{(2)}(0)$ equals 0.38.

Time resolved photoluminescence from the biexciton transition shows lifetime 0.7 ns at 10 K, which is in excellent agreement with the value obtained from the analysis (Fig. 4.16). The exciton and biexciton lifetimes derived from the analysis are 1.1 ns and 0.71 ns, respectively. The value of the exciton lifetime is nearly twice that of the

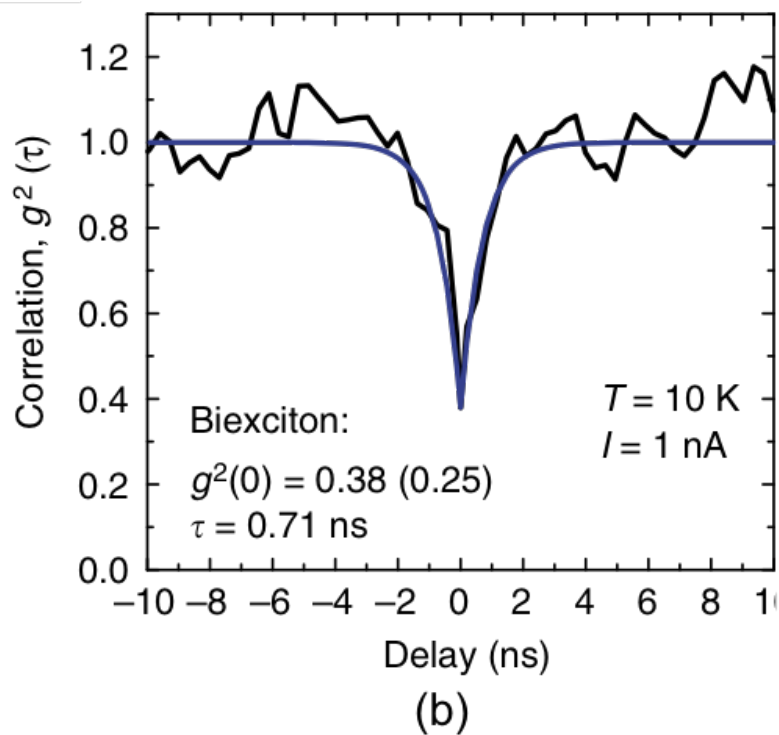
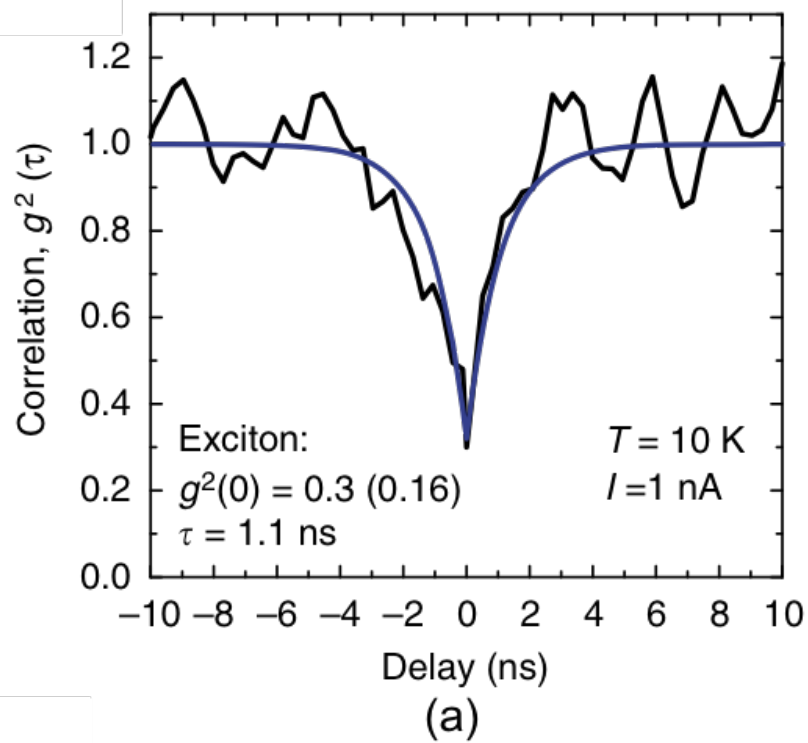


Figure 4.15: Second order correlation from (a) exciton and (b) biexciton electroluminescence from single dot-in-nanowire in the blue spectral range at 10 K

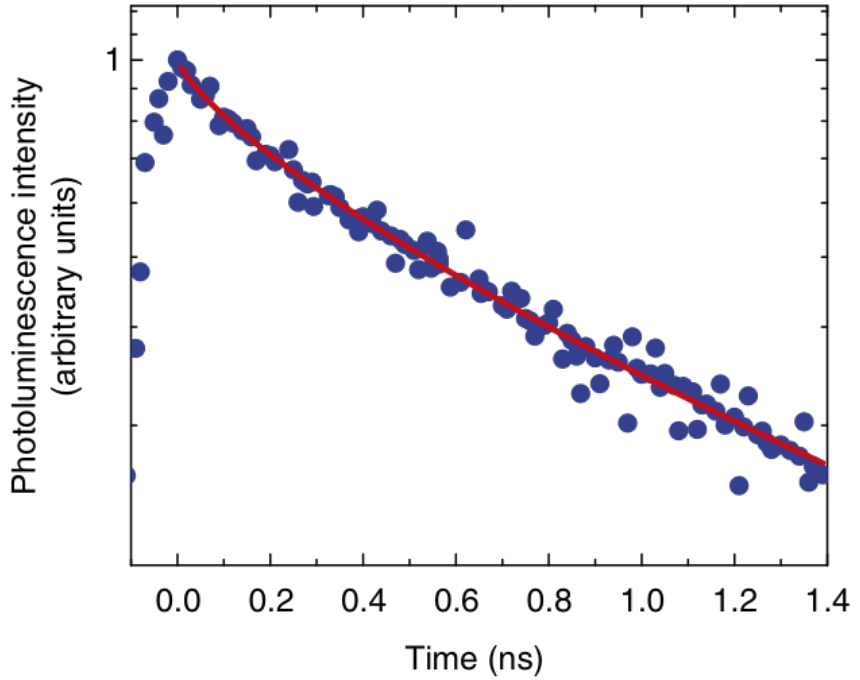


Figure 4.16: Time resolved PL from the biexciton transition

biexciton lifetime. This implies that the exciton emission follows that of biexciton, which is to be expected since the biexciton state first relaxes radiatively into the single exciton ($XX \rightarrow X + \text{photon}$) [90].

4.6.2 Green Single-Photon Emission

The second-order autocorrelation from the exciton luminescence at 10 K and 125 K are seen in Figs. 4.17 (a) and (b). The pronounced dip in the correlation signal with respect to the Poisson-normalized level verifies suppression of multiphoton emission events. The correlation data can be analyzed with equation (4.2) to derive a $g^{(2)}(0)$ and lifetime. For the exciton transition, at 10 K, the $g^{(2)}(0)$ equal to 0.25 and the recombination lifetime τ of 1.4 ns. The inset shows the transient decay of the exciton transition which was independently measured at 10 K by TRPL. The data can be analyzed with a stretched exponential model, which gives values of the stretching parameter: 0.90 and recombination lifetime: 1.1 ns. The latter is in good

agreement with the lifetime obtained from the analysis of second order correlation data. Assuming that all non-radiative recombination centers are frozen at 10 K, this lifetime approximates the radiative lifetime of exciton emission. The β value of 0.85 indicates the absence of significant clustering effects in the quantum dot.

At 150 K, the exciton linewidth broadens to 14 meV and merges with the biexciton transition, which causes a degradation in the $g^{(2)}(0)$ value to 0.42. The inset of Fig. 4.16 (b) shows a periodic stream of single photons recorded by a single photon detector. The start trigger to the counter was provided by the 80 MHz Ti:Sapphire laser and stop signal is received from the single QD electroluminescence. A single-photon emission event is recorded within 1 ns of each start trigger, which implies the single-photon source can be driven at frequencies in the GHz range.

4.6.3 Analysis

The finite value of the second-order correlation at zero time delay may be attributed to the finite time resolution of the measurement system and the background. The jitter associated with the photon counting avalanche photodiodes limits the time resolution of the HBT system. Since the InGaN dot recombination lifetime is short (1.1 ns for green and 700 ps for blue emitting dots) the linewidth of the correlation trace at zero delay becomes comparable to the jitter, causing broadening of the dip accompanied by a significant reduction of its amplitude.

To eliminate the effect of background counts, which could originate from stray light or merely dark counts, we apply a correction using equation 3.6 [28].

The $g^{(2)}(0)$ values derived after background correction for the blue exciton and biexciton emission are 0.16 and 0.25, respectively. The poor $g^{(2)}(0)$ value of the biexciton compared to the exciton may be due to the faster recovery of the biexciton owing to its shorter lifetime.

The $g^{(2)}(0)$ values derived after background correction for the green exciton emission

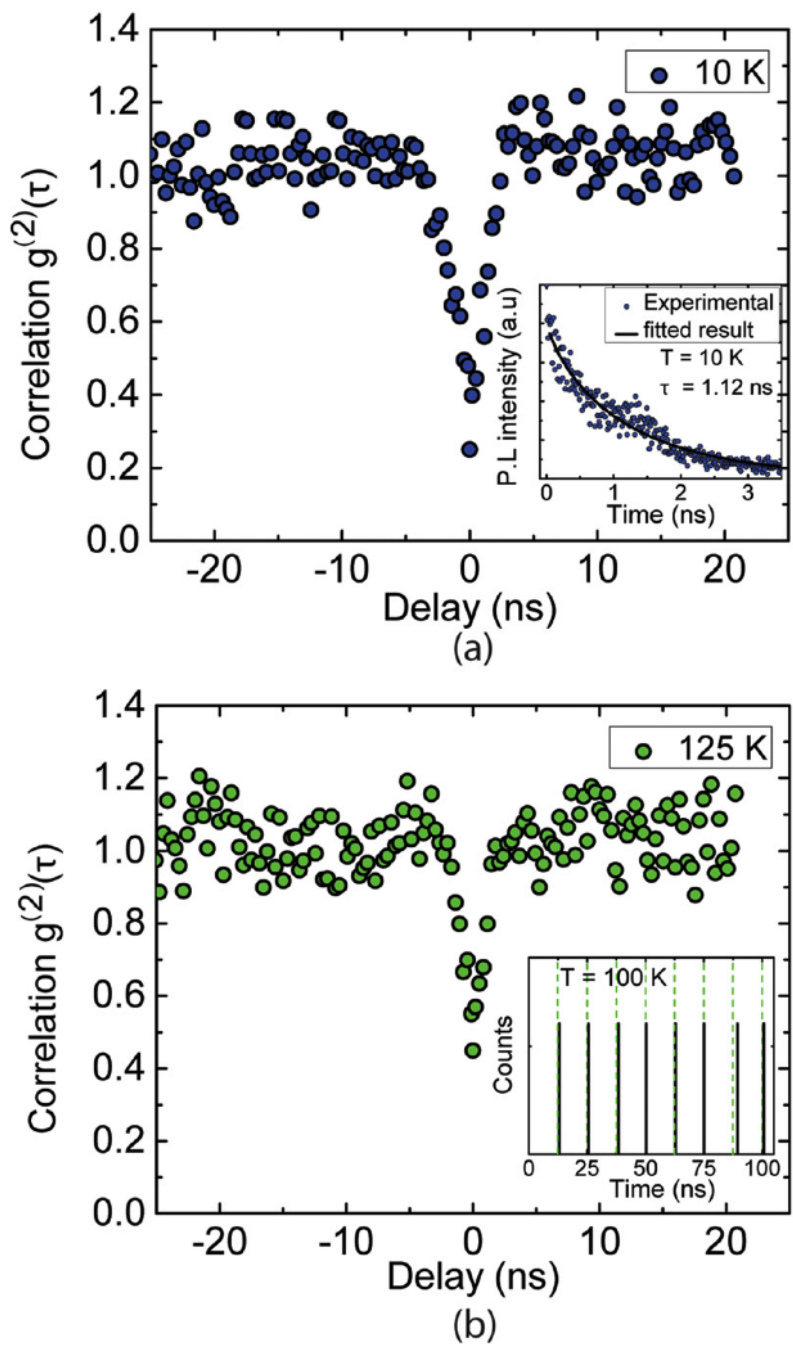


Figure 4.17: Second order correlation from exciton electroluminescence of single dot-in-nanowire emitting in green spectral range at 10 K and 125 K . Inset of figure (a) shows the transient decay of exciton PL. Inset of figure (b) shows a periodic stream of single photons recorded by a single photon detector

at 10 K and 125 K are 0.11 and 0.35, respectively.

4.7 Output Polarization

The polarization of the emitted single photons was also investigated by placing a linear polarizer in front of the monochromator. The measured intensity of the single dot biexciton emission as a function of the angle of the polarizer from the c axis of the nanowire is shown in the polar plot of Fig. 4.18. The solid line indicates the fit of the experimental data to the function:

$$I(\theta) = a + b \times \cos^2(\theta - \theta_0) \quad (4.3)$$

where a and $(a + b)$ are minimum and maximum values of the PL intensity, respectively, θ is the polarizer angle and θ_0 is the angle of polarization. The QD emission is linearly polarized with a degree of polarization,

$$\rho = \frac{I_{\parallel} - I_{\perp}}{I_{\parallel} + I_{\perp}} \quad (4.4)$$

of 70% along the c-axis of the nanowire, where $I_{\parallel}(I_{\perp})$ denotes the light intensity parallel (perpendicular) to the c-axis of the nanowire. Strong linear polarization along the nanowire is attributed to the large dielectric constant contrast between the nanowire and the surrounding air, attenuating the electric field amplitude in the direction perpendicular to the nanowire [91].

4.8 Junction Temperature

It is important to note at this point that because of Joule heating caused by the large series resistance of the nanowire diode, the real device (and hence the InGaN QD) temperature might be significantly larger than the ambient temperature of 10 K.

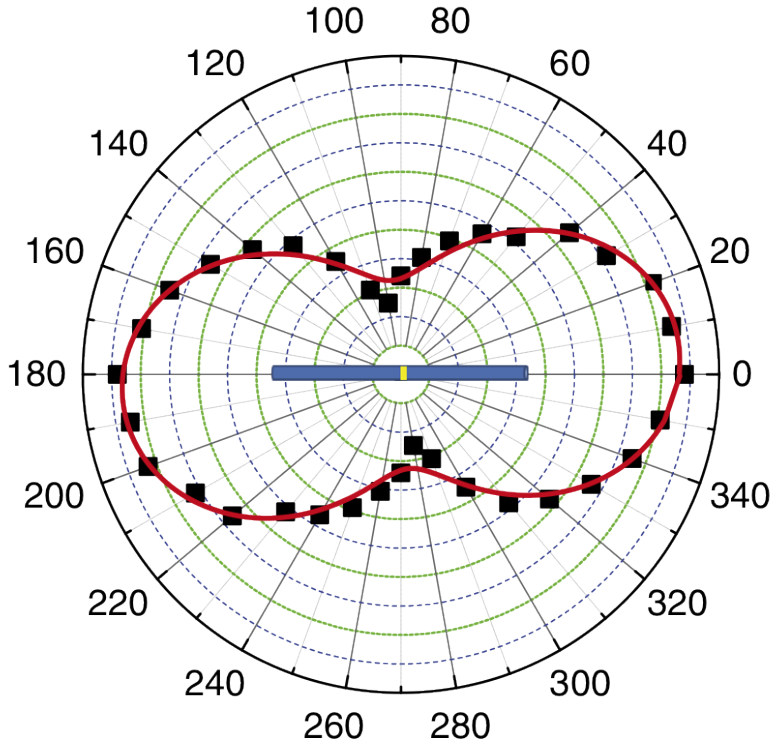


Figure 4.18: Polarization of electroluminescence from single dot-in-nanowire

We have performed a simulation of the heat-transfer problem by solving the Laplace equation using COMSOL Multiphysics software. The device is modelled as a uniform nanowire lying on 100 nm of thermal SiO_2 on the surface of a 500 μm silicon wafer, which is cooled to 10 K by the cold finger of the cryostat. The GaN region of the nanowire is the Joule heat source and the silicon wafer is effectively an infinite heat sink. The thermal oxide presents a thermal resistance between the nanowire and the heat sink. Heat loss due to convection may be ignored as the cryostat is evacuated before it is cooled down to 10 K. Radiation effects are also negligible as the temperature and area under consideration are small. Low temperature values of all material constants were considered.

Figure 4.19 shows the simulated nanowire temperature distribution at steady state at a current density of $283A/cm^2$. While the generated heat is effectively dissipated by silicon through SiO_2 , the finite heat conductivity of SiO_2 results in a steady-state

temperature as high as 60 K in the nanowire.

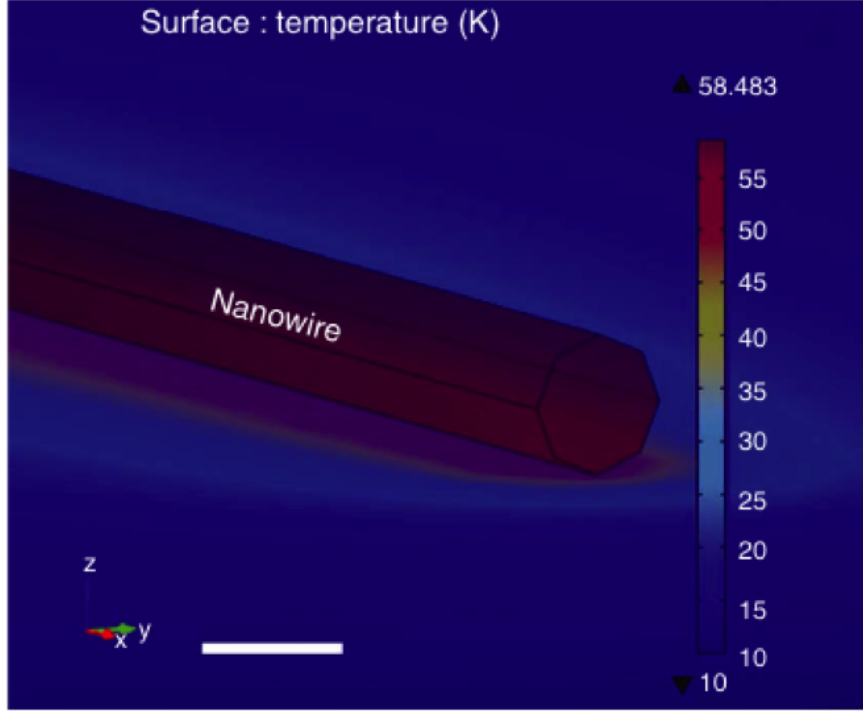


Figure 4.19: Steady state temperature profile of nanowire p-n junction

The junction temperature was similarly simulated for other injection currents at an ambient temperature of 10 K and the results are shown in Fig. 4.20. As the injection current increases, the calculated steady- state temperature increases quadratically as the heat generation is proportional to the square of the current. As shown in the transient profile in the inset of Fig. 4.20, the temperature of the device reaches steady state within 30 ns. Hence, in electroluminescence measurements, any transient temperature effect can be ignored and the injected currents determine the device temperature. In Fig. 4.21, we plot the ideal variation of the InGaN emission peak with current density, calculated from Varshni coefficients that were previously derived and with temperatures that were estimated from injection current density (Fig. 4.20). We may assume that in the temperature range of 10-60 K, the exciton binding energy does not change significantly, and the variation of InGaN bandgap is the dominant contributor to the emission peak energy over this temperature range.

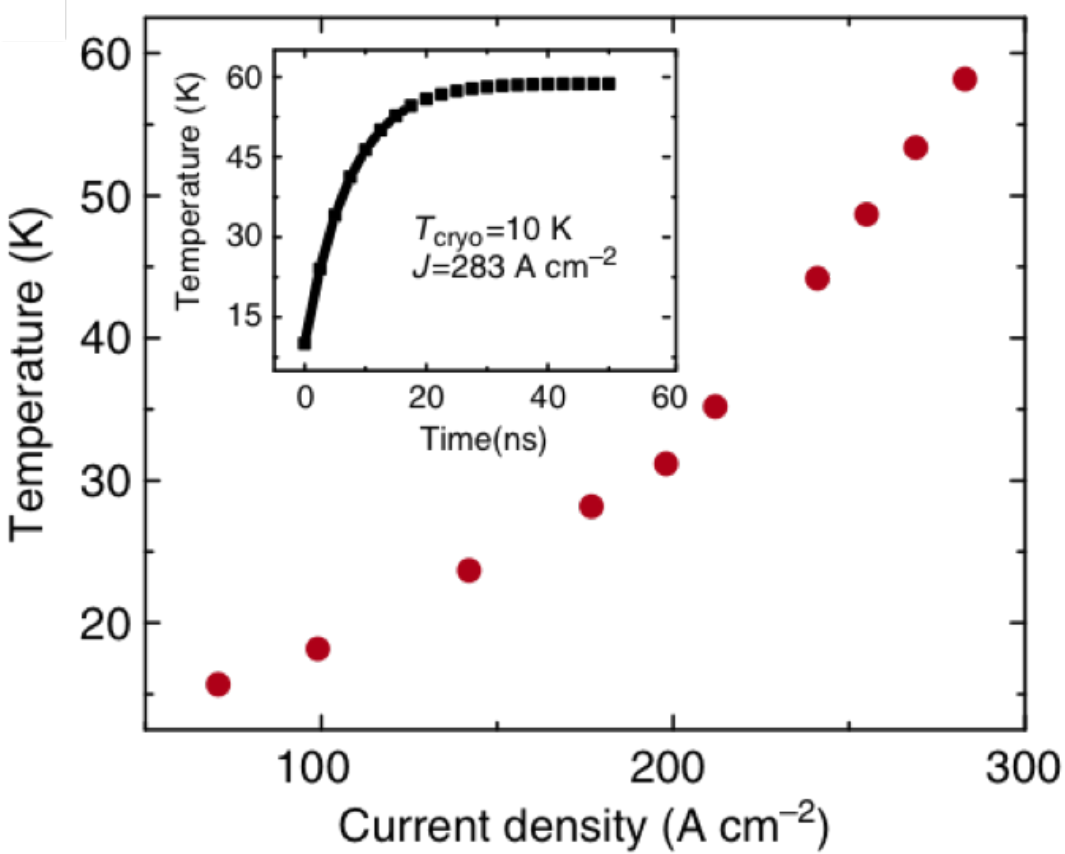


Figure 4.20: Estimated device temperature as a function of injection current density.
Inset shows temporal variation of device temperature.

Also plotted in Fig. 4.21 is the measured variation of the EL excitonic peak energy with injected current density. Within the limits of experimental error the two curves follow each other very closely; the measured energy shift is marginally smaller than the theoretically predicted value. This suggests that there is no significant blue shift of the emission with injection, which is important in the context of single-photon emission.

It should be noted that the red shift in the QD emission due to increase of temperature associated with Joule heating is smaller than the value theoretically predicted by the Varshni equation. We attribute this difference to a small blue shift (less than 2meV) that is likely to arise from the screening of the very small polarization field with excitation. As a consequence of the two competing effects, we observe that

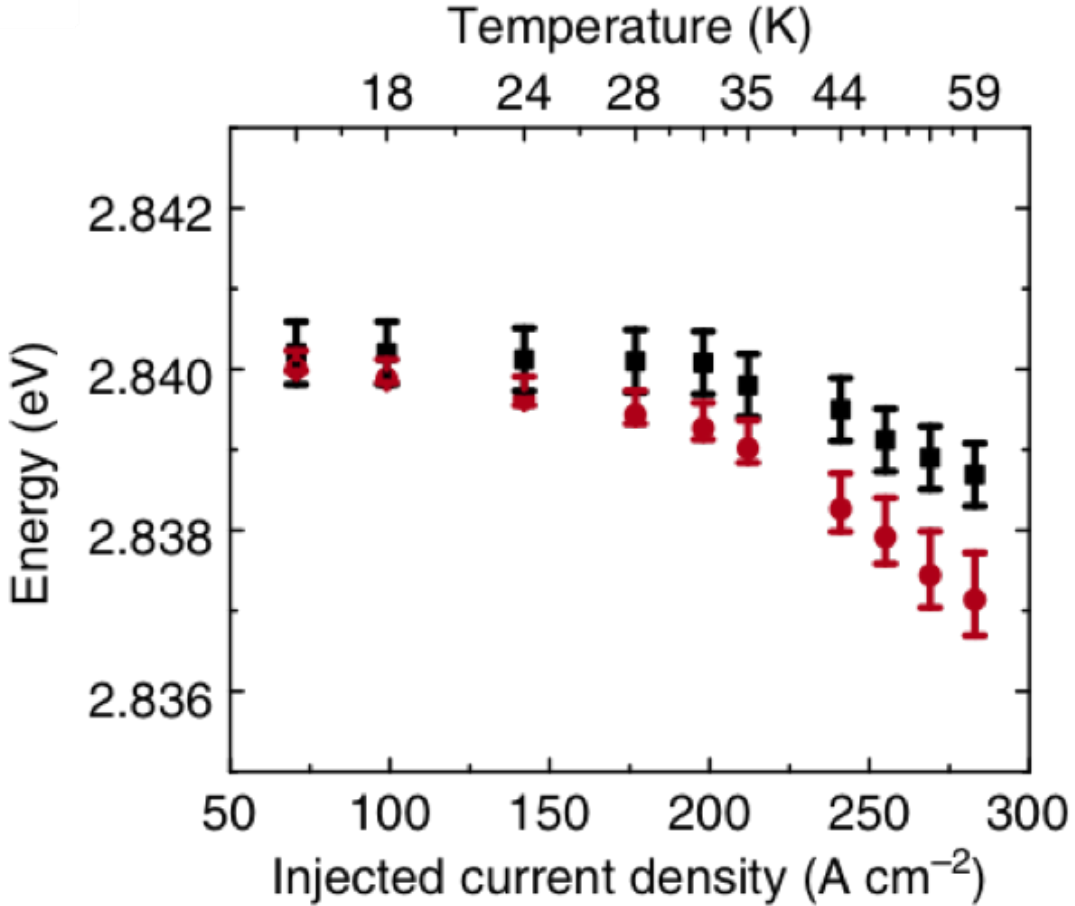


Figure 4.21: Calculated and measured emission energy shift as a function of the injected current density (calculated: red dots, measured: black squares)

the excitonic emission remains almost invariant with injection. Typically, nitride-based quantum wells and self-organized QDs show blue shifts of the order of tens of meVs due to screening of the piezoelectric field and band filling of localized states [92, 93]. The negligibly small blue shift in our device indicates that both these effects are greatly suppressed due to the dot-in-nanowire geometry. Pseudomorphic strain in InGaN/GaN and GaN/AlGaN nanowires has been known to relax efficiently at the sidewalls during growth [94]. Consequently, the piezoelectric field in such dot-in-nanowire heterostructures is significantly lower than that in quantum wells or self-organized QDs. Additionally, band filling effects induced by compositional inho-

mogeneities and alloy disorders, which lead to excitation dependent energy shifts, are also absent in this device.

At 10 K, the biexciton decay time is 0.71 ns. The biexciton lifetime derived from analysis of the second-order correlation data is also 0.7 ns. The second-order correlation was measured at an injection current injection of 1 nA, for which we estimate the actual device temperature to be 25 K due to Joule heating. The close agreement between the two lifetime values indicates that the electrically injected carriers do not encounter recombination through non-radiative channels and both lifetime values correspond almost exclusively to radiative recombination. From temperature-dependent lifetime measurements performed on similar dot-in-nanowire ensemble samples, we have observed that the radiative lifetime is nearly constant with temperature. Hence, it can be assumed that the biexciton decay rate in our single dot device would be 0.7 ns at higher temperatures too. The relatively small radiative decay time is a remarkable advantage of the dot-in-nanowire geometry as it potentially allows for large repetition rates in single-photon emitters.

Finally, the nanowires were grown on (111) Si and the single nanowire junction devices were fabricated on (001) Si, which make the single-photon sources reported here very attractive from the standpoint of compatibility and integration with silicon technology.

4.9 Summary

GaN based single dot-in-nanowire light emitting diodes, containing an InGaN active region were fabricated. The single nanowire diode resistance was reduced to $25M\Omega$ through optimization of the p-contact metallurgy. The electroluminescence from the nanowire LED shows sharp excitonic lines in the blue-green spectral range. The exciton line in the green emitting device is observable up to 150 K. Second-order correlation performed on the filtered exciton emission shows anti-bunching with

$g^{(2)}(0)=0.42$ at 125 K. The emission is polarized along the c-axis of the nanowires with a degree of linear polarization $\sim 70\%$. The actual temperature of the device and quantum dot is estimated to be higher due to the Joule heating in the high resistance diode.

The following chapter will discuss a room temperature single-photon source using a self-organized quantum dot to overcome these limitations.

CHAPTER V

Electrically Driven Single-Photon Emission At Room Temperature

5.1 Introduction

The earliest demonstrations of electrically driven single-photon emission used Coulomb blockade in a mesoscopic junction but these devices operated at milli-kelvin temperatures and generated a very low photon count. In contrast, electrical excitation of single quantum dots (QDs) in the active region of a semiconductor p-n junction is a robust scheme to achieve single-photon emission, and has been successfully demonstrated in III-V and II-VI QDs [33–37, 39, 95–98].

However, with the exception of nitrogen vacancy (NV)-based diamond p-i-n diodes, all other reported electrically pumped devices operated only around cryogenic temperatures. While the NV based diamond diode was grown on high quality p-doped diamond, it would be desirable to generate single photons from a single quantum dot grown on more readily available substrates [32]. Additionally, integration with microcavities or implementation of other photonic engineering schemes would be more feasible in a semiconductor QD system. Also, unlike NV centers, quantum dots are more suitable for generation of entangled photon pairs by exploiting the exciton-biexciton cascade.

Single-photon emission from an InGaN/GaN disk-in-nanowire was investigated in Chapter 4. However, the highest temperature up to which single dot electroluminescence was observed was 125 K [61]. For practical applications, a single-photon source operating at or near room temperature would be desirable. Other heterostructures were investigated for high temperature single-photon emission.

A single GaN/AlGaN quantum dot-nanowire diode was fabricated as a potential high-temperature emitter. GaN quantum dots have the advantage of lower linewidths than tertiary InGaN alloys due to the lack of inhomogeneous broadening. Additionally, the Al composition in the AlGaN can be adjusted to vary the band offset in the quantum dot and provide adequate confinement for high temperature operation. Other groups have demonstrated optically triggered single-photon sources up to 200 K using GaN quantum dots. However, the heterostructure was not suitable from the viewpoint of an electrically injected device. Current-voltage characteristics of a single $Al_{0.35}Ga_{0.65}N$ nanowire with a GaN disk shows highly resistive behavior (Fig. 5.1). P-doping of AlGaN alloys is challenging due to the large activation energy of Mg, which increases with bandgap. As a result, the hole doping and mobility is poor and the diode shows poor electrical characteristics with a large turn on voltage (10 V) and series resistance. The electroluminescence from such a diode, measured at 10 K under an applied bias of 15 V is seen in Fig. 5.2. The spectrum shows a broad spectrum due to recombination from the acceptor level.

The InGaN/GaN self-organized quantum-dot (QD) has emerged as a promising nanostructure for photonics and lighting. Visible lasers with QD gain media have demonstrated superior performance in terms of threshold current density, speed, and temperature stability compared to InGaN/GaN quantum well devices [99, 100]. Epitaxially grown InGaN/GaN QDs are formed by strain-relaxation, which leads to a small piezoelectric field [101] and short radiative lifetimes [102, 103]. Additionally, strong three-dimensional confinement of carriers in the dots makes them less vulnera-

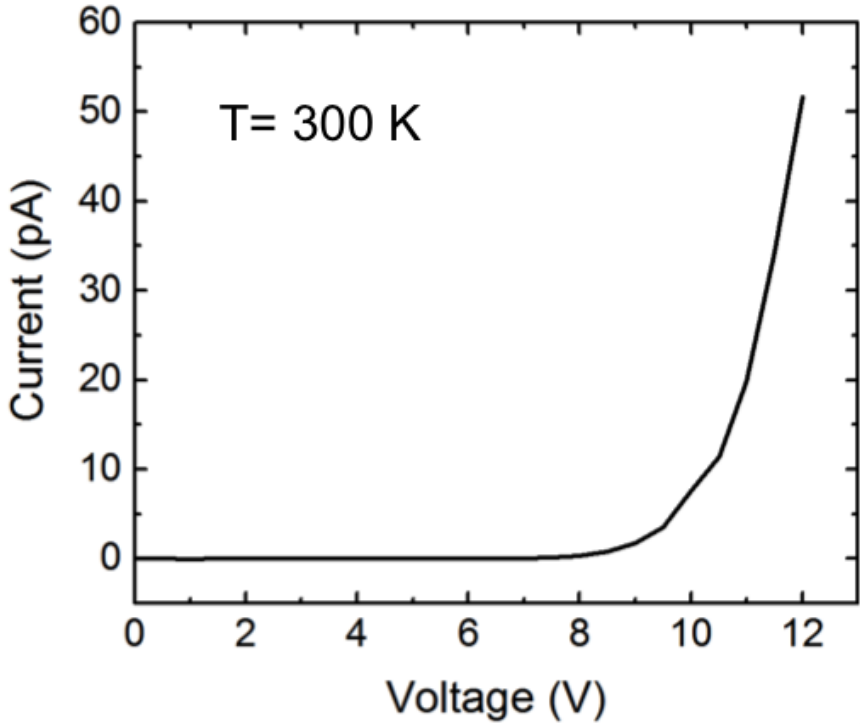


Figure 5.1: Electrical characteristics of a single GaN/AlGaN disk-in-nanowire diode at room temperature.

ble to non-radiative recombination at defect centers [104]. Another advantage of the nitrides is their large exciton binding energy, which allows the exciton to remain stable up to room temperature [105]. This has enabled the realization of GaN-based room temperature exciton-polariton lasers [106, 107] and an optically pumped single-photon source [45]. The exciton binding energy in QDs further increases with confinement and can be significantly larger than room temperature thermal energy ($k_B T$) [108].

Here we report, room temperature operation of an electrically driven single-photon emitter based on a single $In_{0.4}Ga_{0.6}N/GaN$ QD integrated with a simple, monolithically grown semiconductor light-emitting diode structure. The electroluminescence from the diode exhibits excitonic transitions from individual dots up to room temperature, which follow sub-poissonian photon statistics with a $g^{(2)}(0) \sim 0.29$.

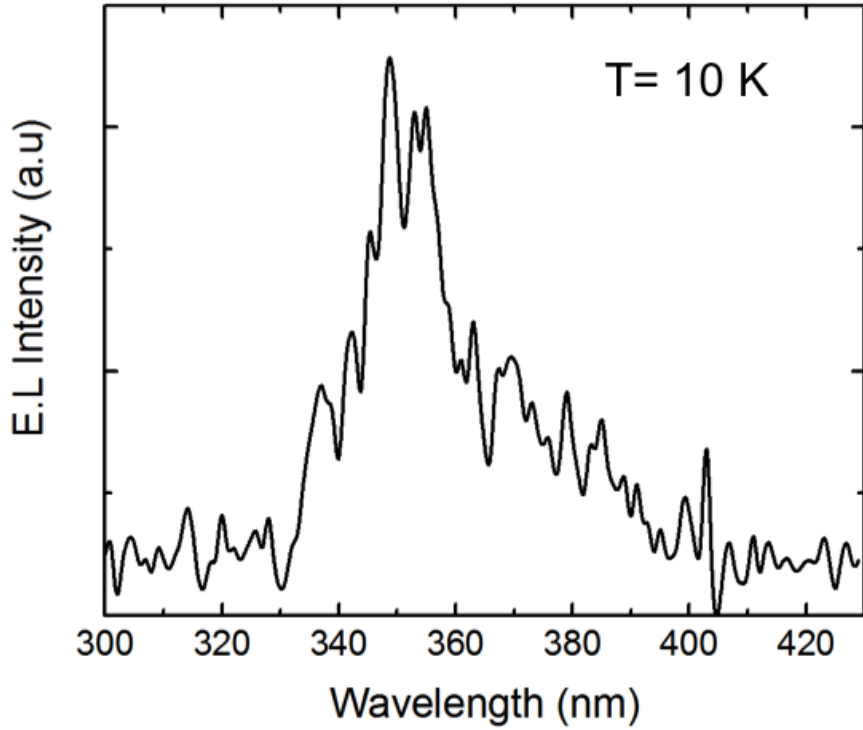


Figure 5.2: Electroluminescence from a single GaN/AlGaN disk-in-nanowire diode at 10 K.

5.2 Growth And Characterization

The device heterostructure (Fig. 5.3) comprising of a GaN p-i-n diode with a single layer of self-organized InGaN QDs inserted in the intrinsic region, was grown by PA-MBE on the Veeco Gen-930 on GaN-on-sapphire templates.

5.2.1 MBE Growth Of Quantum Dot Diode

The heterostructures were grown on bulk c-plane GaN-on-sapphire substrates (grown by HVPE). The substrates were first cleaned using standard solvents, and then thermally degassed at 200°C/60 min followed by 450°C/60 min in the MBE chambers to reduce surface contamination. After cleaning, a 400 nm thick n-doped ($n \sim 3 \times 10^{18} cm^{-3}$) GaN buffer layer was grown at 740°C at a flux of 4.5 nm/min. The growth was performed under metal rich conditions with periodic (every 10 minute) growth interruptions to prevent metal build up on the surface. The pyrometer tem-

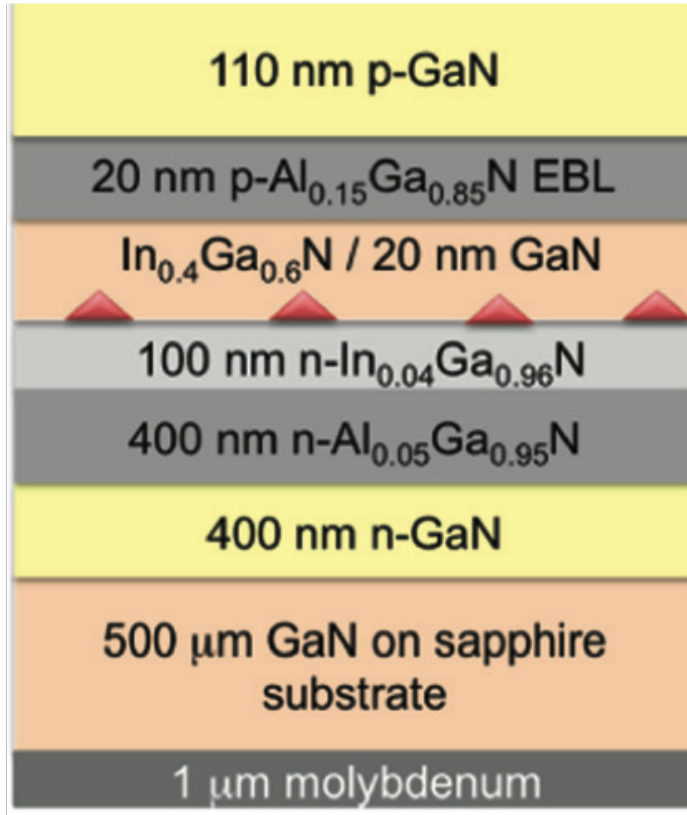


Figure 5.3: Schematic of the quantum dot diode heterostructure.

perature was calibrated using the (1×1) to (7×7) RHEED transition in the surface reconstruction in silicon. Following the growth of the buffer layer, 400 nm of $n - Al_{0.07}Ga_{0.93}N$ was grown at 740°C and 100 nm $In_{0.04}Ga_{0.96}N$ layer was grown at 690°C . These layers (GaN, AlGaN and InGaN) were doped at a concentration of $\sim 5 \times 10^{18} \text{ cm}^{-3}$ with the addition of Si dopant species. The n-doped layers show a smooth surface morphology as seen in the AFM in Fig.5.4. The $In_{0.4}Ga_{0.6}N$ quantum dots/GaN barrier layer, emitting at $\lambda = 630\text{nm}$ were grown at a substrate temperature of 520°C under nitrogen rich conditions at equivalent pressures of $\Phi_{Ga}/\Phi_{In} \sim 2 : 1$ and at a growth rate of 0.5\AA/s . Formation of the quantum dots follows the growth of a 2 nm wetting layer, as evidenced from the RHEED pattern. After the growth of the dots, a 20 nm thick $p - Al_{0.15}Ga_{0.85}N$ electron blocking layer was grown at 750°C with a doping concentration of $p \sim 6 \times 10^{17} \text{ cm}^{-3}$. Finally, a 110 nm

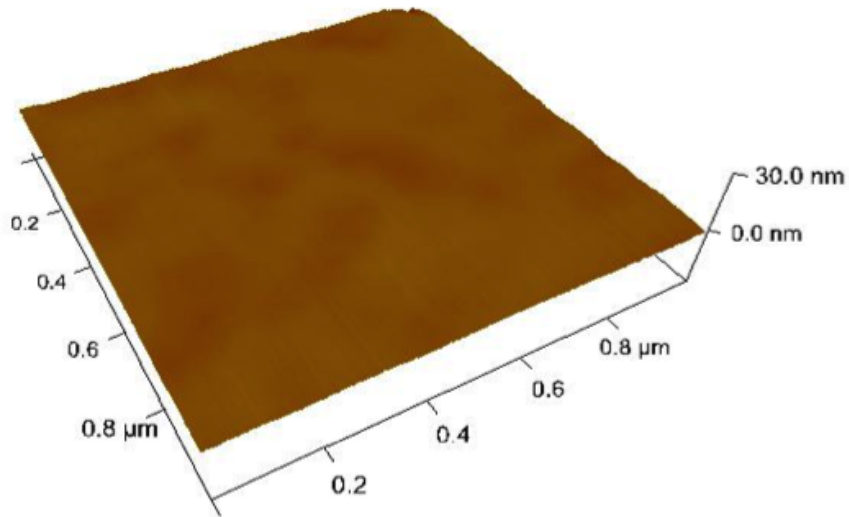


Figure 5.4: AFM of n-doped layers shows smooth surface morphology.

thick Mg-doped GaN layer was grown($p \sim 7 \times 10^{17} cm^{-3}$) as the uppermost layer for injections of holes.

5.2.2 AFM Characterization Of QD Layer

Under nitrogen rich conditions and at a low substrate temperature, which is employed to facilitate In incorporation, the QD growth follows a kinetic growth model. Atomic force microscopy (AFM) was performed on an identical sample grown up to the QD layer using a Veeco Dimension Icon AFM in tapping mode with Bruker TESPA tips. Analysis of this AFM data shows that the size distribution of the grown QDs follows a scaling distribution given by:

$$f_i(u) = c_i u e^{-ia_i u^{1/a_i}} \quad (5.1)$$

where c_i and a_i are constants which satisfy the sum rules for $f_i(u)$, i is defined as one less than the critical dot cluster size, and u is the normalized size. As seen in Fig.

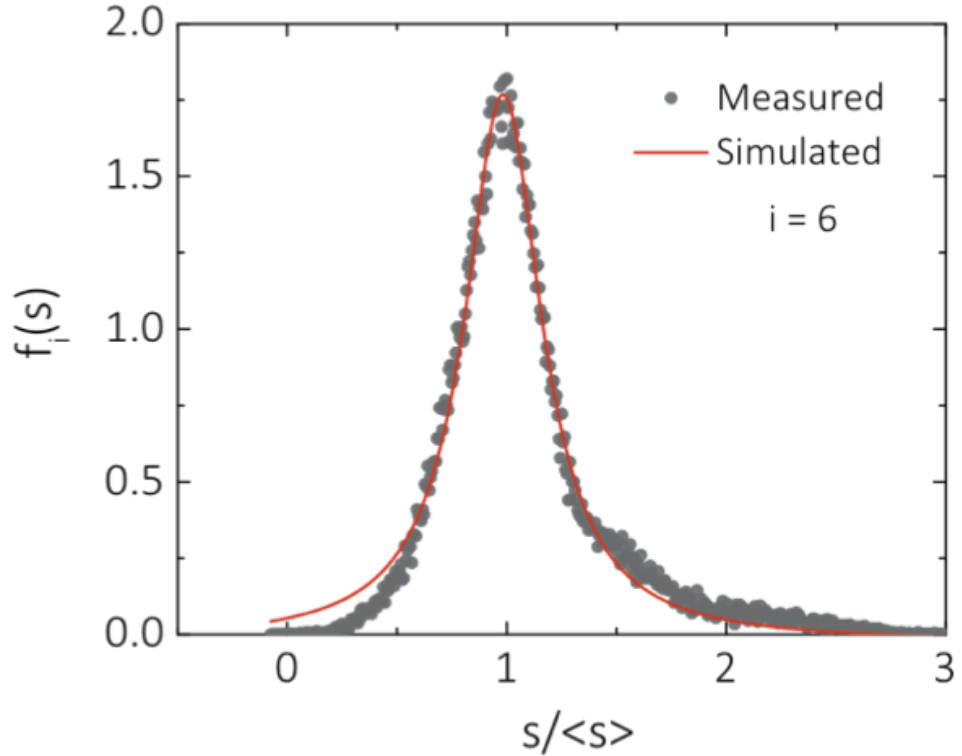


Figure 5.5: Quantum dot heights follow scaling distribution. Plot of scaling function versus normalized dot height.

5.5, QD heights fit well with the scaling function, with an average height of $\langle s \rangle \sim 3$ nm and a critical island size of 7 atoms, confirming the kinetically driven epitaxial growth of InGaN/GaN QDs.

Growth parameters were controlled to obtain a low QD density of 2×10^9 dots/ cm^2 , measured by AFM imaging. The base width of QD varies between 15-20 nm (Fig. 5.6), which is much smaller than conventional Stranski-Krastanov (SK) InGaN/GaN dots.

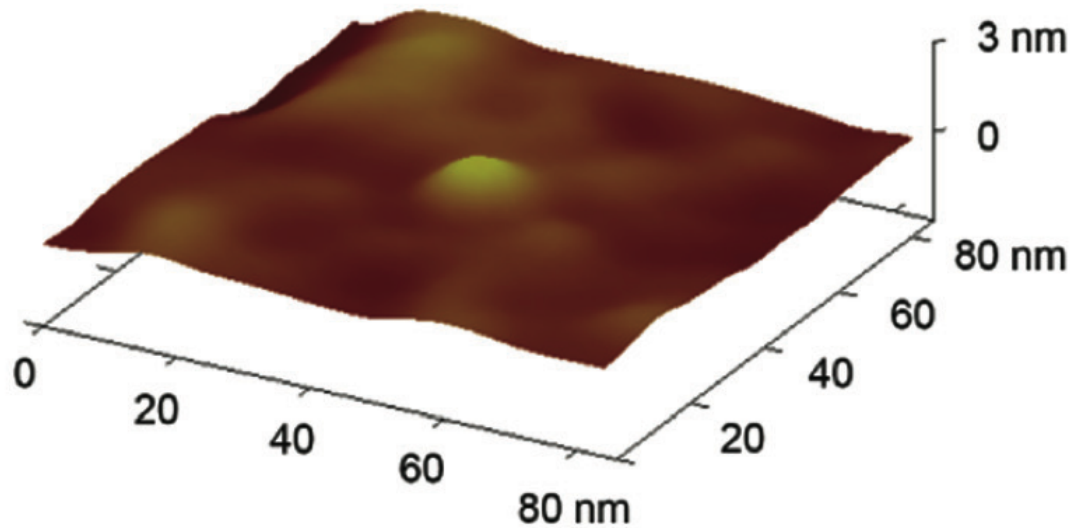


Figure 5.6: Atomic force micrograph of a single InGaN dot

5.2.3 XRD Characterization Of Heterostructure

The X-ray diffraction (XRD) spectrum of the complete heterostructure is shown in Fig.5.7 and it exhibits peaks corresponding to all layers.

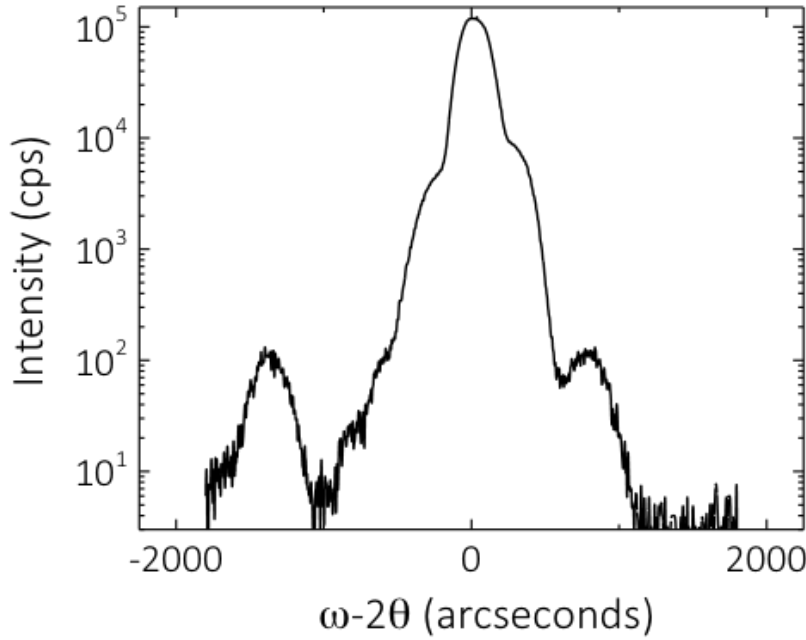


Figure 5.7: XRD spectrum of the complete heterostructure.

5.2.4 Analysis Of In Composition Using STEM-EDX

Transmission electron microscopy (TEM) measurements were performed on identical structures grown on GaN substrates for ease of sample preparation. Two pieces of the QD heterostructures were bonded together with M-Bond 600 to protect the QD surface and the specimen was mechanically thinned to $50 \mu\text{m}$ by polishing with diamond coated lapping films. The sample was fixed onto a Moly TEM ring using M-Bond and further polished to $\sim 500 \text{ nm}$ in a Gatan Precision Ion Polishing System. The cross-sectional QD heterostructure was imaged using a JEOL 2100F aberration corrected high resolution scanning TEM. Figure 5.8 shows a cross-sectional high-

resolution transmission electron micrograph (HRTEM) of a single QD. The InGaN QD shows good crystalline quality. The existence of a 2 nm thick wetting layer is also evident by TEM imaging. Fig. 5.9 shows a EDX line-scan performed along the c-axis of the QD cross-section. Energy dispersive x-ray spectroscopy (EDX) and X-Ray diffraction were used to measure an indium composition of $\sim 40\%$ in the InGaN QDs.

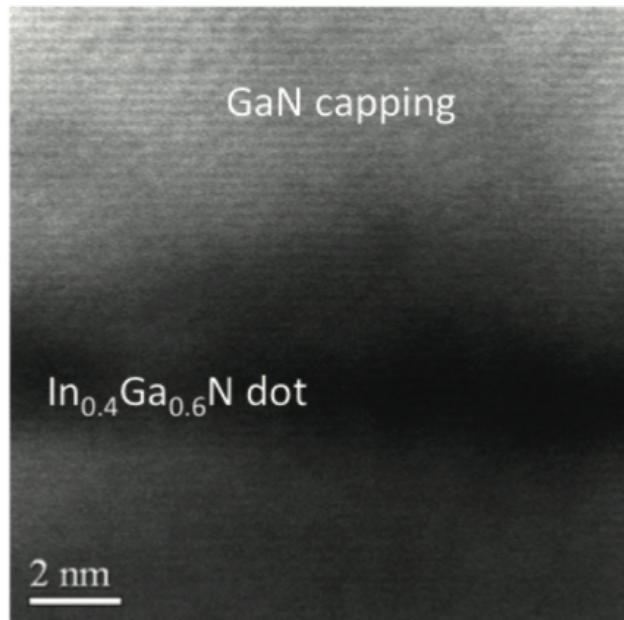


Figure 5.8: Transmission electron micrograph of a cross-section of single InGaN dot

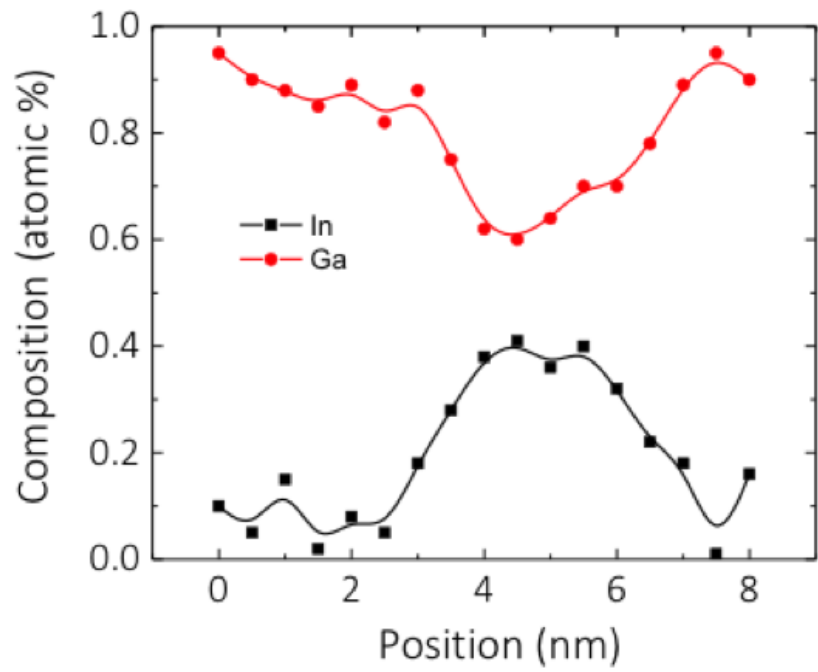


Figure 5.9: Elemental composition across the cross-section of single InGaN dot measured in an EDX spectrum.

5.2.5 Photoluminescence From Ensemble Of QDs

Photoluminescence (PL) from the ensemble of QDs measured at room temperature under saturation excitation, shows a peak at 630 nm (Fig. 5.10). The spectra show Fabry-Perot resonances arising due to difference in the refractive indices of sapphire ($n=1.77$), GaN ($n=2.39$) and air ($n=1$). The ratio of the integrated PL intensities at room temperature and low temperature is 42%, which is a measure of the IQE of the QD sample. In addition to the QD emission peak, a high-energy shoulder with a lower intensity is also observed in the spectra. This may be attributed to emission from the two-dimensional wetting layer. The low energy QD peak has a Gaussian profile indicative of inhomogeneously broadened InGaN emission, while the wetting layer emission can be fit to a Lorentizan lineshape.

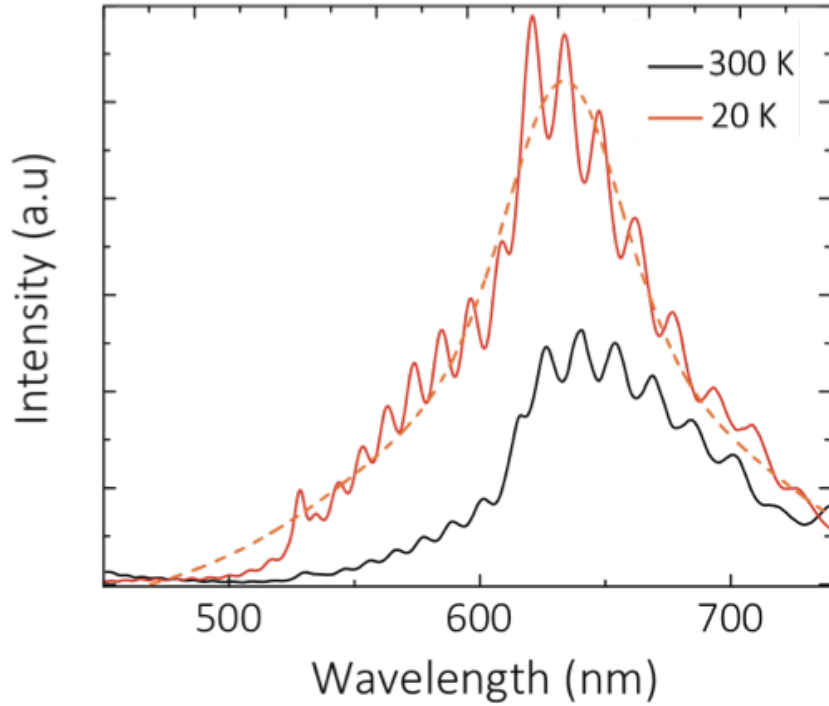


Figure 5.10: Photoluminescence measured under non-resonant saturation excitation, from an ensemble of quantum dots at low temperature and room temperature.

5.3 Single Quantum Dot LEDs

Standard fabrication techniques are used to fabricate a high speed light emitting diode (LED). An opaque metal mask containing a periodic array of nanoscale apertures ($\sim 200\text{nm}$ in diameter, $10\mu\text{m}$ spacing) is photolithographically defined on top to collect luminescence from a single QD. Reactive ion etching with $\text{Cl}_2/\text{BCl}_3/\text{Ar}$ was used to create the mesa. Due to the relatively sparse density of quantum dots, about 10% of all apertures show quantum dot emission. Ohmic contacts were formed to the n- and p-type regions using Ti/Au and Ni/Au contacts, respectively.

Figure 5.11 shows the room temperature current-voltage (I-V) curve and an optical micrograph of the fabricated p-i-n diode in the inset. The diode shows nearly ideal I-V characteristics, with a turn on voltage around 3.5 V and a very low series resistance of $10\ \Omega$. High-speed ground-source-ground (G-S-G) probes are used to bias the device.

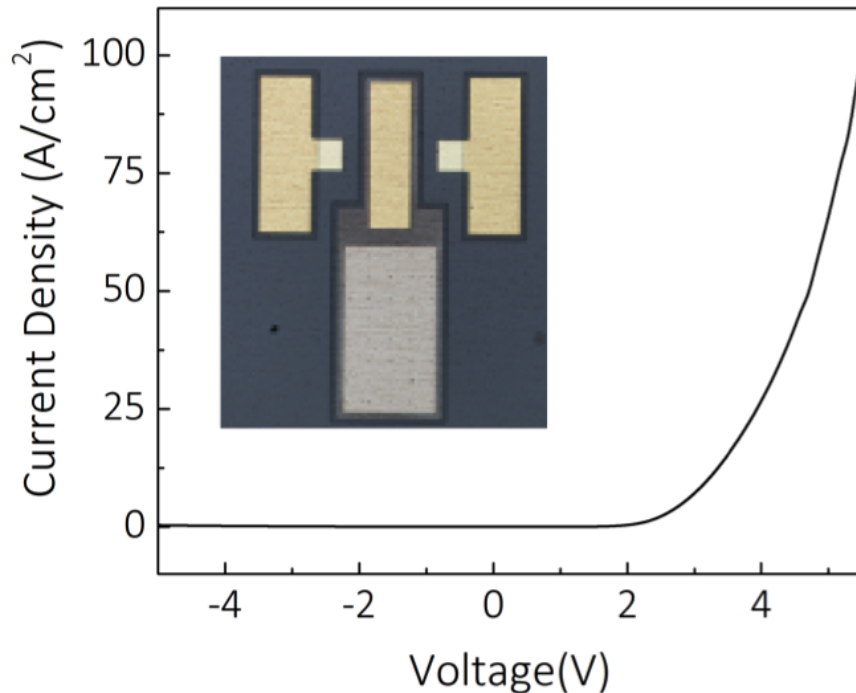


Figure 5.11: Current voltage characteristics of a single quantum dot diode at room temperature. Inset shows an optical micrograph of a fabricated device with a GSG probing geometry.

5.3.1 Electroluminescence From A Single Aperture At Low Temperature

To observe the single QD electroluminescence (EL) at low temperature, the sample was first wirebonded and mounted in a continuous flow He cryostat. Luminescence collected by an infinity-corrected objective lens ($\times 100$, NA: 0.55) in the normal direction was analyzed with a high-resolution monochromator with a spectral resolution of 0.03 nm and detected with a photomultiplier tube using phase-sensitive lock-in amplification. A pin-hole was used to spatially resolve a single aperture. The μ -EL spectra from a single aperture show several sharp peaks with linewidths ~ 6 meV at 20 K (Fig. 5.12). Peaks labeled 1 and 2, at 2.1 eV and 2.13 eV, are assigned to the exciton and biexciton transition, respectively, based on the rate of increase of their integrated emission intensities with injection. The relatively large biexciton binding of ~ 35 meV probably originates from the small lateral size of the QD [43]. A low-intensity third peak 3, at a separation of ~ 80 meV from the exciton peak, shows a super-linear increase with injection current. At this point, it is unclear if this peak is a charged state of the exciton or a phonon replica of the exciton emission.

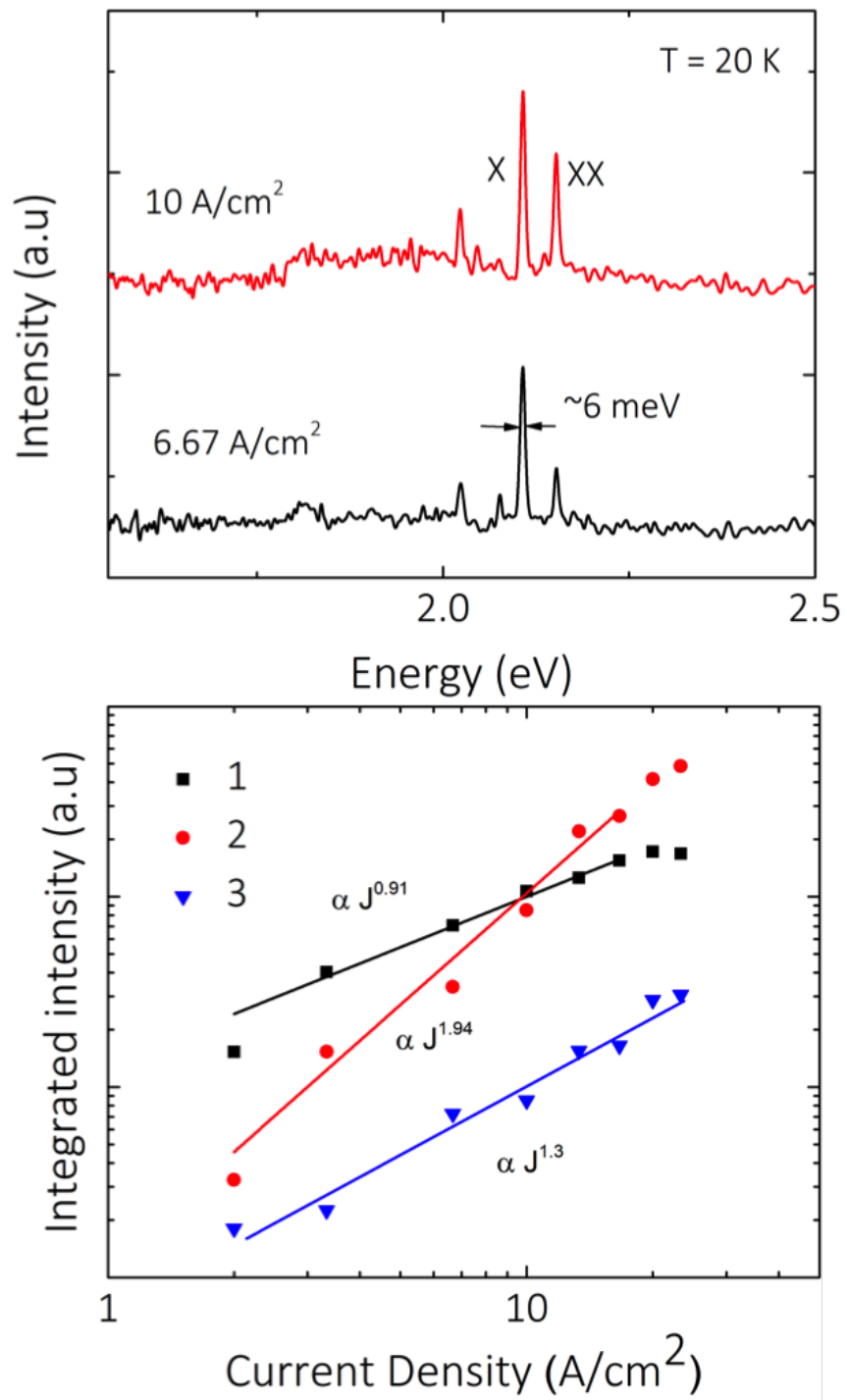


Figure 5.12: Electroluminescence from a single aperture at 20 K and variation of integrated intensities of peaks with injection.

5.3.2 Electroluminescence From A Single Aperture At Room Temperature

At room temperature, the electroluminescence linewidth broadens to ~ 22 meV due to phonon-interaction and the emission energy shifts to 2.0 eV due to bandgap shrinkage of $In_{0.4}Ga_{0.6}N$ (Fig. 5.13). The intensity of the main peak increases almost linearly with excitation, confirming its excitonic nature (Fig. 5.14). No biexciton or higher order exciton emission was observed at room temperature in these QDs. The emission does not show a discernable blue-shift with increasing current in the excitonic regime, which points to a small polarization field in a single dot due to strain relaxation and hence the piezoelectric field in the dots is significantly smaller than in equivalent quantum wells [102, 103]. Consequently, the quantum confined Stark effect (QCSE), which leads to the blue shift with increasing injection current density, is very small.

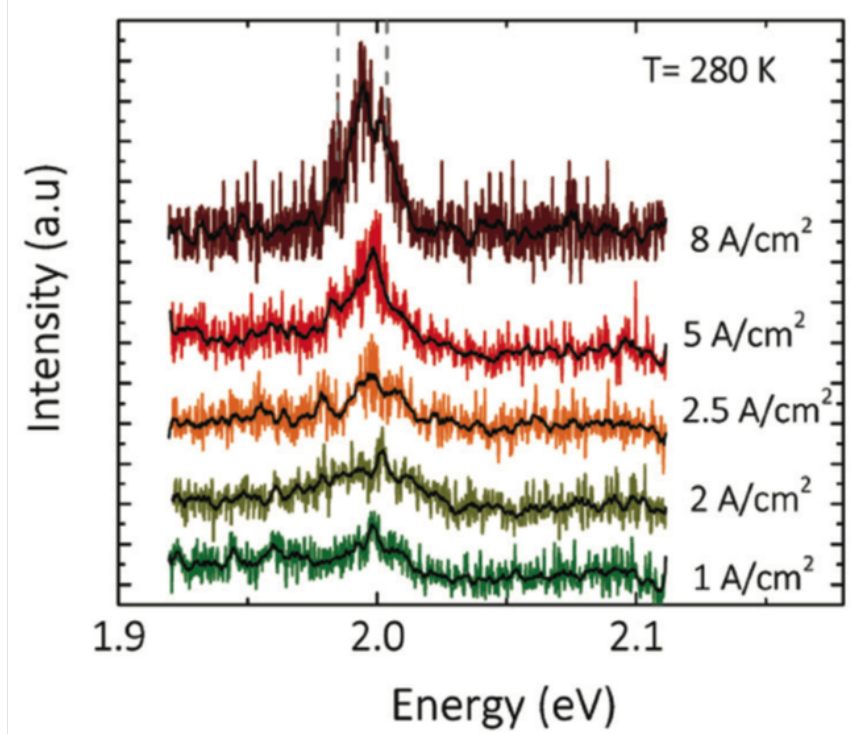


Figure 5.13: Electrominescence from a single aperture at room temperature.

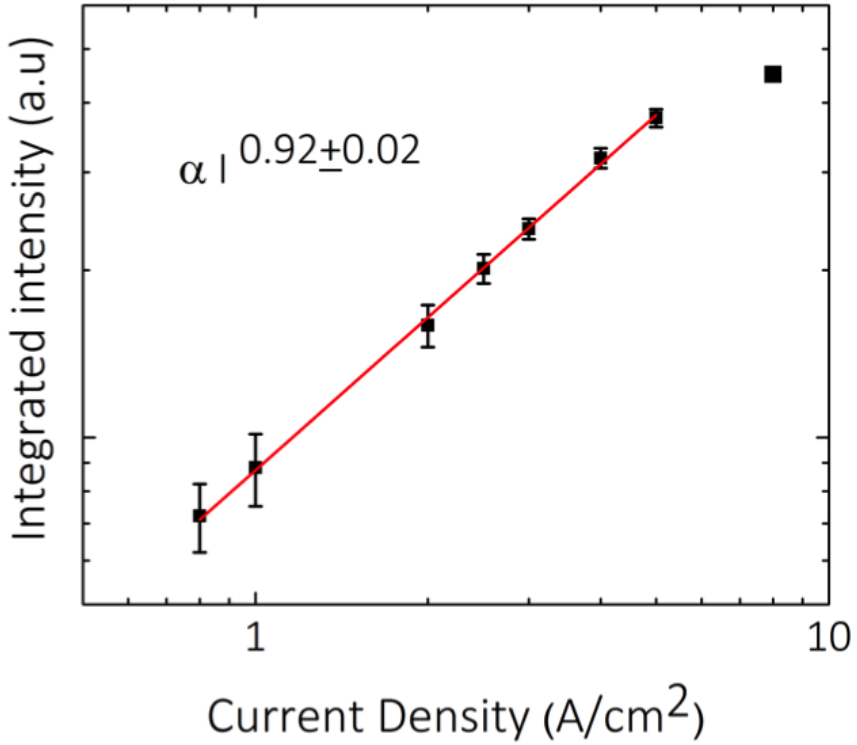


Figure 5.14: Integrated intensity of exciton transition increases linearly with injected current density.

Control QD LEDs without opaque metal masks were fabricated on the same chip. The energy position of the EL peak from the ensemble of QDs in these devices, when monitored over a larger excitation range (up to $500\text{A}/\text{cm}^2$), shows a blue shift of 8 nm (Fig. 5.15), which corresponds to a polarization field of $\sim 100 \text{ KV}/\text{cm}$. This value is much smaller than that reported in InGaN quantum wells on c-plane.

5.4 Single-Photon Emission From A Single Quantum Dot

Figure 5.16 shows the correlation traces recorded at 280 K and 15 K, measured under cw excitation. A classic signature of photon anti-bunching, the dip in the correlation signal $g^{(2)}(\tau)$ at zero time delay $g^{(2)}(0)$, is clearly observed up to room temperature. The measured data are analyzed to obtain a $g^{(2)}(0)$ value of 0.11 at 15 K, indicating a ten-fold decrease in multi-photon emission probability. At room

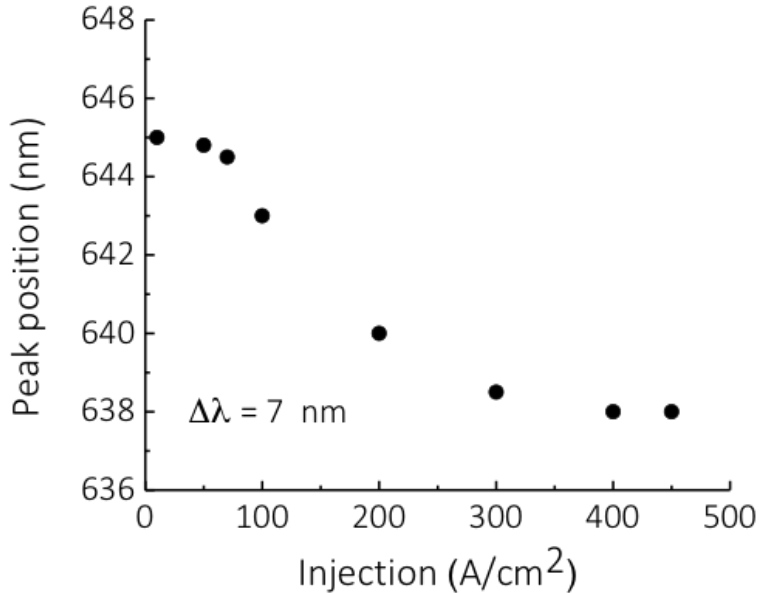


Figure 5.15: Blue-shift of emission peak measured from a control ensemble LED, as a function of injection current.

temperature, the $g^{(2)}(0)$ increases to 0.32. As seen in Fig.5.17, this value increases with increasing injection current density. Even at the lowest excitation current density of $1A/cm^2$ at room temperature, $g^{(2)}(0)$ does not go to zero but has a finite value of 0.32. This may be, in part, due to the background and dark counts picked up by the detectors and the finite time resolution of the measurement system. The $g^{(2)}(0)$ obtained after background subtraction is 0.29. The value of $g^{(2)}(0)$ does not decrease to 0 even after correction for the finite time resolution of the system (100 ps) and this may be due to the thermal broadening of the exciton line. At high injection currents, the single-dot LED approaches the behavior of a classical emitter with $g^{(2)}(0)$ equal to 0.8. Fitting parameter b is the decay time corresponding to the second-order correlation curve near zero delay.

Since the biexciton or multiexciton state was not observed under this weak excitation regime, the fitted decay rate ($1/b$) can be considered to be the sum of the pumping rate p and exciton decay rate τ_X ($1/b = 1/\tau_X + p$). The exciton lifetime

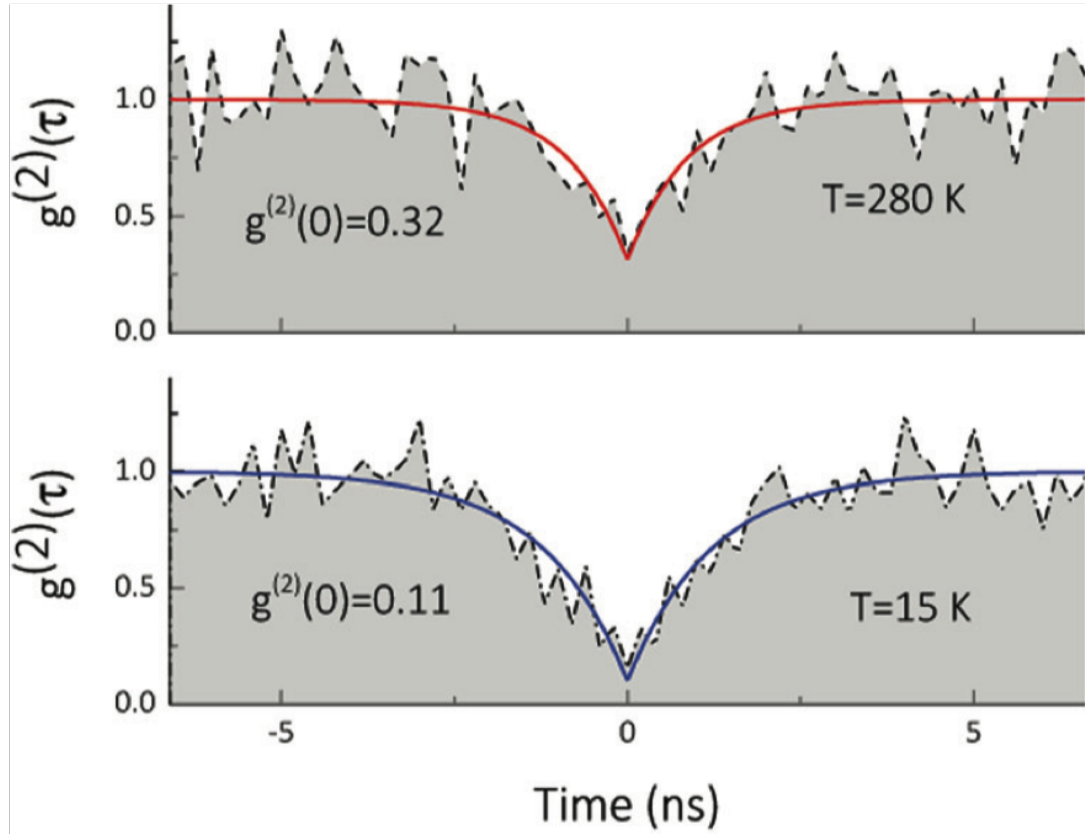


Figure 5.16: Second-order correlation from an exciton line at room temperature and 15 K.

derived from the fit decreases from ~ 1.4 ns to 1.0 ns with increasing injection due to increase in electron-hole capture rate which leads to a higher probability of exciton occupation as shown in Fig. 5.18. Since no higher order excitons are observed at room temperature, the exciton occupation probability can be calculated for various injection current densities J , using the Poisson formula $P_X = \alpha \exp(-\alpha)$ where $\alpha = J/J_0$ where J_0 is the saturation injection current density. After the initial decrease, at higher injections the lifetime increases to ~ 1.6 ns. The onset of this trend is almost coincident with the exciton intensity saturation.

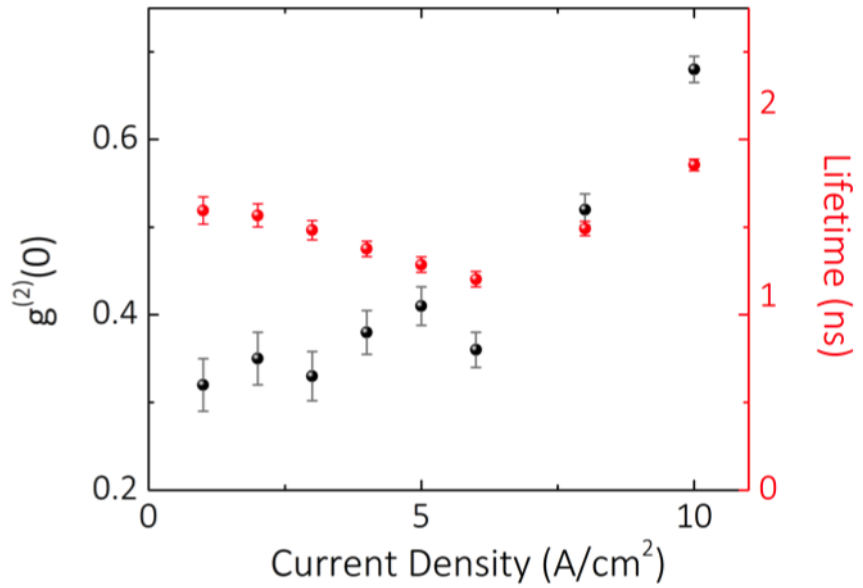


Figure 5.17: $g^{(2)}(0)$ and lifetime as a function of injected current density.

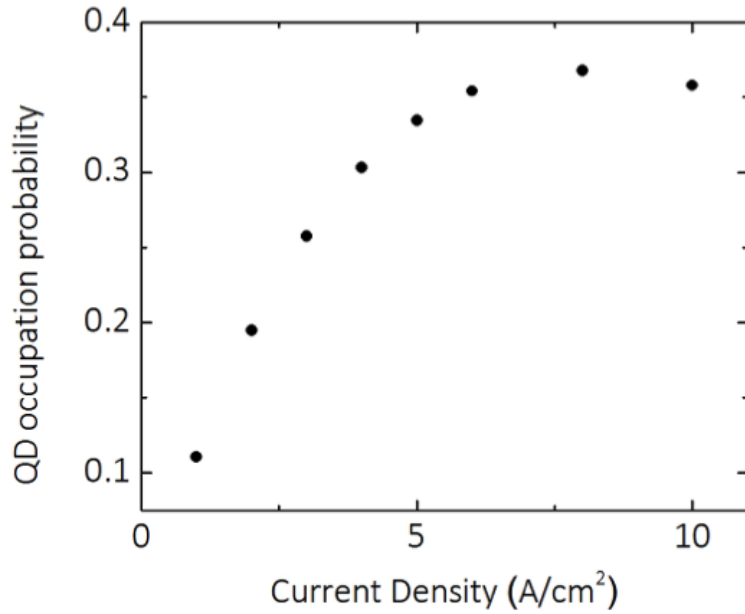


Figure 5.18: Calculated exciton occupation probability of a quantum dot.

5.4.1 Single Photons On Demand

Single photons can be generated on-demand by exciting the diode using a pulsed source, if the pulse width is much shorter than the exciton lifetime. High frequency, sharp (200 ps) pulses are superimposed on a dc bias, set around the diode turn-on

voltage to periodically trigger the diode into the ON state. For pulsed measurements, a high frequency pulse generator Agilent 81134A (3.35 GHz 2-channel Pulse-/ Pattern Generator) was used. The second-order correlation data recorded at an injection of $2A/cm^2$ and excitation repetition rate (ERR) of 200 MHz, shows the area of the zero delay peak is about 0.37 times that of the peaks at finite delays (Fig. 5.19). This suppression of the peak at zero time delay indicates a reduced probability of multi-photon emission events.

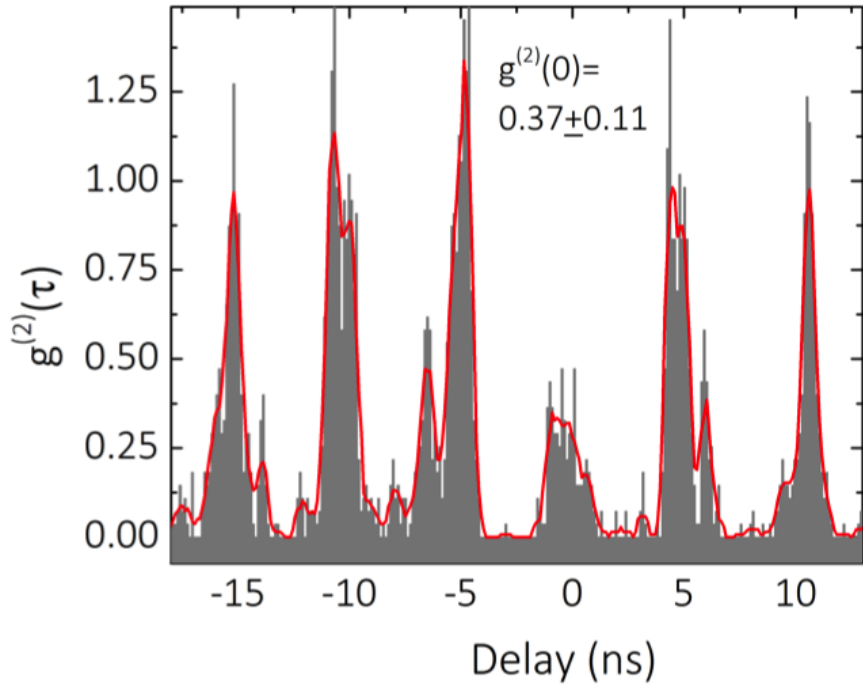


Figure 5.19: On demand single photons using a pulsed electrical trigger at 200 MHz.

We have also measured the TREL from the single QD, with the same pulsed excitation (200 MHz) for different bias voltages. The biasing scheme used for the electrical excitation of the device for TR-EL measurements is shown in Fig. 5.20. Transient data seen in Fig. 5.21 exhibits mono-exponential decay and derived lifetime values are in good agreement with lifetimes obtained from the fit of the $g^{(2)}(\tau)$. The mono-exponential decay confirms the high degree of 3D confinement in the dot and small polarization field. At the highest excitation, which is close to the injection at

which exciton intensity saturates, a delay in the rise of the zero peak ($\Delta \sim 200\text{ps}$) was observed. This indicates an increase in the carrier capture time from the wetting layer continuum of states into the quantum dot exciton state.

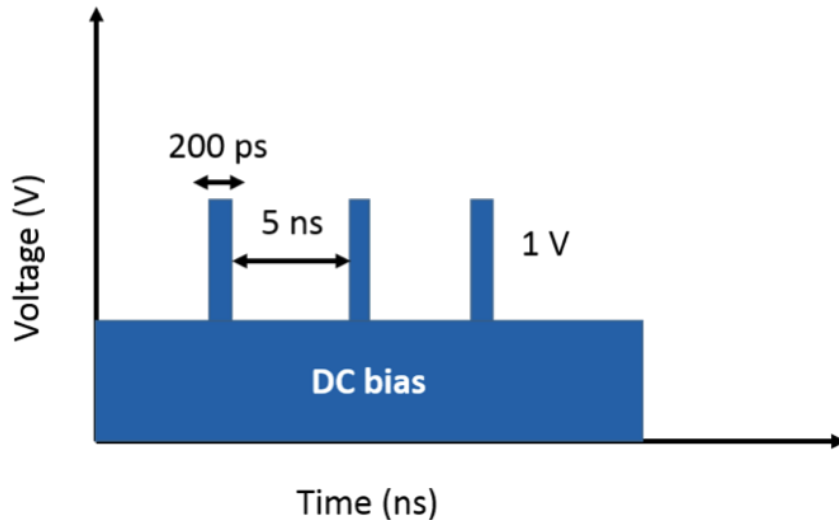


Figure 5.20: Biasing scheme for TRELs measurement.

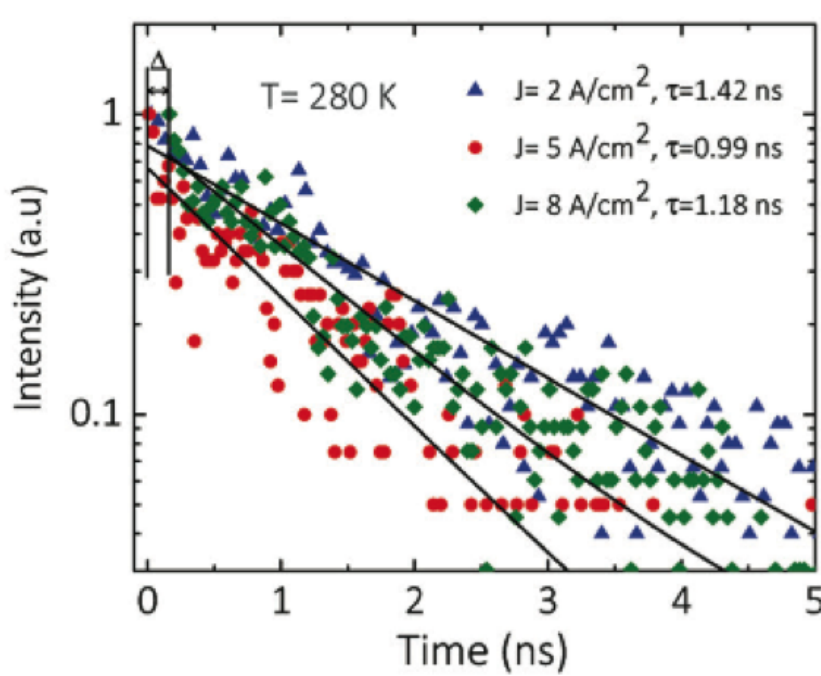


Figure 5.21: TREL from a single exciton line at room temperature at varying injections.

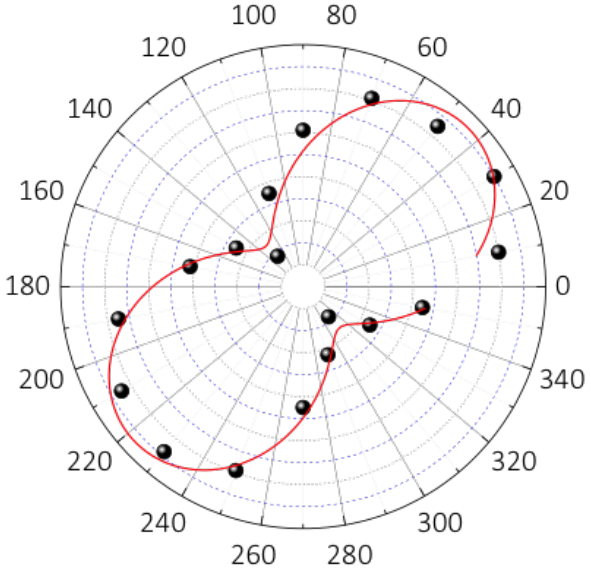


Figure 5.22: Polarization of InGaN quantum dot emission.

The delay in the exciton emission is almost concurrent with the increase in carrier lifetime seen in Fig.5.21, both of which indicate an electron-hole capture bottleneck at elevated carrier densities, previously observed in InGaAs quantum dots.

In the present measurement, a highest photon count rate of $\sim 8kHz$ was detected and a source efficiency $\sim 2\%$ was measured. Further improvements in the heterostructure design, injection and collection geometry would facilitate more efficient single-photon emission and higher operating speeds. The study of polarization of the emitted single photons in this device (Fig. 5.22) and other InGaN/GaN quantum dots reveals that the emission is linearly polarized without a fixed preferred direction of polarization, due to the anisotropy in the strain profile, arising from asymmetry in the quantum dot structure [109, 110]. However, a detailed investigation of the polarization of single photons has not been performed in this study.

5.5 Summary

A single layer of $In_{0.4}Ga_{0.6}N/GaN$ quantum dots with a low density ($2\times10^8/cm^{-2}$) was grown. The quantum dot layer was embedded in a GaN p-i-n diode. Single QD LEDs were fabricated with nanoscale apertures in an Al mask, to collect emission from a single dot. The emission shows excitonic emission at 2.0 eV at room temperature. The filtered exciton emission was studied by second-order correlation measurements. Single-photon emission with $g^{(2)}(0)=0.29$ is measured at room temperature. The $g^{(2)}(0)$ shows a steady degradation with injection current. On-demand single-photon emission is achieved using a pulsed source at 200 MHz. The recombination lifetime obtained from TREL measurements and fitting of $g^{(2)}(\tau)$ data, shows a trend suggestive of a phonon-bottleneck in these quantum dots, which is studied in greater detail in the next chapter.

CHAPTER VI

On The Formation And Nature Of InGaN Quantum Dots In GaN Nanowires

6.1 Introduction

Gallium nitride (GaN) nanowires and related indium gallium nitride (InGaN) heterostructures have been extensively studied in this thesis and for solid-state lighting and nanophotonics, in general. InGaN/GaN disk-in-nanowire (DINW) based emitters are being developed and investigated as light emitting diodes (LEDs)[50, 56, 111], optically and electrically pumped lasers [59], single-photon sources [47, 60, 61] and polariton lasers[112, 113]. As described in Chapter 2, GaN nanowires have several inherent advantages compared to bulk GaN usually grown on sapphire or SiC. The efficient strain relaxation, reduced polarization field and QCSE has allowed access to red and near-infrared regions of the spectrum using nitrides [111, 114, 115]. The many favorable properties of InGaN/GaN DINWs, coupled with the ability to grow these heterostructures on silicon, have led to technologically significant advances such as high internal quantum efficiency (IQE) and reduced droop in LEDs, low threshold currents and large differential gain in lasers and high temperature operation of single-photon sources.

Despite tremendous progress in the field, InGaN/GaN DINWs are still not very

well understood in terms of their structural and electronic properties. Single InGaN/GaN DINWs exhibit characteristics typical of quantum dots (QDs) such as single-photon emission demonstrated by second-order correlation at zero delay, $g^{(2)}(0)$ less than 0.5 and small radiative lifetimes. Remarkably, this behavior is seen in nanowire heterostructures with diameters larger than the GaN exciton Bohr radius, which necessitates a better understanding of the formation and nature of the InGaN/GaN quantum disks. It is important to investigate the possible formation of quantum dots, by either Stranski-Krastanow (SK) or Volmer-Weber (VW) growth modes, during epitaxy of an InGaN/GaN DINW.

We have grown InGaN/GaN and GaN/AlGaN DINW heterostructures on silicon substrates by molecular beam epitaxy and have investigated their optical properties by temperature dependent and time resolved photoluminescence (TRPL) measurements and their structural characteristics by transmission electron microscopy (TEM). These measurements have been performed on nanowires with average diameters ranging from 20 nm to 100 nm. InGaN/GaN DINWs with relatively large In composition ($\sim 50\%$), emitting in the red spectral range were studied. The objective has been to establish the origin and nature (dimensionality) of quantum confinement in the disks.

The formation and existence of a self-organized InGaN island in the disk region of the GaN nanowires is evident in TEM images and has been previously reported by Mi et al [116]. In this study we have established that these islands exhibit QD-like behavior. Three-dimensional quantum confinement is supported by results obtained from the TRPL measurements, which reveal an increase in radiative lifetime with increase in temperature, a trend previously observed in InGaAs/GaAs self-organized QDs. This behavior is explained by invoking electron-hole scattering [117], instead of optical phonon scattering, as the dominant mechanism for the cooling of injected hot electrons in the QDs. We have measured single-photon emission from single DINWs

and quantum dot-like behavior of the linewidth enhancement factor of electrically modulated DINW lasers and these results strongly suggest the formation of self-organized InGaN quantum dots in the disk region of the GaN nanowires.

6.2 Growth And Characterization

Undoped GaN nanowires containing single or multiple InGaN disks were grown on (111) Si substrates in a Veeco Gen II plasma-assisted molecular beam epitaxy (PA-MBE) system.

6.2.1 MBE Growth Of InGaN/GaN and GaN/AlGaN Disk-In-Nanowires

Growth of GaN nanowires was carried out at $780^{\circ}C$ - $850^{\circ}C$, depending on the desired nanowire diameter, under N-rich conditions with the N flow rate maintained constant at 1 sccm. The Ga flux was varied between 8×10^{-8} Torr to 1.5×10^{-7} Torr, to achieve different nanowire diameters. After one hour of growth (300 nm of GaN), the substrate temperature was lowered to about $550^{\circ}C$ for the growth of a single disk or eight pairs of 2-3 nm InGaN disks, separated by 15 nm GaN barriers. The In composition in the disk is estimated to be $\sim 40 - 55\%$ by energy dispersive x-ray spectroscopy (EDX). Figure 6.1 shows scanning electron microscope (SEM) images of ensembles of nanowires with average diameters in the range of 25 nm to 100 nm. The density of nanowires also varies as growth conditions are adjusted to change nanowire size. Detailed growth parameters for all the samples are provided in Table 6.1.

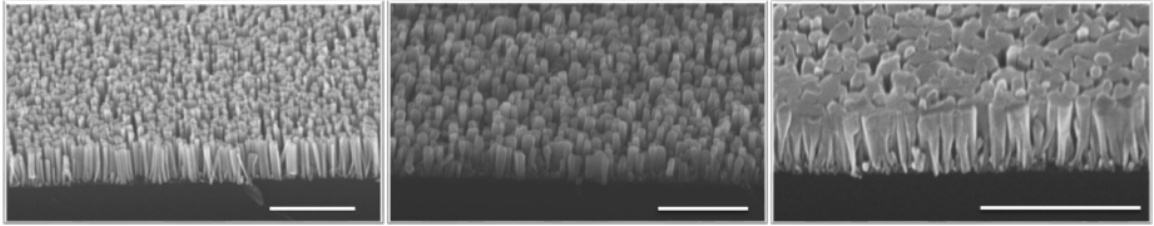


Figure 6.1: SEM images showing 45° oblique view of InGaN/GaN dot-in-nanowire ensembles with different average diameters. The scale bar for all figures is $1\mu\text{m}$.

Heterostructure	Nanowire growth	Disk growth
InGaN/GaN DINW (100 nm)	$T_{sub} = 780^\circ\text{C}$ Ga flux = 1.5×10^{-7} Torr	$T_{sub} = 550^\circ\text{C}$ In flux = 1×10^{-7} Torr Growth time= 90 s
InGaN/GaN DINW (50 nm)	$T_{sub} = 800^\circ\text{C}$ Ga flux = 1×10^{-7} Torr	$T_{sub} = 550^\circ\text{C}$ In flux = 8×10^{-8} Torr Growth time= 90 s
InGaN/GaN DINW (25 nm)	$T_{sub} = 830^\circ\text{C}$ Ga flux = 8.8×10^{-8} Torr	$T_{sub} = 525^\circ\text{C}$ In flux = 6×10^{-8} Torr Growth time= 90 s
GaN/AlGaN DINW (80 nm)	$T_{sub} = 840^\circ\text{C}$ Ga flux = 1.4×10^{-7} Torr Al flux = 2×10^{-8} Torr	$T_{sub} = 800^\circ\text{C}$ Ga flux = 1.2×10^{-7} Torr Growth time=120 s
GaN/AlGaN DINW (60 nm)	$T_{sub} = 840^\circ\text{C}$ Ga flux = 1.2×10^{-7} Torr Al flux = 1.5×10^{-8} Torr	$T_{sub} = 800^\circ\text{C}$ Ga flux = 1×10^{-7} Torr Growth time=120 s
GaN/AlGaN DINW (25 nm)	$T_{sub} = 840^\circ\text{C}$ Ga flux = 9×10^{-8} Torr Al flux = 1×10^{-8} Torr	$T_{sub} = 800^\circ\text{C}$ Ga flux = 9×10^{-8} Growth time=120 s

Table 6.1: MBE growth conditions of disk-in-nanowire samples

6.2.2 Photoluminescence from InGaN/GaN and GaN/AlGaN Disk-In-Nanowires

The photoluminescence (PL) emission peak from the InGaN disks is observed in the range of $\sim 580 - 630$ nm at room temperature and has a full-width half maximum ~ 100 nm, as seen in Fig. 6.2. Differences in the PL peak position may be due to variation in the In incorporation with nanowire diameter or quantum confinement effects leading to blue shift of PL emission. The substrate temperature and In/Ga flux ratio are optimized to achieve a relatively high radiative efficiency of $\sim 40\%$.

Similarly, GaN/AlGaN DINW samples of varying diameters were grown on (111) Si substrates. Thickness of the GaN disks is 4 nm. The AlGaN nanowire growth is carried out at 840°C to compensate for the high sticking coefficient of Al adatoms. The resulting Al composition using an Al flux of 1.5×10^{-8} Torr is $Al_{0.2}Ga_{0.8}N$. Photoluminescence from the GaN/AlGaN disks is in the UV spectral range, as shown in Fig. 6.2. The PL from the DINWs is redshifted from the bandgap of bulk GaN as a result of the QCSE, originating from a strong built-in electric field in the GaN/AlGaN disks.

6.3 Carrier Lifetime Measurements

To obtain the PL decay transient, DINW samples were excited by a frequency-tripled (267 nm) mode-locked Tsunami $Al_2O_3:\text{Ti}$ laser (repetition rate 80 MHz).

6.3.1 Carrier Lifetime Measurement In InGaN/GaN Disk-In-Nanowires

The filtered DINW emission was transmitted to a single photon avalanche photodiode with a timing resolution of 40 ps. The measurements were performed at different temperatures in the range of 10-300 K. Figure 6.3 shows typical low temperature transient photoluminescence data obtained from an InGaN/GaN DINW sample

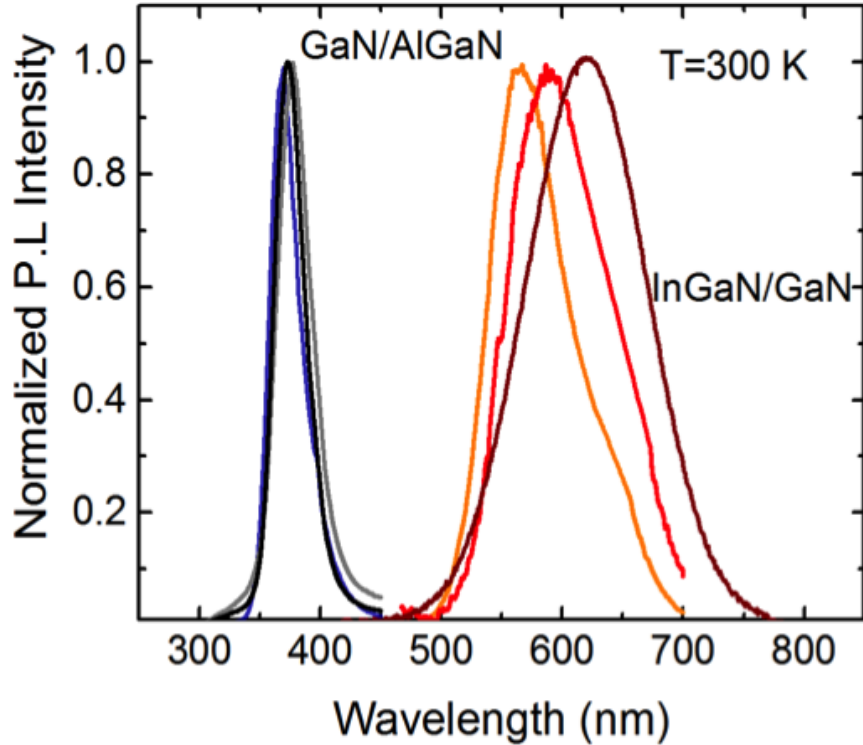


Figure 6.2: Room temperature PL from InGaN/GaN and GaN/ $Al_{0.2}Ga_{0.8}N$ DINW nanowire samples of different diameters measured under non-resonant saturation excitation. The In composition in InGaN/GaN DINWs is $\sim 40 - 55\%$ and varies with the nanowire diameter.

with a diameter of 50 nm. The measured TRPL data were analyzed by a stretched exponential model. The quantum disk lifetimes at 300 K derived from the analysis are $\sim 1\text{ns}$. The values of β are in the range of 0.74-0.98.

The radiative (τ_r) and non-radiative (τ_{nr}) lifetimes can be derived from the measured total recombination lifetime and internal quantum efficiency (IQE) η_{int} . The value of η_{int} at any temperature T can be estimated from temperature dependent PL measurements, as the ratio of integrated intensities at T and 10 K under saturation excitation. At low temperature (10 K), non-radiative recombination centers are frozen and the overall recombination can be attributed to radiative recombination alone. Lifetimes for two InGaN/GaN DINW samples with different diameters, 25 nm and 50 nm, are shown as a function of temperature in Fig.6.4. It is evident that radiative lifetimes derived here are significantly smaller than those measured in

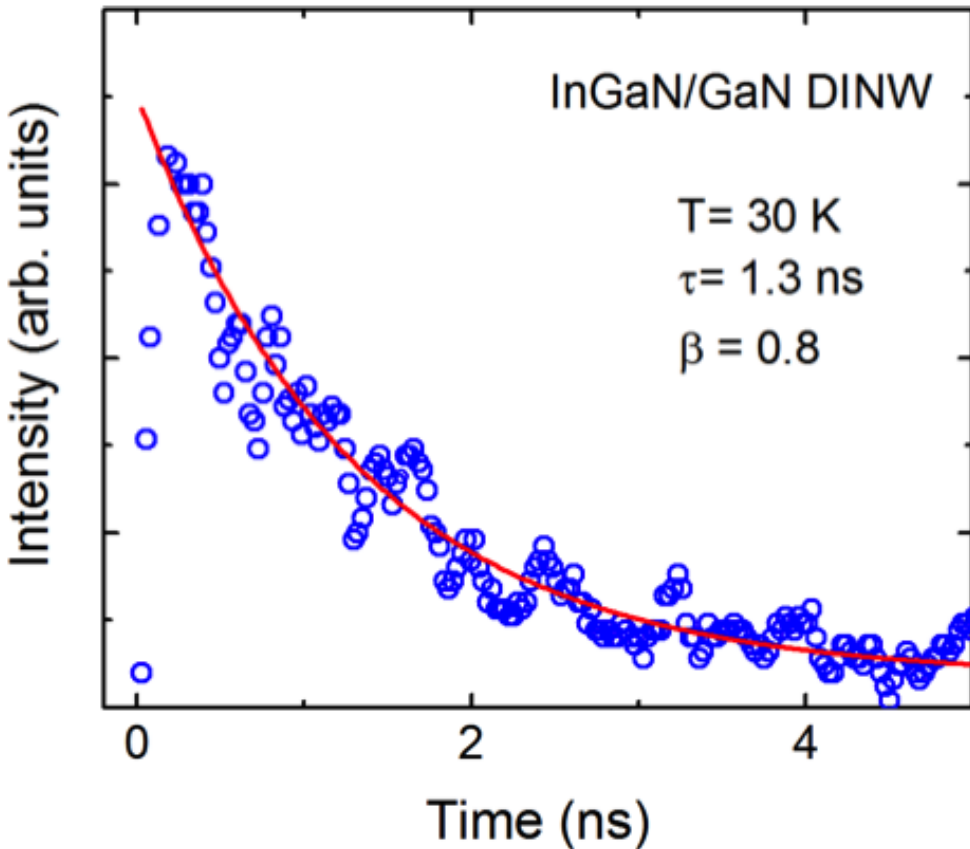


Figure 6.3: Transient decay typically observed from ensemble of InGaN/GaN DINWs with an average diameter of 50 nm. The measured data are analyzed using a stretched exponential model with β parameter 0.8.

InGaN/GaN quantum wells, largely due to the weaker piezoelectric field in the disks compared to that in planar quantum wells and perhaps, to a smaller extent, due to lateral confinement in the small diameter disks. However, the non-radiative lifetimes are also small, which could be related to surface recombination arising from the large surface-to-volume ratio.

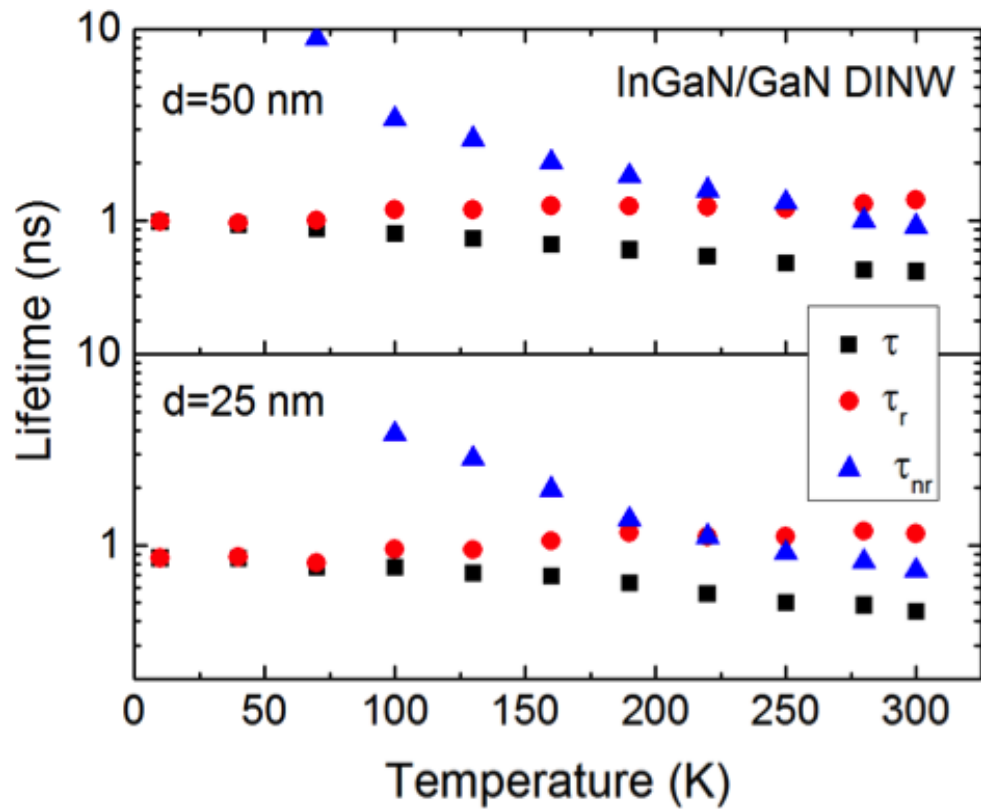


Figure 6.4: Total lifetime and its radiative and non-radiative components derived from temperature dependent PL and TRPL measurements, for InGaN/GaN dot-in-nanowires with two different diameters 50 nm and 25 nm. Both InGaN/GaN DINW samples show an increase in radiative lifetime with temperature.

The most significant feature depicted in Fig. 6.4 is that the radiative lifetime for both samples increases with increasing temperature. In contrast, the trend of carrier lifetimes measured in similar compressively strained $GaN/Al_{0.2}Ga_{0.8}N$ DINWs is very different. TRPL measurements performed on the GaN disks exhibit monoexponential lifetime decay, as shown in Fig.6.5. The radiative and non-radiative lifetimes as a function of temperature are again derived from temperature dependent PL and TRPL measurements. The trends of radiative lifetimes for two samples with nanowire diameters of 25 nm and 60 nm, are illustrated in Fig. 6.6. The radiative lifetime τ_r is almost invariant with temperature.

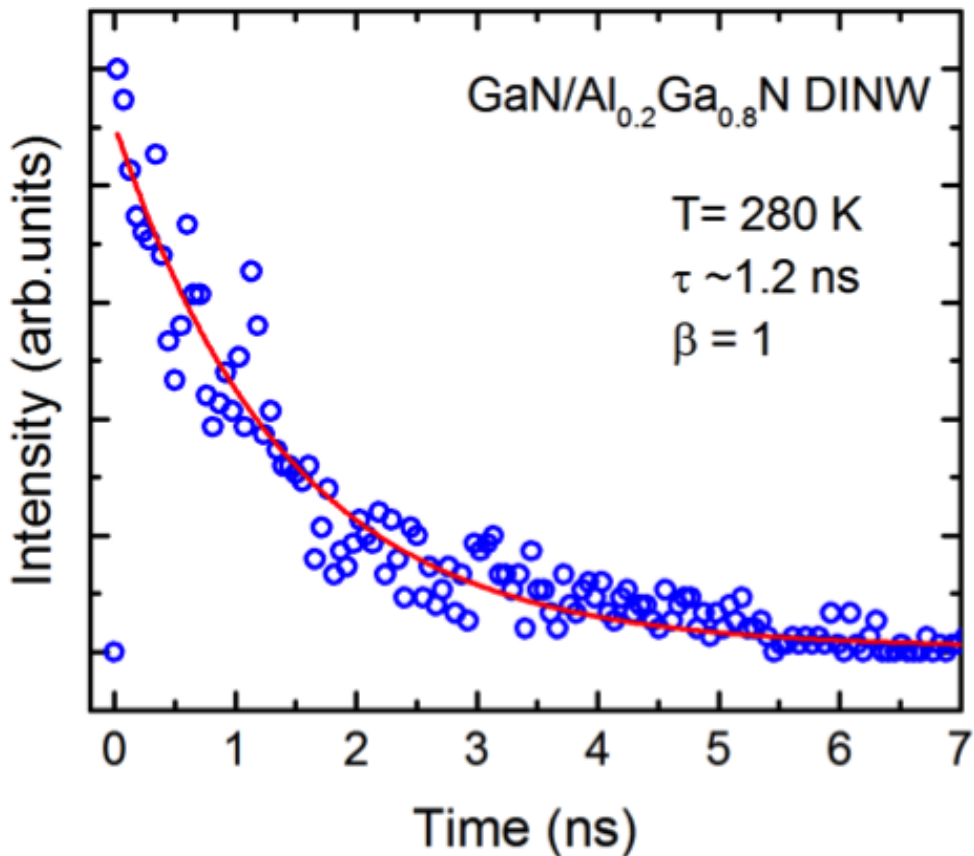


Figure 6.5: Transient decay typically observed from $GaN/Al_{0.2}Ga_{0.8}N$ DINW. The measured data are analyzed using a mono-exponential model.

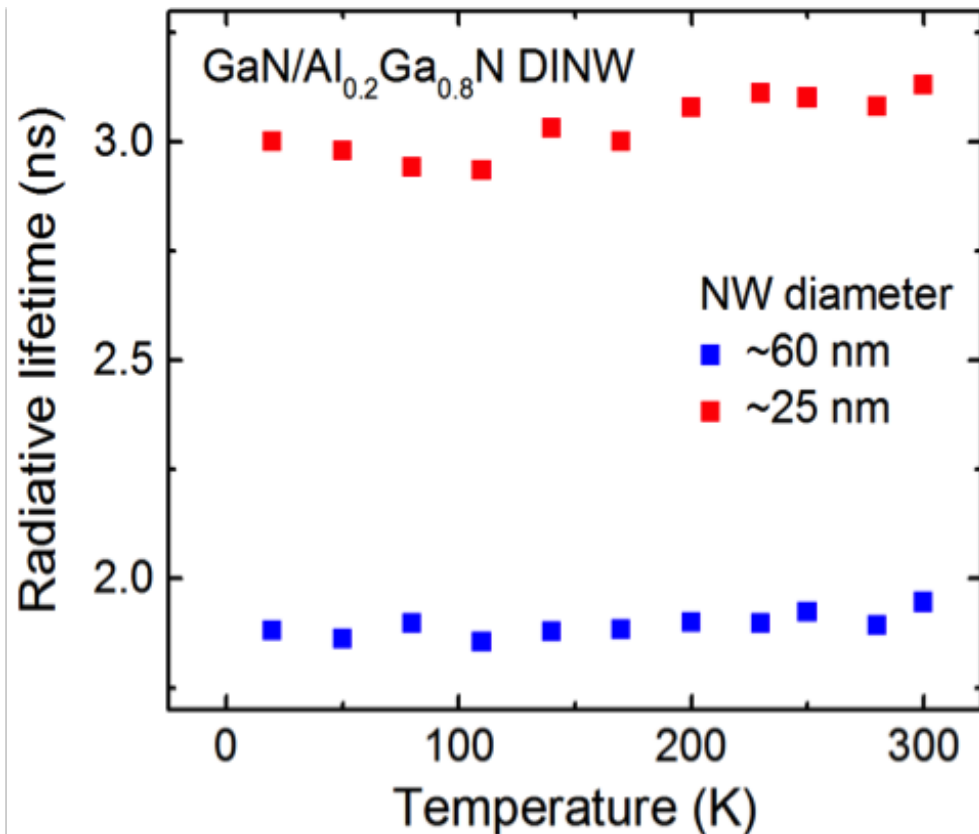


Figure 6.6: Radiative lifetime of GaN/ $Al_{0.2}Ga_{0.8}N$ dot-in-nanowires with two different diameters 60 nm and 25 nm shows a nearly constant trend with temperature.

6.3.2 Carrier lifetime measurement in InGaN/GaN quantum dots

In bulk semiconductors and quantum wells, the radiative lifetime generally remains constant with increase of temperature. In order to understand the apparently anomalous behavior of the radiative lifetime in InGaN/GaN DINWs, we have compared these results with lifetimes measured in self-organized $In_{0.4}Ga_{0.6}N$ QDs grown in the Stranski-Krastanow growth mode by plasma-assisted MBE on GaN-on-sapphire substrates [118]. Details regarding the epitaxial growth of the QD samples are provided in Chapter 5. Figure 6.7 shows an atomic force microscope (AFM) image of the self-organized QDs, from which a dot density of $\sim 5 \times 10^{10} cm^{-2}$ is estimated. The

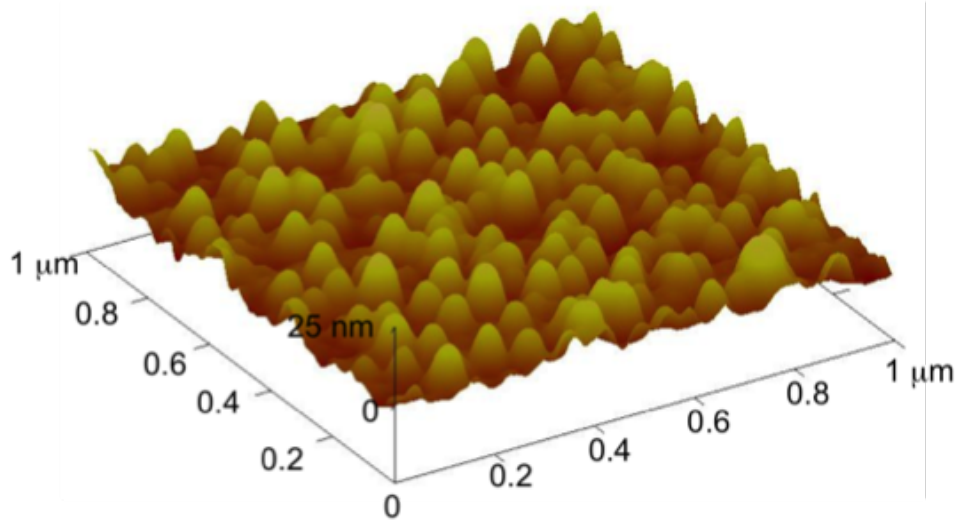


Figure 6.7: Atomic force micrograph of InGaN/GaN quantum dot layer grown by molecular beam epitaxy. The In composition is estimated to be $\sim 40\%$ and quantum dot density is $\sim 5 \times 10^{10} cm^{-2}$.

average height and base dimension of the dots are 3 nm and 40 nm, respectively. Temperature dependent and time resolved luminescence measurements were performed on the QD samples in much the same way as on the nanowires described earlier. The radiative and non-radiative lifetimes in the dots were derived from temperature dependent PL and TRPL measurements. The trend of the lifetimes is depicted in Fig. 6.8. A monotonic increase in radiative lifetime with temperature, similar to that

observed for the InGaN/GaN DINWs, is seen for the quantum dots.

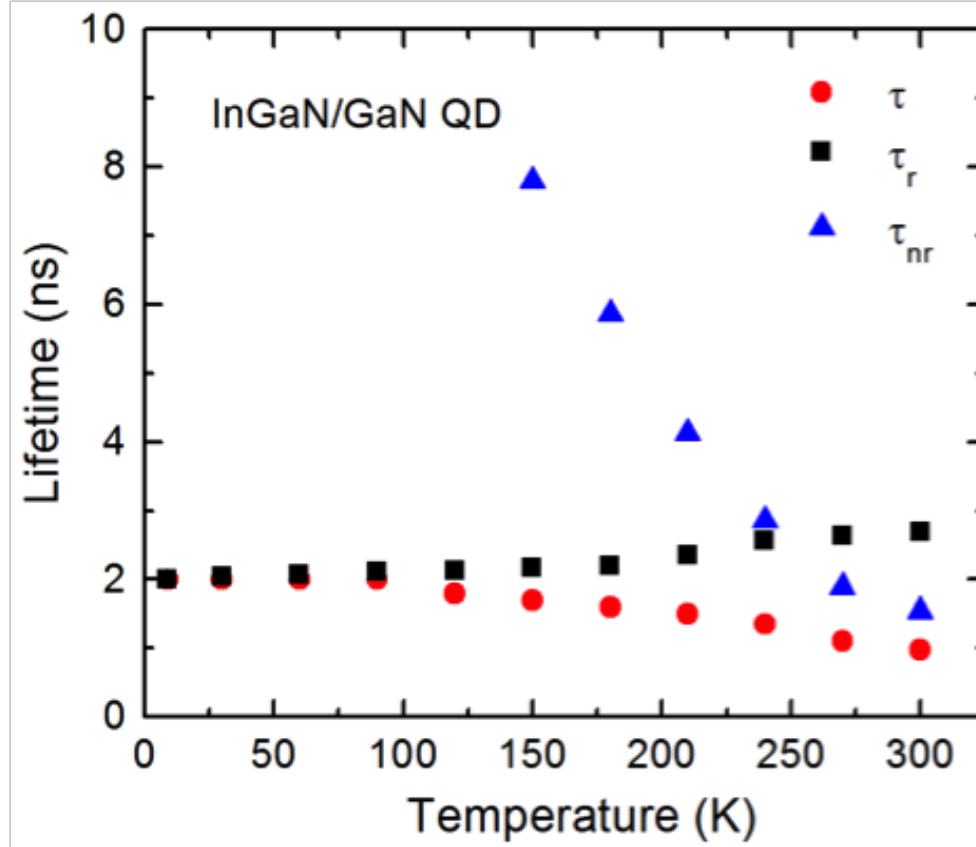


Figure 6.8: Total carrier lifetime and its radiative and non-radiative components for InGaN/GaN QDs. The sample shows an increase in radiative lifetime with temperature.

6.4 Electron-hole scattering

The increase of radiative lifetime with increasing temperature has been previously observed in InGaAs/GaAs self-organized QDs. The anomalous behavior was explained by invoking electron-hole scattering, instead of phonon scattering, as the dominant mechanism to cool high energy electrons to the ground state [117]. The electron states in the QDs are discrete in contrast to other systems, and the separation between them can exceed the LO phonon energy (phonon energies of InN : 86 meV and GaN : 91 meV), presenting a phonon bottleneck. In contrast, there is

a continuum of hole states due to degeneracy and band mixing. Occupation of the low-lying electron states, which participate in the luminescence process, depends on electron-hole scattering and hole occupation of the ground state. In electron-hole scattering (Fig.6.9) at low temperatures, hot electrons scatter with cold ground state holes and relax to the ground state. The energy gained by the holes excites them to higher levels, from which they can relax rapidly by multi-phonon emission. With increase of temperature the thermal excitation of cold holes from the ground state will leave fewer holes to scatter with hot electrons and the rate of electron-hole scattering and electron relaxation to the ground state decreases. This results in an increase of the radiative lifetime. We believe that the same processes are operative in the InGaN/GaN self-organized QDs and in the InGaN/GaN DINWs wherein quantum dot-like self-organized islands are formed.

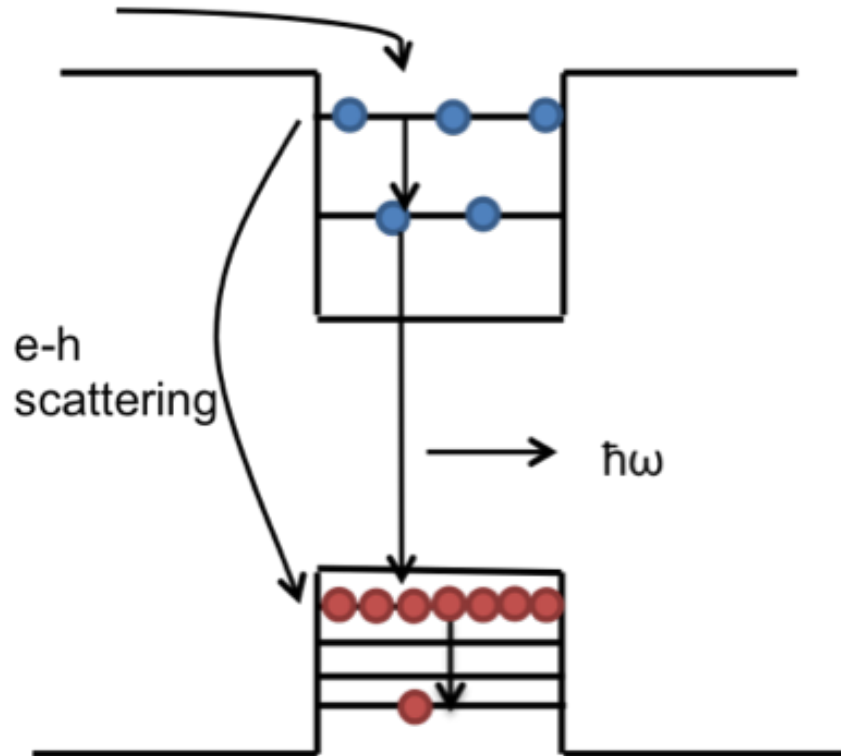


Figure 6.9: The electron-hole scattering process in a quantum dot at low temperatures

6.5 TEM characterization

In order to completely understand the similarity in the trend of temperature dependent lifetimes in the self-organized $II_{n=0.4}Ga_{0.6}N/GaN$ QDs and the InGaN/GaN DINWs and to elucidate the compositional and structural nature of the InGaN/GaN and GaN/AlGaN DINWs, high-resolution transmission electron microscopy (TEM) on such DINW samples were performed in the groups of Prof. J. Millunchick and Prof. Z.Mi. Figures 6.10 and 6.11 depict TEM images of InGaN/GaN DINW samples of diameters 25 nm and 80 nm, respectively. The high resolution TEM image in Fig. 6.10 shows the formation of a self-organized InGaN island at the core of the nanowire. The inset depicts a low magnification TEM image of a single GaN nanowire of ~ 30 nm diameter with a single InGaN disk.

Similarly, in the 80 nm nanowire sample, shown in the high-angle annular dark-field image (HAADF) of Fig. 6.11, QD-like InGaN islands with diameters smaller than the nanowire are clearly visible.

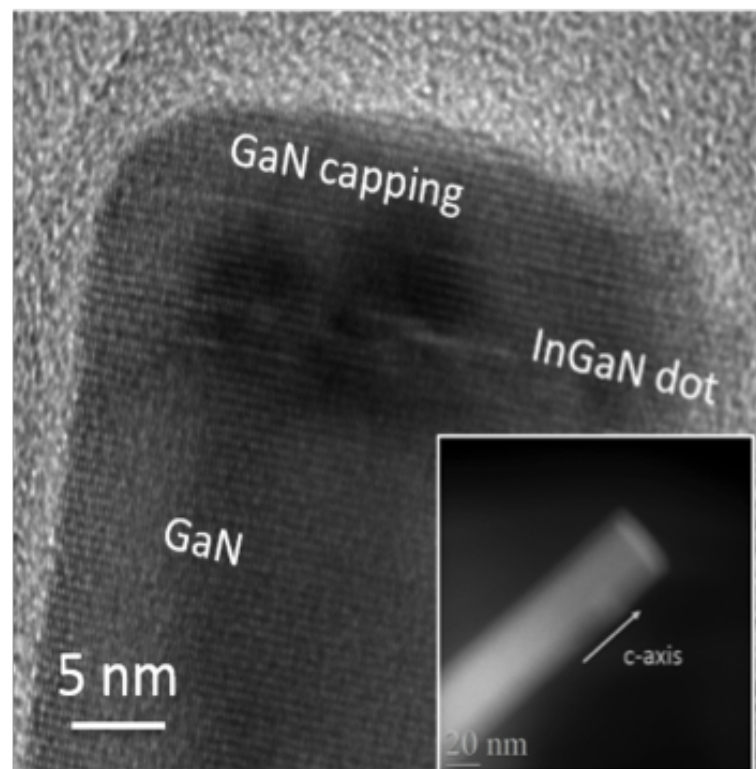


Figure 6.10: HRTEM image of 25 nm GaN nanowire with a single InGaN disk showing InGaN quantum dot formation. Inset shows a low magnification image of a single InGaN/GaN DINW (Courtesy: Lifan Yan)

As growth of the nanowire heterostructure proceeds, there is adatom incorporation and desorption on both the sidewalls and the top (0001) surface. As the latter has the lowest energy, growth proceeds in that direction. Strain relaxation on the sidewalls occurs during nanowire growth and this catalyzes the formation of the self-organized island during epitaxy of the InGaN disk region. These results are consistent with previous findings of Mi et al [116]. Figure 6.12 depicts the formation of islands within the InGaN disk region (In content: 35 – 50%) of GaN nanowires, similar to those seen in Fig. 6.11. Although this DINW sample was grown by Mi et al. in a different MBE chamber, they show remarkably similar characteristics in the structure and nature of the InGaN/GaN islands.

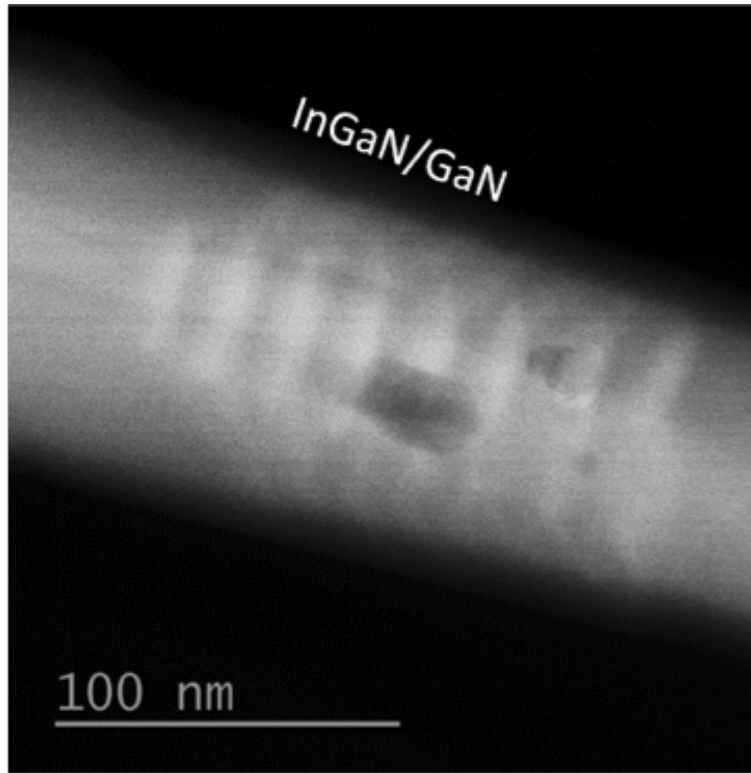


Figure 6.11: HAADF image of 80 nm GaN nanowire with multiple InGaN islands (Courtesy: Lifan Yan).

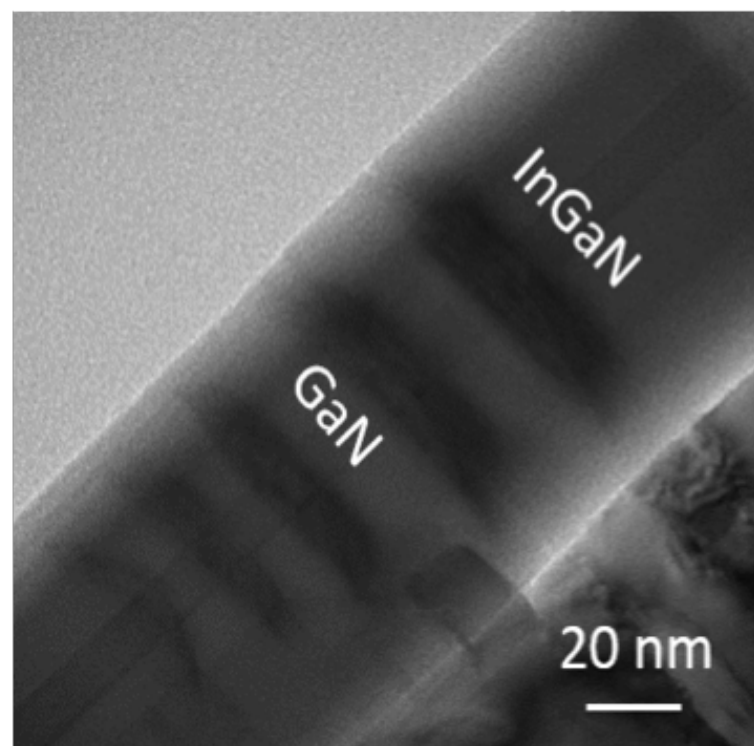


Figure 6.12: HRTEM shows similar InGaN QD-like islands in a 100 nm diameter GaN nanowire grown under entirely different growth conditions. The InGaN QD-island size increases with growth time, as seen in subsequent QD-islands (Courtesy: Prof. Zetian Mi).

It may be noted that a wetting layer is not observable in the images of Figs. 6.10-12. We believe, therefore, that the InGaN island formation process is of the Volmer-Weber type.

On the other hand, island formation is not evident in the TEM image of a 30 nm diameter $Al_{0.2}Ga_{0.8}N$ nanowire with 4 nm GaN disks, shown in Fig. 6.13. The absence of any island formation in this sample is explained by the small lattice mismatch between GaN and $Al_{0.2}Ga_{0.8}N$ (0.6%). The measured temperature dependence of the radiative lifetimes in the various samples can now be explained. The increasing radiative lifetime with temperature in the InGaN/GaN DINW originates from self-organized islands, which behave as quantum dots, forming at the core of the ternary disks.

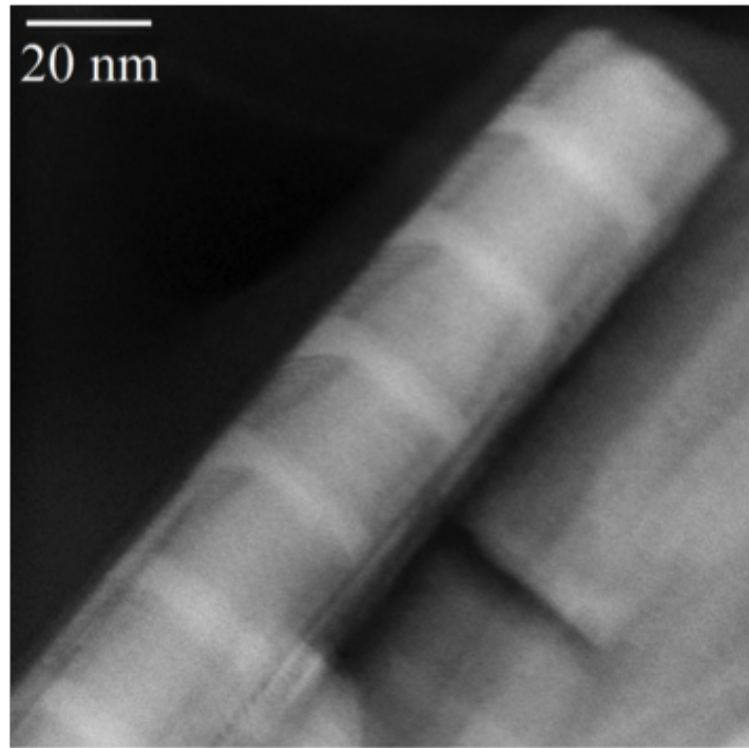


Figure 6.13: TEM image of GaN/ $Al_{0.2}Ga_{0.8}N$ DINW shows sharp quantum well like interfaces with no island formation (Courtesy: Lifan Yan).

6.6 Single-Photon Emission

A single QD can emit a single photon upon electrical or optical excitation through exciton or bi-exciton recombination. We have measured the photon pair correlation statistics of the luminescence from a single DINW transferred to a Si substrate in a Hanbury, Brown and Twiss (HBT) system to confirm single-photon emission [5]. At 30 K, under pulsed optical excitation, the 25 nm diameter InGaN/GaN DINW sample displays clear anti-bunching characteristics at zero time delay between the two photon counters, as shown in the Fig. 6.14. The second order correlation function at zero time delay $g^{(2)}(0)$ is 0.27, a clear indication of single-photon emission.

In contrast, the 25 nm diameter GaN/ $Al_{0.2}Ga_{0.8}N$ DINW sample exhibits the characteristics of a classical multiphoton emitter, shown in Fig. 6.15, with $g^{(2)}(0) \sim 1$ as expected from quantum well emission. These results elucidate the fundamental difference in the nature of quantum confinement in InGaN/GaN and GaN/AlGaN DINW quantum light sources.

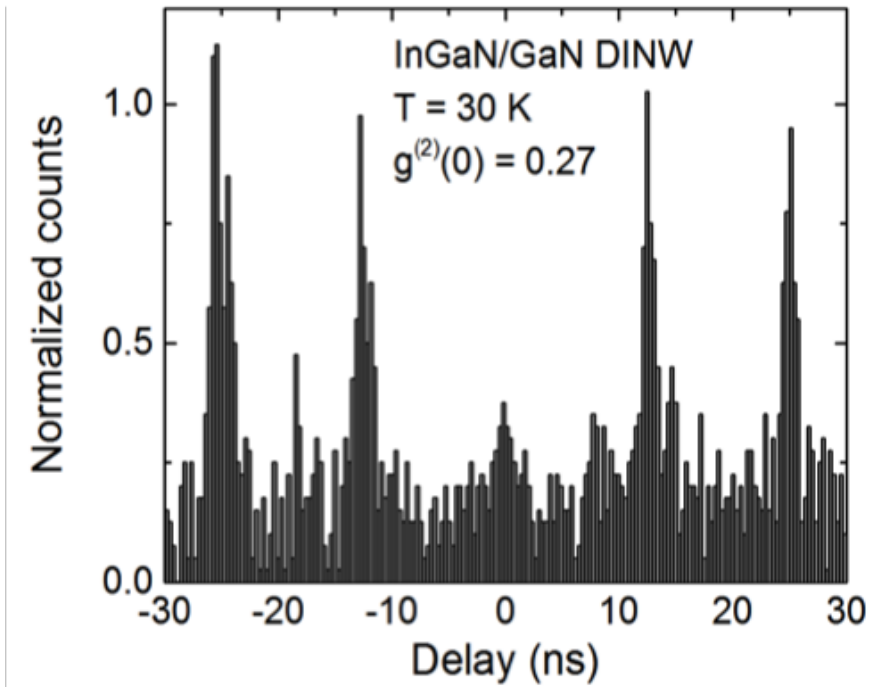


Figure 6.14: Second-order correlation under pulsed optical excitation (at 80 MHz) in a Hanbury-Brown and Twiss (HBT) measurement from a single 25 nm InGaN/GaN DINW showing anti-bunching with $g^2(0)$ is 0.27

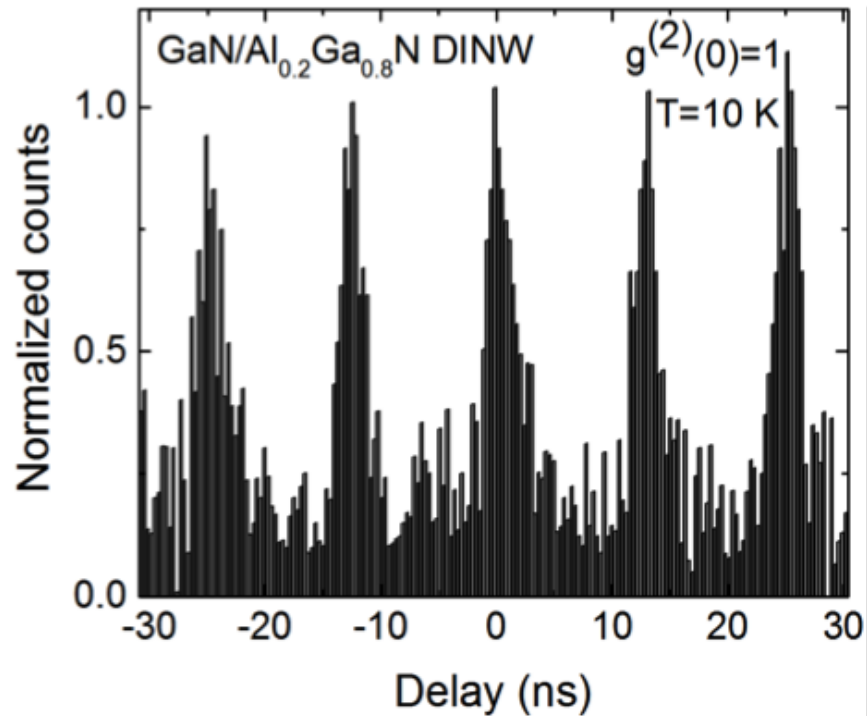


Figure 6.15: Second-order correlation under pulsed optical excitation (at 80 MHz) in a Hanbury-Brown and Twiss (HBT) measurement from a single 25 nm GaN/Al_{0.2}Ga_{0.8}N DINW which does not show anti-bunching

6.7 DINW Edge Emitting Laser

To study of effect of the formation of self-organized quantum dots in the disk-in-nanowire gain media, we have grown, fabricated and characterized InGaN/GaN DINW red-emitting ($\lambda = 610$ nm) electrically pumped edge-emitting lasers on (001) Si substrates. A schematic of an identical green-emitting DINW laser and its calculated mode profile are shown in Fig. 6.16.

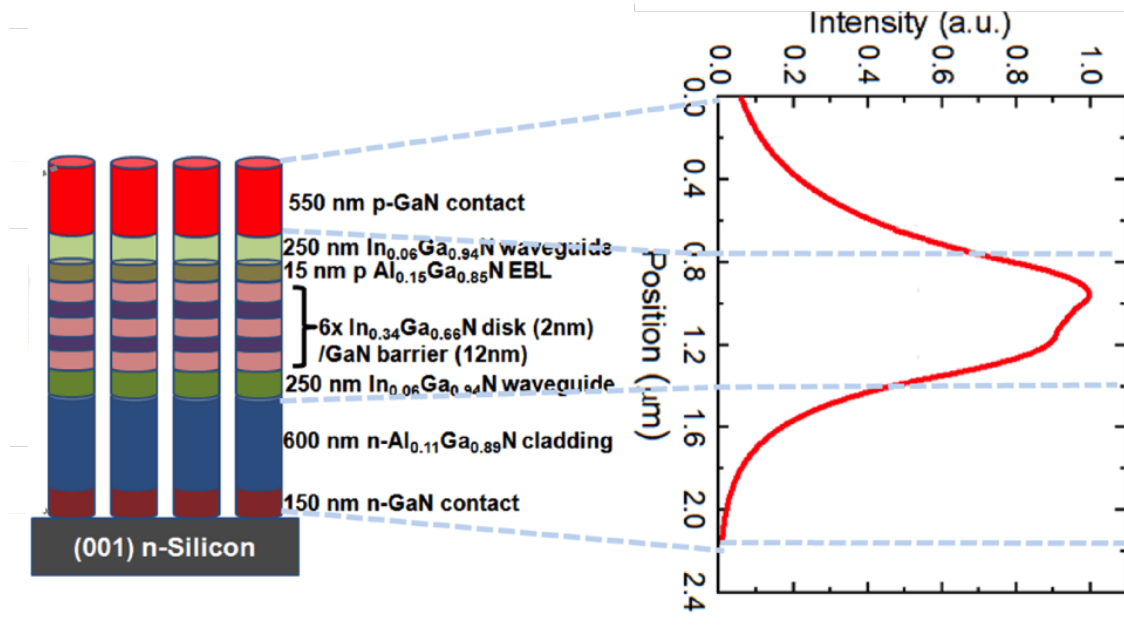


Figure 6.16: Schematic of the edge emitting disk-in-nanowire laser ($\lambda=533$ nm) and its calculated mode profile [59]

The InGaN/GaN DINW edge-emitting laser diode was grown on (001) silicon with an optimized nanowire areal density of $2 \times 10^{10} cm^{-2}$ to prevent coalescing of nanowires. The nanowires have an average diameter of 60 nm. Following the n-GaN contact layer, a 200 nm $n - In_{0.18}Al_{0.82}N$ cladding layer, lattice matched to the GaN was grown. The waveguide layer consists of $In_{0.06}Ga_{0.94}N$. The active region contains 6 pairs of InGaN disks/GaN barrier. Following that, a 15 nm $p - Al_{0.15}Ga_{0.85}N$ electron blocking layer (EBL), 250 nm $p - In_{0.18}Al_{0.82}N$ cladding layer and p-GaN contact layer were grown. The DINW sample shows a radiative efficiency of 54% after parylene passivation. For fabrication of the edge-emitting lasers, mesas in a ridge geometry were defined by dry-etching. The nanowires were planarized and passivated using PVD-deposited parylene. Semitransparent Ni/Au (5 nm/5 nm) and ITO (250 nm) current spreading layer were used as ohmic contacts to the p-GaN. n-GaN contacts were formed with Al/Au (100 nm/300 nm). The end mirrors were formed by cleaving the device along the direction perpendicular to the laser cavity, followed by focused ion beam (FIB) etching to form optically flat laser facets. Finally, dielectric DBRs (TiO_2/SiO_2) were deposited on the facets by electron beam evaporation to enhance the reflectivities to 0.35 and 0.95.

The spectral characteristics of the laser below and above threshold are shown in Fig. 6.17. The device shows a narrow lasing peak with linewidth 0.9 nm at $\lambda = 610$ nm. The optical output power as a function of injected current density is shown in Fig. 6.18. The device shows a lasing threshold around $2.6 kA/cm^2$.

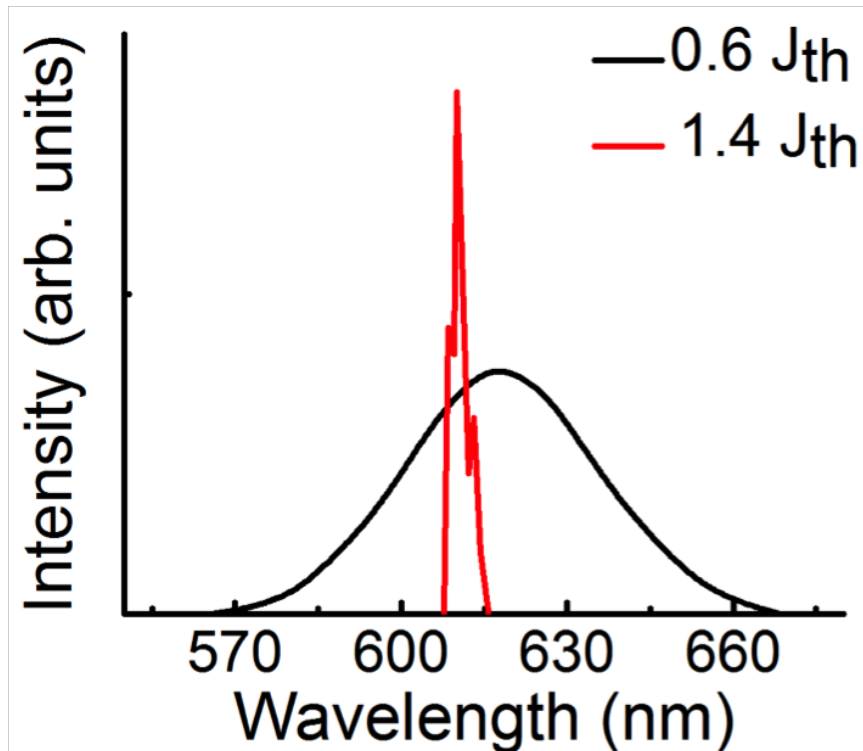


Figure 6.17: Electroluminescence spectrum of the laser below and above threshold, under cw excitation (Courtesy: Shafat Jahangir).

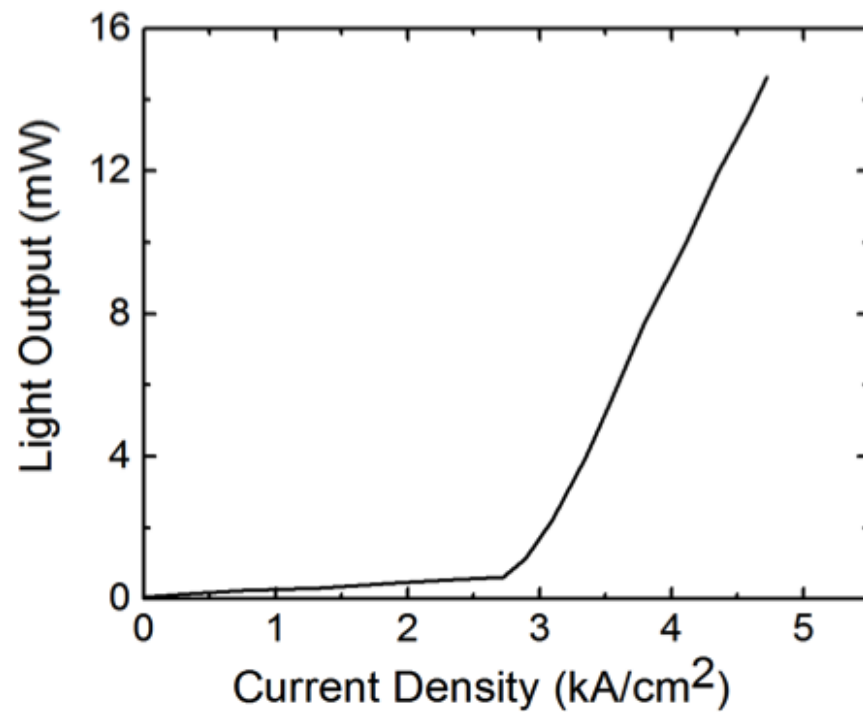


Figure 6.18: Light-output measured as a function of injected current density for the InGaN/GaN DINW laser (Courtesy: Shafat Jahangir).

6.7.1 Linewidth Enhancement Factor

Modulation of the injection current of a semiconductor laser leads to deleterious effects such as linewidth enhancement and chirping, arising from the change in the refractive index of the gain medium.

The fundamental limit for the linewidth of a single-mode laser was first calculated by Schawlow and Townes. Several solid-state lasers experimentally approached this value but they all showed significantly higher linewidth values. The increased linewidth results from the coupling between intensity and phase noise, caused by a dependence of the refractive index on the carrier density in the semiconductor. The linewidth enhancement factor α is mathematically expressed as:

$$\alpha = -\frac{4\pi}{\lambda} \left(\frac{dn_r}{dn} \right) / \left(\frac{dg}{dn} \right) \quad (6.1)$$

where $\frac{dg}{dn}$ is the differential gain. The α -parameters were determined from Hakki-Paoli measurements [119] and the measured values of α as function of the emission wavelength are shown in Fig. 6.19. The observed dip in the value of α at ~ 610 nm strongly points to a quantum dot gain medium in the nanowire laser. Theoretical calculations of the α -parameter of lasers by Miyake and Asada show a sharp decrease, followed by an increase, in the value of α as a function of wavelength for QD lasers [120]. This singularity is related to the sharp peak in the gain spectrum of quantum dots and is not observed in calculated or experimental results from bulk or quantum well lasers. A sharp dip has been observed in the wavelength dependence of the α parameter of 1.55 m InAs/InP QD lasers [121, 122].

6.8 Simulation Of Quantum Dot Size

Nakajima et al. have calculated thickness-composition phase diagrams for Frank and van der Merwe (FM), Stranski-Krastanov (SK) and Volmer-Weber (VW) growth

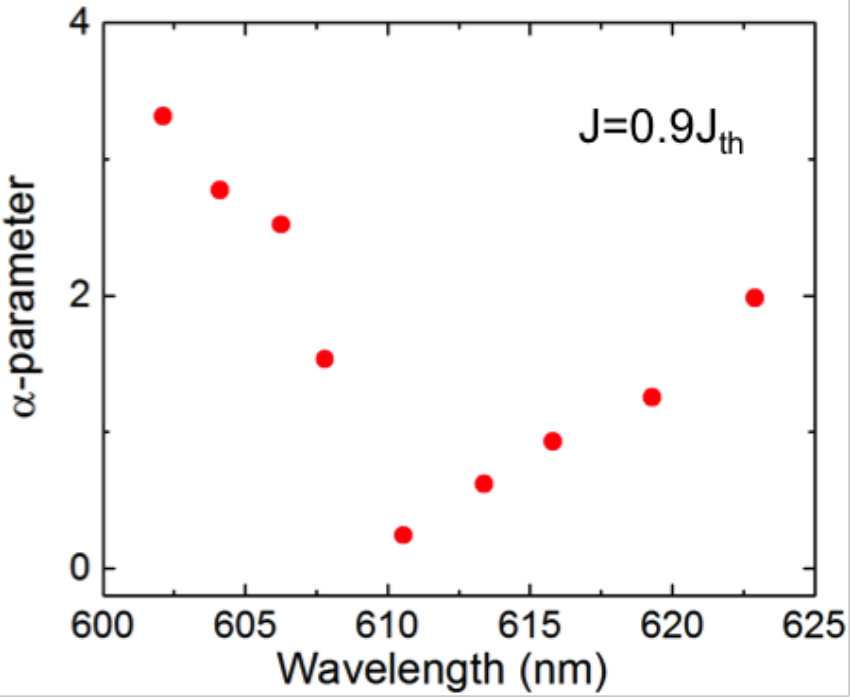


Figure 6.19: Linewidth enhancement factor α as function of the emission derived from Hakki-Paoli measurements below lasing threshold (Courtesy: Shafat Jahanmir).

modes of InGaN on finite-sized (0001)-oriented GaN [123]. The particular growth mode depends on the alloy composition, strain distribution in the heterostructure, defect density and adatom kinetics on the (0001) surface. In general, the layer-by-layer FM growth mode is not favored for large In compositions, as observed in this study. The VW mode, in which the island is formed without a 2D wetting layer, is generally favored. However, the SK mode of island formation is also possible for larger thicknesses or with increasing defect density. The total formation energy of an InGaN VW QD in a GaN nanowire is calculated using finite element method and plotted in Fig. 6.20 for nanowires of three different diameters. The energy incorporated in the calculation includes the strain energy, interfacial energy, and surface energy of GaN and InGaN. The formation of a 40-50 nm QD is energetically favored in a 92 nm diameter nanowire. This is in fair agreement with the TEM images. Smaller diameter (20 and 30 nm) nanowires can accommodate smaller QDs, whose size is limited only

by the NW diameter itself.

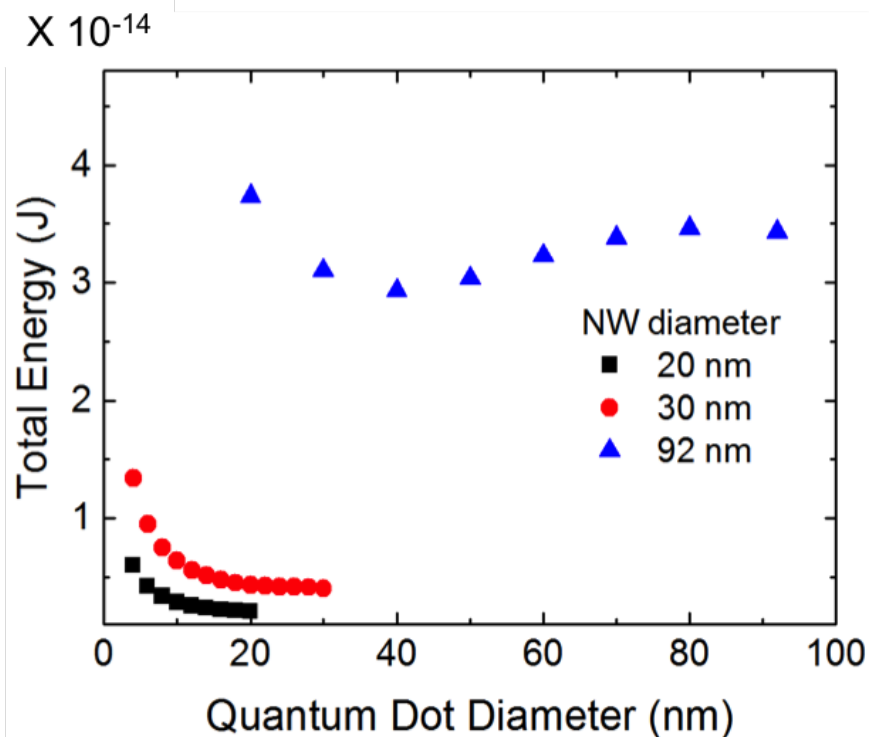


Figure 6.20: Calculated energetically stable diameter for a Volmer-Weber InGaN QD formed in GaN nanowires of different dimensions (Courtesy: Prof. Zetian Mi)

6.9 Summary

The nature of quantum confinement in InGaN/GaN disks-in-nanowires and similar GaN disks in AlGaN nanowires on silicon was investigated. The radiative lifetime measured in InGaN/GaN disks shows an increase with temperature, indicative of an electron-hole scattering mechanism which is seen only in quantum dots with discrete energy states. HRTEM images show island formation in the InGaN disk regions. Finally, single-photon emission was observed from a 25 nm InGaN/GaN disk-in-nanowire. All aforementioned results point to the existence of a quantum dot in the InGaN disk in GaN nanowire. Contrasting results were obtained from GaN/AlGaN disk-in-nanowires, with a constant radiative lifetime as a function of

temperature, no island formation seen in TEM imaging and classical $g^{(2)}(0)$ behavior. The formation of self-organized quantum dots within the disk regions allows long wavelength emission, which is not achievable using InGaN/GaN quantum wells. Red emitting lasers with InGaN/GaN disk-in-nanowires as the active gain media were fabricated and studied. The linewidth enhancement factor of this device shows a dip at 610 nm, a behavior expected from a quantum dot gain region.

CHAPTER VII

Conclusions And Future Directions

7.1 Summary

Nitride based nanostructures: disk-in-nanowires and quantum dots have been investigated as single-photon emitters. The large exciton binding energy in nitride materials, oscillator strength of the radiative transition and large band offsets make nitride-based heterostructures suitable for high temperature emitters. We have demonstrated high temperature single-photon emitters that operate under both optical and electrical excitation. Single-photon emission in the visible spectral regime, ranging from blue to red has been shown.

7.1.1 Quantum Disk-In-Nanowire Based Single-Photon Source Operating At 200 K

Blue emitting single $In_{0.2}Ga_{0.8}N/Al_{0.1}Ga_{0.9}N$ disk-in-nanowires were grown by MBE. Structural and optical characterization was performed on the sample. Single InGaN disks show anti-bunching under optical excitation, with a background corrected $g^{(2)}(0)$ of 0.44 at 200 K, without the use of a microcavity. The single-photon emitter could potentially be operated at a repetition rate of $\sim 1GHz$, due to the short radiative lifetime (0.7 ns) of emitted photons. Blue single photons have applications in free-space quantum cryptography.

7.1.2 Single Disk-In-Nanowire Based Electrically Injected Single-Photon Source

Nanowire p-n junctions with a single InGaN disk in the active region were grown on (111) Si and single nanowire light emitting diodes were fabricated on (001) Si. This is the first demonstration of electroluminescence from a single disk-in-nanowire. The electroluminescence shows exciton and biexciton transitions in blue and green wavelength range. Single-photon emission was observed from both exiton and biexciton lines. The relatively small radiative decay time is a remarkable advantage of the dot-in-nanowire geometry as it potentially allows for large repetition rates in single-photon emitters. The emission is polarized along the c-axis of the nanowire, which means this device can offer polarization control which is very important in most single-photon application. At this point, the device operates as a single-photon source only up to 125 K. Operation of the device at higher temperatures will require engineering of the dot heterostructure to allow for better carrier confinement in the disk. This device is very attractive from the standpoint of compatibility and integration with silicon technology.

7.1.3 Quantum Dot Based Single Photon Diode Operating At Room Temperature

Single $In_{0.4}Ga_{0.6}N/GaN$ quantum dot diodes were grown and fabricated with nanoscale apertures to collect the luminescence from a single emitter. Red emitting single photons are important for a variety of applications. The layer of InGaN/GaN quantum dots shows a very low density compared to previous reports. Room temperature single-photon emission with $g^{(2)}(0)$ of only 0.29 was observed. This is the first semiconductor based single-photon source to operate at room temperature under electrical excitation. The source can be triggered up to an excitation repetition rate of 200 MHz due to the short excitonic lifetime ($\sim 1\text{ns}$) and very low series resistance

of the diode.

7.1.4 Understanding The Nature Of Quantum Confinement In Disk-In-Nanowires

Having studied InGaN/GaN disks-in-nanowires for a variety of applications such as single-photon emitters, light emitting diodes and lasers, we have investigated the nature of quantum confinement in these nanostructures in more detail. We studied thin ($\sim 2 - 4$ nm) InGaN disks incorporated in GaN nanowires and similar GaN disks in AlGaN nanowires grown on silicon substrates by plasma-assisted molecular beam epitaxy. An examination of the trend of the radiative lifetime with variation of temperature – lifetime increasing with temperature – for the InGaN disks suggests the formation of a self-organized island within the disk, which behaves as a quantum dot. This is supported by direct observation of the islands by HRTEM imaging and the recording of single-photon emission from the single quantum dot. Additionally, the linewidth enhancement factor of an InGaN/GaN DINW electrically modulated laser shows behavior expected from a quantum dot gain region. In contrast, such island (QD) formation is not observed in the GaN disk regions in the AlGaN nanowires.

7.2 Future Directions

7.2.1 Site-Controlled Nanowire Growth

In all devices investigated in this study, there is no preferential nucleation or growth position for the self-organized quantum dots or nanowires. The location of the nanowires is further randomized once they are dispersed. This requires extensive mapping of the substrate by SEM imaging and looking at many nanowires by brute force in search of the desired emission characteristics. It would much more convenient to deterministically position a single nanowire/quantum dot. Additionally, the emis-

sion properties are likely to be more uniform, with a high yield of single emitters. Many techniques for quantum-dot placement have recently been investigated such as droplet epitaxy, etching etc. In the case of PA-MBE, site-controlled growth of GaN nanowires has been shown by selective growth of GaN nanowires in holes, in a patterned silicon oxide mask [124]. The oxide is deposited on a thin AlN buffer layer previously grown on Si(111) substrate. Regular arrays of holes are patterned in the oxide layer by e-beam lithography. The size and pitch of the holes are critical to obtain selectivity. By adjusting the growth parameters- substrate temperature and fluxes, nanowires can be selectively grown in the holes of the patterned oxide with complete suppression of the unwanted growth on the oxide. The occupation probability of a hole with a single or multiple NWs depends strongly on its diameter.

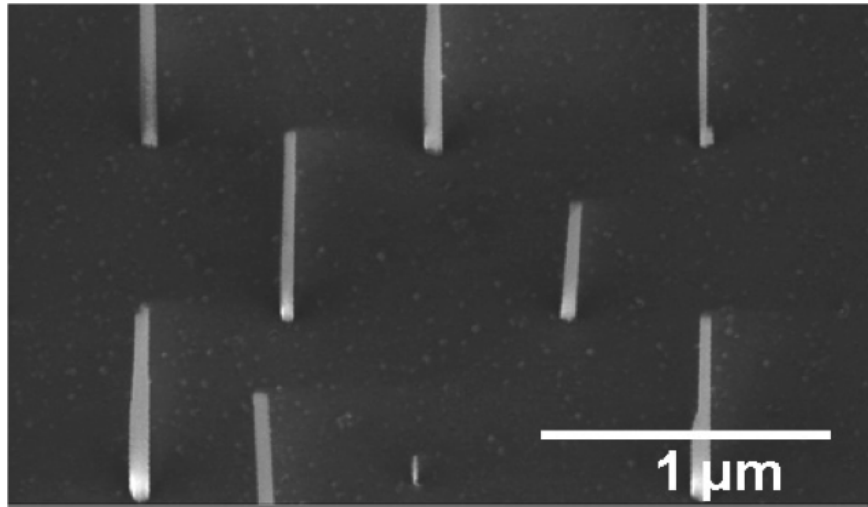


Figure 7.1: SEM micrograph of selective area GaN nanowire growth within holes in oxide mask [124].

7.2.2 Improving single-photon source Efficiency Using A Microcavity

While a single quantum dot spontaneously emits single photons due to its discrete states that resemble a two-level system, it suffers from a poor overall efficiency without a microcavity. The efficiency in most devices in this work has been limited to 1 – 2%.

The coupling efficiency of a quantum dot can be increased by embedding it in a high quality microcavity providing three dimensional photon confinement. Coupling a single emitter to a cavity is very desirable for a number of reasons. The Purcell effect can be used to significantly increase the spontaneous emission rate and brightness of a single-photon emitter. It can lead to higher repetition rates, high quantum efficiencies, and increased indistinguishability of emitted photons. Coupling the quantum dot emission to a cavity will direct this emission into the cavity mode, which can be engineered to be easily coupled to fiber or to free-space optics.

Epitaxial deposition techniques such as MBE allow for the fabrication of monolithic Fabry-Perot microcavities. In the GaAs system, the DBRs consist of alternating layers of GaAs and AlGaAs, with the thickness of each layer equal to one quarter of the optical wavelength in the material. For a range of wavelengths and incidence angles known as the stopband, the partial reflections from all of the interfaces in the DBRs add up in phase, making the structure a high reflector. Between the DBRs, a spacer layer of GaAs (or AlGaAs) is grown with an optical thickness of one or multiple half-wavelengths. The reflections from the two DBRs form a standing wave, whose antinode is located in the center of the spacer layer, where the active region is located.

The MBE growth of nitride DBRs with a large refractive index contrast (AlN, GaN) is challenging and would necessitate the growth of a very large number of pairs which is not feasible due to the slow growth rate of MBE. Thus, as an alternative to MBE grown DBRs, dielectric DBRs can be employed.

Polariton lasing at room temperature was recently demonstrated using a GaN nanowire in dielectric DBRs [112]. Similarly, an InGaN/GaN disk-in-nanowire can be dispersed on a substrate with pre-deposited bottom DBRs and a half cavity. Following the dispersion of nanowires, the cavity is completed and top DBRs are deposited by electron beam evaporation.

Since the technology for electrically injected single nanowire LEDs has been developed to fabricate LEDs on a variety of substrates, it can easily be used to fabricate a nanowire diode on a substrate composed of the bottom DBR and half-cavity. Thus, the nanowire embedded within a DBR microcavity can be electrically excited. A single InGaN/GaN nanowire diode will be dispersed on top of the half cavity layers composed of alternating SiO_2 and TiO_2 layer, p-and n-type contacts will be fabricated. The device is shown schematically in Fig. 7.2 [125]. The mesa definition after deposition of the top DBR will allow the contacts to be probed.

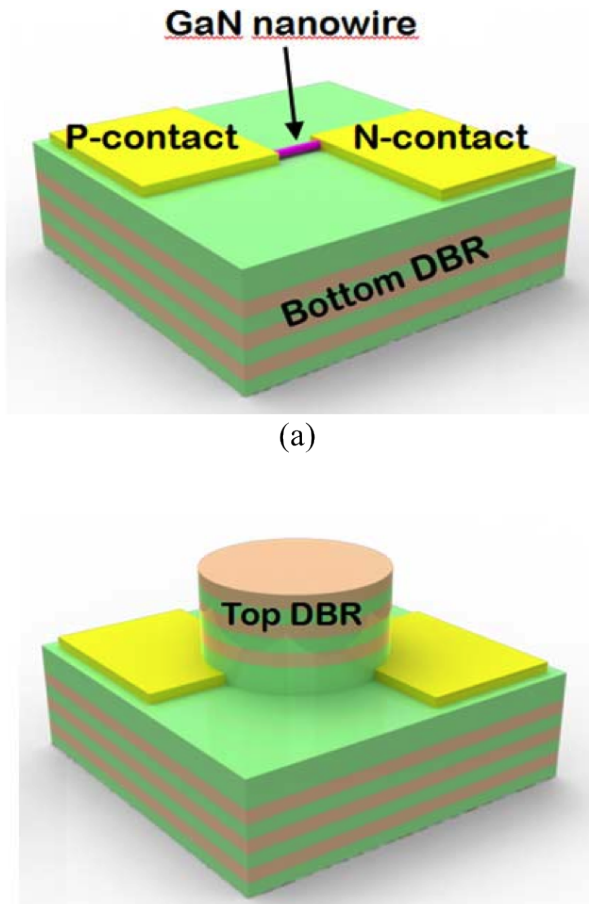


Figure 7.2: Schematic of an electrically driven nanowire LED in a microcavity [125].

The aforementioned approach suffers from the limitation of transferring the nanowires to a Si substrate before fabricating the cavity. An alternate approach is to create a 2D

photonic crystal microcavity centered around InGaN/GaN disk-in-nanowire directly grown on a Si substrate. By careful control of growth conditions, a very low nanowire density of $10^8/cm^2$ can be achieved. The device heterostructure, shown in Fig. 7.3 shows a e-beam lithographically defined 2D photonic crystal pattern in a dielectric layer such as titanium dioxide and a single GaN nanowire at the center of an H2 point defect. To minimize optical losses from the titanium oxide layer to the Si substrate, a spin-on-glass layer is placed beneath underneath it, as a low-refractive-index material. Optically pumped lasing at room temperature has been observed previously using this system [126].

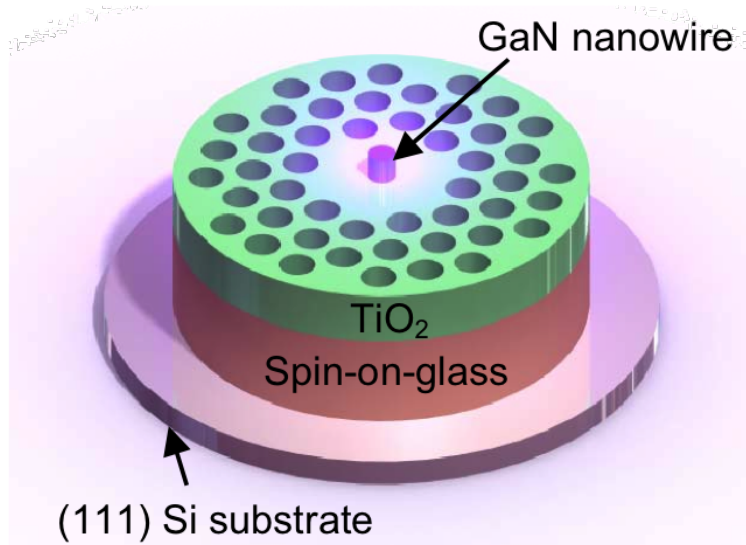


Figure 7.3: Schematic of photonic crystal GaN nanowire laser [126]

7.2.3 Strong Coupling And Lasing

By inserting a quantum dot in a microcavity, emission in two distinct regimes can be obtained, depending on the strength of the interaction between the QD exciton and cavity mode. In the weak coupling regime, as described in the previous section, the spontaneous emission rate is modified by the Purcell effect. The emission rate from a quantum dot, however, does not continue to increase indefinitely as the cavity quality factor increases. Eventually, coupling between the dot and the cavity mode

becomes larger than the decay rate of either the exciton or the cavity photon and it enters the strong-coupling regime of emission. In this case, the photons emitted in the cavity continue to be re-absorbed and re-emitted giving rise to Rabi oscillations. Anti-bunching in a strongly coupled exciton/photon system has been demonstrated using micropost cavities and photonic crystal array in the III-As system [127, 128] and similar approaches could be adopted in InGaN quantum dots. Achieving high temperature single-photon emission in a strongly coupled cavity will have important implications to quantum information processing.

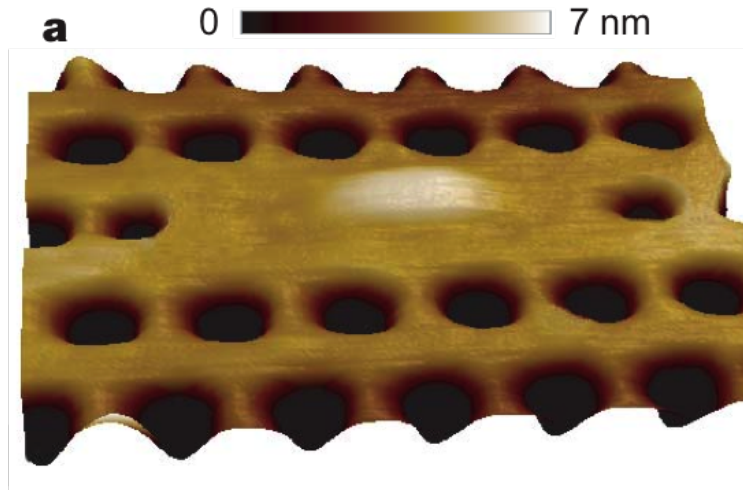


Figure 7.4: AFM topography of a photonic crystal nanocavity aligned to a hill of material on the surface arising from a InAs QD buried below [127]

7.2.4 Generation Of Entangled Photon-Pairs

Since most of the emitters we have studied, show both exciton and biexciton emission it may be possible to use single InGaN quantum dots to generate polarization-entangled photon pairs. Instead of spectrally isolating only the single-exciton peak, as we do in single-photon measurements, both the exciton and biexciton lines will be filtered and studied. The two photons collected for each pump pulse should have anticorrelated polarizations, if radiative recombination in the quantum dot follows

selection rules [129]. The generation of entangled photons, starting from the biexcitonic state, is similar to two-photon cascade decay in an atom [40]. One of the two excitons recombines first and emits a left- or right-circularly polarized photon. The remaining exciton, with opposite carrier spins, then recombines and emits a photon of opposite polarization. If the two decay paths are indistinguishable, the two photons are in a maximally entangled (Bell) state:

$$|\psi\rangle = \frac{1}{\sqrt{2}}(|\psi^+\rangle_1|\psi^-\rangle_2 + |\psi^-\rangle_1|\psi^+\rangle_2) \quad (7.1)$$

7.2.5 Electron Energy Loss and Gain Spectroscopy In Biased InGaN/GaN Disk-In-Nanowires

TEM/EELS are well established techniques for studying modes of plasmonic structures like metal nanowires. The single nanowire diode fabrication technology has been developed to fabricate single nanowires LEDs on a variety of substrates, including TEM grids (as seen in Fig. 7.5). Single nanowire diodes fabricated on 30 nm Si_3N_4 TEM membranes are shown schematically in Fig. 7.5 (a). Fabrication steps for the device are described in Section 4.4.1. An SEM image and I-V curve of one such fabricated device is seen in (b) and (c), respectively. The device shows diode behavior but is more resistive and less robust than devices on Si substrates. The lithography and liftoff performed on TEM membranes may be leaving behind organic or metal residue, which is hard to remove because of the gentle approach adopted during cleaning and liftoff. A similar device can be fabricated by Pt deposition in a focused ion beam tool, where SEM imaging and metal deposition can be performed in-situ simultaneously without any lithography. The device will be used to investigate the electron energy loss spectra in the InGaN quantum dot through in-situ bias dependent TEM-EELS measurements.

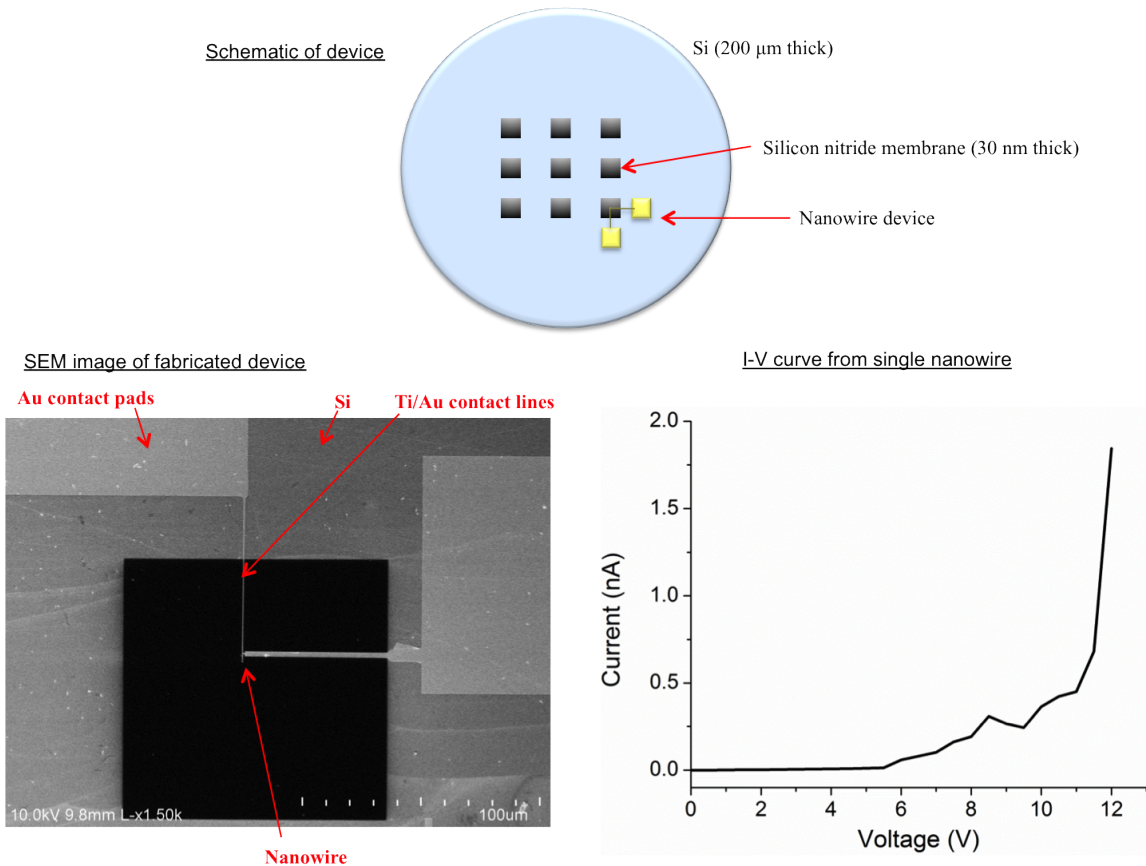


Figure 7.5: Single nanowire diodes fabricated on TEM membranes shown schematically in (a). (b) depicts a low-magnification SEM image of fabricated device and (c) shows the I-V characteristics of the device measured at room-temperature.

APPENDICES

APPENDIX A

Determining average nanowire diameter

Top view SEM images of nanowires are analyzed with ImageJ and Matlab. This routine detects the illuminated pixels corresponding to the nanowires, based on a set threshold of brightness/darkness values, and counts them against the dark background to give a measure of the no. of nanowires, density and their diameter.

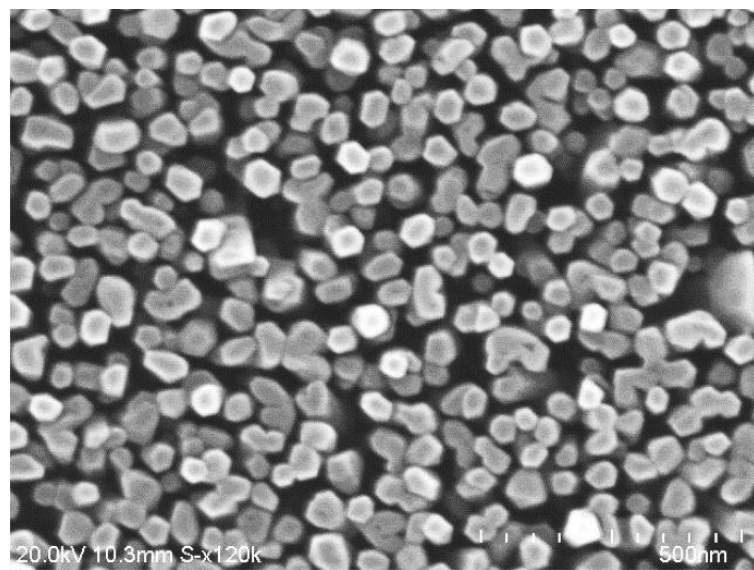


Figure A.1: Top view SEM image: Input to MATLAB

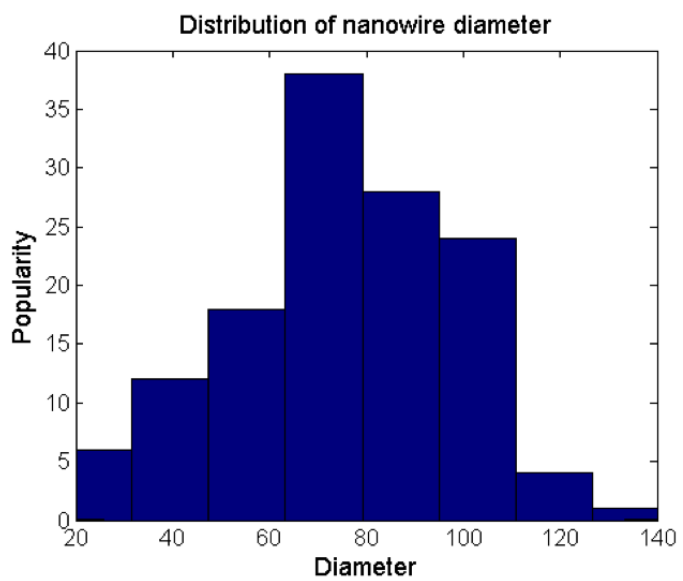


Figure A.2: Distribution of nanowire diameters: Output from MATLAB

APPENDIX B

Fabrication of single nanowire LED

1. Sample preparation and cleaning

1.1. Piranha clean ($H_2SO_4 : H_2O_2 = 3 : 1$) (001) Si wafers to remove organic residues.

Rinse with DI water.

1.2. Pre-furnace clean.

1.3. Oxidation 100 nm of thermal oxide on wafer.

2. Patterning alignment marks:

2.1 Electron beam lithography

2.1.1. Spin MicroChem 950K A4 at 4000 rpm for 45 seconds.

2.1.2. Baking the sample at 180°C on hot plate.

2.2. Electron beam lithography.

2.2.1 Apply Nickel beads on sample corner to adjust focus.

2.2.2. Set Accelerating voltage 20 kV, Apperture size 10 μm , Dose 180-200 C/cm^2 .

2.2.3 Expose cross alignment marks (200 nm width) separated by a Write Field (100 μm)

2.3 Development

- 2.3.1. Developer solution (IPA: MIBK = 3 : 1) must be made 1 hour prior to use.
- 2.3.2. Stir the sample in developer for 1min.
- 2.3.3. Rinse the sample in IPA for 45 sec.
- 2.3.4. Blow IPA on the sample with nitrogen.

2.4. Descum

- 2.4.1. March ash in GaAs bay is used.
- 2.4.2. Pressure : 200 mT.
- 2.4.3. Power : 30 W.
- 2.4.4. Time : 15 sec.

2.5 Electron beam evaporation

- 2.5.1 Load sample in electron beam evaporation chamber (SJ-20, Energet evaporator)
- 2.5.2 Pump down chamber for 90 minutes to achieve low vacuum $2e - 6$ Torr.
- 2.5.3 Deposit Ti/Au (5nm/45nm)

2.6 Liftoff

- 2.6.1 Unload sample with metal deposition.
- 2.6.2 Place sample in acetone until metal liftoff is achieved.
- 2.6.3 Final solvent clean with IPA and water, dry with nitrogen gun.

3 Dispersing nanowires:

- 3.1 Use a blade to remove nanowires from as-grown substrate into a beaker of 10 mL IPA.
- 3.2 Seal the beaker and place in ultra-sonic bath for 20 minutes.
- 3.3 Pipette out one drop of liquid on prepared substrate.

4. Contacting nanowires:

4.1 Identify thin isolated nanowires under SEM.

4.1.1 Set Accelerating voltage : 20 kV, Apperture size : 10 μm , Dose : 180-200 C/cm^2 .

4.1.2 Perform angle compensation to ensure sample is perfectly straight.

4.1.3 Find x,y co-ordinates of nanowire from closest alignment crossmark.

4.1.4 Note down this position for several nanowires. Choose one nanowire in each Write Field.

4.2 Electron beam lithography

4.2.1. Prepare GDS with $2\mu\text{m} \times 10\mu\text{m}$ at each end of nanowires, based on recorded cor-ordinates.

4.2.2. Spin MicroChem 950K A4 at 4000 rpm for 45 seconds.

4.2.3. Bake the sample at 180°C on hot plate.

4.2.4 Apply Nickel beads on sample corner to adjust focus.

4.2.5. Set Accelerating voltage 20 kV, Apperture size 10 μm , Dose 180-200 C/cm^2 .

4.2.6 Perform Write Field Alignment.

4.2.7 Expose contacts all at once.

4.3 Electron beam evaporation

4.3.1 Load sample in electron beam evaporation chamber (Cooke for p-contact deposition, SJ-20 or Energet evaporator for n-contact)

4.3.2 Pump down chamber for 90 minutes to achieve low vacuum $2e - 6$ Torr.

4.3.3 Deposit Ti/Au (5nm/45nm) for n-contact and Pd/Au (5nm/45nm) for p-contact

4.4. Liftoff: Follow 2.6.

4.5 Deposit large contact pads ($100\mu\text{m} \times 100\mu\text{m}$) following 4.1, 4.2, 4.3. MicroChem

950K A6 can be used with the same recipe to have a thicker resist layer. Larger aperture of $60\mu m$ will be used to minimize write-time for large pads. Metal thickness deposited is Ti/Au (100nm/900nm).

4.6 Anneal sample by rapid thermal annealing for 5 minutes at $450^{\circ}C$ in $N_2 + O_2$ ambient. Recipe used p-GaNmengnair450C5min.

5. Wirebonding

Wirebond sample to chip carrier at elevated temperature to allow easy bonding and prevent excessive force applied to nanowire.

APPENDIX C

Fabrication of single QD LED

1. Deposition of Alignment Mark

1.1 Solvent clean:

Acetone: 10 min on hot plate IPA 10 min

DI water Rinse: 2 min

1.2 Lithography

Dehydrate bake: 2 min, 115°C hotplate

Resist coating: HMDS, SPR 220-3.0 4.0 krpm, 30 sec Pre-bake: 90 sec at 115°C on hotplate

Exposure: 0.34 sec in projection stepper (GCA AS200 AutoStep stepper)

Post-bake: 90 sec at 115°C

Resist development: AZ 300 MIF 55 sec;

DI water rinse 3 min

1.3 Descum:

30 sec, 80 W, 250mT, 17% O_2

1.4 Metal Deposition Ti/Au 10 nm /30 nm

1.5 Metal Lift-off in Acetone

2. P-contact deposition

2.1 Solvent clean

2.2 Lithography

2.3 Descum:

2.4 Metal Deposition Ni/Au 5 nm /5 nm

2.5 Metal Lift-off in Acetone

3. Metal mask with apertures (Trimming technique to obtain nanoscale apertures)

3.1 Solvent clean

3.2 Lithography: Overexpose 15% (0.4 sec) and overdevelop 25% (70 seconds)

3.3 5 minutes Ar etch in Yes Plasma Stripper

3.4 Metal Deposition Al (300 nm) in Enerjet Evaporator

3.5 Metal Lift-off overnight in Acetone

4. Defining Mesa Geometry

4.1 Solvent clean

4.2 Lithography

4.3 Plasma Etching LAM

ICP etching, etching recipe chlorine based. The etching rate is calibrated to be 4.5-5.5 nm/s.

4.4 Descum

4.5 Dektak: measure mesa height

5. Etching till n-GaN

5.1 Solvent clean

5.2 Lithography

5.3 Plasma Etching LAM

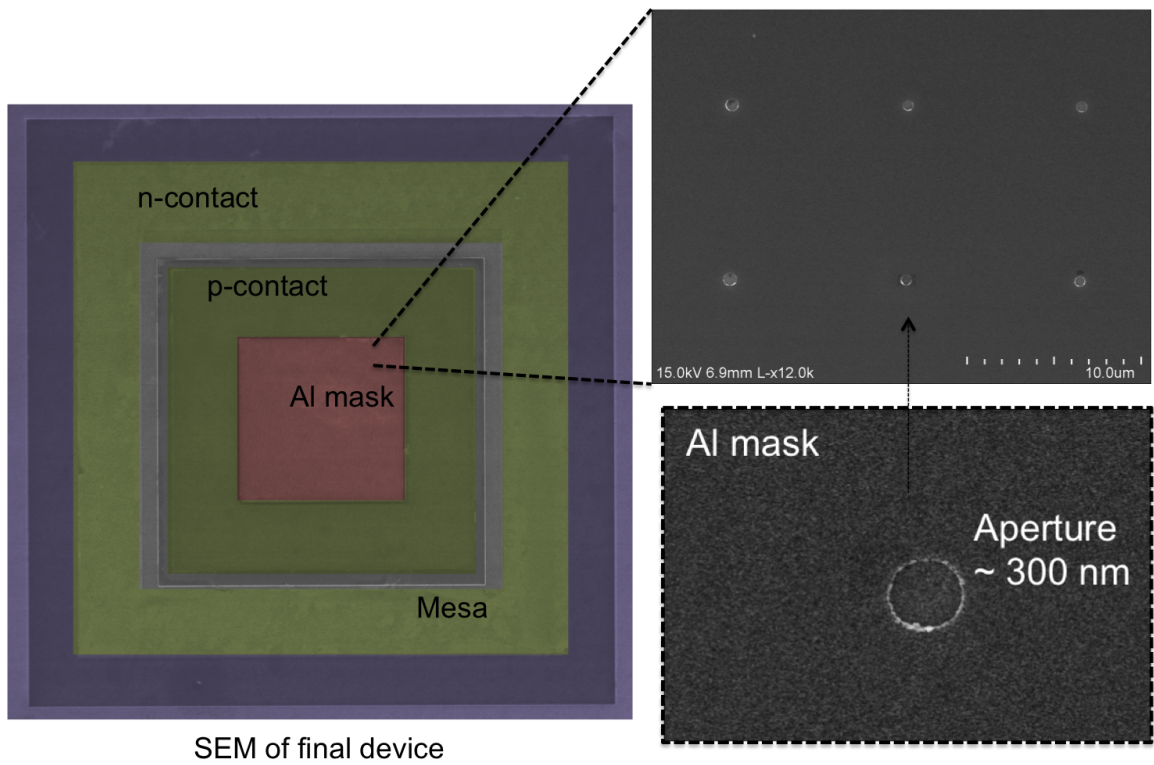


Figure C.1: SEM micrograph of fabricated device, shown in increasing levels of magnification

5.4 Resist Removal

5.5 Etch rate measurement: Dektak

7. SiO_x deposition: 1000 nm using GSI PECVD

7. Deposition of n-contact and contact pads

7.1 Lithography

7.2 Descum

7.4 Metal deposition

Ti/Au = 25nm/300nm

7.5 Lift-off

APPENDIX D

COMSOL simulation of nanowire temperature

For the simulation nanowire temperature COMSOL Multiphysics was used. The model used was Heat Transfer. It can be assumed that conduction is the only mode of heat loss in the system based on these assumptions:

1. The cryostat is pumped down before it is cooled to cryogenic temperatures, so it is valid to assume heat loss due to convection is negligible.
2. The area of the nanowire is very small ($6.6e - 14m^2$), so we can neglect radiative heat loss.

Heat transfer model: Radiation and convection losses are set to 0.

The oxide and Si wafer act like thermal resistors and the helium cold finger is a heat sink at 10 K.

The I^2R electrical power is converted to thermal power, which makes its way through the thermal resistors to the heat sink at 10K. Thus heat source for each current is provided through I^2R calculation in Watts.

The model is built using actual nanowire dimensions (See figure). Mesh size used is “Extremely fine.”

All material constants used for wurtzite GaN are provided below.

Bulk modulus $20.4 \times 10^{11} dyn cm^{-2}$

Debye temperature 600 K

Melting point 2500°C

Specific heat $0.49 Jg^{-1}C^{-1}$

Thermal conductivity $1.3 Wcm^{-1}C^{-1}$

Thermal diffusivity $0.43 cm^2 s^{-1}$

Thermal expansion coefficient, linear $\alpha = 3.17 \times 10^{-6} K^{-1}$

$C_p = 38.1 + 8.96 \times 10^{-3} T (Jmol^{-1}K)$

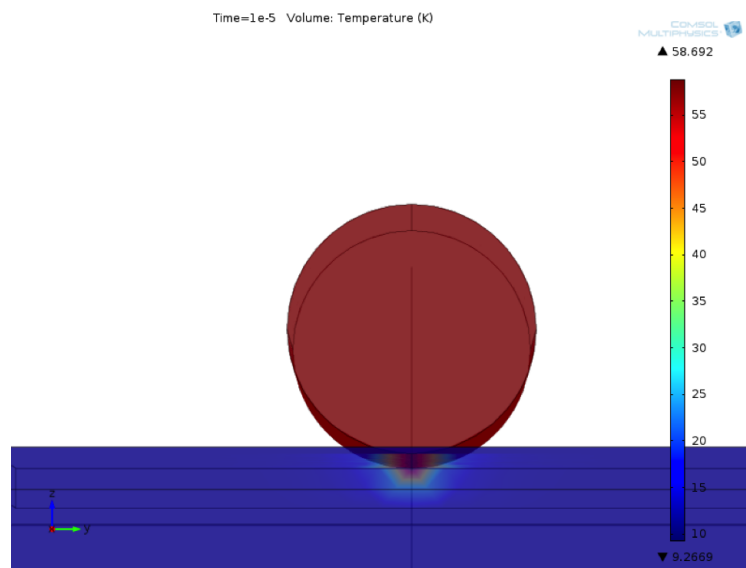


Figure D.1: Raw output file showing nanowire temperature

BIBLIOGRAPHY

BIBLIOGRAPHY

- [1] Albert Einstein. ber einen die Erzeugung und Verwandlung des Lichtes betreffenden heuristischen Gesichtspunkt. *Annalen der Physik*, 17:132–4, 1905.
- [2] H Kimble, L Dagenais, M. and Mandel, and Mandel Dagenais. Photon Anti-bunching in Resonance Fluorescence. *Physical Review Letters*, 39(11):691–695, 1977.
- [3] D Groom. Silicon photodiode detection of bismuth germanate scintillation light. *Nucl. Instrum. Methods Phys. Res.*, 219(141), 1984.
- [4] R Glauer. The Quantum Theory of Optical Coherence. *Phys. Rev.*, 130(2529), 1963.
- [5] R Hanbury, Brown, and R Twiss. A Test of a New Type of Stellar Interferometer on Sirius. *Nature*, 178(4541), 1956.
- [6] M Fox. Quantum Optics: An Introduction. *Oxford University Press*, 2006.
- [7] M Eisaman, J Fan, A Migdall, and S Polyakov. Single-photon sources and detectors. *Review Of Scientific Instruments*, 82(071101), 2011.
- [8] C Bennett and G Brassard. Quantum cryptography: Public key distribution and coin tossing. *Proceedings of IEEE International Conference on Computers, Systems, and Signal Processing, Bangalore, India*, pages 175–179, 1984.
- [9] C Bennett. Quantum cryptography using any two nonorthogonal states. *Phys. Rev. Lett.*, 68(3121), 1992.
- [10] C Bennett, G Brassard, and J Robert. Experimental Quantum Cryptography. *J.Comput.*, 17(210), 1988.
- [11] C Bennett, F Bessette, G Brassard, L Salvail, and J Smolin. Experimental Quantum Cryptography. *J.Cryptol.*, 5(3):3–28, 1992.
- [12] P Pownsend, J Rarity, and P Tapster. Single photon interference in a 10 km long optical fibre interferometer. *Electron. Lett.*, 29(634), 1993.
- [13] S Stucki, G Gisin, and O Guinnard. Quantum key distribution over 67 km with a plug and play system. *New J. Phys.*, 4(41), 2002.

- [14] Y Liu. Decoy-state quantum key distribution with polarized photons over 200 km. *Opt. Express*, 18(8), 2010.
- [15] E Waks, E Inoue, and C Santori. Quantum key distribution over 67 km with a plug and play system. *Nature*, 420(726), 2000.
- [16] T Pittman, B Jacobs, and Franson J. Demonstration of Nondeterministic Quantum Logic Operations Using Linear Optical Elements. *Phys. Rev. Lett.*, 88(6), 2002.
- [17] C Monroe. Quantum information processing with atoms and photons. *Nature*, 416(4):238–246, 2002.
- [18] M Xiao, L Wu, and L Kimble. Precision measurement beyond the shot noise limit. *Phys. Rev. Lett.*, 59(278), 1987.
- [19] M Hennrich, T Legero, A Kuhn, and G Rempe. Photon statistics of a non-stationary periodically driven single-photon source. *New Journal Phys*, 6(86), 2004.
- [20] T Wilk, S Webster, H Specht, G Rempe, and A Kuhn. Polarization-Controlled Single Photons. *Phys. Rev. Lett.*, 98(063601), 2007.
- [21] T Aoki, A Parkins, D Alton, C Regal, B Dayan, E Ostby, K Vahala, and H Kimble. Efficient Routing of Single Photons by One Atom and a Microtoroidal Cavity. *Phys. Rev. Lett.*, 102(083601), 2009.
- [22] B Blinov, D Moehring, L Duan, and C Monroe. Observation of entanglement between a single trapped atom and a single photon. *Nature*, 428(153), 2004.
- [23] M Keller, B Lange, K Hayasaka, W Lange, and H Walther. Continuous generation of single photons with controlled waveform in an ion-trap cavity system. *Nature*, 431:1075, 2004.
- [24] C Maurer, C Becher, C Russo, J Eschner, and R Blatt. A single-photon source based on a single Ca+ ion. *New Journal Phys.*, 6(94), 2004.
- [25] Lounis. B and Moerner.W. Single photons on demand from a single molecule at room temperature. *Nature*, 407(7), 2000.
- [26] A Beveratos, R Brouri, T Gacoin, J Poizat, and P Grangier. Nonclassical radiation from diamond nanocrystals. *Phys. Rev. A*, 64(061802(R)), 2001.
- [27] C Brunel, B Lounis, P Tamarat, and M Orrit. Triggered Source of Single Photons based on Controlled Single Molecule Fluorescence. *Phys. Rev. Lett.*, 83(2722), 1999.
- [28] R Brouri, A Beveratos, J Poizat, and P Grangier. Photon antibunching in the fluorescence of individual color centers in diamond. *Opt. Lett.*, 25, 2000.

- [29] J. Choy, B. Hausmann, I. Bulu, M. Khan, P. Maletinsky, A. Yacoby, and M. Loncar. Enhanced single-photon emission from a diamond-silver aperture. *Nat. Photonics*, 5(738), 2011.
- [30] T. Babinec, B. Hausmann, M. Khan, Y. Zhang, J. Maze, P. Hemmer, and M. Loncar. A diamond nanowire single-photon source. *Nat. Nanotechnology*, 5(195), 2010.
- [31] X. Brokmann, L. Coolen, M. Dahan, and J. Hermie. Triggered Source of Single Photons based on Controlled Single Molecule Fluorescence. *Phys. Rev. Lett.*, 93(107403), 2004.
- [32] N. Mizuuchi et al. Electrically driven single-photon source at room temperature in diamond. *Nat. Photonics*, 6, 2012.
- [33] O. Fedorych, C. Kruse, A. Ruban, D. Hommel, G. Bacher, and T. Kummell. Room temperature single photon emission from an epitaxially grown quantum dot. *Appl. Phys. Lett.*, 100(061114), 2012.
- [34] W. Unrau, D. Quandt, J.-H. Schulze, T. Heindel, T. D. Germann, O. Hitzenmann, A. Strittmatter, S. Reitzenstein, U. Pohl, and D. Bimberg. Electrically driven single photon source based on a site-controlled quantum dot with self-aligned current injection. *Appl. Phys. Lett.*, 101(211119), 2012.
- [35] T. Heindel, C. Schneider, M. Lermer, S. H. Kwon, T. Braun, S. Reitzenstein, S. Hofling, M. Kamp, and A. Forchel. Electrically driven quantum dot-micropillar single photon source with 34% overall efficiency. *Appl. Phys. Lett.*, 96(011107), 2010.
- [36] F. Hargart, C. A. Kessler, T. Schwarzback, E. Koroknay, S. Weidenfeld, M. Jetter, and P. Michler. Electrically driven quantum dot single-photon source at 2 GHz excitation repetition rate with ultra-low emission time jitter. *Appl. Phys. Lett.*, 102(011126), 2013.
- [37] M. Reischle, G. J. Beirne, W.-M. Schulz, M. Eichfelder, R. Robach, M. Jetter, and P. Michler. Electrically pumped single-photon emission in the visible spectral range up to 80 K. *Opt. Express*, 16(12771), 2008.
- [38] C. Santori, D. Fattal, J. Vuckovic, G. Solomon, and Y. Yamamoto. Indistinguishable photons from a single-photon device. *Nature*, 10, 2002.
- [39] Z. Yuan, B. Kardynal, R.M Stevenson, A.J Shields, C.J Lobo, K. Cooper, N.S Beattie, D.A Ritchie, and M. Pepper. Electrically driven single-photon source. *Science*, 295, 2002.
- [40] O. Benson, C. Santori, M. Pelton, and Y. Yamamoto. Regulated and Entangled Photons from a Single Quantum Dot. *Phys. Rev. Lett.*, 84, 2000.

- [41] S Buckley, K Rivoire, and J Vuckovic. Engineered quantum dot single-photon sources. *Rep. Prog. Phys.*, 75(126503), 2012.
- [42] L Zhang, C Teng, T Hill, L Lee, P Ku, and H Deng. Single photon emission from site-controlled InGaN/GaN quantum dots. *Appl. Phys. Lett.*, 103(192114), 2013.
- [43] S. Kako, C. Santori, K. Hoshino, S. Gotzinger, Y. Yamamoto, and Y. Arakawa. A gallium nitride single photon source operating at 200 K. *Nat. Materials*, 5, 2006.
- [44] S Deshpande, T Frost, A Hazari, and P Bhattacharya. Electrically pumped single-photon emission at room temperature from a single InGaN/GaN quantum dot, volume = 105. *App. Phys. Lett.*, (141109), 2014.
- [45] M Holmes, K Choi, S Kako, M Arita, and Y Arakawa. Room-Temperature Triggered Single Photon Emission from a III-Nitride Site-Controlled Nanowire Quantum Dot. *Nanoletters*, 14(2), 2014.
- [46] J-H. Kim, Y-H Ko, Gong S-H, S-M. Ko, and Y-H. Choa. Ultrafast single photon emitting quantum photonic structures based on a nano-obelisk. *Scientific Reports*, 3(2150), 2013.
- [47] S.Deshpande, A.Das, and P.Bhattacharya. Blue single photon emission up to 200 K from an InGaN quantum dot in algan nanowire. *Appl. Phys. Lett.*, 102(161114), 2013.
- [48] K.Bertness, A.Sanford, and A.Davydov. GaN nanowires grown by molecular beam epitaxy. *IEEE J. Select. Topics Quantum Electron*, 17:847–858, 2011.
- [49] L.Cerutti et al. Wurtzite GaN nanocolumns grown on Si(001) by molecular beam epitaxy. *Appl. Phys. Lett.*, 88(213114), 2006.
- [50] K.Kishino, A.Kikuchi, H.Sekiguchi, and S.Ishizawa. InGaN/GaN nanocolumn LEDs emitting from blue to red. *Proc. SPIE*, 6473, 2007.
- [51] V.Consonni. Self-induced growth of GaN nanowires by molecular beam epitaxy:A critical review of the formation mechanisms. *Phys. Status Solidi*, 7, 2013.
- [52] N.Sanford et al. Steady-state and transient photoconductivity in c-axis GaN nanowires grown by nitrogen-plasma-assisted molecular beam epitaxy. *J.Appl.Phys.*, 107(034318), 2010.
- [53] A Armstrong et al. Deep level optical spectroscopy of GaN nanorods. *J. Appl. Phys.*, 106(053712), 2009.
- [54] X Duan and C Lieber. Laser-assisted catalytic growth of single crystal GaN nanowires. *C. J. Am. Chem. Soc*, 122, 2011.

- [55] S. Hersee et al. Threading defect elimination in GaN nanowires. *Journal of Materials Research*, 26(17), 2011.
- [56] W.Guo, M.Zhang, A.Banerjee, and P.Bhattacharya. Catalyst-free InGaN/GaN nanowire light emitting diodes grown on (001) silicon by molecular beam epitaxy. *Nano Lett.*, 10, 2010.
- [57] W. Guo, A.Banerjee, P.Bhattacharya, and B.Ooi. InGaN/GaN disk-in-nanowire white light emitting diodes on (001) silicon. *Appl. Phys. Lett.*, 98(193102), 2011.
- [58] J Johnson et al. Single gallium nitride nanowire lasers. *Nature Mater.*, 1, 2002.
- [59] T Frost et al. Monolithic electrically injected nanowire array edge-emitting laser on (001) silicon. *Nanoletters.*, 14(8), 2014.
- [60] S.Deshpande, J.Heo, A.Das, and P.Bhattacharya. Electrically driven polarized single-photon emission from an InGaN quantum dot in a GaN nanowire. *Nature Communications*, 4(1675), 2013.
- [61] S.Deshpande and P.Bhattacharya. An electrically driven quantum dot-in-nanowire visible single photon source operating up to 150 k. *Appl. Phys. Lett.*, 103(24), 2013.
- [62] M Kotrla et al. Atomistic aspects of epitaxial growth. *Springer*, 1, 2002.
- [63] M. Knelangen. Nucleation and growth of group iii-nitride nanowires. (*Doctoral Dissertation*), 2013.
- [64] R.Calarco et al. Nucleation and growth of GaN nanowires on Si(111) performed by molecular beam epitaxy. *Nano Lett.*, 7, 2007.
- [65] K. Bertness, A. Roshko, L. Mansfield, T.Harvey, and N.Sanford. Nucleation conditions for catalyst-free GaN nanowires. *J.Cryst. Growth*, 310, 2008.
- [66] K Grossklaus, A Banerjee, S Jahangir, P Bhattacharya, and J Millunchick. Misorientation defects in coalesced self-catalyzed GaN nanowires. *Journal of Crystal Growth*, 371, 2013.
- [67] J. Ristic et al. On the mechanism of spontaneous growth of III-nitride nano columns by plasma assisted molecular beam epitaxy. *Journal of Cryst. Growth*, 310(4035), 2008.
- [68] V.Consonni et al. Nucleation mechanisms of self-induced GaN nanowires grown on an amorphous interlayer. *Phys. Rev. B*, 83(035310), 2011.
- [69] L. Lymparakis and J. Neugebauer. Large anisotropic adatom kinetics on nonpolar GaN surfaces: Consequences for surface morphologies and nanowire growth. *Phys. Rev. B*, 79(241308), 2009.

- [70] R Debnath et al. Mechanism of molecular beam epitaxy growth of gan nanowires on si(111). *App. Phys. Lett.*, 90(123117), 2007.
- [71] S.Fernandez-Garrido, J.Grandal, E. Calleja, M.Sanchez-Garcia, and D.Lopez-Romero. A growth diagram for plasma-assisted molecular beam epitaxy of GaN nanocolumns on Si(111). *J.Appl.Phys.*, 106(126102), 2009.
- [72] M Zhang, P Bhattacharya, W Guo, and A Banerjee. Mg doping of gan grown by plasma-assisted molecular beam epitaxy under nitrogen-rich conditions. *App. Phys. Lett.*, 96(13), 2010.
- [73] G. Li et al. Nature and elimination of yellow-band luminescence and donor acceptor emission of undoped gan. *Appl. Phys. Lett.*, 74(19), 1999.
- [74] L Tan, R Martin, K. O'Donnell, and I Watson. Photoluminescence and phonon satellites of single InGaN/GaN quantum wells with varying GaN cap thickness. *Appl. Phys. Lett.*, 89(101910), 2009.
- [75] Y.Varshni. Temperature dependence of the energy gap in semiconductors. *Physica*, 39, 1967.
- [76] C.Chen, Y.Lu, D.Yeh, and C.Yang. Influence of the quantum-confined stark effect in an InGaN/GaN quantum well on its coupling with surface plasmon for light emission enhancement. *Appl. Phys. Lett.*, 90(183114), 2007.
- [77] A Das. Strong Coupling and Magnetic Field Effects in Microcavity Light Sources . Thesis, 2012.
- [78] H.Zhao et al. Analysis of internal quantum efficiency and current injection efficiency in iii-nitride light-emitting diodes. *Journal of Display Tech.*, 9(4), 2013.
- [79] H.Schomig et al. Probing individual localization centers in an InGaN/GaN quantum well. *Phys. Rev. Lett.*, 92(106802), 2004.
- [80] J. Renard, R. Songmuang, C. Bougerol, B. Daudin, and B. Gayral. Exciton and biexciton luminescence from single GaN/AlN quantum dots in nanowires. *Nano Lett.*, 8(7), 2008.
- [81] R. Oliver, A. Jarjour, R. Taylor, A. Tahraoui, Y. Zhang, M. Kappers, and C. Humphreys. Growth and assessment of InGaN quantum dots in a microcavity: A blue single photon source. *Mater. Sci. Eng. B*, 147, 2008.
- [82] J Kim, O Benson, H Kan, and Y Yamamoto. A single photon turnstile device. *Nature*, 397(500), 1999.
- [83] S. Kako, M.Holmes, S.Sargent, M.Burger, D. J. As, and Y. Arakawa. Single-photon emission from cubic GaN quantum dots. *Appl. Phys. Lett.*, 104(011101), 2014.

- [84] A. Jarjour, R. Taylor, R. Oliver, M. Kappers, C. Humphreys, and A. Tahraoui. Cavity-enhanced single-photon emission from a single InGaN quantum dot. *Appl. Phys. Lett.*, 91(052101), 2007.
- [85] S. Bounouar, M. Elouneig-Jamroz, M. Hertog, C. Morchutt, E. Bellet-Amalric, R. Andre, C. Bougerol, Y. Genuist, J.-P. Poizat, S. Tatarenko, and K. Kheng. Ultrafast room temperature single-photon source from nanowire-quantum dot. *Nano Lett.*, 12, 2012.
- [86] P. Michler, A. Imamoglu, M. Mason, P. Carson, G. Strouse, and S. Buratto. Quantum correlation among photons from a single quantum dot at room temperature. *Nature*, 406(968), 2000.
- [87] S Strauf et al. High-frequency single-photon source with polarization control. *Nature Photonics*, 1:704–708, 2007.
- [88] J Jang, S Park, and T Seong. High Quality Non-Alloyed Pt Ohmic Contacts to P-Type GaN Using Two-Step Surface Treatment. *MRS Proceedings*, 595, 1999.
- [89] J Kim. Low resistance Pd/Au ohmic contacts to p-type GaN using surface treatment . *Appl. Phys. Lett.*, 73(2953), 1998.
- [90] A Shields et al. Generation of single photons using semiconductor quantum dots. *Nano-Physics and BioElectronics A New Odyssey*, Elsevier, New York, 2002.
- [91] J.Wang, M.Gudiksen, X.Duan, Y.Cui, and C.Lieber. Highly polarized photoluminescence and photodetection from single indium phosphide nanowires. *Science*, 293, 2001.
- [92] S Chichibu, T Sota, and S Nakamura. Spontaneous emission of localized excitons in InGaN single and multiquantum well structures. *Appl. Phys. Lett.*, 69, 1996.
- [93] Y Jho, J Yahng, E Oh, and K Kim. Field-dependent carrier decay dynamics in strained In_xGa_{1-x}N/GaN quantum wells. *Phys. Rev. B*, 66(035334), 2002.
- [94] Y Kawakami et al. Origin of high oscillator strength in green-emitting InGaN/GaN nanocolumns. *Appl. Phys. Lett.*, 89(163124), 2006.
- [95] S Strauf et al. High-frequency single-photon source with polarization control. *Nat. Photonics*, 1, 2007.
- [96] S Kremling et al. Single photon emission from InGaN/GaN quantum dots up to 50 K. *App. Phys. Lett.*, 100(06115), 2012.
- [97] L Zhang, C Teng, P Ku, and H Deng. Electrically driven single-photon emission from site-controlled ingan/gan quantum dots. *CLEO QELS Fundamental Science. Optical Society of America*, 2014.

- [98] W Quitsch et al. Electrically driven single photon emission from a CdSe/ZnSSe/MgS semiconductor quantum dot. *Phys. Status Solidi C*, 11(7-8), 2014.
- [99] S.Nakamura et al. Room-temperature continuous-waveoperation of InGaN multi-quantum-well structure laser diodes. *Appl. Phys. Lett.*, 69(26), 1996.
- [100] T. Tanaka K. Okamoto, J. Kashiwagi and M. Kubota. Nonpolar μ -plane InGaN multiplequantum well laser diodes with a lasing wavelength of 499.8 nm. *Appl. Phys. Lett.*, 94(7), 2009.
- [101] M.Zhang, P. Bhattacharya, and W. Guo. InGaN/GaN self-organized quantum dot green light emitting diodes with reduced efficiency droop. *Appl. Phys. Lett.*, 97(011103), 2010.
- [102] T Wu, Y Lin, H Huang, and J Singh. Electronic and optical properties of ingan quantum dot based light emitters for solid state lighting. *J. Appl. Phys.*, 105(013117), 2009.
- [103] S. Schulz and E. O'Reilly. Theory of reduced built-in polarization field in nitride-based quantum dots. *Phys. Rev. B*, 82(033411), 2010.
- [104] A. Banerjee. Iii nitride self-assembled quantum dot light emitting diodes and lasers. (*Doctoral Dissertation*), 2014.
- [105] M. Monemar. Fundamental energy gap of GaN from photoluminescence excitation spectra. *Phys. Rev. B*, 10(676), 1974.
- [106] S. Christopoulos et al. Direct generation of linearly polarized photon emission with designated orientations from site-controlled InGaN quantum dots. *Phys. Rev. Lett.*, 98(126405), 2007.
- [107] P.Bhattacharya et al. Direct generation of linearly polarized photon emission with designated orientations from site-controlled InGaN quantum dots. *Phys. Rev. Lett.*, 112(236802), 2014.
- [108] G Bastard, E Mendez, L Chang, and L Esaki. Exciton binding energy in quantum wells. *Phys. Rev. B*, 26(1974), 1982.
- [109] M. Winkelnkemper et al. Polarized emission lines from A- and B-type excitonic complexes in single InGaN/GaN quantum dots. *J. Appl. Phys.*, 101(113708), 2007.
- [110] A. Lundskog et al. Direct generation of linearly polarized photon emission with designated orientations from site-controlled InGaN quantum dots. *Light: Sci. Appl.*, 3(e139), 2014.
- [111] S.Jahangir et al. Red-Emitting ($\lambda = 610nm$) $In_{0.51}Ga_{0.49}N/GaN$ Disk-in-Nanowire Light Emitting Diodes on Silicon. *IEEE J. Quantum Electron.*, 50(7), 2014.

- [112] A.Das et al. Room Temperature Ultralow Threshold GaN Nanowire Polariton Laser. *Phys. Rev. Lett.*, 107(066405), 2011.
- [113] J Heo, S Jahangir, B Xiao, and P Bhattacharya. Room-Temperature Polariton Lasing from GaN Nanowire Array Clad by Dielectric Microcavity. *Nanoletters*, 13(6), 2013.
- [114] S Jahangir, M Mandl, M Strassburg, and Bhattacharya P. Molecular beam epitaxial growth and optical properties of red-emitting ($\lambda = 650\text{nm}$) InGaN/GaN disks-in-nanowires on silicon. *IEEE J. Quantum Electron.*, 102(7), 2013.
- [115] T.Ng et al. Red to Near-Infrared Emission from InGaN/GaN Quantum-Disks-in-Nanowires LED. *CLEO: Science and Innovations*, SM2J, 2014.
- [116] H. Nyugen et al. p-Type Modulation Doped InGaN/GaN Dot-in-a-Wire White-Light-Emitting Diodes Monolithically Grown on Si(111). *Nanoletters*, 11(5), 2011.
- [117] J Urayama, T Norris, J Singh, and P Bhattacharya. Observation of Phonon Bottleneck in Quantum Dot Electronic Relaxation. *Phys. Rev. Lett.*, 86(4930), 2001.
- [118] T Frost et al. InGaN/GaN Quantum Dot Red ($\lambda = 630 \text{ nm}$) Laser. *IEEE J. Quantum Electron*, 49(923), 2013.
- [119] B Hakki and T Paoli. Gain spectra in GaAs double-heterostructure injection lasers. *J. Appl. Phys.*, 46(3), 1975.
- [120] Y Miyake and M Asada. Spectral Characteristics of Linewidth Enhancement Factor of Multidimensional Quantum Wells. *Jpn. J. Appl. Phys*, 28(1280), 1989.
- [121] A Ukanov, A Stintz, P Eliseev, and K Malloy. Comparison of the carrier induced refractive index, gain, and linewidth enhancement factor in quantum dot and quantum well lasers. *Appl. Phys. Lett.*, 84(1058), 2004.
- [122] S Bhowmick et al. High Performance $\text{InAs}/\text{In}_{0.53}\text{Ga}_{0.23}\text{Al}_{0.24}\text{As}/\text{InP}$ Quantum Dot $1.55\mu\text{m}$ Tunnel Injection Laser. *IEEE J. Quantum Electron.*, 50(1), 2013.
- [123] K Nakajima et al. Effects of misfit dislocations and AlN buffer layer on the GaInN/GaN phase diagram of the growth mode. *J. Appl. Phys.*, 89(1), 2001.
- [124] T Schumann, T Gotschke, F Limbach, T Stoica, and R Calarco. Selective-area catalyst-free MBE growth of GaN nanowires using a patterned oxide layer. *Nanotechnology*, 22(095603), 2011.
- [125] J.Heo. Nanoscale lasers with optical microcavities. (*Doctoral Dissertation*), 2011.

- [126] J.Heo, W. Guo, and P. Bhattacharya. Monolithic single GaN nanowire laser with photonic crystal microcavity on silicon. *Appl. Phys. Lett.*, 98(021110), 2011.
- [127] K. Hennessy et al. Quantum nature of a strongly coupled single quantum dot cavity system. *Nature*, 445(22), 2007.
- [128] J.Raithmaier et al. Strong coupling in a single quantum dot semiconductor microcavity system. *Nature*, 432, 2004.
- [129] M Pelton. An efficient source of single photons: a single quantum dot in a micropost microcavity. PhD Thesis, 2002.